

Searches for Particle Dark Matter

Dark stars, dark galaxies, dark halos and global supersymmetric fits

Pat Scott

Doctoral Thesis in Theoretical Physics

Department of Physics
Stockholm University
Stockholm 2010



Stockholm
University

Doctoral Thesis in Theoretical Physics

Searches for Particle Dark Matter

Dark stars, dark galaxies, dark halos and global supersymmetric fits

Pat Scott



**Stockholm
University**



Oskar Klein Centre for
Cosmoparticle Physics

and

Cosmology, Particle Astrophysics
and String Theory

Department of Physics
Stockholm University
SE-106 91 Stockholm

Stockholm, Sweden 2010

Cover images, clockwise from top left: Artist's impression of a black hole in a globular cluster; G. Bacon (STScI), NASA. An 'artistic simulation' of the collision which produced the Bullet Cluster (see Figure 1.3); NASA/CXC/M. Weiss. A false-colour X-ray image of the Galactic Centre; D. Wang (UMass) et al., CXC, NASA. Computer-generated model image of the *Fermi* Gamma Ray Space Telescope; General Dynamics C4 Systems/NASA. *Inset:* An artist's impression of a protostar, which dark stars at the Galactic Centre may resemble; D. Darling.

ISBN 978-91-7447-031-4 (pp. i–xiv, 1–84)

pp. i–xiv, 1–84 © Patrick Scott, 2010

Printed by Universitetsservice US-AB, Stockholm, Sweden, 2010.

Figures 1.1, 1.4, 1.5, 2.1 and 4.1 used with permission.

Typeset in pdfL^AT_EX

Abstract

The identity of dark matter is one of the key outstanding problems in both particle and astrophysics. In this thesis, I describe a number of complementary searches for particle dark matter. I discuss how the impact of dark matter on stars can constrain its interaction with nuclei, focussing on main sequence stars close to the Galactic Centre, and on the first stars as seen through the upcoming James Webb Space Telescope. The mass and annihilation cross-section of dark matter particles can be probed with searches for gamma rays produced in astronomical targets. Dwarf galaxies and ultracompact, primordially-produced dark matter minihalos turn out to be especially promising in this respect. I illustrate how the results of these searches can be combined with constraints from accelerators and cosmology to produce a single global fit to all available data. Global fits in supersymmetry turn out to be quite technically demanding, even with the simplest predictive models and the addition of complementary data from a bevy of astronomical and terrestrial experiments; I show how genetic algorithms can help in overcoming these challenges.

Key words: dark matter, supersymmetry, gamma rays, dwarf galaxies, stellar evolution, cosmological perturbations, phase transitions, statistical techniques

List of Papers

Papers included in this thesis

- Paper I** Malcolm Fairbairn, Pat Scott & Joakim Edsjö. *The zero age main sequence of WIMP burners*, Phys. Rev. D **77**, 047301 (2008) [arXiv:0710.3396](#).
- Paper II** Pat Scott, Malcolm Fairbairn & Joakim Edsjö. *Dark stars at the Galactic Centre – the main sequence*, MNRAS **394**, 82–104 (2009) [arXiv:0809.1871](#).
- Paper III** Pat Scott & Sofia Sivertsson. *Gamma-rays from ultracompact primordial dark matter minihalos*, Phys. Rev. Lett. **103**, 211301 (2009) [arXiv:0908.4082](#).
- Paper IV** Pat Scott, Jan Conrad, Joakim Edsjö, Lars Bergström, Christian Farnier & Yashar Akrami. *Direct Constraints on Minimal Supersymmetry from Fermi-LAT Observations of the Dwarf Galaxy Segue 1*, JCAP **01**, 031 (2010) [arXiv:0909.3300](#).
- Paper V** Yashar Akrami, Pat Scott, Joakim Edsjö, Jan Conrad & Lars Bergström. *A Profile Likelihood Analysis of the Constrained MSSM with Genetic Algorithms*, JHEP in press, (2010) [arXiv:0910.3950](#).
- Paper VI** Erik Zackrisson, Pat Scott, Claes-Erik Rydberg, Fabio Iocco, Bengt Edvardsson, Göran Östlin, Sofia Sivertsson, Adi Zitrin, Tom Broadhurst & Paolo Gondolo. *Finding high-redshift dark stars with the James Webb Space Telescope*, Submitted to ApJ, (2010) [arXiv:1002.3368](#).

Papers and proceedings not included in this thesis

Paper VII Martin Asplund, Nicolas Grevesse, A. Jacques Sauval & Pat Scott. *The chemical composition of the Sun*, Ann. Rev. A&A **47**, 481–522 (2009) [arXiv:0909.0948](#).

Paper VIII Pat Scott, Martin Asplund, Nicolas Grevesse & A. Jacques Sauval. *On the solar nickel and oxygen abundances*, ApJ **691**, L119–L122 (2009) [arXiv:0811.0815](#).

Paper IX Pat Scott, Martin Asplund, Nicolas Grevesse & A. Jacques Sauval. *Line formation in solar granulation. VII. CO lines and the solar C and O isotopic abundances*, A&A **456**, 675–688 (2006) [arXiv:astro-ph/0605116](#).

Proceeding X Nicolas Grevesse, Martin Asplund, A. Jacques Sauval & Pat Scott. *The chemical composition of the Sun*, Ap&SS special issue *Proceedings of the 5th HELAS Asteroseismology Workshop: Synergies between solar and stellar modelling*, Online First, Feb 11 (2010).

Proceeding XI Pat Scott, Joakim Edsjö & Malcolm Fairbairn. *The Dark-Stars code: a publicly available dark stellar evolution package*, Proceedings of *Dark Matter in Astroparticle and Particle Physics: Dark 2009* (eds. H. K. Klapdor-Kleingrothaus and I. V. Krivosheina), 320–327, World Scientific Publishing, Singapore (2010) [arXiv:0904.2395](#).

Proceeding XII Pat Scott, Malcolm Fairbairn & Joakim Edsjö. *Impacts of WIMP dark matter upon stellar evolution: main-sequence stars*, Proceedings of *Identification of Dark Matter 08 PoS(idm2008)*, 073 (2008) [arXiv:0810.5560](#).

Proceeding XIII Pat Scott, Joakim Edsjö & Malcolm Fairbairn. *Low mass stellar evolution with WIMP capture and annihilation*, Proceedings of *Dark Matter in Astroparticle and Particle Physics: Dark 2007* (eds. H. K. Klapdor-Kleingrothaus and G. F. Lewis), 387–392, World Scientific Publishing, Singapore (2008) [arXiv:0711.0991](#).

Contents

Abstract	iii
List of Papers	v
Contents	vii
Acknowledgments	ix
Preface	xi
I Introduction	1
1 The need for dark matter	3
1.1 Kinematics	3
1.2 Gravitational lensing	5
1.3 The large scale structure of the Universe	7
1.4 Big bang nucleosynthesis	8
1.5 Concordance cosmology	11
2 Models for dark matter	15
2.1 The good, the bad and the ugly	16
2.2 Axions	18
2.3 WIMPs	20
2.3.1 Thermal relics	21
2.3.2 The hierarchy problem	24
2.4 Supersymmetry	25
2.4.1 General features	26
2.4.2 Supersymmetric WIMPs	31
2.4.3 SUSY breaking and parameterisations	33

2.4.4	SUSY scanning	37
2.5	Gravitinos and Axinos	37
2.6	Sterile neutrinos	38
2.7	Other candidates	39
3	Searches for dark matter	41
3.1	Direct detection	41
3.2	Indirect detection	44
3.3	Accelerator searches	48
3.4	Dark stars	50
3.5	High-energy solar neutrinos	51
3.6	Searches for other dark matter candidates	52
4	Nuisances	55
4.1	The distribution of dark matter	55
4.2	Production and propagation of cosmic rays	57
4.3	Standard Model nuisances	59
5	Summary of results	61
5.1	Outlook	70
	References	73
II	Papers	85
	Paper I: The zero age main sequence of WIMP burners	87
	Paper II: Dark stars at the Galactic Centre – the main sequence	93
	Paper III: Gamma-rays from ultracompact primordial dark matter minihalos	119
	Paper IV: Direct constraints on minimal supersymmetry from Fermi-LAT observations of the dwarf galaxy Segue 1	127
	Paper V: A profile likelihood analysis of the Constrained MSSM with genetic algorithms	151
	Paper VI: Finding high-redshift dark stars with the James Webb Space Telescope	201

Acknowledgments

My first and foremost thanks go to Joakim Edsjö for his encouraging and enthusiastic supervision, and for his energy and creativity; these have made working together a genuine pleasure. Thanks also to my secondary supervisors Lars Bergström and Jan Conrad, for much sage advice on scientific matters and the practicalities of working as a physicist. Thanks to all three for the confidence they have shown in me, and the scientific and organisational independence they have granted me here in Stockholm.

I have also had the benefit of many other highly-skilled and motivated collaborators in the work of this thesis; without the particular efforts of Yashar Akrami, Malcolm Fairbairn, Christian Farnier, Sofia Sivertsson and Erik Zackrisson, many of these projects would not have come to fruition. I have also benefited greatly from helpful discussions on various topics with Marcus Berg, Ross Church, Melvyn Davies, Steen Hansen, Fabio Iocco, Paolo Gondolo, Ariel Goobar, Antje Putze, Are Raklev, Riccardo Rando, Joachim Ripken, Chris Savage, Aldo Serenelli, Roberto Trotta and the Dark Matter & New Physics Group within the *Fermi*-LAT Collaboration. Although our work together is not part of this thesis, Martin Asplund, Nicolas Grevesse and Jacques Sauval have also been steady sources of inspiration and wisdom over the last six years.

My thanks also to the other students and postdocs of the OKC and its forerunner, HEAC, for the pleasure of their company, lunch table, Swedish lessons, couch or beer glass over the last three and a half years, and to Yashar, for managing to put up so stoically with sharing an office with me all this time.

Thanks to my parents and sister Adele for all their encouragement over the years, and to my wife Susan for her companionship and unwavering support, from the moment I suggested moving overseas to do my PhD to its ultimate completion.

I gratefully acknowledge travel funding from the IAU Commission 46 Exchange of Astronomers Program, the European Network of Theoretical Astroparticle Physics ILIAS/N6 under contract number RII3-CT-2004-506222, the Helge Axelsson Johnsons Foundation, the C. F. Liljevalchs Scholarship Fund and the G & E Kobbs Scholarship Fund, as well as general financial support from the Swedish Research Council (Vetenskapsrådet) through grants to HEAC and the OKC.

Preface

This thesis deals with strategies for detecting and identifying dark matter. Identification means somewhat more than simply establishing that dark matter is a particle with a certain mass, and belongs to one or another proposed phenomenological candidate class (WIMPs, axions, etc). Although this alone would be a tremendous achievement, it would be just the first step. In my opinion, it is the second that is actually the more interesting (and difficult) of the two.

Rather, true identification means establishing which particle (or particles) are responsible for dark matter, and characterising the actual field theory to which they belong. The papers included in this thesis all work towards achieving the first of these goals, but some (Paper IV and Paper V especially) also make contributions towards the second.

Thesis plan

This thesis is divided into two parts: Part I gives an introduction to the field and my work in particular, and Part II provides the included papers. Chapter 1 of Part I describes the observational evidence for dark matter, Chapter 2 details the various models proposed to explain it, and Chapter 3 discusses the strategies which may be used to search for it. Chapter 4 gives a brief exposition of some of the most important uncertainties entering dark matter searches, and Chapter 5 summarises the results presented in the papers of Part II.

The papers included in this thesis span quite a broad range of topics within the theme of dark matter searches. Many of them include introductory sections with specific background material on the physics, existing literature and computational techniques relevant to their respective topics. Each paper also includes extensive discussion and interpretation of the results it presents; as one should expect, they are quite self-contained and largely self-explanatory. In most cases, it was I who was responsible

for actually writing those sections (or at least extensively revising them). Instead of simply repeating material already included in the papers themselves, I have thus intentionally written the first four Chapters of Part I with the character of a textbook-level introductory review, so as to explain and justify the broader scientific context in which the six papers have been written. In this undertaking I have not aimed for comprehensive coverage of the literature. Full historical references and further details on the topics covered in Chapters 1–4 can be found in extensive review articles by Jungman, Kamionkowski & Griest (1996), Bergström (2000) and Bertone, Hooper & Silk (2005), as well as the recent reference volume edited by Bertone (2010).

Unlike in some theses, the included papers of Part II should not be considered appendices. They are in fact the main body of this thesis, equivalent to Results, Discussion and Conclusion chapters in a traditional monograph. Their main results, figures and conclusions are summarised for the reader’s convenience in Chapter 5, but the actual papers should be recognised as the definitive exposition of the work contained in this thesis. In short, the ethos I have adopted is that Part I should essentially contain information not provided already by Part II; there should be as little regurgitation as possible of content which is already contained in the six included manuscripts. Accordingly, Chapter 5 also places the results of Part II back into the broader context established by Chapters 1–4, and presents an outlook for future work.

Contribution to papers

My contribution to the included papers is as follows. For Paper I, I wrote and ran the stellar evolution code (as opposed to the static stellar structure code), and revised the manuscript. I discussed methods, results and conclusions together with the other authors. For Paper II, I designed most of the study, wrote the code and ran it using orbital and velocity data provided by Malcolm, and the results of neutrino simulations performed by Joakim. We discussed methods, results and conclusions together. I wrote the paper. I had the original idea for Paper III, designed the bulk of the study, wrote most of the paper and performed all calculations except for adiabatic contractions, which were done by Sofia. We interpreted results together. I designed almost all aspects of the work in Paper IV, with significant input on statistical matters from Jan. I wrote the software and ran it using data reduced by Christian, and wrote the paper. I interpreted results together with the other authors. For Paper V, I made

large contributions to the design and implementation of the study. I wrote sections of the paper and revised the remainder. I also organised the constituent physical codes into a consistent and functional starting point, from which Yashar added the genetic algorithm code and ran it. We discussed and interpreted results together with the other authors. For **Paper VI**, I helped design the study, wrote sections of the paper and computed TLUSTY model atmospheres. I discussed methods and results primarily with Erik, Fabio and Sofia.

Pat Scott
Stockholm, March 2009

Part I

Introduction

Chapter 1

The need for dark matter

Dark matter has become such an established paradigm in modern astrophysics and particle physics that its existence is generally accepted with little explanation. Such blithe and widespread adoption of a cosmology in which an unknown matter plays the pivotal role has led some to become a little sceptical about its existence. It is worth reminding ourselves, from time to time, of the strong and compelling evidence on which this paradigm actually stands. As it so happens, we will also pick up a good deal of information along the way about what properties dark matter must have.

1.1 Kinematics

The earliest identification of dark matter came from the velocity dispersions of galaxies within clusters. [Zwicky \(1933\)](#) noticed that the outer members of the Coma cluster were moving far too quickly to be merely tracing the gravitational potential of the visible cluster mass. The only way the observed velocities of the cluster members could be reconciled with the virial theorem was to postulate that the cluster also contained another large, but unseen, mass component: dark matter. Today, an equivalent technique is used to weigh clusters in large-scale X-ray surveys (e.g. [Vikhlinin et al. 2006](#); [Pacaud et al. 2007](#)). In this case, because the hot, X-ray-emitting intracluster medium is entirely virialised, its temperature can be used to infer the total potential energy of the system, and therefore the cluster mass. Such surveys consistently confirm [Zwicky's](#) finding that clusters contain far more dark than luminous matter.

It was not until similar effects were seen at the galactic level by Rubin and collaborators ([Rubin & Ford 1970](#); [Rubin et al. 1978, 1985](#)) that the

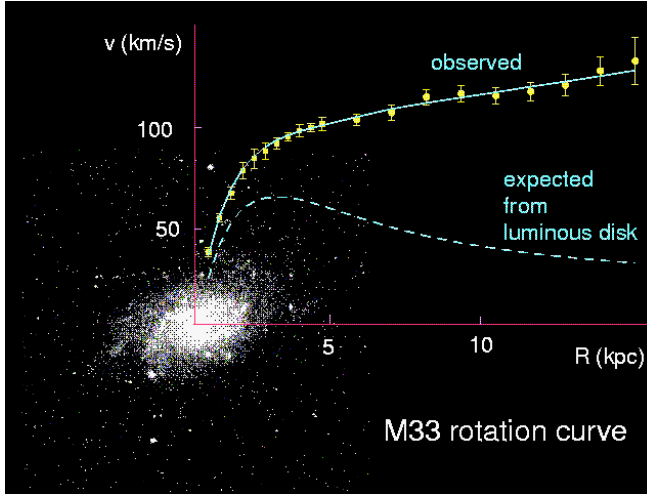


Figure 1.1. The observed rotation curve of the dwarf spiral galaxy M33, and the curve one would predict purely on the basis of the luminous disc. The fact that the curve is flatter than predicted suggests the presence of a halo of dark matter, extending to large galactic radii. From [Bergström \(2000\)](#).

idea of dark matter really began to gain traction. Like the galaxies in the outer region of the Coma cluster, stars in the outer reaches of spiral galaxies are seen to rotate far more quickly than would be expected if each galaxy consisted only of the matter visible in stars and gas. An example of such anomalous circular velocities is shown in Fig. 1.1 for a dwarf spiral galaxy, M33. Here, the rotation curve expected purely on the basis of the stellar mass drops off markedly at long distances from the centre of the galaxy, whereas the observed curve is far flatter. This can be explained by the presence of an additional halo of dark matter, far more extended than the observed stellar disk.

Similarly, the observed proportionality between the luminosity L of spiral galaxies and the maximum circular velocity V_{\max} of their members,

$$L \propto V_{\max}^{\beta}, \quad \beta = 3 \sim 4, \quad (1.1)$$

known as the Tully-Fisher relation ([Tully & Fisher 1977](#)), can be explained by dark matter and the virial theorem ([Aaronsen et al. 1979](#)). The virial theorem leads to a direct correspondence between the total galactic mass M and V_{\max} . The self-similarity of hierarchically-formed dark matter

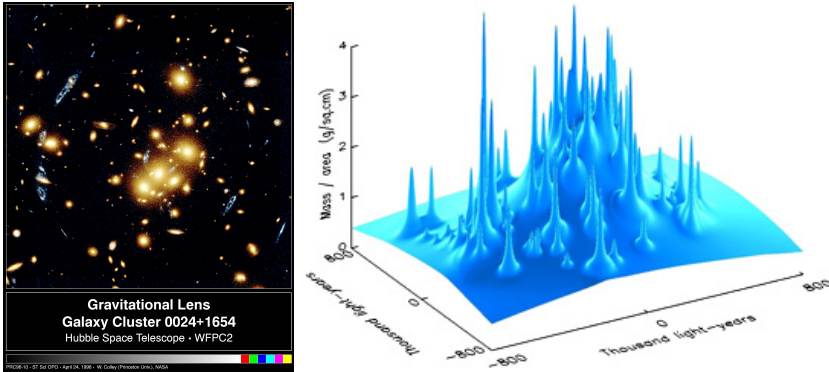


Figure 1.2. An image of a gravitationally lensed cluster (left), along with the corresponding mass map of the foreground cluster. In the image on the left, the foreground cluster can be seen in yellow, with the lensed image of the background cluster visible in blue. The reconstructed mass map shows a large, broad peak around the centre of the cluster which is not visible in the optical image, indicating the presence a massive dark halo. Credit: Greg Kochanski, Ian Dell’Antonio, and Tony Tyson (Bell Labs, Lucent Technologies). See also [Tyson et al. \(1998\)](#).

halos (e.g. [Navarro, Frenk & White 1996](#)) and their resident baryonic disks causes this to be a power-law dependency. Assuming that for a given class of spiral galaxies (early-type, late-type, etc.) the mass-to-light ratio (M/L) is approximately constant, the relationship translates directly into a power-law dependency of L upon V_{\max} . A similar argument holds for the analogous relation for elliptical galaxies, the Faber-Jackson relation ([Faber & Jackson 1976](#)).

1.2 Gravitational lensing

According to General Relativity, the presence of any mass causes the space in its vicinity to curve. Curvature of space implies curvature of geodesics, which results in bending of light rays around massive bodies. In this way, light from background objects can be ‘lensed’ by massive foreground objects, as the light rays passing through the foreground objects’ gravitational field are bent towards a distant observer. At the simplest level, this causes a background object to appear brighter than it otherwise would. This phenomenon provides a clean and unambiguous means by which to probe the mass distribution in a foreground object.

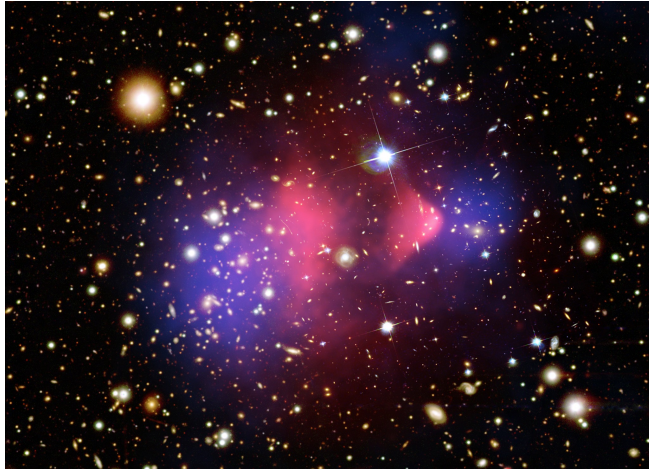


Figure 1.3. Composite image of the colliding ‘Bullet Cluster’, obtained with gravitational lensing. The lensing mass map is shown in blue, and the X-ray observations tracing the gas component are shown in pink. The offset of the mass and gas maps indicates that the mass of each cluster does not consist predominantly of gas, nor does it track the gas. Whilst the gas has collided with and exerted friction on the other cloud, leading to the characteristic ‘punch-through’ shape of the cluster to the right, the bulk of the mass has simply passed through the collision unimpeded. This proves that the majority of the matter in each cluster is collisionless dark matter. X-ray data: NASA/CXC/CfA/[Markevitch \(2006\)](#). Lensing Map: NASA/STScI; ESO WFI; Magellan/U.Arizona/[Clowe et al. \(2006\)](#). Optical data: NASA/STScI; Magellan/U.Arizona/[Clowe et al. \(2006\)](#).

Distant clusters lensed by closer ones show evidence of extensive gravitational lensing, far more than can be explained by the observed distribution of luminous matter in the foreground cluster (e.g. [Tyson et al. 1998](#); [Massey et al. 2007](#)). Fig. 1.2 gives an example of such a cluster, exhibiting a large, smooth mass component in the lensing map to the right, which is not accounted for by the distribution of luminous matter shown in the optical image to the left.

Probably the most famous example of a dark matter lens is the so-called Bullet Cluster ([Clowe et al. 2006](#)), shown in Fig. 1.3. This object is in fact two clusters that have recently collided. In this case, not only does the lensing map (in blue) exhibit large amounts of dark matter not evident in the X-ray gas map (in pink), but the distribution of the two components also provides crucial insight into the properties of the dark matter. That is, the dark matter halos have passed straight through both

the gas clouds and each other, and appear essentially undisturbed after the collision. The gas clouds, on the other hand, have clearly exerted friction on each other as they have collided, leading to the characteristic ballistic shape of the rightmost cloud. This shows that dark matter does not necessarily have to track luminous matter in any way, and that it does not interact strongly with either gas or itself; this means that it is effectively collisionless.

1.3 The large scale structure of the Universe

On large scales, the Universe shows a wealth of structure: galaxies are gathered into clusters, clusters are part of superclusters, and superclusters are arranged into large-scale sheets, filaments and voids. This cosmic scaffolding has been revealed by large-scale surveys such as 2dFGRS (the 2-degree Field Galaxy Redshift Survey; [Colless et al. 2001](#)) and SDSS (the Sloan Digital Sky Survey; [Tegmark et al. 2004](#)). Presumably, the pattern of galactic superstructure reflects the history of gravitational clustering of matter since the Big Bang. If dark matter were present during structure formation, it should have influenced the pattern of large-scale structure we see today.

Large-scale cosmological ‘N-body’ simulations (e.g. [Navarro et al. 1996](#); [Springel et al. 2005](#); [Diemand et al. 2007](#); [Springel et al. 2008a](#); [Diemand et al. 2008](#)) demonstrate that the observed large-scale structure of luminous matter could only have been formed in the presence of a substantial amount of dark matter. Furthermore, the bulk of dark matter must be both cold and non-dissipative for the correct structures to be produced. ‘Cold’ in this context means that it moves very non-relativistically, and so has a short free-streaming length (less than the size of a gas cloud undergoing gravitational collapse, for example). Being cold means that the dark matter can gather gravitationally on small scales and so seed galaxy formation, but being non-dissipative prevents it from cooling and collapsing with the luminous matter, which would produce larger and more abundant galactic disks than are observed. Hot (highly relativistic) and warm (borderline relativistic) dark matter could still make up a fraction of the total dark matter, though just how large a fraction depends critically upon how warm that fraction is.

Large-scale galaxy surveys not only provide information as to the amount and pattern of structure present in the Universe, but also a handle on the total mass contained within it (e.g. [Tegmark et al. 2004](#); [Cole et al.](#)

2005; Percival et al. 2010). To a first approximation, the characteristic size of baryonic density perturbations which can survive until matter-radiation equality (and therefore collapse to form galaxies and clusters) is set by the mean density of baryons in the Universe (Silk 1968); smaller perturbations are destroyed by radiative and neutrino damping, larger ones fragment. In the presence of an additional matter component which gravitates but does not couple radiatively to the baryons, the power spectrum of perturbations which ultimately survive to form galaxies is modified by the enhanced gravitational clustering. The resulting large-scale galaxy power spectrum is thus strongly dependent upon the total matter density of the Universe, and weakly dependent upon the fraction of matter contained in baryons. Recent surveys indicate a total matter (i.e. dark plus luminous matter) density of $\Omega_m \equiv \rho_m/\rho_c \approx 0.29$ (Percival et al. 2010), where ρ_c is the critical density required to close the Universe.

1.4 Big bang nucleosynthesis

A critical prediction of the hot Big Bang cosmology is that protons and neutrons were fused in the primordial fireball to create the light elements, as it cooled to temperatures of the order of an MeV. Modulo the effect of neutrinos, the resulting elemental abundances depend only on the nuclear reaction rates and the baryon-to-photon ratio (η) at the time. Laboratory and theoretically-calculated nuclear reaction rates (e.g. Angulo et al. 1999) can therefore be used to derive the primordial abundances of the elements as a function of η (e.g. Coc et al. 2004; Steigman 2007; Iocco et al. 2009), as shown in Fig. 1.4.

The parameter η is completely equivalent to $\Omega_b h^2$ (up to a constant of proportionality), where Ω_b is the baryon density of the Universe and $h \equiv H_0/100 \text{ km s}^{-1} \text{ Mpc}^{-1}$ is the dimensionless Hubble parameter. $H_0 \equiv v/d$ is the Hubble constant, describing the speed v at which galaxies at a distance d appear to be receding due to the expansion of the Universe. With observations of the true primordial abundances of the elements and an independent measurement of h , Big Bang Nucleosynthesis (BBN) therefore allows us to measure the primordial value of Ω_b . Measurements of the Hubble parameter are abundant; the most widely-used comes from the Hubble Key Project ($h = 0.72 \pm 0.08$; Freedman et al. 2001). The primordial abundances of the light isotopes are somewhat more difficult to come by, requiring direct observations of extremely unevolved systems.

Because deuterium (D) is easily destroyed in stellar interiors and not produced in substantial amounts by other processes, its abundance shows a roughly steady decrease with time. The D/H ratio is often obtained by observing absorption lines in very old hydrogen clouds backlit by high-redshift quasars, and extrapolating backwards to nucleosynthesis. ^3He , on the other hand, is created and destroyed in stellar interiors, the interstellar medium and the Earth’s atmosphere, so its primordial abundance is very difficult to estimate reliably. The best upper limits to its primordial abundance come from emission line observations of the least evolved Galactic H II regions, or the protosolar nebula. Similarly, ^4He is produced ubiquitously in hydrogen fusion via the *pp*-chain in stars, so its abundance is substantially polluted relative to BBN; its higher abundance than ^3He at least allows determinations using emission from *extragalactic* H II regions.

^7Li is observed in absorption in the atmospheres of extremely metal-poor halo stars, where its abundance may eventually plateau with decreasing metallicity (Spite & Spite 1982). ^6Li has also been seen in such stars (Asplund et al. 2006), though its presence can only be inferred from a very careful treatment of the isotopic broadening of spectral lines, along with the related three-dimensional effects of convection and departures from local thermodynamic equilibrium (LTE) on the line shapes. The heavier elements are rarely considered because their tiny primordial abundances make any reliable observational determination virtually impossible.

The abundances of D and the He isotopes point very consistently to a baryon density of $\Omega_b \approx 0.04$. The corresponding prediction for the lithium isotopic abundances do exhibit some tension with observation: ^7Li is seen to be under-abundant relative to the BBN prediction, and ^6Li is not expected to have been produced in BBN at all. Both lithium isotopes are intrinsically unstable however, and subject to assorted processing in different stellar layers and the interstellar medium. The stellar determinations are also extremely difficult, depending crucially upon the input atomic data required for isotopic shifts and non-LTE calculations, and the fine points of detailed convective line shapes in stars known to be heavily effected by 3D corrections to their inferred abundances. Although it remains to be seen if the discrepancies will indeed be borne out by future observations, there is speculation that they might be explained by non-standard BBN caused by particle physics beyond the standard model (BSM; beyond the SM), including some specific dark matter models (e.g. Jedamzik & Pospelov 2009).

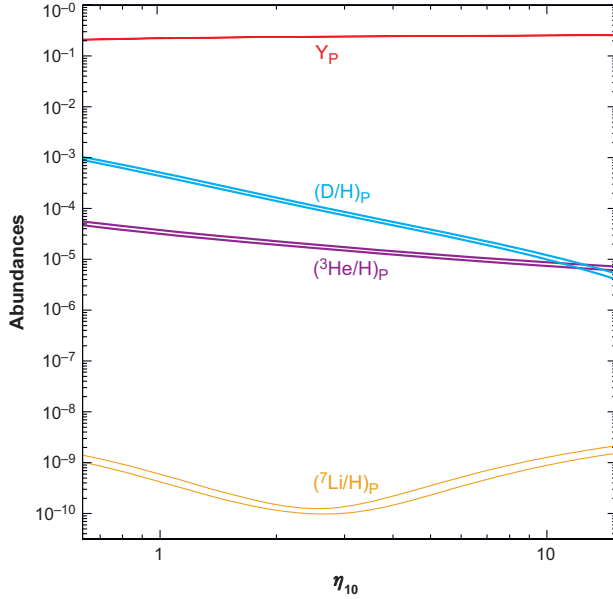


Figure 1.4. Abundances of the light isotopes produced in Big Bang nucleosynthesis (BBN), as a function of the baryon-to-photon ratio $\eta_{10} \equiv 10^{10}\eta$, which directly corresponds to the baryon fraction of the universe ($\eta \propto \Omega_b h^2$). By comparing such predictions with observations of very old astronomical systems, one can use BBN to derive Ω_b . Abundances are given as mass fractions. The bands between the two curves for each isotope indicate the degree of uncertainty arising from nuclear reaction rates and other theoretical sources. Y_P refers to primordial ^4He . From Steigman (2007).

The independent measurements of Ω_b from BBN and Ω_m from large-scale structure together provide incontrovertible evidence for the existence of dark matter. Since all luminous matter essentially consists of baryons, $\Omega_m \approx 0.29$ and $\Omega_b \approx 0.04$ together imply that the remaining $\Omega_{\text{leftover}} \approx 0.25$ must be dark matter. Furthermore, we have another invaluable piece of information about its nature: we see immediately that dark matter must be predominantly non-baryonic. Being non-baryonic allows the possibility that the dark matter is not capable of interacting with photons electromagnetically (something baryons clearly *are* capable of), which sits very well with the fact that it does indeed appear dark. This is also consistent with dark matter being dissipationless; were it able to absorb and re-emit photons, it would obscure stars within distant ha-

los, as well as radiate away angular momentum and collapse with baryons to form stellar and galactic disks.

It is worth mentioning that some amount of *baryonic* dark matter also remains unaccounted for today in the figure $\Omega_b \approx 0.04$, in that it has not been directly observed in surveys of gas or galaxies. Nevertheless, we know this to be far less than what exists in non-baryonic dark matter. For the purposes of this thesis, ‘dark matter’ is taken as shorthand for the dominant, non-baryonic component.

1.5 Concordance cosmology

In a sense, the evidence presented in Sects. 1.1–1.4 is already sufficient to conclude that dark matter definitely exists, and must be neither baryonic nor able to interact substantially with baryons, photons or itself. Final confirmation of this comes from observations of the cosmic microwave background (CMB).

The large-scale distribution of galaxies shows density variations on scales which reflect the situation at matter-radiation equality. Similarly, the temperature inhomogeneities of the CMB exhibit characteristic scales which reflect the situation shortly after, at the time of recombination (see e.g. Hu & Dodelson 2002; Samtleben et al. 2007). Unlike the galaxy power spectrum however, the angular temperature anisotropies of the CMB exhibit the primordial density perturbations of the coupled baryon-photon fluid directly; following recombination, the angular distribution of the massless photons is held nearly uniform by radiation pressure, whereas the matter collapses due to gravity. The angular power spectrum of the CMB observed today is therefore sensitive to the full range of cosmological parameters which play a role in the evolution of the baryon-photon oscillations: the total energy density of the Universe, the baryon fraction and the spectral shape of the primordial perturbations. It is also sensitive to the large-scale geometry of the Universe *since* recombination, as the observed angular diameter of the characteristic scales frozen into the CMB at recombination depends upon the geometry of the space through which they have travelled to reach us.

Thanks to the extremely high resolution of recent CMB missions, fits to the microwave background provide accurate measurements of the matter density of the Universe, as well as the baryon fraction. The 7-year Wilkinson Microwave Background Probe (WMAP) results (Larson et al. 2010) give posterior mean values of $\Omega_m = 0.267 \pm 0.026$,

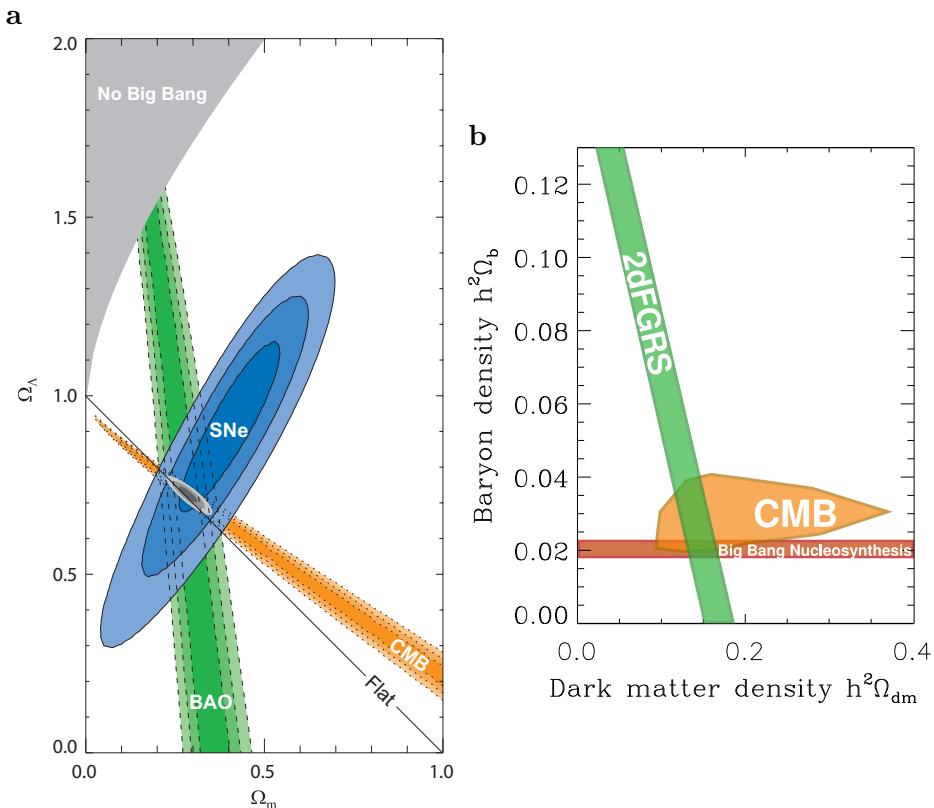


Figure 1.5. The current concordance model of cosmology, indicating that the Universe is dominated by dark energy and dark matter, and essentially flat. These figures illustrate the agreement between cosmological fits to BBN, observations of the cosmic microwave background (CMB), large scale structure (BAO/2dFGRS) and Type Ia supernovae. The fit is so good that any one of the data sets could be removed and essentially the same cosmology would be inferred from the remainder. Contours in the figure on the left (a) indicate 1-, 2- and 3 σ plausible ranges, whilst areas plotted on the right (b) are 1 σ ranges. Left figure from Kowalski et al. (2008, reproduced by permission of the AAS), right figure adapted from Tegmark et al. (2001) with additional 2dF results from Cole et al. (2005).

$\Omega_b = 0.0449 \pm 0.0028$, $\Omega_{\text{DM}} = 0.222 \pm 0.026$. These results are in excellent agreement with those obtained from BBN and large-scale structure, confirming the need for non-baryonic dark matter beyond any doubt.

The CMB fits also indicate that the Universe is approximately flat, requiring some form of ‘dark energy’ to make up the remaining $\Omega_\Lambda = 0.734 \pm 0.029$. Although difficult to explain theoretically, the need for this component was confirmed by observations that distant supernovae are apparently dimming, indicating that the expansion of the Universe is accelerating (Riess et al. 1998; Perlmutter et al. 1999). The CMB, Type Ia supernovae, large scale structure and BBN together paint an entirely self-consistent picture of the Universe in which we live: baryons make up little more than a few percent of the energy budget of the Universe, non-baryonic dark matter about a quarter, and dark energy the remaining three quarters. The remarkable level of consistency between these different data sets can be seen in Fig. 1.5; were any one of the data sets to be removed, the model would stand perfectly well constrained with the remaining three. A combined fit to all data (Komatsu et al. 2009) gives $\Omega_m = 0.274 \pm 0.013$, $\Omega_b = 0.0456 \pm 0.0015$, $\Omega_{\text{DM}} = 0.228 \pm 0.013$ and $\Omega_\Lambda = 0.726 \pm 0.015$.

Chapter 2

Models for dark matter

As we have seen in the previous chapter, the identity of dark matter is not entirely unconstrained. Firstly, it must be massive, because we see its gravitational influence. We know that it must of course also be dark, which implies that it can neither absorb nor emit photons at rates comparable to normal matter. This means that it must have a very small effective coupling to photons, either because it exists in some very special geometry that prevents it coming into contact with them very often, or due to its intrinsic particle properties. In this case, it must be electrically neutral or possess some extremely small fractional charge, as any particle with charge $q \neq 0$ couples to photons via tree-level QED processes, leading to cross-sections proportional to $q^4\alpha^2$ (where α is the fine-structure constant).

We know that dark matter must be non-dissipative in order to produce the correct structures in the early Universe. This also implies that there can be no substantial (i.e. electromagnetic-strength or stronger) interaction between dark matter and normal matter. If there were, energy would be efficiently transferred from the dark matter to the normal matter and radiated away as photons, allowing the dark matter to form disks along with normal matter. Dark matter is thus effectively collisionless with respect to all normal matter: baryons, leptons and photons. We know then that it must be non-baryonic, because it does not couple to photons or baryons; this is spectacularly confirmed by the anisotropies in the CMB. Observations of systems such as the Bullet Cluster provide even more direct proof that dark matter does not couple substantially to baryons, and even show that dark matter must be effectively collisionless with respect to itself.

Dark matter must also be cold in order for structure formation to proceed correctly, which places limits on the mass(es) of its constituent particle(s) in some cases. Finally, any dark matter candidate must be produced with the correct relic abundance to plausibly explain observations that $\Omega_{\text{DM}} = 0.23$ today. This also means that it must be stable, or at least very long-lived, in order to have persisted in significant numbers to the present day.

2.1 The good, the bad and the ugly

A great many theories have been put forward for the identity of dark matter. A good candidate theory fulfils all the requirements above, fits all other experimental constraints (most of which are described below or in Chapter 3), requires minimal arbitrary choices in its parameter values, and makes some testable predictions. The last two points are debatable; one is the requirement that the candidate presents a subjectively ‘natural’ solution to the problem, and the other simply makes the theory practically useful. Mainly due to the non-baryonic requirement, all theories which qualify as ‘good’ today fall into the realm of particle dark matter: namely, that dark matter consists of some as-yet undiscovered particle. The most notable theories of this kind are outlined in Sects. 2.2–2.7.

A theory that was rather popular in astronomical circles for a time was that of MACHOs (Paczynski 1986), MAssive Compact Halo Objects. These were hypothesised to be dim but otherwise quite normal astrophysical objects, which populated the outer halos of galaxies. Known candidate objects were red, white and brown dwarfs, black holes and substellar-mass objects (in effect, hostless planets). These systems of condensed baryons would appear dark because they would be so dim, but would also be effectively transparent to background light because their compact nature would cause the effective cross-section for light absorption per unit mass across an entire halo to be very small. The obvious trouble with MACHOs was that they would have been baryonic dark matter, violating the non-baryonic requirement. There was also never any convincing argument for why such objects should preferentially conglomerate in the outer halo, whereas other more luminous stars should not. Nonetheless, MACHOs were popular because they were testable (not because they were logical): microlensing searches towards the Magellanic Clouds (Alcock et al. 2000; Tisserand et al. 2007; Wyrzykowski et al. 2009) promptly ruled MACHOs out as the dominant contributor to dark matter some years ago.

Primordial black holes (PBHs) are another dark matter candidate with significant problems. These would be formed from small-scale primordial density perturbations which are so strong that they cause the entire horizon mass at the time (or at least a very substantial fraction of it) to collapse directly into a black hole. The fluctuations would be produced before matter-radiation equality, either during inflation or by phase transitions in the early Universe. Because PBHs form before BBN or the CMB, the baryons of which they consist are effectively sequestered from the rest of the Universe, allowing them to act like non-baryonic dark matter. Like MACHOs, they would escape detection via shadowing effects today simply by virtue of their compactness. The difficulty with this scenario is that the density contrast

$$\delta \equiv \frac{|\rho_{\text{perturbation}} - \rho_{\text{ambient}}|}{\rho_{\text{ambient}}} \quad (2.1)$$

required to form a PBH is of the order of $\delta \gtrsim 30\%$ (e.g. [Green et al. 2004b](#)). In comparison, the initial density perturbations from inflation were about $\delta \sim 10^{-5}$. A very bottom-heavy spectrum of perturbations is then required in order to provide enough power on small scales to produce a substantial number of PBHs without violating the level of large-scale anisotropy seen in the CMB.

Another problem is that PBHs can be produced with virtually any primordial abundance, creating a major fine-tuning problem. Their relic density is obtained by integrating the probability distribution of primordial density perturbations between their formation threshold ($\delta \sim 30\%$) and $\delta = 1$. Assuming e.g. a Gaussian power spectrum of perturbations for simplicity (e.g. [Green & Liddle 1997](#)), this produces a density at matter-radiation equality of

$$\Omega_{\text{PBH}}(M_{\text{H}}) = \int_{0.3}^1 \frac{\delta}{\sqrt{2\pi}\sigma(M_{\text{H}})} \exp\left(-\frac{\delta^2}{2\sigma(M_{\text{H}})^2}\right) d\delta. \quad (2.2)$$

Here $\sigma(M_{\text{H}})^2$ is the variance of perturbations at the time when the horizon mass is M_{H} . With a scale-independent perturbation spectrum of index n ,

$$\sigma(M_{\text{H}}) \propto M_{\text{H}}^{-n/4}. \quad (2.3)$$

On CMB scales, n is close to 1 ([Komatsu et al. 2010](#)), but at small scales, it could be very different. The resultant relic density from Eq. 2.2 is extremely sensitive to n , even for a single epoch of formation (i.e. a single

value of M_{H}). The same is essentially true for other reasonable choices of the power spectrum and scale-dependence. See [Paper III](#) for a more detailed discussion. To the best of my knowledge, there is no known mechanism which naturally produces exactly the values of n and M_{H} required to reproduce the observed cosmological density of dark matter with PBHs. Even more disastrously though, PBHs are mostly disfavoured now by experiment. More massive PBHs should have been picked up by microlensing searches, and the Hawking radiation produced in the evaporation of low mass PBHs should have created effects on the extragalactic diffuse gamma-ray background, BBN, the CMB or cosmic ray data that have not been seen (see [Josan et al. 2009](#), for an extensive compilation of limits).

SM neutrinos were also considered viable dark matter candidates for a time (e.g. [Steigman et al. 1978](#)), since they are massive, stable, non-baryonic and do not interact electromagnetically with other matter. With the current limits on their masses however (e.g. [Schwetz et al. 2008](#)), they are far too light to meet the definition of cold dark matter, and can only have a quite small cosmological abundance ($\Omega_{\nu} \lesssim 0.03$; [Bergström 2009](#)).

For a time, the notion of a heavy fourth-generation SM-like neutrino was popular as a candidate for dark matter. In order to achieve the correct relic abundance, its mass would have to be either 1–50 eV, or more than about a few GeV ([Jungman et al. 1996](#); [Bergström 2000](#)); the former is ruled out for SM-like neutrinos by the Tremaine-Gunn limit ([Tremaine & Gunn 1979](#)), and the latter is excluded by direct searches for dark matter (Sect. [3.1](#)).

To some, the MOND paradigm (MODified Newtonian Dynamics; [Milgrom 1983](#); [Bekenstein 2004](#)) is appealing. This approach involves modifying gravity in an ad hoc fashion at long distances in order to fit galactic rotation curves without the need for dark matter. In this sense, one could say that it is quite a successful empirical fitting formula for parameterising the effects of dark matter on the kinematic observables discussed in Sect. [1.1](#). As a physical theory however, it has no basis to speak of, and fails entirely to explain any of the additional evidence for dark matter presented in Sects. [1.2–1.5](#).

2.2 Axions

Because gluons should be pure gauge fields at spatial infinity, the QCD vacuum possesses a rather complex structure ([Peccei 2008](#)). Being a pure

gauge field implies only that these boundary values must be drawn from the set of field configurations which can be obtained by gauge transformations on the null field (i.e. 0). The vacuum structure arises because the pure gauge boundary condition introduces a freedom in the choice of boundary field, which translates into similar freedom in the choice of QCD vacuum. Because of this vacuum structure, the QCD Lagrangian picks up an additional effective term

$$\mathcal{L}_\theta = \theta \frac{g_s^2}{32\pi^2} G_a^{\mu\nu} \tilde{G}_{a\mu\nu}. \quad (2.4)$$

Here g_s is the strong coupling constant, $G_a^{\mu\nu}$ is the QCD field strength tensor for the a th gluon, and $\tilde{G}_{a\mu\nu} = \frac{1}{2}\epsilon_{\mu\nu\alpha\beta}G_a^{\alpha\beta}$ is its dual. Unlike the rest of the QCD Lagrangian, \mathcal{L}_θ does not conserve CP. This is a problem, as the strong interaction is known empirically to conserve CP rather well. This additional term would induce effects which have not been observed, like a non-zero electric dipole moment for the neutron. The limits on such a moment to date constrain the vacuum angle θ to be less than 10^{-9} (Peccei 2008). Understanding why θ is so small is known as the ‘strong CP problem’.

One widely held suspicion is that the solution to the strong CP problem lies in the existence of an additional spontaneously-broken, global chiral $U(1)$ symmetry of the SM Lagrangian, known as the Peccei-Quinn symmetry (Peccei & Quinn 1977). The axion is the Goldstone boson of this broken symmetry (see e.g. Kim & Carosi 2008, for a review). It possesses a potential with a minimum that naturally sets the field to a value that cancels \mathcal{L}_θ . This is true for essentially any value of the Peccei-Quinn symmetry breaking scale v_a , relieving the naturalness problem posed by the smallness of θ .

The low-energy phenomenology of axions is set almost entirely by their decay constant $f_a = v_a/N$. Here N is an integer which gives the degree of the colour chiral anomaly of the Peccei-Quinn symmetry (a corresponding electromagnetic chiral anomaly also exists, and is typically indexed with another integer E). The axion mass for example is given by (Sikivie 2008)

$$m_a \approx 6 \mu\text{eV} \left(\frac{10^{12} \text{ GeV}}{f_a} \right). \quad (2.5)$$

Axions possess a vertex with two photons (Raffelt 2008),

$$\mathcal{L}_{a\gamma\gamma} = \frac{\alpha}{2\pi f_a} \left(\frac{E}{N} - \frac{2}{3} \frac{4+z}{1+z} \right) \mathbf{E} \cdot \mathbf{B}a, \quad (2.6)$$

where $z \equiv m_u/m_d$ is the ratio of up and down quark masses, \mathbf{E} and \mathbf{B} are the electric and magnetic fields, and a is the axion field itself. The two photon vertex not only allows axion decay to two photons, but allows axion conversion to photons (and vice versa) in the presence of electromagnetic fields. This feature is used as the prime phenomenological means for searching for axions, as discussed in Sect. 3.6.

Certain classes of axions, dubbed ‘invisible axions’, make very good dark matter candidates because they interact extremely weakly with normal matter. This class of axion involves a very high Peccei-Quinn breaking scale, and therefore very light axions. Such axions have virtually no kinematically-accessible decay channels, so are stable on cosmological timescales. These axions constitute cold dark matter despite being so light, because they are never in thermal equilibrium in the early Universe, so are never heated to relativistic temperatures along with the other forms of matter.

There are two commonly discussed mechanisms for the primordial production of dark matter axions: vacuum misalignment and string decay. Depending on the timing of Peccei-Quinn breaking relative to inflation, the correct relic density of dark matter axions can be obtained either only for a very specific value of f_a ($\sim 7 \times 10^{10}$ GeV), or for a tightly correlated corridor of values in the f_a - φ_i plane (Visinelli & Gondolo 2009). The variable φ_i is the initial value of the misalignment angle between the axion field and its minimum; in this model, it is the initial offset from the minimum which causes the field to oscillate and create particles. In this sense axions have some fine-tuning issues of their own as dark matter candidates, though they are not nearly as severe as for e.g. primordial black holes.

2.3 WIMPs

The most widely-studied dark matter candidates are the Weakly Interacting Massive Particles (WIMPs). WIMPs interact with SM fields only via the weak nuclear force, making them non-baryonic and electrically neutral by definition. WIMPs must carry some sort of conserved quantum number to keep them stable on cosmological timescales. This is usually achieved by making the WIMP the lightest member of a matter sector which is charged under some discrete symmetry. More often than not, this symmetry needs to be essentially imposed by hand on the underlying theory. Being members of $SU(2)_L$ multiplets, in the absence

of any other symmetries which might force their masses down, WIMPs should naturally acquire masses m_χ within a few orders of magnitude of the $SU(2)_L \times U(1)_Y$ electroweak symmetry-breaking scale (i.e. a few GeV or TeV). This makes them sufficiently heavy to constitute cold dark matter even if they have been produced thermally in the early Universe. Examples of WIMPs include the lightest neutralino in supersymmetry (Sect. 2.4.2), the lightest Kaluza-Klein (KK) particle (Servant & Tait 2003) and an additional inert Higgs boson (Barbieri et al. 2006).

2.3.1 Thermal relics

A thermal relic is a particle whose cosmological abundance is set by thermal production of the particle in the early Universe. ‘Thermal production’ actually refers to *chemical* decoupling of a species from the primordial particle soup created in the Big Bang. Here ‘chemical’ has the meaning of particle creation and destruction by quantum processes, not the usual meaning of creation and destruction of molecules and free atoms by atomic interactions. True *thermal* decoupling on the other hand, otherwise known as kinetic decoupling, refers to the time when the velocities of a relic species cease to reflect the temperature of the Universe.

Chemical decoupling, or ‘freeze out’, happens when the expansion of space eventually overcomes the rate at which the species is created and annihilated in interactions with other particles. The primordial fireball necessarily begins in chemical (and thermal) equilibrium at some very high temperature T_i . The populations of different particle species are set by the equilibrium rates of particle creation and annihilation at T_i , and their velocities follow a Maxwellian distribution with temperature T_i . As the Universe expands, it cools, and for a time, the equilibrium populations of the particles adjust accordingly as chemical equilibrium is maintained. At some point in the expansion, when $T = T_c$, the creation and annihilation of a particular species will cease to be able to keep pace with the expansion, and the particle will fall out of chemical equilibrium. If it is stable, at this point the comoving density of the species will become essentially fixed.¹ Similarly, when elastic collisions between particles become sufficiently infrequent, both due to the increasing scale and decreasing temperature of the Universe, it will fall out of kinetic equilibrium.

¹This is analogous to the transition from LTE to non-LTE populations of atomic energy levels in astrophysical plasmas as one considers progressively lower gas densities or temperatures.

The time of chemical freeze out therefore sets the final population of any stable relic, and the time of kinetic decoupling sets its temperature. In general, kinetic decoupling of WIMPs happens after chemical decoupling (see e.g. [Bringmann 2009](#)). With weak-scale masses and creation/annihilation cross-sections, $T_c \approx 0.05m_\chi$ ([Jungman et al. 1996](#)). As kinetic decoupling happens at comparable or even lower temperatures than this, WIMPs freeze out at sub-relativistic energies. They are therefore guaranteed to be moving non-relativistically at the time of structure formation, so qualify as cold dark matter.

The resultant abundance of the relic species depends upon the history of the expansion rate up until freeze out, and the rate at which the species annihilates into lighter particles. The expansion rate is $H \equiv \dot{a}/a$ (where a is the scale factor of the Universe and the dot denotes time differentiation), and is obtained from the cosmological model. To a first approximation, the evolution of the population is thus described by the Boltzmann equation ([Jungman et al. 1996](#))

$$\frac{dn_\chi}{dt} + 3Hn_\chi = \langle\sigma v\rangle(n_{\chi,\text{eq}}^2 - n_\chi^2) \quad (2.7)$$

where $n_{\chi,\text{eq}}$ and n_χ are the equilibrium and actual number densities of the species χ , and $\langle\sigma v\rangle$ is the thermally-averaged product of the relative velocity and the total annihilation cross-section for $\chi\bar{\chi} \rightarrow \text{other particles}$. Eq. 2.7 holds whether χ is Majorana or Dirac, though in the Dirac case it is only valid if there is no particle-antiparticle asymmetry to begin with, meaning that the total particle population is given by $2n_\chi$.

Eq. 2.7 can be solved numerically in order to obtain the relic density of any species of interest; Fig. 2.1 gives solutions for the chemical freeze out of some example WIMPs. To a good approximation ([Jungman et al. 1996](#); [Bergström 2000](#)), for particles with masses in the relevant range for WIMPs

$$\Omega_\chi h^2 = 0.1 \frac{3 \times 10^{-26} \text{ cm}^3 \text{ s}^{-1}}{\langle\sigma v\rangle}. \quad (2.8)$$

As seen in Eq. 2.8 and Fig. 2.1, larger self-annihilation cross-sections cause the particle to freeze out later, and so exhibit a lower relic density. In practice, co-annihilations between the WIMP and other particles nearly degenerate with it in mass, as well as effects such as annihilation thresholds and resonances, can make the calculation a little bit trickier than Eqs. 2.7 and 2.8 might suggest. Dedicated computer packages have been

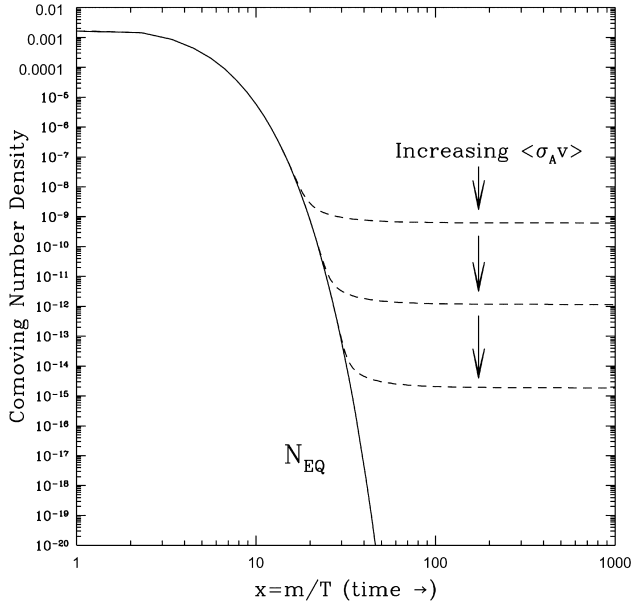


Figure 2.1. Freeze out of a stable thermal relic. At early times, the relic particle is in chemical and thermal equilibrium with other particles, with its abundance set by the equilibrium rates of particle creation and annihilation. Because of thermal coupling, these are set entirely by the temperature of the cooling Universe. At later times, the expanding Universe cools to the point where the equilibrium density is too low to maintain chemical contact with other particles. At this point, the particle falls out of chemical equilibrium with the rest, and its comoving density becomes fixed. The density at which this occurs depends upon the annihilation cross-section of the particle; larger cross-sections allow equilibrium to be maintained for longer, resulting in lower relic abundances. From [Jungman et al. \(1996\)](#), modelled on a figure from [Kolb & Turner \(1990\)](#).

developed to solve Eq. 2.7 in detail, for a variety of specific WIMP models (e.g. [Gondolo et al. 2004](#); [Bélanger et al. 2007](#)).

Eq. 2.8 shows that the canonical annihilation cross-section implied by the cosmological observations discussed in Chapter 1 is $\langle\sigma v\rangle \approx 3 \times 10^{-26} \text{ cm}^3 \text{ s}^{-1}$. The natural value of the annihilation cross-section for a weakly-interacting particle can be estimated as $\langle\sigma v\rangle \approx \alpha^2/E_{\text{weak}}^2 \approx 10^{-8} \text{ GeV}^{-2} = 10^{-25} \text{ cm}^3 \text{ s}^{-1}$, where $E_{\text{weak}} \sim 100 \text{ GeV}$ is the electroweak scale.² Here we have an amazing coincidence: purely by postulating that

²That this is approximately true can be verified by e.g. considering Z -mediated χ self-annihilation, such that $|\mathcal{M}|^2 \sim g^4 E_\chi^4/m_Z^4$, and using Eq. 4.84 of [Peskin &](#)

dark matter is a stable weakly-interacting particle, we have predicted the relic density to within an order of magnitude. The naturalness with which WIMPs can provide the correct relic density has lead this to be dubbed ‘the WIMP miracle’. Whilst far from definitive, it is a very strong hint that WIMPs might be the correct solution to the dark matter puzzle.

2.3.2 The hierarchy problem

Indeed, the process of chemical freeze out is so generic that if a stable neutral particle exists around the electroweak scale, then we really should *expect* it to be dark matter. But what reason do we actually have for believing that such stable particles might exist around or just above the electroweak scale? This is a question of why we think there might be new physics at such an energy scale, as new physics generically means new particles (though not necessarily stable ones). There are a number of reasons to expect that new physics exists beyond the SM, since the SM cannot explain phenomena such as the net baryon asymmetry of the Universe, neutrino masses, the imperfect unification of the known gauge couplings, and the spectrum of particle masses – but the one compelling reason to believe that new physics exists specifically at the TeV scale is the mass of the Higgs boson.

As a fundamental scalar, the mass of the Higgs is not protected by any symmetry; quadratic divergences generated by fermionic loop diagrams such as Fig. 2.2 have no apparent cancellation or suppression, nor can they be absorbed into the renormalisation group running of any coupling constant. For fermions, the case is different: similar mass corrections are controlled by the approximate chiral symmetry of the fermionic part of the SM Lagrangian (Luty 2005). For the gauge bosons, gauge symmetry suppresses the divergences and shifts them into the running of the gauge couplings. For the SM Higgs however, the quadratic divergences remain bare, causing extreme corrections to its mass. There is therefore no reason to believe that the SM Higgs should have a mass any lower than the GUT scale. That is, except for the pesky detail of its fundamental role in

Schroeder (1995) to arrive at

$$\sigma v \approx \frac{|\mathcal{M}|^2}{128\pi^2 E_\chi^2} \approx \frac{G^2 E_\chi^2}{4\pi^2}, \quad (2.9)$$

where g is the electroweak coupling and G is the Fermi coupling constant. In the case where the incoming χ s are moving non-relativistically (as WIMPs do), $E_\chi \approx m_\chi \approx E_{\text{weak}}$, giving the zero-velocity limit $\langle\sigma v\rangle_0 \approx 10^{-8} \text{ GeV}^{-2} = 10^{-25} \text{ cm}^3 \text{ s}^{-1}$.

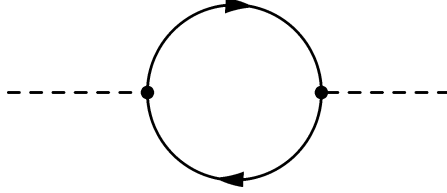


Figure 2.2. An example one-loop contribution to the Higgs mass from a fermionic loop. The amplitude of this diagram is quadratically divergent, so the Higgs mass is sensitive to some large mass scale (which may be expressed as the cut-off used to regularise the diagram’s amplitude, amongst other presentations; see e.g. [Luty 2005](#)).

electroweak symmetry breaking and the generation of mass for the entire spectrum of SM fermions, which it needs an electroweak-scale vacuum expectation value (VEV) to achieve. How then is the Higgs mass stabilised at the weak scale? This problem is known as the gauge hierarchy problem, and strongly suggests that some new physics must kick in at energies just above the electroweak scale, allowing us to calculate the effective Higgs mass below this scale by regularising the amplitudes of the divergent diagrams with a cut-off at $\Lambda \sim 1 \text{ TeV}$.

The hierarchy problem is a very generic motivation for new physics at or just above the electroweak scale. That is to say, it is independent of what the nature of this new physics might be, so there is no *a priori* reason for us to naively expect that it necessarily has anything to do with dark matter. The fact that its resolution would appear to require new physics at exactly the right scale for the associated particles to be WIMPs is thus another amazing coincidence, and a second very strong hint that WIMPs constitute the majority of dark matter.

2.4 Supersymmetry

Although this chapter is primarily intended as something of a bestiary of dark matter models, here it is worth detouring slightly into the theory of supersymmetry (SUSY). This is because SUSY not only provides multiple examples of WIMPs, but because it is also exactly the sort of ‘new physics’ discussed in the previous section as necessary to solve the hierarchy problem.

2.4.1 General features

The basic idea of SUSY is to give every SM particle one (or more) superpartner(s), which differ from their SM counterparts only by their spins (see e.g. [Martin 1997](#); [Baer & Tata 2006](#); [Aitchison 2007](#), for reviews; the bulk of the treatment in this section follows [Baer & Tata](#)). Every SM fermion has a sfermionic superpartner (which is a boson) and every SM boson has a bosino superpartner (which is a fermion). The symmetry is a continuous extension of the Poincaré group to fermionic (i.e. anti-commuting) degrees of freedom. Supersymmetry is thus essentially an extension of special relativity into a four-dimensional fermionic ‘super-space’; the fermionic dimensions can be viewed either as four additional anti-commuting dimensions, or simply as fermionic extensions of the existing four. Correspondingly, the generators of SUSY transformations are themselves spinorial, in contrast to the vector and scalar generators associated with traditional spacetime and internal symmetries. It is entirely possible for there to exist multiple distinct supersymmetry generators, and therefore multiple supersymmetries (known as $N > 1$ supersymmetries, where N is the number of generators). $N = 1$ supersymmetry is the only version which permits chiral fermions, so known phenomenology dictates that supersymmetry can only be of the $N = 1$ variety at low energies.

It is often said that SUSY provides a non-trivial way of unifying spacetime and internal symmetries, since the anti-commutation relation for the spinor components of the SUSY generator Q

$$\{Q_a, \bar{Q}_b\} = (\gamma_\mu)_{ab} P^\mu \quad (2.10)$$

gives the generator of spacetime translations, P^μ .³ This means that the combination of any two SUSY transformations is equivalent to a spacetime translation. So, the supersymmetry algebra mixes spacetime transformations with boson-fermion exchange, which would seem to be something of an ‘internal’ operation because it directly modifies particle properties. This interpretation seems unreasonable though, as the swapping of bosons for fermions or vice versa involves modifying only the particle’s spin, which is arguably no less of a spacetime property than momentum or position. Even if supersymmetry were gauged (more on this later), the

³Here I am working with 4-component spinor notation as per [Baer & Tata \(2006\)](#). The bar denotes the spinor adjoint $\bar{Q} \equiv Q^\dagger \gamma^0$, and γ_μ are the standard Dirac gamma matrices, forming a representation of the Clifford algebra of Minkowski space.

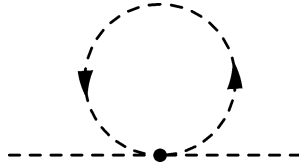


Figure 2.3. An example one-loop contribution to the Higgs mass from a sfermionic loop. The amplitude of this diagram has exactly the same sensitivity to the high-scale cut-off as the fermionic loop diagram of Fig. 2.2, except for a factor of $-\frac{1}{2}$. In unbroken supersymmetry, two of these diagrams appear for each fermionic one, exactly cancelling the fermionic loop’s contribution to the Higgs mass. The same occurs to all orders in perturbation theory. This removes the sensitivity to the high scale, stabilising the Higgs mass against higher-order corrections.

resulting gauge theory of gravity would still seem to be an entirely space-time symmetry, and all the other gauge symmetries of particle physics still entirely internal ones. This is effectively what was said by the SUSY version (Haag et al. 1975) of the celebrated Coleman-Mandula ‘no-go’ theorem (Coleman & Mandula 1967): it is not possible to have a larger spacetime symmetry than the super-Poincaré algebra, so there are no non-trivial ways to unify spacetime and internal gauge symmetries into the same group.

SUSY solves the hierarchy problem in a very simple and elegant way: because every fermion has a bosonic superpartner and vice versa, every divergent loop diagram containing a SM fermion like Fig. 2.2 is matched by corresponding scalar sfermion loop diagrams like Fig. 2.3. In this case there are actually two scalar loop diagrams, because chiral fermions have two degrees of freedom, so their scalar superpartner fields must be complex, resulting in two oppositely charged sfermions for each chiral fermion. Because closed fermionic loops introduce a factor of -1 to their diagram’s amplitude (whereas bosonic loops do not), and the particles are otherwise identical, the (regularised) contributions of the two copies of the scalar loop diagram cancel that of the fermionic one. The same is so to all orders in perturbation theory, so the Higgs mass receives no extreme corrections, and is stabilised somewhere near the SUSY-breaking scale.

SUSY must clearly be a broken symmetry, as we have not observed any of the superpartners to date (known particles cannot be the superpartners of each other, as they do not fit correctly into the supermultiplet structure

required by the supersymmetry algebra). Except for some very specific scenarios where particular superpartners happen to be especially sneaky, we can infer that they must all be considerably more massive than the SM particles, as they have yet to show up in e.g. collider experiments. We would expect then that the SUSY particles should generally have masses of around the SUSY-breaking scale. The cancellation of divergences thus cannot be exact following SUSY-breaking, as particles and sparticles must have different masses. We can then conclude that if SUSY is a viable solution to the hierarchy problem, it must be broken at about a TeV, otherwise the cancellation of the different loop contributions would again require an unexplained fine-tuning. In fact, another appealing feature of SUSY is that it can actually *cause* electroweak symmetry-breaking (EWSB), in that the Higgs mass term in the $SU(2)_L \times U(1)_Y$ Lagrangian can be driven negative by SUSY renormalisation group evolution – but only if the SUSY-breaking scale is about a TeV. So, we might expect EWSB to have been induced by SUSY breaking, and hence taken place at only a slightly lower energy than SUSY-breaking itself. Since we know the electroweak scale to be a few hundred GeV, this gives further credence to the idea that SUSY-breaking should occur at around a TeV.

Actually, the cancellation of quadratic divergences depends a lot more crucially upon the gauge coupling constants in the SM and SUSY sector being identical than the particle masses. It is possible to introduce explicit mass terms to the SUSY Lagrangian which break SUSY ‘softly’, in that they give the sparticles different masses to the SM particles, but do not introduce any quadratic divergences.

The simplest prescription then for writing down a minimal supersymmetric theory is to take the supersymmetrised version of the SM Lagrangian, $\mathcal{L}_{\text{SUSY-SM}}$, and augment it with all possible renormalisable soft SUSY-breaking terms (Baer & Tata 2006)

$$\mathcal{L}_{\text{soft}} = -\frac{1}{2} \left[M_1 \bar{\tilde{B}}^0 \tilde{B}^0 + M_2 \bar{\tilde{W}}_A \tilde{W}_A + M_3 \bar{\tilde{g}}_B \tilde{g}_B \right] \quad (2.11a)$$

$$- \frac{i}{2} \left[M'_1 \bar{\tilde{B}}^0 \gamma_5 \tilde{B}^0 + M'_2 \bar{\tilde{W}}_A \gamma_5 \tilde{W}_A + M'_3 \bar{\tilde{g}}_B \gamma_5 \tilde{g}_B \right] \quad (2.11b)$$

$$+ \left[b H_u^a H_{da} + \text{h.c.} \right] + m_{H_u}^2 |H_u|^2 + m_{H_d}^2 |H_d|^2 \quad (2.11c)$$

$$+ \sum_{i,j=1,3} \left\{ - \left[\tilde{Q}_i^\dagger(\mathbf{m}_Q^2)_{ij} \tilde{Q}_j + \tilde{d}_{Ri}^\dagger(\mathbf{m}_d^2)_{ij} \tilde{d}_{Rj} \right. \right. \\ \left. \left. + \tilde{u}_{Ri}^\dagger(\mathbf{m}_u^2)_{ij} \tilde{u}_{Rj} + \tilde{L}_i^\dagger(\mathbf{m}_L^2)_{ij} \tilde{L}_j + \tilde{e}_{Ri}^\dagger(\mathbf{m}_e^2)_{ij} \tilde{e}_{Rj} \right] \right\} \quad (2.11d)$$

$$+ \left[(\mathbf{A}_u)_{ij} \epsilon_{ab} \tilde{Q}_i^a H_u^b \tilde{u}_{Rj}^\dagger + (\mathbf{A}_d)_{ij} \tilde{Q}_i^a H_{da} \tilde{d}_{Rj}^\dagger + (\mathbf{A}_e)_{ij} \tilde{L}_i^a H_{da} \tilde{e}_{Rj}^\dagger + \text{h.c.} \right] \quad (2.11e)$$

$$+ \left[(\mathbf{C}_u)_{ij} \epsilon_{ab} \tilde{Q}_i^a H_d^{*b} \tilde{u}_{Rj}^\dagger + (\mathbf{C}_d)_{ij} \tilde{Q}_i^a H_{ua}^* \tilde{d}_{Rj}^\dagger + (\mathbf{C}_e)_{ij} \tilde{L}_i^a H_{ua}^* \tilde{e}_{Rj}^\dagger + \text{h.c.} \right] \}. \quad (2.11f)$$

Here the generation indices i and j are explicitly summed over, whilst summation is implied over the $SU(2)_L$ indices $a, b = 1, 2$ and the gauge generator indices $A = 1..3$ and $B = 1..8$. Tilded operators denote superparticle fields (\tilde{Q}_j , \tilde{u}_{Rj}^\dagger , etc.), where \tilde{B}^0 , \tilde{W}_A and \tilde{g}_B are the superpartners of the familiar SM gauge bosons. Other capitalised fields are $SU(2)_L$ doublets, whilst lowercase fields are singlets: $Q_i \equiv (u_{Li}, d_{Li})^T$, $L_i \equiv (e_{Li}, \nu_{eLi})^T$, $H_u \equiv (H_u^+, H_u^0)^T$ and $H_d \equiv (H_d^-, H_d^0)^T$. The doublet definitions for the superpartner fields are simply tilded versions of the same. Notice that there are now two Higgs doublets instead of the normal one from the SM. After EWSB, this gives rise to two additional charged Higgs bosons and a further two neutral Higgs compared the SM (recall that three real degrees of freedom are lost to the gauge bosons in EWSB, so two doublets means $8 - 3 = 5$ real degrees remaining, instead of $4 - 3 = 1$ real degree in the SM). The two doublets give masses separately to the up-type and down-type quarks, hence the subscripts u and d ; the up-type doublet corresponds to the SM Higgs. The down-type doublet is required because the up-type Higgs cannot couple to the down-type quarks without breaking the SUSY-invariance of the action. Unless multiple Higgs doublets are present, Higgsinos also ruin certain anomaly cancellations which exist in the SM.

The first two terms in Eq. 2.11 (2.11a and 2.11b) give explicit masses to the gauginos via the real parameters M_1, M_2, M_3 and M'_1, M'_2, M'_3 . The second of these terms violates CP , so M'_1, M'_2 and M'_3 should be small or zero. The Higgs sector (2.11c) includes explicit mass terms with real parameters $m_{H_u}^2$ and $m_{H_d}^2$, as well as a bilinear coupling with complex parameter b . Explicit sfermion masses (2.11d) are given by five 3×3 Hermitian mass-squared matrices \mathbf{m}_Q^2 , \mathbf{m}_u^2 , \mathbf{m}_d^2 , \mathbf{m}_L^2 and \mathbf{m}_e^2 . The final two terms (2.11e and 2.11f) give trilinear couplings between the Higgs and squarks or sleptons, with general Yukawa-type complex 3×3 matrices $\mathbf{A}_u, \mathbf{A}_d, \mathbf{A}_e$ and $\mathbf{C}_u, \mathbf{C}_d, \mathbf{C}_e$. The latter terms, proportional to the \mathbf{C} matrices (2.11f), tend to be left out of most low-energy effective models because they are suppressed in many SUSY-breaking schemes.

$\mathcal{L}_{\text{SUSY-SM}}$ is itself straightforward to write down, but lengthy and not especially phenomenologically illuminating (see for example Eq. 6.44 of Baer & Tata 2006). For the purposes of this general description, the most important aspect is that it contains derivatives of the ‘superpotential’

$$\begin{aligned} \hat{W} = \mu \hat{H}_u^a \hat{H}_{da} + \sum_{i,j=1,3} \Big[(\mathbf{Y}_u)_{ij} \epsilon_{ab} \hat{Q}_i^a \hat{H}_u^b \hat{U}_j^c \\ + (\mathbf{Y}_d)_{ij} \hat{Q}_i^a \hat{H}_{da} \hat{D}_j^c + (\mathbf{Y}_e)_{ij} \hat{L}_i^a \hat{H}_{da} \hat{E}_j^c \Big]. \end{aligned} \quad (2.12)$$

Here the indices i and j are again generation number, and a and b are $SU(2)_L$ indices. The carets indicate superfields, containing both the SM fields (and where applicable, $SU(2)_L$ doublets) such as u_{Ri} , L_i , etc. and their superpartners \tilde{u}_{Ri} , \tilde{L}_i , etc. The terms \hat{U}_j^c , \hat{D}_j^c and \hat{E}_j^c are the left chiral superfields containing the charge conjugates of the right-handed $SU(2)_L$ singlets: up-type (s)quarks, down-type (s)quarks and (s)electrons, respectively. Derivatives of \hat{W} with respect to its scalar fields give rise to all non-gauge interaction terms in $\mathcal{L}_{\text{SUSY-SM}}$. In this sense, it is somewhat analogous to the non-gauge part of the scalar potential seen in non-supersymmetric quantum field theories. Here it plays a similar role, specifying the Higgs potential via the complex parameter μ , as well as the Higgs-fermion interactions and ultimately, the fermion masses, via the general complex 3×3 Yukawa coupling matrices \mathbf{Y}_u , \mathbf{Y}_d and \mathbf{Y}_e .

In Eqs. 2.11 and 2.12, only terms which conserve baryon (B) and lepton number (L) have been retained. B and L are known to be broken non-perturbatively in the SM (‘t Hooft 1976a,b, see also e.g. the introductory remarks of Morrissey et al. 2005). This happens as the B and L currents become anomalous (non-conserved) due to a freedom in the electroweak vacuum, similar to that discussed for the QCD vacuum in the context of the axion in Sect. 2.2. ‘Instanton’ transitions between these vacua can then cause simultaneous violation of B and L by 3 units. Nevertheless, B and L are observed to be very good (albeit accidental) symmetries of the SM at tree level; the electroweak vacuum doesn’t seem to have done much tunnelling recently. Exactly why the SM contains no B or L -violating operators is an open question. Certain other terms which explicitly violate B and L are allowed in $\mathcal{L}_{\text{soft}}$ and the superpotential by all other considerations, but in the interests of constructing a model with minimal new interactions, and which agrees with experimental constraints, they are generally excluded.

Together, $\mathcal{L}_{\text{SUSY-SM}}$ and the soft terms in Eq. 2.11 give the Lagrangian for the Minimal Supersymmetric Standard Model (MSSM)

$$\mathcal{L}_{\text{MSSM}} = \mathcal{L}_{\text{SUSY-SM}} + \mathcal{L}_{\text{soft}}, \quad (2.13)$$

after SUSY breaking but prior to EWSB. The model is minimal in that it contains the least additional field content possible for a supersymmetrised version of the SM. Note that the only new parameter actually introduced in initially supersymmetrising the SM is μ , the Higgs parameter in the superpotential. Once we demand a low-energy theory for broken supersymmetry, the soft terms introduce more than a hundred additional parameters.

2.4.2 Supersymmetric WIMPs

In order for a SUSY particle to realistically constitute dark matter, it must somehow be stabilised against decay into lighter SM states. The most common way this is achieved is to postulate that aside from supersymmetry, a discrete \mathbb{Z}_2 symmetry exists between the SM particles and their SUSY partners. The corresponding conserved quantum number is known as R -parity, and has the form

$$R = (-1)^{3(B-L)+2s}, \quad (2.14)$$

where s is the particle's spin. All SM particles thus have R -parity $+1$ and all their SUSY partners R -parity -1 . Clearly any theory which simultaneously conserves L and B automatically conserves R ; the MSSM superpotential and soft terms (Eqs. 2.11 and 2.12) hence conserve R -parity by construction. Note that the converse is emphatically not true: R -parity conservation does not imply B or L conservation. For example, the most interesting of the B and L -violating terms discussed in the previous subsection (the ones which are arguably valid additions to the MSSM Lagrangian), include some which conserve R -parity.

Although R -parity is generally imposed by hand in most SUSY variants (either via B and L conservation, or directly), it is not plucked entirely from thin air. Some grand unified theories (GUTs) give rise to R -parity conservation naturally in their group and/or representation structure; examples are certain supersymmetric $SO(10)$ GUTs (e.g. Lee & Mohapatra 1995). Indeed, R -parity conservation in a higher theory might be part of the reason B and L are approximate symmetries of the SM today. If R -parity is conserved, then the lightest SUSY particle (LSP) is

absolutely stable. If it is also weakly-interacting and electrically neutral, then it is a viable WIMP.

The quintessential SUSY WIMP is the lightest neutralino, the lightest linear combination of the two neutral Higgsinos, the neutral wino and the bino,

$$\tilde{\chi}_1^0 = V_{1l}^* \tilde{H}_u^0 + V_{2l}^* \tilde{H}_d^0 + V_{3l}^* \tilde{W}_3^0 + V_{4l}^* \tilde{B}^0, \quad (2.15)$$

which mix following EWSB because they share quantum numbers. There are thus four neutralinos in the MSSM, corresponding to the different linear combinations; only the lightest is ever stable, and it is always this particle that is meant when people talk about ‘the neutralino’ as a WIMP. Their masses are given by the eigenvalues of the mass mixing matrix which appears in the post-EWSB Lagrangian

$$\mathcal{M}_{\chi^0} = \begin{pmatrix} 0 & \mu & -\frac{gv_u}{\sqrt{2}} & \frac{g'v_u}{\sqrt{2}} \\ \mu & 0 & \frac{gv_d}{\sqrt{2}} & -\frac{g'v_d}{\sqrt{2}} \\ -\frac{gv_u}{\sqrt{2}} & \frac{gv_d}{\sqrt{2}} & M_2 & 0 \\ \frac{g'v_u}{\sqrt{2}} & -\frac{g'v_d}{\sqrt{2}} & 0 & M_1 \end{pmatrix}, \quad (2.16)$$

in the basis $\vec{G} \equiv (\tilde{H}_u^0, \tilde{H}_d^0, \tilde{W}_3^0, \tilde{B}^0)^T$. Here v_u and v_b are the VEVs obtained by the up- and down-type Higgs during EWSB, and $g' = g \tan \theta_W$, with θ_W the weak mixing angle. The coefficients $V_{1l}^*, V_{2l}^*, V_{3l}^*, V_{4l}^*$ of the individual gaugino/Higgsino components of each mass eigenstate are the entries in the inverse of the unitary matrix V which diagonalises \mathcal{M}_{χ^0} ,

$$\vec{\chi} = V^\dagger \vec{G}, \quad (2.17)$$

where $\vec{\chi} \equiv (\tilde{\chi}_A^0, \tilde{\chi}_B^0, \tilde{\chi}_C^0, \tilde{\chi}_D^0)^T$. The index l in the $V_{1l}^*, V_{2l}^*, V_{3l}^*, V_{4l}^*$ refers to the column of V which applies to the lightest mass eigenstate. The usual labelling for mass eigenstates is to sort $\tilde{\chi}_A^0, \tilde{\chi}_B^0, \tilde{\chi}_C^0, \tilde{\chi}_D^0$ in increasing mass and assign them the numbers from 1 to 4, i.e. $\tilde{\chi}_1^0, \tilde{\chi}_2^0, \tilde{\chi}_3^0, \tilde{\chi}_4^0$.

Sneutrinos, the spin-0 partners of neutrinos, are also weakly-interacting and neutral, so qualify as SUSY WIMPs when the lightest of their number is the LSP. Unfortunately, this is not usually the case, because in most models one of the sleptons has a slightly lower mass than the lightest sneutrino (Jungman et al. 1996). In any case, constraints on the sneutrino-nucleon scattering cross-section from direct detection (Sect. 3.1) all but rule it out as the dominant component of dark matter, as the nuclear scattering cross-section for sneutrinos is even higher than for Dirac neutrinos (Falk et al. 1994).

It also is worth pointing out that in certain (generally non-minimal) SUSY scenarios, the dark matter particle might not be absolutely stable, but metastable on cosmological timescales. In some cases, this removes the need for R -parity conservation. This applies to some types of gravitinos (the SUSY partner of the graviton, the gauge quantum of gravity), an example of non-WIMP SUSY dark matter discussed in Sect. 2.5.

2.4.3 SUSY breaking and parameterisations

As a low-energy effective theory, the MSSM involves no specification of the mechanism by which SUSY is broken. In its full form (Eqs. 2.11–2.13), the MSSM possesses a vast number of free parameters that are not present in the SM. All but one (μ) come from the soft terms in the SUSY-breaking sector (Eq. 2.11). Counting parameters, in the gauge sector we have the normal 3 gauge couplings (e, g, g_s) and the QCD vacuum angle θ (Eq. 2.4) of the SM, as well as 6 gaugino masses (2.11a, 2.11b). One of the CP-violating masses can be removed following a field transformation, leaving 9 free parameters. From the Higgs sector (2.11c) there are two real squared masses $m_{H_u}^2$ and $m_{H_d}^2$, and one complex coefficient b . Together with the complex parameter μ and the fact that one degree of freedom can again be removed by a field definition, this leaves 5 real parameters. In the fermion sector, there are 5 Hermitian 3×3 mass-squared matrices (2.11d), as well as 9 general complex 3×3 trilinear coupling matrices (2.11e, 2.11f, 2.12), giving $5 \times 9 + 9 \times 18 = 207$ real parameters. Careful treatment of field redefinitions (Baer & Tata 2006) reduces this number by 43, leaving $5 + 9 + 207 - 43 = 178$ free parameters in the full B and L -conserving MSSM, and $178 - 3 \times 18 = 124$ in the version where the ‘C-terms’ (2.11f) are excluded. Given 19 parameters in the SM, there are therefore either 159 or 105 more parameters in the full MSSM than the SM.

SUSY-breaking itself is a jungle, and even the zoo of viable breaking schemes is vast and varied (see e.g. Luty 2005, for an introduction). Spontaneous SUSY breaking is hard to achieve at tree level, because none of the MSSM supermultiplets can easily acquire an appropriate VEV (this is related to a particular sum rule for the tree-level masses; see e.g. Martin 1997; Baer & Tata 2006). The solution seems to be for SUSY to be broken in a particle sector which has only very weak or indirect interactions with the MSSM, and then communicated to the MSSM by some heavy mediator particle X . The mass at which SUSY is broken in the other

sector is related to the mass of the mediator by

$$\frac{M_{\text{SUSY}}^2}{M_X} \sim m_{\text{soft}} \sim 1 \text{ TeV}. \quad (2.18)$$

The decoupled matter sector is often referred to by the unfortunate sobriquet of ‘the hidden sector’, which (at least for this author) evokes notions of fine-tuning and careful sequestering away of a whole matter sector because experimentally, it should be ‘seen and not heard’. In reality though, most hidden sectors required in SUSY-breaking scenarios have a very high characteristic mass scale. We should therefore expect them to decouple from the low-energy theory as the influence of the heavy particles is integrated out, into mass dimension $d > 4$ operators suppressed by $d-4$ powers of the large mass scale. In that case, the ‘hidden sector’ is then simply one which is phenomenologically disjoint (effectively hidden) from the SM because of its high energy scale.

Three scenarios have received the bulk of attention to date: gravity mediation (Chamseddine et al. 1982), gauge mediation (Giudice & Rattazzi 1999) and anomaly mediation (Randall & Sundrum 1999). In gravity-mediated scenarios, SUSY-breaking occurs in the matter sector associated with new physics around the Planck scale M_P . The breaking is hence mediated by particles with $M_X \sim M_P$, leading to hidden sector SUSY-breaking at about 10^{11} GeV. The coupling between the hidden and observable sectors is naturally very weak because gravity is so weak, and in this case can actually even occur at tree level. This is because SUSY-breaking in the gravitational sector actually implies that we are talking about supergravity (SUGRA), where SUSY has been made a local rather than a global symmetry, and gauged. This happens to modify the tree-level mass sum rule in such a way that an appropriate VEV is possible to come by from within the MSSM. It is important to note that gravity-mediation must always occur at some level if all interactions are supersymmetric, the issue is just whether or not it dominates over other contributions to SUSY breaking. Aside from string theory, $N = 8$ SUGRA is also the only known potentially-viable theory of quantum gravity (Bern et al. 2009).

Gauge-mediated SUSY breaking (GMSB) takes an entirely orthogonal approach, where SUSY breaking is mediated by a particle which has both hidden sector and SM gauge couplings. Actually, the mediator gets an entire sector of its own in many GMSB scenarios, known as the ‘messenger sector’; here the hidden sector breaks SUSY, passes it on to the messenger

sector, which then communicates it to the observable sector. The mediator conveys SUSY breaking radiatively from the messenger sector to the observable sector, coupling to the MSSM only at loop level. In this case the mediator can be of almost any mass; if it is light, SUSY breaking in the messenger sector can occur at much lower masses than in the gravity-mediated scenario. Anomaly-mediated SUSY breaking (AMSB) relies on extra dimensions and somewhat contrived brane geometries and dynamics to suppress gravity mediation to a level where loop contributions from a particular anomaly dominate the mediation.

For the purposes of phenomenology, the full 124 or 178-parameter MSSM is not really very practical to work with. Indeed, many of the terms should be suppressed anyway in order to agree with experiment: the M' gaugino masses should be small or absent in order to prevent excessive CP -violation, as should the various CP -violating phases arising from complex MSSM parameters. The off-diagonal entries in the mass matrices are constrained to be small by the level of flavour-changing neutral currents (FCNCs) they cause. One approach to SUSY phenomenology is thus to work with the effective low-energy theory, but approximate all these dangerous terms to zero. One can go a step further and assume reality and universality in the mass and trilinear coupling matrices, such that each is just a real constant times the identity matrix. One could even be so bold as to assume that some of *those* constants are equal to one another. Many different low-energy parameterisations have been used in the literature: 6, 7, 8, 19, 24-parameter versions and so on, depending upon the individual authors' computational resources and the nuances of the specific observable under investigation.

The alternative is to take one of the scenarios for SUSY breaking, which invariably predict universality and reality in the structure of their soft terms at the scale of the mediator particles M_X . Investigating the phenomenology then requires evolving the soft terms down to the weak scale using the renormalisation group equations (RGEs). In the minimal supergravity (mSUGRA) model, all scalar masses, gaugino masses and trilinear couplings are unified at respective values m_0 , $M_{\frac{1}{2}}$ and A_0 , either at M_P or more commonly, M_{GUT} . The only remaining non-SM parameters are $\tan\beta$, the ratio of up-type to down-type Higgs VEVs at the weak scale, and the sign of the μ parameter. The bilinear coupling $B \equiv b/\mu$ and the magnitude of μ are set by the condition that SUSY-breaking

radiatively generates EWSB. The parameter space is thus⁴

$$m_0, M_{\frac{1}{2}}, A_0, \tan \beta, \text{sgn}(\mu). \quad (2.19)$$

The minimal gauge-mediated model (mGMSB) is characterised by the parameter set

$$\Lambda, M, n_5, \tan \beta, \text{sgn}(\mu), C_{\text{grav}}, \quad (2.20)$$

where

$$\Lambda \equiv \frac{M_{\text{SUSY, mess.}}^2}{\langle S \rangle}, \quad (2.21)$$

with $M_{\text{SUSY, mess.}}$ the SUSY-breaking scale in the messenger sector and $\langle S \rangle$ the VEV of the scalar part of a gauge singlet superfield \hat{S} which also couples to the messenger sector. M is the mass scale of the messenger sector, which consists of n_5 generations of vector-like multiplets of quark and lepton superfields carrying SM charges. C_{grav} is the gravitino mass parameter

$$C_{\text{grav}} = \frac{M_{\text{SUSY, hidd.}}^2}{\lambda M_{\text{SUSY, mess.}}^2}, \quad (2.22)$$

where $M_{\text{SUSY, hidd.}}$ is the SUSY-breaking scale in the hidden sector and λ is the common messenger-sector Yukawa coupling between \hat{S} and the messenger quark and lepton supermultiplets. The trilinear couplings are essentially absent in this model, so $\mathbf{A}_u = \mathbf{A}_d = \mathbf{A}_e = 0$.

The minimal version of AMSB (mAMSB) is specified by

$$m_0, m_{\frac{3}{2}}, \tan \beta, \text{sgn}(\mu), \quad (2.23)$$

where $m_{\frac{3}{2}}$ is the gravitino mass, which is also ultimately responsible for determining the gaugino masses and the trilinear couplings. The other three parameters are defined identically to their mSUGRA counterparts.

⁴Strictly speaking, what I describe here is the ‘constrained MSSM’ (CMSSM). According to some definitions, the mSUGRA model differs from the CMSSM, in that the condition of EWSB does not necessarily have to be imposed, making μ a parameter, B is used instead of $\tan \beta$, and the relation $A_0 = B + m_0$ is sometimes used to eliminate B as a free parameter (or equivalently, $\tan \beta$ in versions where EWSB is imposed). The distinction typically only matters to those not-so-subtly trying to establish precedence for certain prizes.

2.4.4 SUSY scanning

In order to compare any particular version of SUSY with experimental data, one generally needs to consider a number of different points in the model parameter space, covering a large range of each of the free parameters. One then scans over the parameters using some sort of search algorithm, evaluating the values of the relevant observables at each point. These can then be compared with existing data to determine if the point is consistent with experiment, or to make predictions for future experiments.

With such high-dimensional parameter spaces, and a very nonlinear mapping from some of the model parameters to actual observables like cross-sections, it is no surprise that scanning SUSY parameter spaces is not a simple exercise. This is especially so if one wants to make meaningful statements about which regions of the parameter space are allowed or disallowed, and to what degree of statistical significance. Traditional analyses simply assigned a status of either ‘allowed’ or ‘excluded’ to a point if it lay within or beyond a certain confidence level of the measured data. These were often based on brute-force random scans, with little concern for convergence or any sort of statistical interpretation. The modern approach is to consider the full likelihood for each point, and analyse the resultant map in terms of either a Bayesian or frequentist statistical framework. These scans have often also employed sophisticated scanning techniques like Markov Chain Monte Carlo (MCMCs), nested sampling or genetic algorithms. The reader is referred to p. 3 of [Paper V](#) for a detailed background on the differences between the Bayesian and frequentist approaches in this context. Details of the differences between scanning techniques and a review of significant work in SUSY scanning can be found on p. 3 of [Paper IV](#) and pp. 4–5 of [Paper V](#).

In particular, the most well-known products of SUSY scanning are the various regions of mSUGRA compatible with the relic density from the CMB. These regions, as well as benchmark points drawn from them, have been widely used for collider studies and design over the last 20 years. A short review of these regions is given on p. 3 of [Paper IV](#).

2.5 Gravitinos and Axinos

If supersymmetry is made local and extended to supergravity, the graviton acquires a spin- $\frac{3}{2}$ superpartner, the gravitino. In gravity-mediated SUSY-breaking scenarios, the gravitino obtains a similar mass to the

other sparticles, i.e. m_{soft} , whereas in gauge-mediated schemes it has a mass of the order of a few keV (Martin 1997). It can therefore be the LSP in some cases, the next-to-lightest SUSY particle (NLSP) in others, or just another more massive member of the SUSY spectrum.

If it is the LSP and R -parity is conserved, the gravitino is stable, so it can constitute a viable but depressing dark matter candidate. This is because it interacts only gravitationally with the rest of the spectrum, easily fulfilling the collisionless, non-dissipative and electrically-neutral requirements of a good dark matter candidate – but the very weakness of the interaction means that it is however virtually undetectable. If the gravitino is the NLSP, the weakness of its interactions can make it meta-stable, potentially leading to non-thermal LSP dark matter production by decay. The caveat is that the long lifetime can interfere with later-time processes like BBN, depending upon which SM particle the gravitino predominantly decays into along with the LSP. The same is also true if the gravitino is the LSP, as in this case the weakness of its interactions again make the NLSP long-lived. Their long lifetimes mean that gravitinos can be viable dark matter candidates even if R -parity is violated, since they would again be meta-stable. Because thermal gravitinos decouple from the primordial bath around the Planck mass, their cosmology is particularly complicated and uncertain; they could constitute either warm or cold dark matter, depending upon their mass and cosmological history.

If one extends the SM to include the axion (cf. Sect. 2.2) as a solution the strong CP problem, then the supersymmetrised version of the theory of course also contains a spin- $\frac{1}{2}$ axino (see e.g. Covi & Kim 2009). Like the gravitino, the axino is extremely weakly interacting, so would be perfectly viable as dark matter if it were the LSP. In contrast to the gravitino though, the axino should at least be detectable indirectly through the observation of the axion itself. Because of its ultra weak coupling to other particles, if it is the LSP or NLSP the axino might have any of the same features and issues as the gravitino with regard to long-lived states.

2.6 Sterile neutrinos

The fact that neutrinos have been observed to oscillate indicates that they have masses, though experimental limits constrain them to be sub-eV. This presents quite a fine-tuning problem, as the masses must be many orders of magnitude less than any other known massive particles. The favoured mechanism for producing such small masses is known as

the see-saw, which operates by introducing heavy singlet (right-handed) neutrino states of mass $\sim M$. The observed neutrino masses become inversely proportional to M when the mass matrix is diagonalised. The singlet neutrinos do not interact with other particles because they carry no charges under any of the SM gauge groups. Being massive fermions, the actual neutrino mass eigenstates differ from the weak eigenstates; the splitting is sufficiently large that the light neutrinos are almost entirely left-handed in character, and the heavy ones almost entirely singlet. This makes the heavy states very weakly interacting, or ‘sterile’, and sufficiently long-lived to constitute dark matter.

M can in principle take on almost any value (there are valid naturalness arguments for it being around M_{GUT} , or for being rather small). If it is in the keV mass range, then the sterile neutrino can be a viable warm dark matter candidate, with the correct relic abundance (see e.g. [Kusenko 2009](#), for a recent review). Depending on the production mechanism in the early Universe, it is also possible to make sterile neutrinos cold(ish) dark matter.

2.7 Other candidates

I will not attempt to detail the myriad other viable dark matter candidates which exist; this subsection merely provides a summarising ‘sound bite’ on some of the more notable ones, and some references for further reading.

A range of ‘WIMP-derivative’ models build upon the basic idea of WIMP dark matter, or at least make use of a number of its desirable features. WIMPless dark matter ([Feng & Kumar 2008](#); [Feng 2010](#)) employs the WIMP miracle in a hidden sector, by tuning the WIMP mass and interaction strength to achieve the desired relic density, à la Eq. 2.9. WIMPzillas ([Kolb et al. 1999](#)) are superheavy, weakly-interacting particles formed out of thermal equilibrium, arising from e.g. the GMSB messenger sector. Minimal Dark Matter ([Cirelli et al. 2006](#); [Cirelli & Strumia 2009](#)) involves the trial-and-error addition of any colourless $SU(2)_L$ multiplet with a neutral lightest member to the SM, in the search for a WIMP. Inelastic Dark Matter (iDM; [Smith & Weiner 2001](#); [Tucker-Smith & Weiner 2005](#)) and eXciting Dark Matter (XDM; [Finkbeiner & Weiner 2007](#)) are WIMPs with excited states, nowadays often paired with models exhibiting Sommerfeld-enhanced annihilation ([Arkani-Hamed et al. 2009](#); [Nomura & Thaler 2009](#)). These models are all designed to explain specific observational anomalies.

SIMPs (Starkman et al. 1990) are Strongly Interacting Massive Particles which could form colourless bound states (Kang et al. 2008) and hide their strong interactions, whilst milli-charged particles (Holdom 1986; Davidson et al. 2000) might manage to appear dark because they carry only a very small fractional electric charge. Both these options are very strongly constrained at the present time (Taoso et al. 2008).

Chapter 3

Searches for dark matter

Dark matter can be sought in a number of complimentary ways. In Sects. 3.1–3.5 I give an overview of the main techniques used to search for WIMPs, followed in Sect. 3.6 by a quick exposition of other tests, including those for non-WIMP models. It is unlikely that any single search technique will ultimately be enough for us to confidently characterise or completely exclude a particular dark matter model; combining results from different searches is precisely the strategy adopted in Paper IV and Paper V, and discussed in Sect. 2.4.4 in the context of SUSY.

3.1 Direct detection

Because WIMPs interact with SM particles by the weak force, they should have weak-scale scattering cross-sections with normal nuclei. One of the most promising ways to detect WIMPs is thus to look for nuclear recoils in large-volume target materials on Earth (Goodman & Witten 1985).

The expected number of WIMP-nucleon scattering events dN per nuclear recoil energy window dE_r is given (Gaitskell 2004) by

$$\frac{dN}{dE_r} = \frac{\sigma \rho}{2\mu^2 m_\chi} F^2 \int_{v_{\min}(E_r)}^{v_{\text{esc}}} \frac{f(v)}{v} dv, \quad (3.1)$$

where σ is the WIMP-nucleus cross-section, ρ the local WIMP density, m_χ the WIMP mass and F the nuclear form factor. The WIMP-nucleus reduced mass is $\mu \equiv (m_\chi m_{\text{nuc}})/(m_\chi + m_{\text{nuc}})$. The distribution of WIMPs in the halo with velocities v is given by $f(v)$, which is integrated over all possible velocities. These range from $v_{\min}(E_r)$, the minimum velocity necessary to produce a recoil of energy E_r , to the halo escape velocity v_{esc} .

Nuclear recoil searches attempt to measure $\frac{dN}{dE_r}$ directly. By assuming a certain halo model, this then allows a relation to be inferred between the WIMP mass and cross-section. The standard halo model assumes a Maxwellian velocity distribution with $v_{\text{RMS}} \approx 220 \text{ km s}^{-1}$ and a local density of 0.3 GeV cm^{-3} ; alternative halo models and their influence upon direct detection results have also been discussed (e.g. [Belli et al. 2002](#); [Stiff & Widrow 2003](#); [Green 2007, 2008](#); [Read et al. 2009](#)).

The cross section has two parts: a spin-independent interaction σ_{SI} between WIMPs and all nucleons, and a spin-dependent component σ_{SD} coupling only to nucleons with net spin. The kinematics of WIMP-nucleon collisions mean that both parts are proportional to the square of the WIMP-nucleon reduced mass. This dependence is generally suppressed in practice however, as direct detection experiments are never sensitive to the full WIMP recoil spectrum. The spin-independent part has a further dependence on the square of the nuclear mass. The spin-dependant component instead depends upon the nuclear spin J and the spins of the individual proton and neutron subsystems in the nucleus (see e.g. Eq. 2.8 of [Paper II](#), or [Jungman et al. 1996](#); [Gondolo et al. 2004](#); [Cerdeño & Green 2010](#)). Target nuclei with different isotopic compositions can be chosen to optimise an experiment for spin-dependent or spin-independent searches.

Three physical consequences of nuclear recoils are used to search for evidence of WIMP scattering. One is ionisation of target atoms caused by energy transfer from the recoiling nucleus. Another is fluorescent radiation given off by electrons of target atoms, as they decay after having been excited by energy transfer from the recoiling nucleus. Materials known as scintillators, which are transparent at their fluorescent wavelength and have a very fast decay time, are used extensively for this purpose; in this case, the process is referred to as scintillation. The third technique is to measure phonon excitations generated in crystals by the nuclear recoils, where minute heat changes corresponding to the absorption of individual vibrational quanta are measured. Various combinations of these detection methods are employed in different experiments.

Due to the proper motion of the solar system within the galactic halo, there should be a mean net velocity between WIMPs and the Earth. This should result in both a diurnal modulation of WIMP-nucleus collisional directions, and an annual modulation of the total detection rate due to the non-perpendicularity of the solar ecliptic and galactic planes.

Exclusion limits placed upon the WIMP mass and spin-independent

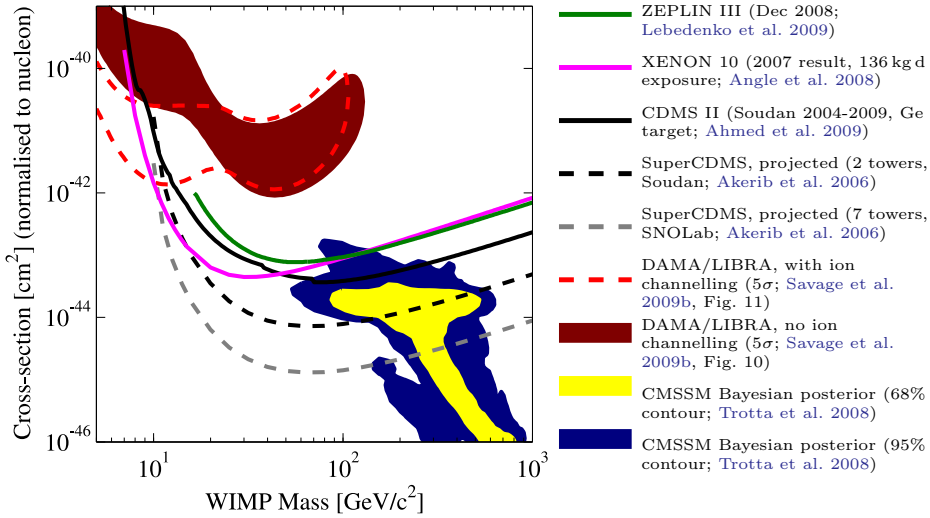


Figure 3.1. Exclusion curves, fit regions and SUSY predictions for WIMP masses and spin-independent nuclear scattering cross-sections. The areas above each curve are excluded by the respective experiments, listed to the right. The red regions are claimed detections of an annual modulation signal by the DAMA collaboration, under different assumptions about channeling by the detector crystal. The yellow and blue regions are Bayesian posterior predictions within the CMSSM, taking into account all other experimental constraints.

nuclear scattering cross-sections by various direct detection experiments are shown in Fig. 3.1. The plot also shows a theoretical prediction from a Bayesian CMSSM parameter scan (blue and yellow solid region; Trotta et al. 2008), as well as the area compatible (Savage et al. 2009b, red solid region) with the claimed detection of an annual modulation signal by the DAMA collaboration (Bernabei et al. 2000, 2008). Other experiments appear to disfavour a dark matter interpretation for this signal. However, the solid compatible region on this plot has been drawn assuming standard WIMP, halo and target models; the annual modulation signal can be made marginally compatible with other experiments if these assumptions are relaxed (e.g. Savage et al. 2009a,b; Fairbairn & Schwetz 2009). An example of how the compatibility region changes when channeling in the detector crystals is included (Savage et al. 2009b) is outlined in red dashes. A similar story holds for interpretation of the DAMA signal in terms of spin-dependent WIMP scattering (not shown). Predicted sensitivity curves for upcoming experiments are also shown, showing that a substantial part of the CMSSM parameter space should become accessible

in the near future.

3.2 Indirect detection

If WIMPs are thermal relics, they should generically possess weak-scale self-annihilation cross-sections. This is true whether the particles are Majorana or Dirac. In the Dirac case, being a thermal relic implies that there is no net matter-antimatter asymmetry, since any excess of WIMPs or anti-WIMPs would cause the relic abundance to be determined by the asymmetry rather than thermal production. If dark matter is produced non-thermally, it could also have a comparable, or even higher, self-annihilation cross-section. Except in the case of a non-thermally produced Dirac particle with an initial matter-antimatter asymmetry, WIMPs should therefore annihilate at a non-vanishing rate today.

Indirect detection methods aim to detect the primary or secondary products of these annihilations, in the form of photons, neutrinos or other cosmic rays. The same techniques can also be used to search for the products of decaying dark matter, such as the LSP in versions of SUSY which weakly violate R -parity. Searches place constraints on annihilation cross-sections in annihilating models (and therefore the relic density, in ones where the particle is thermally-produced), and on the lifetime in decaying models. As a two-body process, the annihilation rate is proportional to the square of the dark matter density, whereas the single-body decay process is proportional to the first power of the density.

Whether searching for annihilations or decays, the most promising targets are those with large dark matter densities and/or low astrophysical backgrounds. The Galactic Centre (GC) would seem the most obvious target given its distance and dark matter concentration, but it is also one of the most difficult areas to work with because of its complex and poorly-understood background (Vitale et al. 2009; Acero et al. 2010), and uncertain dark matter profile (Stoehr et al. 2003; Merritt 2010). Better prospects might be had just outside the GC, in a broken annulus which excludes the galactic disc (Stoehr et al. 2003; Serpico & Zaharijas 2008). Dwarf galaxies are a good option because they are extremely dark-matter-dominated, leading to a low background, but have the disadvantage of also having rather low predicted fluxes (e.g. Bringmann et al. 2009; Pieri et al. 2009; Martinez et al. 2009). Smaller, previously unidentified clumps of dark matter with no association to any known astrophysical sources (e.g. Green et al. 2004a; Green et al. 2005; Kuhlen et al. 2008; Bringmann

2009; Paper III) would make for a spectacular, background-free discovery if any were detected, but there is significant theoretical uncertainty in their expected number, mass and proximity to Earth. Galaxy clusters and the total integrated contribution to the extragalactic background have also been considered competitive targets.

The relative merits of the different targets depend upon whether limits are sought on annihilation or decay, and the observation channel. Massive charged particles like electrons are attenuated and deflected by magnetic fields, causing them to almost always arrive isotropically. Further discussion of the uncertainties in dark matter density profiles and the astrophysical production and propagation of cosmic rays can be found in Chapter 4.

The expected differential primary gamma-ray flux per unit solid angle (e.g. Bergström et al. 1998) from WIMP annihilations is

$$\frac{d\Phi}{dE d\Omega} = \frac{1 + BF}{8\pi m_\chi^2} \sum_f \frac{dN_f^\gamma}{dE} \sigma_f v \int_{\text{l.o.s.}} \rho_\chi^2(l) dl, \quad (3.2)$$

where BF is the boost factor from unresolved substructure in the source, f labels different final states, dN_f^γ/dE is the differential photon yield from any particular final state, σ_f is the cross-section for annihilation into that state, v is the WIMP relative velocity, and the integral runs over the line of sight to the source. In the absence of any bound states (i.e. Sommerfeld enhancements), WIMPs move so slowly that they can effectively be considered to collide at rest, allowing $\sigma_f v$ to be replaced with the velocity-averaged term in the zero-velocity limit, $\langle \sigma_f v \rangle_0$.

In the case of neutralino annihilation, three main channels contribute to the gamma-ray spectrum. Through loop processes, annihilation can proceed directly into two photons (Bergström & Snellman 1988; Bergström & Ullio 1997)

$$\frac{dN_{\gamma\gamma}^\gamma}{dE} = 2\delta(E - m_\chi), \quad (3.3)$$

or into a Z boson and a photon (Ullio & Bergström 1998)

$$\frac{dN_{Z\gamma}^\gamma}{dE} = \delta(E - m_\chi + \frac{m_Z^2}{4m_\chi}). \quad (3.4)$$

This gives a monochromatic gamma-ray line. Because no other known process produces such a line, this would be a smoking gun signal for

WIMP dark matter. Unfortunately, the loop suppression means that very few models actually have substantial branching fractions into monochromatic photons. A hard spectrum can also be produced by internal bremsstrahlung (final-state radiation plus virtual internal bremsstrahlung), generated when a photon is emitted from a virtual particle participating in the annihilation (Bergström 1989; Bringmann et al. 2008). Continuum gamma-rays can also be produced by annihilation into quarks, leptons and heavy gauge bosons (including the Z from the $Z\gamma$ line), which subsequently decay via π^0 and the emission of bremsstrahlung to softer photons.

Indirect detection with photons is currently dominated by large air-Cherenkov gamma-ray telescopes (ACTs) and the *Fermi* Large Area Telescope (LAT; Atwood et al. 2009), a pair-conversion gamma-ray space telescope. Limits on the total cross-section from dwarf galaxies (Lombardi et al. 2009; Essig et al. 2009; Paper IV; Abdo et al. 2010b), the isotropic diffuse background (Abdo et al. 2010c; Abazajian et al. 2010) and galaxy clusters (Abdo et al. 2010d) are approaching the canonical thermal cross-section ($3 \times 10^{-26} \text{ cm}^3 \text{ s}^{-1}$; cf. Sect. 2.3.1), but cannot yet conclusively exclude it for any range of WIMP masses. LAT limits on annihilation into gamma-ray lines also exist (Abdo et al. 2010a). Claims have been made from outside the collaboration of excesses in public *Fermi* data in the inner Galaxy (Goodenough & Hooper 2009; Dobler et al. 2009), which some have interpreted as signals of WIMP annihilation. Their status as true excesses rather than instrumental foibles or systematics arising from overly simplified background modelling (e.g. Linden & Profumo 2010) have yet to be confirmed or disproved by the LAT collaboration.

Gamma-ray and longer-wavelength observations also make it possible to hunt for secondary photons from WIMP annihilation or decay. In particular, inverse Compton scattering of CMB and interstellar radiation field photons by primary leptons injected in annihilations or decays can lead to substantial signals in gamma rays and X-rays (Regis & Ullio 2008; Cirelli & Strumia 2009; Profumo & Jeltama 2009; Belikov & Hooper 2010; Abdo et al. 2010c,d). Synchrotron emission from primary leptons in regions with significant magnetic fields can also be a competitive probe (Regis & Ullio 2008; Bertone et al. 2009; Bergström et al. 2009a), as can modifications of the CMB by particle injection from dark matter annihilation at early times (Slatyer et al. 2009; Galli et al. 2009).

Recent electron and positron cosmic ray data from *Fermi* (Abdo et al. 2009), the PAMELA satellite (Payload for Anti-Matter Exploration and Light-nuclei Astrophysics; Adriani et al. 2009a) the ATIC balloon mission

(Advanced Thin Ionisation Calorimeter; [Chang et al. 2008](#)) and the HESS ACT (High Energy Stereoscopic System; [Aharonian et al. 2008](#)) indicate a slight excess in the total number of events at ~ 10 GeV–10 TeV over that expected purely from background. A substantial excess is also seen in the fraction of events due to positrons. This has led to a flood of papers explaining the data in terms of dark matter annihilation or decay (e.g. [Bergström et al. 2008](#); [Arkani-Hamed et al. 2009](#); [Nomura & Thaler 2009](#); [Chen et al. 2009](#); [Donato et al. 2009](#)). Almost all annihilation scenarios require a substantial boost to the annihilation cross-section above that expected for a typical thermal relic, either from substructure or specific particle models (these are the Sommerfeld-enhanced models mentioned in Sect. 2.7). Such boosted models are put under rather severe pressure by limits from recent gamma-ray observations (e.g. [Abdo et al. 2010b,c,d](#); [Abazajian et al. 2010](#)). The positron excess can also be explained in terms of conventional astrophysical sources like pulsars ([Profumo 2008](#); [Yüksel et al. 2009](#); [Hooper et al. 2009](#)) and supernova remnants ([Blasi & Serpico 2009](#); [Piran et al. 2009](#); [Fujita et al. 2009](#)), and possibly even standard secondary production ([Katz et al. 2009](#)).

In many models, WIMP annihilation produces a substantial number of antiprotons. Observations of cosmic ray antiprotons by PAMELA ([Adriani et al. 2009b](#)) show no excess above the expected astrophysical background. This places rather severe limits on the types of models which can be invoked to explain the PAMELA positron excess, as they must not overproduce antiprotons. Together with the steepness of the rise observed in the positron fraction, this suggests that such models should annihilate predominantly to lepton-antilepton pairs (so-called ‘leptophilic’ dark matter; [Cholis et al. 2009](#); [Bergström 2009](#); [Bergström et al. 2009b](#)), which is somewhat difficult to achieve in the MSSM ([Bergström et al. 2008](#)).

Antideuterons are another promising indirect detection channel. Although predicted yields from dark matter annihilation ([Donato et al. 2000](#); [Baer & Profumo 2005](#)) and decay ([Ibarra & Tran 2009](#)) are certainly smaller than those for antiprotons, the very low backgrounds expected ([Donato et al. 2008](#)) could make antideuterons a useful detection method. This is especially true for low WIMP masses, where kinematics would prevent background antideuteron formation from spallation. Future experiments, such as the imminent Alpha Magnetic Spectrometer space shuttle mission (AMS-02; [Choutko & Giovacchini 2008](#)) and the dedicated balloon mission GAPS (General AntiParticle Spectrometer; [Hailey 2009](#)), should make interesting inroads into model parameter spaces.

In certain models, such as Kaluza-Klein dark matter in Universal Extra Dimensions (UED), WIMPs can annihilate directly into neutrinos. Other models produce neutrinos in secondary decays and/or cascade interactions with baryonic matter. Whilst their weak interactions, small masses and atmospheric background make neutrinos a difficult indirect detection prospect, they have the advantage of pointing directly back to a source in the same way photons do. With observations of the GC (Bertone et al. 2004) and the inner Galactic halo (Yüksel et al. 2007), the SuperKamiokande neutrino telescope has been used with some success to constrain the annihilation cross-section of traditional WIMP models. Upcoming cubic-kilometre telescopes such as IceCube should also prove powerful enough to essentially rule out Sommerfeld-enhanced leptophilic models, through observations of the central regions of our own Galaxy (Hisano et al. 2009; Liu et al. 2009; Buckley et al. 2010; Mandal et al. 2010) or dwarfs (Sandick et al. 2009).

Indirect detection could also include dark stars and searches for neutrinos from WIMP annihilation in the Sun. Unlike the indirect searches just described, stellar probes depend more upon nuclear scattering than the annihilation cross-section, so I will describe them separately (in Sects. 3.4 and 3.5, respectively).

3.3 Accelerator searches

Finding dark matter at accelerators is unlikely to be straightforward. The most obvious collider WIMP signature is expected to be missing transverse energy (missing E_T), which refers to an apparent missing component of the total final-state momentum in the direction transverse to a collider beam. If the outgoing transverse momenta of a reaction do not sum to zero (as they do in the original beam), this can be attributed to the production and escape of a massive particle with a very small interaction cross-section with the detector material. The catch is that whilst the particle must be stable enough to travel beyond the detector, there is no way of to know how stable it is on cosmological timescales. There would hence be no way to infer its relic abundance.

By looking at kinematic endpoints in the momentum distributions of observed particles, one can derive the masses of intermediate states in the decay chain leading to the missing E_T , including the mass of the missing particle itself (Battaglia et al. 2004; White 2007). By carefully examining the shapes of the distributions, in principle one can also distinguish

between different theories giving rise to the same (observable) decay products. The difficulty with this prospect is that in a hadron collider like the LHC (Large Hadron Collider), collisions take place between bound-state quarks. It is therefore impossible to ever know exactly where the rest frame of each interaction is. Whilst there should be a known distribution of rest frames across all collisions, this still introduces a significant uncertainty to the distributions for rare processes like those that would produce WIMPs, and also makes efforts to disentangle the spins of the new particles very difficult (Baltz et al. 2006).

The main alternative is to attempt to reconstruct the whole underlying theory responsible for the new TeV-scale physics, by using other channels (than missing E_T) to constrain the masses and couplings of other new particles. In this way, one might infer the mass, spin and cross-section of the dark matter particle(s) without measuring them directly. A more reliable option would be to employ a lepton collider like the proposed ILC (International Linear Collider), which should allow direct pair production of WIMPs if they exist in the appropriate mass range. This would allow direct measurements of the spin, couplings and mass of the particle, though the issue of proving stability would remain (Baltz et al. 2006). The couplings could however be measured well enough to determine a particle's relic density to a similar level of accuracy as from the CMB (Battaglia 2009); if the two matched, stability would be strongly implied.

Another interesting alternative allowed by a lepton collider would be to search for initial state internal bremsstrahlung in dark matter pair production (Birkedal et al. 2004). If dark matter were a thermal relic, the event rate would be related to the relic density via the production/annihilation cross-section. Some signal should thus be expected for any thermally-produced WIMP, assuming a non-vanishing annihilation branching fraction into the particular leptons used.

In general, an unequivocal identification and characterisation of the particle responsible for dark matter will require verification from a range of different searches. Accelerators will help most in characterising the theory to which it belongs, whilst direct and indirect searches should provide information about its stability and cosmological abundance. All can contribute to determining the mass and couplings.

3.4 Dark stars

If dark matter annihilates at a non-negligible rate today, we might expect that the energy from those annihilations could impact nearby baryonic systems. This might contribute to heating of the intergalactic medium (Ripamonti et al. 2007), reionisation (Natarajan & Schwarz 2008), the CMB temperature fluctuations (Slatyer et al. 2009; Galli et al. 2009), or the energy budget of stars (Steigman et al. 1978; Bouquet & Salati 1989; Salati & Silk 1989). Stars whose structure or evolution are affected in this way are often referred to as ‘dark stars’.

Stars might obtain a substantial amount of dark matter in their cores by nuclear scattering, gravitational contraction, or both. In the same way that we expect WIMPs to collide with nuclei in direct detection apparatuses (Sect. 3.1), we should also expect them to scatter on nuclei in astrophysical objects. Thus, in the first case WIMPs could scatter on nuclei in stars, lose sufficient energy to become gravitationally bound, and return to repeat the process (Press & Spergel 1985; Gould 1987) until they either thermalise with the stellar core or annihilate with each other. In the second case, steepening of the gravitational potential caused by dissipative collapse of a baryonic gas cloud could draw dark matter into a star during its formation (Spolyar et al. 2008; Natarajan et al. 2009; Freese et al. 2009). In either case, conductive heat transport by WIMP-nucleon scattering could in principle also affect the stellar structure or evolution, but current direct detection bounds on the scattering cross-sections make this unlikely (see e.g. Bottino et al. 2002; Paper II).

The effects upon different types of stars in a variety of locations have been considered in recent years: white dwarfs at the GC (Moskalenko & Wai 2007; Hooper et al. 2010) and in globular clusters (Bertone & Fairbairn 2008; McCullough & Fairbairn 2010), population III stars (Spolyar et al. 2008; Iocco 2008; Iocco et al. 2008; Natarajan et al. 2009; Freese et al. 2008a,b, 2010; Paper VI) and main sequence stars near the GC (Paper I; Proceeding XIII; Paper II; Casanellas & Lopes 2009). A review of the historical and recent developments in this field can be found in Sect. 1 of Paper II. The two different dark star simulation strategies employed by different groups are described in Sect. 2.1 of Paper VI. A technical treatment of WIMP capture by scattering, and the subsequent impacts upon stellar evolution can be found in Sect. 2 of Paper II. For constraining dark matter properties, dark stars are most useful for putting limits on either nuclear scattering cross-sections or the growth of dark matter halos.

3.5 High-energy solar neutrinos

In the same way that WIMPs would scatter on nuclei in dark stars and become gravitationally captured, so they should in the Sun as well. The primary difference in this case is that the expected capture rates are far lower in the Sun than at the GC or in early proto-halos, mainly due to the comparatively low dark matter density in the solar system. Although annihilation of WIMPs in the solar core should have essentially no impact on the Sun's structure or evolution, some fraction of the annihilation energy might escape as neutrinos.

These $\mathcal{O}(\text{GeV})$ neutrinos would be much more energetic than the $\mathcal{O}(\text{MeV})$ solar neutrinos from nuclear fusion (e.g. [Ahmad et al. 2001](#)), so would be clear evidence of WIMP dark matter. The only known solar neutrino background at such high energies comes from cosmic ray interactions with the corona, and is expected to be low ([Seckel et al. 1991](#); [Ingelman & Thunman 1996](#)). The main background concerns are atmospheric muons and neutrinos, produced by interactions of cosmic rays with the Earth's atmosphere. This background can be mostly avoided by triggering only on upwards-going events, at times when a terrestrial neutrino telescope is pointing away from the Sun (e.g. [Abbasi et al. 2009a,b](#)).

The capture and annihilation of WIMPs in the Sun has been used together with telescopes such as SuperKamiokande ([Desai et al. 2004](#)), AMANDA ([Ackermann et al. 2006](#)), ANTARES ([Lim et al. 2009](#)) and IceCube ([Abbasi et al. 2009a,b](#); [Flacke et al. 2009](#); [Blennow et al. 2010](#)) to place limits on WIMP-nucleon scattering cross-sections. Because the Sun consists predominantly of hydrogen, the most competitive limits from neutrino telescopes are on the spin-dependent cross section. Spin-dependent limits from IceCube are already stronger than those from direct detection ([Abbasi et al. 2009a,b](#)), and should improve significantly as the DeepCore section of the detector is added ([Ellis et al. 2009](#)).

Neutrino telescope limits from the Sun are considerably more model-dependent than those from direct detection, as the only way to calculate the expected neutrino yields is to have a particular model for the annihilation branching fractions of the WIMP (see e.g. [Wikström & Edsjö 2009](#)). Some channels give rise to more neutrinos than others, producing different limits depending upon the assumed annihilation channel. KK dark matter for example can annihilate directly into monochromatic neutrinos, whilst neutralinos produce neutrinos from a series of secondary interactions between stellar nuclei and daughter quarks and gauge bosons (e.g. [Blennow et al. 2008](#)). The expected signal from neutrino telescopes

also depends critically on the dark matter velocity distribution in the solar neighbourhood (e.g. Bruch et al. 2009); capture is far more efficient for WIMPs which arrive at the Sun with lower velocities, because they need not lose as much energy in the scattering process as faster WIMPs to become gravitationally bound. Perturbations of WIMP orbits by planets (Gould 1991; Lundberg & Edsjö 2004; Peter 2009) adds further uncertainty to the expected capture rates for a given cross-section.

3.6 Searches for other dark matter candidates

Because axions in electromagnetic fields can convert into photons and vice versa (Sect. 2.2), the best places to search for them are in objects with strong magnetic fields. The Sun is a good target, as some fraction of the photons created in the photosphere will convert to axions as they pass through the strong magnetic fields of the chromosphere and corona. The CAST (CERN Axion Solar Telescope, Arik et al. 2009) experiment searches for these axions by attempting to observe the Sun through an opaque screen and a very strong magnet, in the hope that some of the solar axions will convert back to photons in the local magnetic field, after having passed through the screen (which the solar photons could not).

A similar idea is pursued in the ‘light shining through a wall’ experiments (e.g. Robilliard et al. 2007; Pugnati et al. 2008), where a photon source is shone against a barrier after passing through a strong magnetic field. A photodetector and a second magnet on the other side of the wall look for photons regenerated in the magnetic field from axions that have passed through the wall. The same strategy could be used to detect axions by looking at background X-ray sources through the Sun (Fairbairn et al. 2007). Cavity experiments like ADMX (Axion Dark Matter eXperiment, Asztalos et al. 2010) attempt to detect halo axions, by tuning the frequency of a magnetic field to the axion mass and searching for microwaves from resonant conversion. Astrophysical limits on axions can be obtained by considering the maximum amount of energy that they could carry out of supernovae and stellar cores without exceeding observed cooling rates (see e.g. Raffelt 2008, for an up-to-date review).

One of the more promising ways to search for sterile neutrinos is via X-ray line emission produced in the loop decay $\nu_s \rightarrow \gamma\nu$. Such a signal has been claimed in *Chandra* observations of the ultra-faint dwarf galaxy Willman I (Loewenstein & Kusenko 2009), but at less than the 2σ level.

Microlensing searches might also still have some distance to run in determining the identity of dark matter. This is because ultracompact dark matter minihalos (Ricotti & Gould 2009, Paper III) could constitute non-baryonic MACHOs. These would apparently have escaped microlensing searches because they are slightly more extended than traditional MACHOs, but might appear in future surveys (Ricotti & Gould 2009).

Chapter 4

Nuisances

When searching for dark matter, uncertainties in a range of necessary input data can influence results. The most relevant of these are the assumed distribution of dark matter, and the backgrounds to which each search is subject. Backgrounds are comparatively well controlled and understood in terrestrial direct detection and accelerator experiments, but not in indirect searches in astrophysical targets.

In the types of parameter-scanning exercises discussed in Sect. 2.4.4, uncertainties in input data can be fully included in the analysis if they have been statistically quantified. In this case the uncertain quantities are referred to as ‘nuisance’ parameters, because they are parameters one is not actually interested in, but that effect results nonetheless. Here I give a very brief synopsis of the two most dangerous nuisances in dark matter searches. I also provide a brief summary of the most important nuisance parameters in particle physics, which necessarily arise from the SM.

4.1 The distribution of dark matter

Simulations of structure formation using just cold dark matter indicate that halos develop self-similar density profiles, approximately following an NFW (Navarro, Frenk & White 1996) or Einasto (Navarro et al. 2004) profile. Both these profiles include a steep cusp in the central region. This would seem to be at odds with kinematic data, which often indicate that the central parts of halos possess smooth cores of dark matter (de Blok et al. 2001; Gentile et al. 2004; Del Popolo & Kroupa 2009). New simulations which include baryons (Governato et al. 2010) show that feedback from star formation and supernovae might solve this problem, resulting

in cores very much like those observed. This mechanism would not be feasible for such low-mass objects as ultra-faint dwarf galaxies, as they do not possess enough baryons to form sufficient stars and supernovae to make the process efficient. On the other hand, kinematic data from the ultra-faint dwarfs is so sparse (e.g. [Geha et al. 2009](#)) that they show no real preference so far for either cores or cusps anyway, so the smallest galaxies may still actually possess the cusps predicted by simulation.

Because annihilation rates depend on the square of particle densities, the predicted rates for indirect detection depend very sensitively upon the lower end of the halo mass distribution. This is the source of BF in Eq. 3.2, the ‘boost factor’. The minimum possible mass of a dark matter halo depends upon the nature of the dark matter particle. In particular, this is set by the particle’s mass and couplings, as well as the history of its kinetic decoupling and free streaming in the early Universe ([Hofmann et al. 2001](#); [Green et al. 2004a, 2005](#)), and how those might have been influenced by events like the QCD phase transition (e.g. [Bringmann 2009](#)). For thermal WIMPs for example, the most likely minimum mass is $\sim 10^{-6} M_{\odot}$ ([Green et al. 2004a, 2005](#)), though values from 10^{-4} to $10^{-9} M_{\odot}$ are also possible ([Martinez et al. 2009](#)). Smaller halos are expected to be far more numerous than larger ones in the picture of hierarchical structure formation governed by cold dark matter, although just how much more numerous is still a matter of considerable debate between N -body groups ([Diemand et al. 2008](#); [Kuhlen et al. 2008](#); [Springel et al. 2008a,b](#)).

A standard assumption is that the velocities of WIMPs in halos follow an isotropic, spherically-symmetric, isothermal (Gaussian) distribution, with the width determined by the Keplerian velocity at the solar position. In fact none of the details of this assumption turn out to be correct if one looks at N -body simulations: velocity distributions differ in the radial and angular directions, vary with galactocentric radius, and are neither Gaussian nor spherically-symmetric ([Hansen et al. 2006](#); [Fairbairn & Schwetz 2009](#); [Paper II](#)). In any case, the distribution must be truncated at the local Galactic escape velocity, which also has some uncertainty attached to it. Local inhomogeneities in the phase space distribution further complicate matters, due to the presence of streams and cool clumps. If this were not enough, recent simulations ([Read et al. 2009](#)) also suggest that a fraction of Galactic dark matter might exist in a disk that co-rotates with the baryonic disk. The presence of such a ‘dark disk’ would substantially boost the bottom end of the velocity distribution, re-

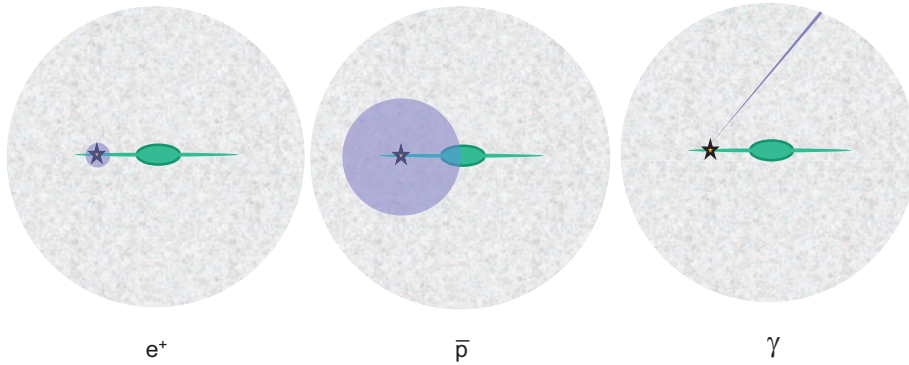


Figure 4.1. Propagation volumes for direct observations of cosmic rays. Positrons sample only the local environment, as they lose energy very efficiently via synchrotron emission, bremsstrahlung and inverse Compton scattering, and are easily deflected by magnetic fields because they are so light. Antiprotons suffer a similar fate, but are not as strongly affected because they are much more massive. Gamma rays are neutral and massless, so point directly back to their production site. From [Bergström \(2009\)](#).

sulting in greater solar capture rates and spectacularly improved limits on the nuclear scattering cross-sections ([Bruch et al. 2009](#)). Other uncertainties in the velocity distribution tend to impact direct detection more than solar capture, as the former is sensitive to WIMPs of any energy above threshold, whereas the Sun only really responds to the low-velocity part of the distribution.

4.2 Production and propagation of cosmic rays

Cosmic rays (CRs) include protons and heavy nuclei, as well as most of the interesting species for indirect detection of dark matter: electrons, positrons, antiprotons, antideuterons and gamma rays. CRs are produced when particles are accelerated in primary sources such as supernova remnants, interstellar shocks, pulsars and active galactic nuclei (AGN), and in secondary interactions or decay of other CRs. Secondary production mechanisms include spallation, radioactive decay of unstable nuclei (including by electron capture), pion production and decay in collisions of primary CRs with diffuse gas, inverse Compton scattering of diffuse radiation, bremsstrahlung and synchrotron emission ([Strong et al. 2007](#)).

The propagation of CRs depends strongly upon the particle in question, as illustrated in Fig. 4.1. Gamma-rays are neutral and massless, so arrive at Earth essentially undeflected and unattenuated. Positrons and antiprotons are massive and charged, so suffer deflection in magnetic fields and energy losses from bremsstrahlung, synchrotron and inverse Compton emission (Moskalenko & Strong 1998; Strong & Moskalenko 1998). At the energies relevant to dark matter searches, positrons are much more strongly effected than antiprotons. These energy loss processes all produce photons, resulting in a diffuse Galactic gamma-ray emission centred on the GC and Galactic disk (Strong et al. 2000). Similar processes produce gamma rays in external galaxies, especially those actively engaged in star formation (Abdo et al. 2010). Unresolved external galaxies and AGN could be responsible for the near-isotropic diffuse gamma ray emission observed by *Fermi* (Abdo et al. 2010) and its predecessors.

Modelling the propagation of CRs essentially requires solving a diffusion equation in the full phase space of the particles (see e.g. Strong et al. 2007), and adding additional terms for particle convection and decay. The diffusion is sometimes solved for analytically in 1- or 2D (e.g. Maurin et al. 2001; Putze et al. 2010), or numerically in 2- or 3D (e.g. Strong & Moskalenko 1998; Strong et al. 2007). The numerical approach allows the inclusion of much more realistic physics, source distributions and geometries. At the present time, the analytic approach is the only one which allows a full statistical estimate of the relevant parameters (e.g. Putze et al. 2009), and also arguably gives a clearer understanding of the physics involved. The parameters of the propagation model can be constrained by comparing with primary-to-secondary ratios such as boron to carbon, which are not strongly dependent upon the primary injection spectrum.

Given a set of propagation parameters, a theoretical source distribution and injection spectrum, and interstellar gas and magnetic field maps, one can then derive a predicted phase space distribution of charged CRs. The local form of the distribution can then be used as a background prediction in e.g. positron or antiproton indirect dark matter searches. To obtain a similar estimate of gamma-ray backgrounds, the charged CR distribution is combined with the gas map to predict yields from bremsstrahlung and pion decay, with interstellar radiation maps (and less importantly, the CMB) to predict inverse Compton yields, and with the magnetic field map to produce synchrotron yields.

4.3 Standard Model nuisances

In principle, uncertainties in all 19 SM parameters constitute nuisances for SUSY scans, and could impact dark matter analyses. In practice though, some parameters dominate over others. The most important experimental uncertainties in the SM are those attached to the measured masses of the particles. As the heaviest fermions, the masses of the top and (to a lesser extent) bottom quarks are the worst constrained of all the SM particles except the Higgs. Unfortunately, the heaviest particles also have the greatest impacts upon SUSY phenomenology. The masses of the Z and W bosons are not substantial nuisances, as they are known very accurately ([Amsler et al. 2008](#)).

The strengths of the gauge coupling constants also have a substantial effect, and can be difficult to constrain accurately because they run with renormalisation group evolution. Only the strong and electromagnetic couplings are significant nuisances, as the weak coupling is known as a function of the electromagnetic coupling and the masses of the W and Z bosons. See e.g. [Allanach & Lester \(2006\)](#), [Ruiz de Austri et al. \(2006\)](#) or [Trotta et al. \(2008\)](#) for the importance of considering gauge couplings and third generation quark masses as nuisance parameters in SUSY scans.

Chapter 5

Summary of results

[Paper I](#), [Paper II](#) and [Paper VI](#) deal with the theory and detection of dark stars, at the GC and in the first dark matter halos.

In [Paper I](#), we perform a first numerical investigation of the possible effects of WIMP dark matter upon main sequence stars. We modify a simple static stellar structure code to show that stable stars supported by the annihilation of dark matter in their cores have surface temperatures and luminosities that make them resemble protostars (Fig. 5.1). The stable solutions we find to the four coupled differential equations of stellar structure (see e.g. [Kippenhahn & Weigert 1991](#); [Carroll & Ostlie 1996](#); [Stix 2002](#), or any other standard stellar astrophysics text) track the protostellar cooling trajectory known as the Hayashi track. The more dark matter is added to the stars, the further their positions are shifted in the Hertzsprung-Russell (HR) diagram, back up the Hayashi track and away from the standard hydrogen-burning solutions of the zero-age main sequence (ZAMS).

We find that the static code is unable to arrive at stable structures across the whole Hayashi track, as it fails to find solutions in the regime where neither fusion nor WIMP annihilation dominates the stellar energy budget. This can be seen as a series of gaps in the evolutionary tracks of Fig. 5.1. We investigate these regions further with a full ‘dark’ stellar evolution code `DarkStars` ([Proceeding XI](#)), and show that the absence of solutions in the intermediate regime is simply due to the numerical limitations of the static code.

We go on to investigate the structure and evolution of main sequence dark stars in detail in [Paper II](#), using `DarkStars`. We carefully describe the input physics for the `DarkStars` code, and proceed to catalogue the changes in evolutionary paths, core temperatures, core densities and convection

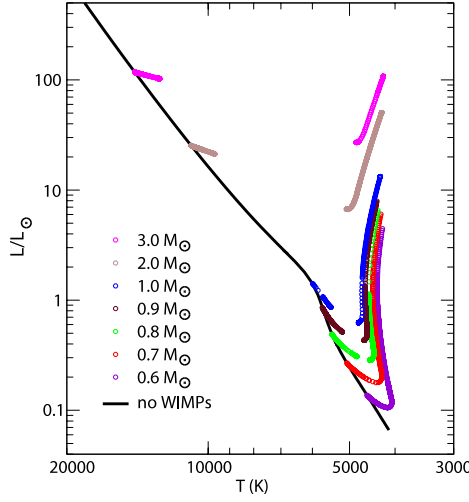


Figure 5.1. HR-diagram showing steady-state solutions for main-sequence stars powered by differing amounts of dark matter annihilation. The solid black line indicates the zero-age main sequence (ZAMS), where standard hydrogen-burning stars reside. Coloured tracks indicate solutions for different stellar masses. Stars situated further along the respective tracks (i.e. further from the ZAMS) have been provided with more dark matter. The tracks strongly resemble the Hayashi track, along which protostars cool as they condense to form main sequence stars. From [Paper I](#).

zones that result from different rates of energy injection by WIMPs, as a function of the stellar mass. We show that low-mass stars are generally much more strongly affected than high-mass ones, and that WIMP annihilation in stellar cores can significantly extend stars’ main sequence lifetimes.

We investigate what injection rates could be realised in stars orbiting close to the supermassive black hole at the GC, paying attention to stellar orbits, dark matter density profiles and velocity distributions. We derive new expressions for the capture rate from a truncated Maxwellian distribution of velocities, and outline an approximate fit to the distribution of velocities seen in the Via Lactea ([Diemand et al. 2007](#)) simulation. We find that low-mass stars on highly elliptical orbits near the GC could exhibit significant signs of WIMP capture and annihilation (Fig. 5.2). The orbits required are very similar to the orbits on which more massive stars have already been observed at the GC. The weakest point in this conclusion is the requirement of an adiabatically-contracted NFW density

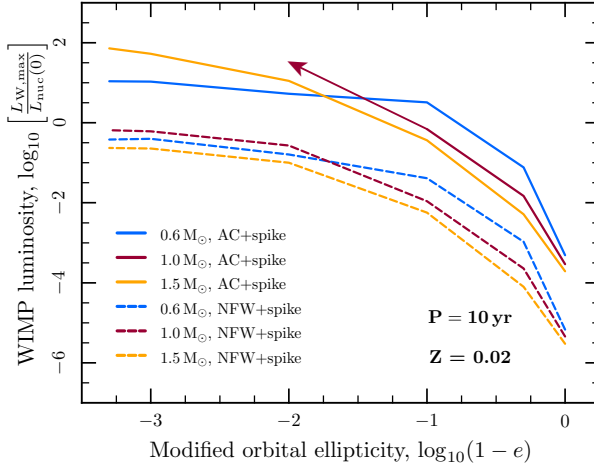


Figure 5.2. WIMP-to-nuclear luminosity ratios achieved by stars on orbits with 10-year periods around the Galactic centre. Dark matter annihilation can produce up to 100 times as much power as nuclear fusion in stars on realistic orbits in our own Galaxy. If the Galactic halo has been adiabatically contracted (AC+spike), annihilation can equal nuclear fusion in stars on orbits with eccentricities greater than $e = 0.9$, for masses less than about $1.5 M_{\odot}$. If not (NFW+spike), stars of a solar mass or less require $e \gtrsim 0.99$ to approach break-even between annihilation and fusion. The arrow indicates that the $1 M_{\odot}$, AC+spike curve is expected to continue in this direction, but converging stellar models becomes rather difficult for such high WIMP luminosities. From [Paper II](#).

profile for the most marked effects of WIMP annihilation to be realised.

We show in [Paper I](#), and then even more clearly in [Paper II](#), that dark stars resemble protostars because the annihilation of WIMP dark matter in their cores causes them to cool and expand. This result is in qualitative agreement with earlier analytical estimates ([Salati & Silk 1989](#)), though our more accurate numerical calculations show that the stars occupy slightly different positions in the HR diagram than simple polytropic models would suggest. We conclude that the reason for this behaviour is the negative specific heat of a self-gravitating system; when extra energy is injected by WIMP annihilation, the self-gravitating body cools and expands. Cooling and expansion of a stellar core reduces the rate of nuclear fusion. Reduced fusion rates mean that stars' core hydrogen lasts longer,

leading to the observed increase in (quasi-)main sequence lifetimes.

The resemblance of the ‘WIMP-burning’ tracks to the Hayashi track can be understood in terms of two aspects of the physics of WIMP annihilation in stellar cores. Our appreciation of these two aspects was not as well developed at the time of writing of either [Paper I](#) or [Paper II](#) as it has since become, so the following discussion is largely absent from those manuscripts. The first aspect is simply that the energy injected by WIMPs plays a similar role to the gravitational energy released during the contraction of a protostar, as they are both responsible for exactly the same type of term in the stellar luminosity equation (one of the four equations mentioned above).

The second and most crucial aspect is that the rate of energy production due to dark matter annihilation is not coupled to the gas pressure or temperature in any substantial way; the WIMP distribution, and hence annihilation rate, depend only very weakly upon the stellar structure. Whereas the fusion rate depends in an essential way on the gas equation of state in the stellar core, the dark matter annihilation rate essentially depends only on the WIMP density, which is mostly decoupled from everything else. Greater energy input from fusion would cause the core to cool and expand in a similar manner to what is seen to occur due to dark matter annihilation. In this case however, the expansion would have the stabilising effect of reducing the fusion yield, and causing the core to recontract. On the other hand, structural changes caused by energy injection from WIMP annihilations have almost no effect upon the net rate of annihilation, so there is no stabilising feedback. This is very much akin to the energy released in gravitational contraction; the amount of energy released depends only upon the changing gravitational potential, not directly upon the thermodynamic gas properties. This is also the main reason we see the gaps in tracks in [Paper I](#) and [Fig. 5.1](#), and see in [Paper II](#) that although we can find viable solutions in these regions, such stars are only barely stable.

We turn to dark stars in the early Universe in [Paper VI](#), investigating their observability with the upcoming James Webb Space Telescope (JWST). We compute model stellar atmospheres and synthetic spectra for the dark stars of [Spolyar et al. \(2009\)](#), and feed them through the JWST filters to ascertain their detectability as single objects. We find that single dark stars in the early Universe will not be detectable by JWST except when viewed through a substantial gravitational lens, and even then only for certain values of their lifetimes and masses. The ex-

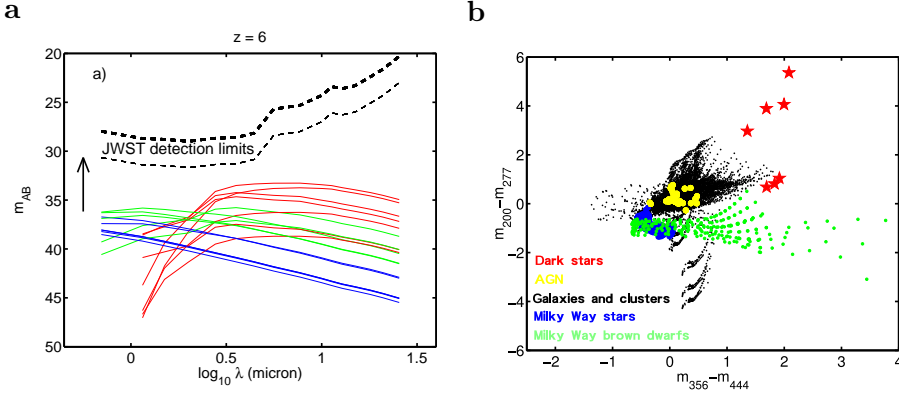


Figure 5.3. *Left (a):* predicted apparent AB magnitudes of dark stars at $z = 6$, as a function the central wavelength observed in JWST broad-band filters. Each line corresponds to a different dark star model, where models differ in their lifetimes and masses. Models differing in stellar mass also necessarily have different intrinsic luminosities, surface temperatures and surface gravities. Colours refer to surface temperatures $T_{eff} \leq 8000$ K (red), $8000 < T_{eff} \leq 30000$ K (green) and $T_{eff} > 30000$ K (blue). Dashed lines refer to 5σ and 10σ JWST detection limits after 3.6×10^5 s (100 hr) and 10^4 s of exposure, respectively. The arrow indicates the degree to which curves would be shifted upwards if dark stars were observed through the lensing cluster MACS J0717.5+3745. In this case, the coolest dark stars would become individually detectable with JWST. *Right (b):* Colour-colour diagram for dark stars and possible interloper populations, based on apparent magnitude differences in different JWST filters. The very red spectra of dark stars mean that if they are bright enough to be seen at all, dark stars would occupy a rather unique corner of the colour-colour plot, and therefore be relatively easy to distinguish from other objects. Both figures from [Paper VI](#).

pected fluxes from different dark stars are shown in comparison to JWST detection thresholds in Fig. 5.3a. The scale arrow in this figure indicates the amount by which the fluxes would be boosted if viewed through the lensing cluster MACS J0717.5+3745, which provides a magnification of $\mu = 160$. Their very red (i.e. cool) spectra mean that if they are visible at all, high-redshift dark stars will occupy a rather unique position in the colour-colour diagram of Fig. 5.3b, so should be clearly distinguishable from interloper objects.

We also show that if early dark stars live long enough, their longevity will combine with their redder spectra to produce a rather peculiar feature in the integrated spectra of high-redshift galaxies. The flux contributed

by the dark stars will tend to amass in redshift space, producing characteristic red bumps in the spectra and significantly redder overall galaxy colours. If at least 1% of stars in early-type galaxies are indeed dark stars, this feature should be detectable in galaxy spectra.

[Paper III](#) and [Paper IV](#) discuss novel aspects of indirect detection of WIMP dark matter using gamma rays, whilst [Paper IV](#) and [Paper V](#) both deal with statistical scanning of SUSY parameter spaces.

In [Paper III](#), we investigate the prospects for indirect detection from a new class of dark matter substructure, proposed by [Ricotti & Gould \(2009\)](#). These ultracompact primordial minihalos would be formed by gravitational collapse of large-amplitude, small-scale density fluctuations in the early Universe. Such perturbations might have been induced by phase transitions such as the QCD confinement transition, or specific late-time features in the inflaton potential.¹ The resultant minihalos could consist of PBHs which have later accreted dark matter, or be made almost entirely of dark matter. The first case requires $\delta \gtrsim 30\%$ for the initial PBH formation (cf. Sect. 2.1), whereas the second only needs $10^{-3} \lesssim \delta \lesssim 30\%$, making the formation of PBH-free minihalos considerably more likely.

We compute the gamma-ray fluxes expected from ultracompact minihalos without a central PBH, formed in phase transitions in the early Universe. We compare the detection prospects for the *Fermi*-LAT and existing ACTs, showing that they provide largely complementary detection capabilities across a range of WIMP masses. We show that single minihalos from the electron-positron annihilation epoch would be eminently observable today with existing instruments (Fig. 5.4), and in some cases should even have been seen by *Fermi*'s immediate predecessor, *EGRET* (the Energetic Gamma Ray Experiment Telescope). We find that minihalos from the QCD confinement phase transition, arguably the best candidate transition for producing sufficient density perturbations to form the minihalos, should also be detectable today if any exist within $\mathcal{O}(1 \text{ pc})$ of Earth. If their population is large enough, it is quite likely that at least one such minihalo would be close enough to detect with existing instruments. We provide an expression for the cosmological density of ultracompact minihalos, which exhibits a strong dependence upon the spectral index n of the density perturbations responsible for their formation.

¹In the submitted version of [Paper III](#) ([arXiv:0908.4082v1](#)), we referred to these objects as ‘PLUMs’ (Primordially-Laid Ultracompact Minihalos) so as to distinguish them from minihalos produced by the standard spectrum of inflationary perturbations. Although that acronym did not ultimately survive to publication, we are pleased to see that it has resurfaced in the literature anyway ([Lacki & Beacom 2010](#)).

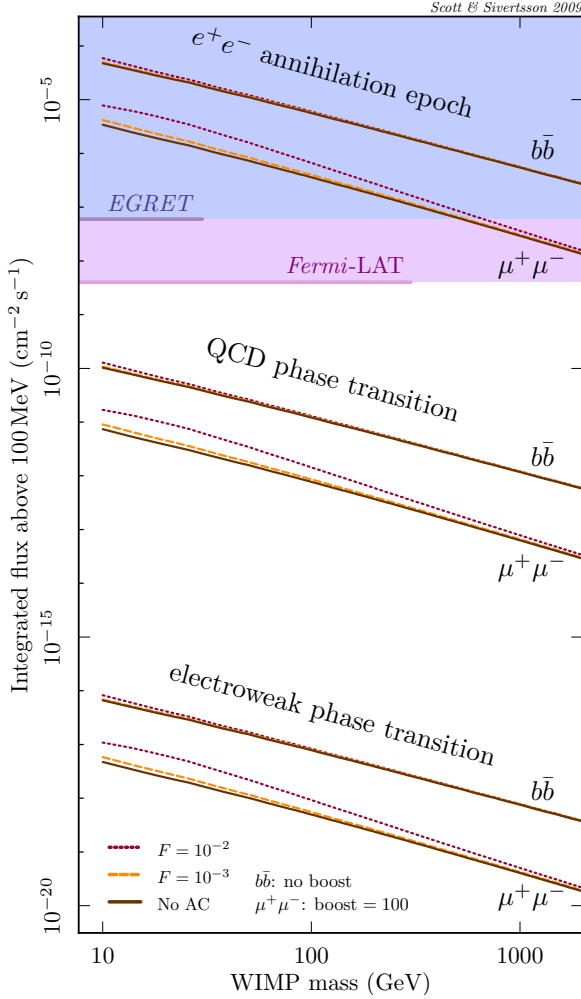


Figure 5.4. Integrated fluxes above 100 MeV for primordial ultracompact minihalos at a distance of $d = 4$ kpc, consisting of WIMPs annihilating into either $b\bar{b}$ or $\mu^+\mu^-$ pairs. Curves are shown for different phase transitions giving rise to minihalos, and various degrees of adiabatic contraction. Adiabatically-contracted minihalos are assumed to have a fraction F of their mass collapsed into a constant-density baryonic core of radius $10^{-3}R_h$. Also shown are approximate 5σ , power-law, high-latitude, point-source sensitivities for 2 weeks of pointed *EGRET* and one year of all-sky *Fermi*-LAT observations. Solid limits indicate instruments' nominal energy ranges. Virtually all types of minihalos produced in the e^+e^- annihilation epoch would be detectable by *Fermi* after 1 year. Minihalos produced in the QCD confinement phase transition would also be detectable if one or more were a little closer than the nominal $d = 4$ kpc used here. From [Paper III](#).

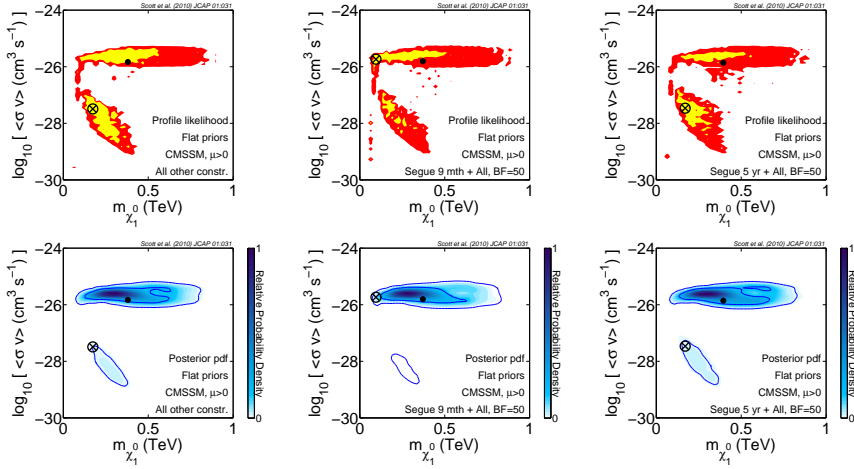


Figure 5.5. CMSSM annihilation cross-sections consistent with all experimental constraints, with and without additional constraints from *Fermi*-LAT observations of the dwarf galaxy Segue 1. Scans assume that dark matter consists predominantly of neutralinos. Plots show regions favoured by existing constraints only (*left*), and with the addition of 9 months of *Fermi* observations towards Segue 1 (*middle*). Also shown is the expected impact upon the favoured masses and cross sections if no signal is observed from Segue 1 after 5 years (*right*). Upper subfigures give profile likelihoods (yellow and red indicate 68% and 95% confidence regions respectively), whereas lower subfigures provide marginalised Bayesian posteriors (with 68% and 95% credible regions given by solid blue contours). Solid dots give posterior means, and crosses indicate best-fit points. The bulk of models disfavoured by observations of Segue 1 are already strongly disfavoured by other constraints, such as the relic density. After 5 years of non-detection, some small inroads will be made into interesting parts of the parameter space at very low masses and high cross-sections. From [Paper IV](#).

In [Paper IV](#), we consider the constraints placed upon the CMSSM by *Fermi* observations of the dwarf galaxy Segue 1. We perform full global SUSY fits, and combine them with likelihoods from *Fermi* data to ascertain which parts of the CMSSM parameter space are most favoured by all current data, and to what degree. Specifically, we include constraints from the relic density, electroweak precision observables, the anomalous magnetic moment of the muon, rare processes in *B*-physics and accelerator bounds on sparticle and Higgs masses. We perform full spectral and spatial fits to the *Fermi* data, including a full convolution with the instrumental energy dispersion and point spread function for all 5.5×10^4

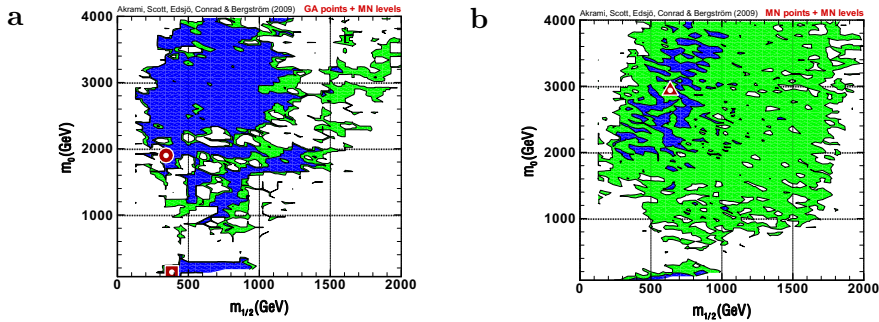


Figure 5.6. Best-fit scalar (m_0) and gaugino ($M_{\frac{1}{2}}$) mass parameters found by genetic algorithms (*left*) and nested sampling (*right*) in the CMSSM. Blue and green shading indicate isolikelihood contours corresponding to 1- and 2 σ confidence regions in the nested sampling scan. Circular, square and triangular markers indicate the best fit in the genetic scan, the best-fit co-annihilation point in the genetic scan, and the best fit in the nested-sampling scan, respectively. The genetic algorithm finds more very good fits, but nested sampling maps the regions where moderately good fits can be found more completely. From [Paper V](#).

CMSSM models we compute.

We show that the lack of any gamma-ray signal from Segue 1 disfavors some CMSSM models with very large annihilation cross-sections and low neutralino masses. These models all possess cross-sections where the neutralino would not be the dominant component of dark matter, so are already disfavoured by the relic density constraint (Fig. 5.5). We also give a topical discussion of the relative merits of the use of the profile likelihood and the Bayesian posterior in SUSY scans. We give examples of the additional physical insight that can be gained by considering both analysis techniques for any given parameter scan, rather than arguing the (rather futile) case that one is somehow more ‘correct’ than the other. Despite the weakness of the constraint drawn on the CMSSM parameter space, this paper makes a significant and concrete contribution to the literature, as it presents the first inclusion of constraints from indirect detection in full statistical SUSY scans. It was also the first dark matter paper to use *Fermi* gamma-ray data, from either within or outside the LAT collaboration.

[Paper V](#) explores the scanning algorithms used in statistical analyses of SUSY parameter spaces. In particular, we test whether genetic algorithms might perform more effective scans in the context of the profile likelihood than Bayesian techniques, such as nested sampling and

MCMCs. We implement the genetic algorithm code PIKAIA (Charbonneau 1995) in the SUSY-scanning code SuperBayeS (Trotta et al. 2008), using the same experimental data as in Paper IV except for observations of Segue 1.

Our results are somewhat surprising: we find a substantial improvement in the likelihood of the best-fit point when using genetic algorithms instead of nested sampling to map the CMSSM likelihood surface (Fig. 5.6). We also uncover a section of the stau co-annihilation region of the CMSSM at large m_0 , consistent with all constraints. This sub-region appears to have been entirely missed in previous scans. Contrary to findings by other authors, often based on Bayesian MCMC methods, our best-fit point occurs in the focus-point region, rather than the stau co-annihilation region. This particular discrepancy likely has more to do with differences in physics codes than the scanning algorithm itself. Nonetheless, our direct comparison with nested sampling in SuperBayeS indicates that all groups using Bayesian techniques to perform SUSY scans in the context of the profile likelihood should have significant concerns about whether the convergence of their scans is sufficient for a non-Bayesian analysis.

5.1 Outlook

This thesis presents a number of novel approaches and techniques for discovering or constraining the nature of dark matter. Its results also provide some initial applications of those techniques to constraining dark matter models, especially SUSY in the form of the CMSSM.

A myriad of extensions to the studies described here could be imagined, from hybrid scanning algorithms, additional observables and nuisances in SUSY scans, to post-main sequence evolution of dark stars and more detailed modelling of the halos in which they reside. The scanning techniques of Paper IV and Paper V, along with the improved solar abundances of Paper VII, Paper VIII and Paper IX, should help sharpen our understanding of the limits on nuclear scattering cross sections provided by neutrino telescopes. Together with an analysis of unidentified point sources in *Fermi* data, the cosmological density of ultracompact minihalos and flux predictions derived in Paper III would also be useful for constraining the spectrum of perturbations produced in various phase transitions in the early Universe.

Together, [Paper I](#), [Paper II](#) and [Paper VI](#) indicate that the prospects for detecting dark stars or using them to constrain nuclear scattering cross-sections are not fantastic, although results are promising enough not to write off the possibility. Dark stars in the early universe are probably more likely to exist and show effects of WIMP annihilation, but those in our own Galaxy might be easier to detect and investigate in detail. Based on the results of [Paper IV](#) and other careful analyses of *Fermi* data ([Abdo et al. 2010b,c,d](#)), it would seem that indirect detection is also unlikely to provide a reliable discovery or exclusion of standard WIMP dark matter in the near future. This statement would not apply if we happen to be very lucky with respect to the identity or early history of dark matter; if it were of a Sommerfeld-enhanced or non-thermal variety, or the QCD phase transition in the early Universe substantially increased the substructure boost factor through the creation of ultracompact minihalos, the picture for indirect would be rather more optimistic.

Notwithstanding these rather fine-tuned scenarios, it would seem that the best hope for dark matter detection in the next few years is probably at the LHC, and in direct detection experiments. In this case, analyses like those of [Paper IV](#) and [Paper V](#) will become especially important as we try to extract information about dark matter from LHC data, and cross-correlate it with dedicated dark matter probes. A credible discovery of dark matter is unlikely to be achieved through a single detection channel, much less a convincing identification in terms of the underlying quantum field theory.

References

- Aaronson, M., Huchra, J. & Mould, J. 1979, *ApJ*, **229**, 1
- Abazajian, K. N., Agrawal, P., Chacko, Z. & Kilic, C. 2010, [arXiv:1002.3820](#)
- Abbasi, R., Abdou, Y., Ackermann, M., Adams, J., Ahlers, M., Andeen, K., Auffenberg, J. & Bai, X. et al. 2009a, *Phys. Rev. Lett.*, **102**, 201302, [arXiv:0902.2460](#)
- . 2009b, [arXiv:0910.4480](#)
- Abdo, A. A., Ackermann, M., Ajello, M., Atwood, W. B., Axelsson, M., Baldini, L., Ballet, J. & Barbiellini, G. et al. 2009, *Phys. Rev. Lett.*, **102**, 181101, [arXiv:0905.0025](#)
- . 2010, *ApJ*, **709**, L152, [arXiv:0911.5327](#)
- Abdo, A. A., Ackermann, M., Ajello, M., Atwood, W. B., Baldini, L., Ballet, J., Barbiellini, G. & Bastieri, D. et al. 2010, *Phys. Rev. Lett.*, **104**, 101101, [arXiv:1002.3603](#)
- Abdo, A. A., Ackermann, M., Ajello, M., Atwood, W. B., Baldini, L., Ballet, J., Barbiellini, G. & Bastieri, D. et al. 2010a, [arXiv:1001.4836](#)
- . 2010b, *ApJ*, **712**, 147, [arXiv:1001.4531](#)
- Abdo, A. A., Ackermann, M., Ajello, M., Baldini, L., Ballet, J., Barbiellini, G., Bastieri, D. & Bechtol, K. et al. 2010c, [arXiv:1002.4415](#)
- Abdo, A. A. et al. 2010d, [arXiv:1002.2239](#)
- Acero, F., Aharonian, F., Akhperjanian, A. G., Anton, G., Barres de Almeida, U., Bazer-Bachi, A. R., Becherini, Y. & Behera, B. et al. 2010, *MNRAS*, **402**, 1877, [arXiv:0911.1912](#)
- Ackermann, M., Ahrens, J., Bai, X., Bartelt, M., Barwick, S. W., Bay, R. C., Becka, T. & Becker, K. et al. 2006, *Astropart. Phys.*, **24**, 459, [arXiv:astro-ph/0508518](#)
- Adriani, O., Barbarino, G. C., Bazilevskaya, G. A., Bellotti, R., Boezio, M., Bogomolov, E. A., Bonechi, L. & Bongi, M. et al. 2009a, *Nature*, **458**, 607, [arXiv:0810.4995](#)
- . 2009b, *Phys. Rev. Lett.*, **102**, 051101, [arXiv:0810.4994](#)
- Aharonian, F., Akhperjanian, A. G., Barres de Almeida, U., Bazer-Bachi, A. R., Becherini, Y., Behera, B., Benbow, W. & Bernlöhner, K. et al. 2008, *Phys. Rev. Lett.*, **101**, 261104, [arXiv:0811.3894](#)
- Ahmad, Q. R., Allen, R. C., Andersen, T. C., Anglin, J. D., Bühler, G., Barton, J. C., Beier, E. W. & Bercovitch, M. et al. 2001, *Phys. Rev. Lett.*, **87**, 071301, [arXiv:nucl-ex/0106015](#)
- Ahmed, Z. et al. 2009, [arXiv:0912.3592](#)

- Aitchison, I. J. R. 2007, *Supersymmetry in Particle Physics: An Elementary Introduction* (Cambridge University Press)
- Akerib, D. S., Attisha, M. J., Bailey, C. N., Baudis, L., Bauer, D. A., Brink, P. L., Brusov, P. P. & Bunker, R. et al. 2006, *Nuc. Inst. Methods A*, **559**, 411
- Alcock, C., Allsman, R. A., Alves, D. R., Axelrod, T. S., Becker, A. C., Bennett, D. P., Cook, K. H. & Dalal, N. et al. 2000, *ApJ*, **542**, 281, [arXiv:astro-ph/0001272](#)
- Allanach, B. C. & Lester, C. G. 2006, *Phys. Rev. D*, **73**, 015013, [arXiv:hep-ph/0507283](#)
- Amsler, C., Doser, M., Antonelli, M., Asner, D. M., Babu, K. S., Baer, H., Band, H. R. & Barnett, R. M. et al. 2008, *Phys. Lett. B*, **667**, 1
- Angle, J., Aprile, E., Arneodo, F., Baudis, L., Bernstein, A., Bolozdynya, A., Brusov, P. & Coelho, L. C. C. et al. 2008, *Phys. Rev. Lett.*, **100**, 021303, [arXiv:0706.0039](#)
- Angulo, C., Arnould, M., Rayet, M., Descouvemont, P., Baye, D., Leclercq-Willain, C., Coc, A. & Barhoumi, S. et al. 1999, *Nucl. Phys. A*, **656**, 3
- Arik, E., Aune, S., Autiero, D., Barth, K., Belov, A., Beltrán, B., Borghi, S. & Bourlis, G. et al. 2009, *JCAP*, **2**, 8, [arXiv:0810.4482](#)
- Arkani-Hamed, N., Finkbeiner, D. P., Slatyer, T. R. & Weiner, N. 2009, *Phys. Rev. D*, **79**, 015014, [arXiv:0810.0713](#)
- Asplund, M., Grevesse, N., Sauval, A. J. & Scott, P. 2009, *Ann. Rev. A&A*, **47**, 481, [arXiv:0909.0948](#), (Paper VII)
- Asplund, M., Lambert, D. L., Nissen, P. E., Primas, F. & Smith, V. V. 2006, *ApJ*, **644**, 229, [arXiv:astro-ph/0510636](#)
- Asztalos, S. J., Carosi, G., Hagmann, C., Kinion, D., van Bibber, K., Hotz, M., Rosenberg, L. J. & Rybka, G. et al. 2010, *Phys. Rev. Lett.*, **104**, 041301, [arXiv:0910.5914](#)
- Atwood, W. B., Abdo, A. A., Ackermann, M., Althouse, W., Anderson, B., Axelson, M., Baldini, L. & Ballet, J. et al. 2009, *ApJ*, **697**, 1071, [arXiv:0902.1089](#)
- Baer, H. & Profumo, S. 2005, *JCAP*, **12**, 8, [arXiv:astro-ph/0510722](#)
- Baer, H. & Tata, X. 2006, *Weak Scale Supersymmetry* (Cambridge University Press)
- Baltz, E. A., Battaglia, M., Peskin, M. E. & Wizansky, T. 2006, *Phys. Rev. D*, **74**, 103521, [arXiv:hep-ph/0602187](#)
- Barbieri, R., Hall, L. J. & Rychkov, V. S. 2006, *Phys. Rev. D*, **74**, 015007, [arXiv:hep-ph/0603188](#)
- Battaglia, M. 2009, *New J. Phys.*, **11**, 105025
- Battaglia, M., Hinchliffe, I. & Tovey, D. 2004, *J. Phys. G*, **30**, 217
- Bekenstein, J. D. 2004, *Phys. Rev. D*, **70**, 083509, [arXiv:astro-ph/0403694](#)
- Bélanger, G., Boudjema, F., Pukhov, A. & Semenov, A. 2007, *Comp. Phys. Comm.*, **176**, 367, [arXiv:hep-ph/0607059](#)
- Belikov, A. V. & Hooper, D. 2010, *Phys. Rev. D*, **81**, 043505, [arXiv:0906.2251](#)
- Belli, P., Cerulli, R., Fornengo, N. & Scopel, S. 2002, *Phys. Rev. D*, **66**, 043503, [arXiv:hep-ph/0203242](#)
- Bergström, L. 1989, *Phys. Lett. B*, **225**, 372
- Bergström, L. 2000, *Rep. Prog. Phys.*, **63**, 793, [arXiv:hep-ph/0002126](#)

- Bergström, L. 2009, *New J. Phys.*, **11**, 105006, [arXiv:0903.4849](#)
- Bergström, L., Bertone, G., Bringmann, T., Edsjö, J. & Taoso, M. 2009a, *Phys. Rev. D*, **79**, 081303, [arXiv:0812.3895](#)
- Bergström, L., Bringmann, T. & Edsjö, J. 2008, *Phys. Rev. D*, **78**, 103520, [arXiv:0808.3725](#)
- Bergström, L., Edsjö, J. & Zaharijas, G. 2009b, *Phys. Rev. Lett.*, **103**, 031103, [arXiv:0905.0333](#)
- Bergström, L. & Snellman, H. 1988, *Phys. Rev. D*, **37**, 3737
- Bergström, L. & Ullio, P. 1997, *Nucl. Phys. B*, **504**, 27, [arXiv:hep-ph/9706232](#)
- Bergström, L., Ullio, P. & Buckley, J. H. 1998, *Astropart. Phys.*, **9**, 137, [arXiv:astro-ph/9712318](#)
- Bern, Z., Carrasco, J. J. M., Dixon, L. J., Johansson, H. & Roiban, R. 2009, *Phys. Rev. Lett.*, **103**, 081301, [arXiv:0905.2326](#)
- Bernabei, R., Belli, P., Cappella, F., Cerulli, R., Dai, C. J., D'Angelo, A., He, H. L. & Incicchitti, A. et al. 2008, *Eur. Phys. J. C*, **167**, [arXiv:0804.2741](#)
- Bernabei, R., Belli, P., Cerulli, R., Montecchia, F., Amato, M., Ignesti, G., Incicchitti, A. & Prosperi, D. et al. 2000, *Phys. Lett. B*, **480**, 23
- Bertone, G., ed. 2010, *Particle Dark Matter: Observations, Models and Searches* (Cambridge University Press)
- Bertone, G., Cirelli, M., Strumia, A. & Taoso, M. 2009, *JCAP*, **3**, 9, [arXiv:0811.3744](#)
- Bertone, G. & Fairbairn, M. 2008, *Phys. Rev. D*, **77**, 043515, [arXiv:0709.1485](#)
- Bertone, G., Hooper, D. & Silk, J. 2005, *Phys. Rep.*, **405**, 279, [arXiv:hep-ph/0404175](#)
- Bertone, G., Nezri, E., Orloff, J. & Silk, J. 2004, *Phys. Rev. D*, **70**, 063503, [arXiv:astro-ph/0403322](#)
- Birkedal, A., Matchev, K. & Perelstein, M. 2004, *Phys. Rev. D*, **70**, 077701, [arXiv:hep-ph/0403004](#)
- Blasi, P. & Serpico, P. D. 2009, *Phys. Rev. Lett.*, **103**, 081103, [arXiv:0904.0871](#)
- Blennow, M., Edsjö, J. & Ohlsson, T. 2008, *JCAP*, **1**, 21, [arXiv:0709.3898](#)
- Blennow, M., Melb  us, H. & Ohlsson, T. 2010, *JCAP*, **1**, 18, [arXiv:0910.1588](#)
- Bottino, A., Fiorentini, G., Fornengo, N., Ricci, B., Scopel, S. & Villante, F. L. 2002, *Phys. Rev. D*, **66**, 053005, [arXiv:hep-ph/0206211](#)
- Bouquet, A. & Salati, P. 1989, *A&A*, **217**, 270
- Bringmann, T. 2009, *New J. Phys.*, **11**, 105027, [arXiv:0903.0189](#)
- Bringmann, T., Bergstr  m, L. & Edsj  , J. 2008, *JHEP*, **1**, 49, [arXiv:0710.3169](#)
- Bringmann, T., Doro, M. & Fornasa, M. 2009, *JCAP*, **1**, 16, [arXiv:0809.2269](#)
- Bruch, T., Peter, A. H. G., Read, J., Baudis, L. & Lake, G. 2009, *Phys. Lett. B*, **674**, 250, [arXiv:0902.4001](#)
- Buckley, M. R., Spolyar, D., Freese, K., Hooper, D. & Murayama, H. 2010, *Phys. Rev. D*, **81**, 016006
- Carrol, B. W. & Ostlie, D. A. 1996, *An Introduction to Modern Astrophysics* (Addison-Wesley, Reading, MA)
- Casanellas, J. & Lopes, I. 2009, *ApJ*, **705**, 135, [arXiv:0909.1971](#)

- Cerdeño, D. G. & Green, A. M. 2010, in *Particle Dark Matter: Observations, Models and Searches*, ed. G. Bertone (Cambridge University Press), 347–369, [arXiv:1002.1912](#)
- Chamseddine, A. H., Arnowitt, R. & Nath, P. 1982, *Phys. Rev. Lett.*, **49**, 970
- Chang, J., Adams, J. H., Ahn, H. S., Bashindzhagyan, G. L., Christl, M., Ganel, O., Guzik, T. G. & Isbert, J. et al. 2008, *Nature*, **456**, 362
- Charbonneau, P. 1995, *ApJS*, **101**, 309
- Chen, S., Mohapatra, R. N., Nussinov, S. & Zhang, Y. 2009, *Phys. Lett. B*, **677**, 311, [arXiv:0903.2562](#)
- Cholis, I., Goodenough, L., Hooper, D., Simet, M. & Weiner, N. 2009, *Phys. Rev. D*, **80**, 123511, [arXiv:0809.1683](#)
- Choutko, V. & Giovacchini, F. 2008, in *Proceedings of the 30th International Cosmic Ray Conference, Mérida, Mexico*, 765–768
- Cirelli, M., Fornengo, N. & Strumia, A. 2006, *Nucl. Phys. B*, **753**, 178, [arXiv:hep-ph/0512090](#)
- Cirelli, M. & Strumia, A. 2009, *New J. Phys.*, **11**, 105005, [arXiv:0903.3381](#)
- Clowe, D., Bradač, M., Gonzalez, A. H., Markevitch, M., Randall, S. W., Jones, C. & Zaritsky, D. 2006, *ApJ*, **648**, L109, [arXiv:astro-ph/0608407](#)
- Coc, A., Vangioni-Flam, E., Descouvemont, P., Adahchour, A. & Angulo, C. 2004, *ApJ*, **600**, 544, [arXiv:astro-ph/0309480](#)
- Cole, S., Percival, W. J., Peacock, J. A., Norberg, P., Baugh, C. M., Frenk, C. S., Baldry, I. & Bland-Hawthorn, J. et al. 2005, *MNRAS*, **362**, 505, [arXiv:astro-ph/0501174](#)
- Coleman, S. & Mandula, J. 1967, *Phys. Rev.*, **159**, 1251
- Colless, M., Dalton, G., Maddox, S., Sutherland, W., Norberg, P., Cole, S., Bland-Hawthorn, J. & Bridges, T. et al. 2001, *MNRAS*, **328**, 1039, [arXiv:astro-ph/0106498](#)
- Covi, L. & Kim, J. E. 2009, *New J. Phys.*, **11**, 105003, [arXiv:0902.0769](#)
- Davidson, S., Hannestad, S. & Raffelt, G. 2000, *JHEP*, **5**, 3, [arXiv:hep-ph/0001179](#)
- de Blok, W. J. G., McGaugh, S. S., Bosma, A. & Rubin, V. C. 2001, *ApJ*, **552**, L23, [arXiv:astro-ph/0103102](#)
- Del Popolo, A. & Kroupa, P. 2009, *A&A*, **502**, 733, [arXiv:0906.1146](#)
- Desai, S., Ashie, Y., Fukuda, S., Fukuda, Y., Ishihara, K., Itow, Y., Koshio, Y. & Minamino, A. et al. 2004, *Phys. Rev. D*, **70**, 083523, [arXiv:hep-ex/0404025](#)
- Diemand, J., Kuhlen, M. & Madau, P. 2007, *ApJ*, **657**, 262, [arXiv:astro-ph/0611370](#)
- Diemand, J., Kuhlen, M., Madau, P., Zemp, M., Moore, B., Potter, D. & Stadel, J. 2008, *Nature*, **454**, 735, [arXiv:0805.1244](#)
- Dobler, G., Finkbeiner, D. P., Cholis, I., Slatyer, T. R. & Weiner, N. 2009, [arXiv:0910.4583](#)
- Donato, F., Fornengo, N. & Maurin, D. 2008, *Phys. Rev. D*, **78**, 043506, [arXiv:0803.2640](#)
- Donato, F., Fornengo, N. & Salati, P. 2000, *Phys. Rev. D*, **62**, 043003, [arXiv:hep-ph/9904481](#)
- Donato, F., Maurin, D., Brun, P., Delahaye, T. & Salati, P. 2009, *Phys. Rev. Lett.*, **102**, 071301, [arXiv:0810.5292](#)

- Ellis, J., Olive, K. A., Savage, C. & Spanos, V. C. 2009, [arXiv:0912.3137](#)
- Essig, R., Sehgal, N. & Strigari, L. E. 2009, *Phys. Rev. D*, **80**, 023506, [arXiv:0902.4750](#)
- Faber, S. M. & Jackson, R. E. 1976, *ApJ*, **204**, 668
- Fairbairn, M., Rashba, T. & Troitsky, S. 2007, *Phys. Rev. Lett.*, **98**, 201801, [arXiv:astro-ph/0610844](#)
- Fairbairn, M. & Schwetz, T. 2009, *JCAP*, **1**, 37, [arXiv:0808.0704](#)
- Falk, T., Olive, K. A. & Srednicki, M. 1994, *Phys. Lett. B*, **339**, 248, [arXiv:hep-ph/9409270](#)
- Feng, J. L. 2010, in *Particle Dark Matter: Observations, Models and Searches*, ed. G. Bertone (Cambridge University Press), 190–203, [arXiv:1002.3828](#)
- Feng, J. L. & Kumar, J. 2008, *Phys. Rev. Lett.*, **101**, 231301, [arXiv:0803.4196](#)
- Finkbeiner, D. P. & Weiner, N. 2007, *Phys. Rev. D*, **76**, 083519, [arXiv:astro-ph/0702587](#)
- Flacke, T., Menon, A., Hooper, D. & Freese, K. 2009, [arXiv:0908.0899](#)
- Freedman, W. L., Madore, B. F., Gibson, B. K., Ferrarese, L., Kelson, D. D., Sakai, S., Mould, J. R. & Kennicutt, Jr., R. C. et al. 2001, *ApJ*, **553**, 47, [arXiv:astro-ph/0012376](#)
- Freese, K., Bodenheimer, P., Spolyar, D. & Gondolo, P. 2008a, *ApJ*, **685**, L101, [arXiv:0806.0617](#)
- Freese, K., Gondolo, P., Sellwood, J. A. & Spolyar, D. 2009, *ApJ*, **693**, 1563, [arXiv:0805.3540](#)
- Freese, K., Ilie, C., Spolyar, D., Valuri, M. & Bodenheimer, P. 2010, [arXiv:1002.2233](#)
- Freese, K., Spolyar, D. & Aguirre, A. 2008b, *JCAP*, **11**, 14, [arXiv:0802.1724](#)
- Fujita, Y., Kohri, K., Yamazaki, R. & Ioka, K. 2009, *Phys. Rev. D*, **80**, 063003, [arXiv:0903.5298](#)
- Gaitskell, R. J. 2004, *Ann. Rev. Nuc. & Part. Sci.*, **54**, 315
- Galli, S., Iocco, F., Bertone, G. & Melchiorri, A. 2009, *Phys. Rev. D*, **80**, 023505, [arXiv:0905.0003](#)
- Geha, M., Willman, B., Simon, J. D., Strigari, L. E., Kirby, E. N., Law, D. R. & Strader, J. 2009, *ApJ*, **692**, 1464, [arXiv:0809.2781](#)
- Gentile, G., Salucci, P., Klein, U., Vergani, D. & Kalberla, P. 2004, *MNRAS*, **351**, 903, [arXiv:astro-ph/0403154](#)
- Giudice, G. F. & Rattazzi, R. 1999, *Phys. Rep.*, **322**, 419, [arXiv:hep-ph/9801271](#)
- Gondolo, P., Edsjö, J., Ullio, P., Bergström, L., Schelke, M. & Baltz, E. A. 2004, *JCAP*, **7**, 8, [arXiv:astro-ph/0406204](#)
- Goodenough, L. & Hooper, D. 2009, [arXiv:0910.2998](#)
- Goodman, M. W. & Witten, E. 1985, *Phys. Rev. D*, **31**, 3059
- Gould, A. 1987, *ApJ*, **321**, 571
- . 1991, *ApJ*, **368**, 610
- Governato, F., Brook, C., Mayer, L., Brooks, A., Rhee, G., Wadsley, J., Jonsson, P. & Willman, B. et al. 2010, *Nature*, **463**, 203, [arXiv:0911.2237](#)
- Green, A. M. 2007, *JCAP*, **8**, 22, [arXiv:hep-ph/0703217](#)
- . 2008, *JCAP*, **7**, 5, [arXiv:0805.1704](#)

- Green, A. M., Hofmann, S. & Schwarz, D. J. 2004a, *MNRAS*, **353**, L23, [arXiv:astro-ph/0309621](#)
- . 2005, *JCAP*, **8**, 3, [arXiv:astro-ph/0503387](#)
- Green, A. M. & Liddle, A. R. 1997, *Phys. Rev. D*, **56**, 6166, [arXiv:astro-ph/9704251](#)
- Green, A. M., Liddle, A. R., Malik, K. A. & Sasaki, M. 2004b, *Phys. Rev. D*, **70**, 041502, [arXiv:astro-ph/0403181](#)
- Haag, R., Lopuszański, J. T. & Sohnius, M. 1975, *Nucl. Phys. B*, **88**, 257
- Hailey, C. J. 2009, *New J. Phys.*, **11**, 105022
- Hansen, S. H., Moore, B., Zemp, M. & Stadel, J. 2006, *JCAP*, **0601**, 014, [arXiv:astro-ph/0505420](#)
- Hisano, J., Kawasaki, M., Kohri, K. & Nakayama, K. 2009, *Phys. Rev. D*, **79**, 043516, [arXiv:0812.0219](#)
- Hofmann, S., Schwarz, D. J. & Stöcker, H. 2001, *Phys. Rev. D*, **64**, 083507, [arXiv:astro-ph/0104173](#)
- Holdom, B. 1986, *Phys. Lett. B*, **166**, 196
- Hooper, D., Blasi, P. & Dario Serpico, P. 2009, *JCAP*, **1**, 25, [arXiv:0810.1527](#)
- Hooper, D., Spolyar, D., Vallinotto, A. & Gnedin, N. Y. 2010, [arXiv:1002.0005](#)
- Hu, W. & Dodelson, S. 2002, *Ann. Rev. A&A*, **40**, 171, [arXiv:astro-ph/0110414](#)
- Ibarra, A. & Tran, D. 2009, *JCAP*, **6**, 4, [arXiv:0904.1410](#)
- Ingelman, G. & Thunman, M. 1996, *Phys. Rev. D*, **54**, 4385, [arXiv:hep-ph/9604288](#)
- Iocco, F. 2008, *ApJ*, **677**, L1, [arXiv:0802.0941](#)
- Iocco, F., Bressan, A., Ripamonti, E., Schneider, R., Ferrara, A. & Marigo, P. 2008, *MNRAS*, **390**, 1655, [arXiv:0805.4016](#)
- Iocco, F., Mangano, G., Miele, G., Pisanti, O. & Serpico, P. D. 2009, *Phys. Rep.*, **472**, 1, [arXiv:0809.0631](#)
- Jedamzik, K. & Pospelov, M. 2009, *New J. Phys.*, **11**, 105028, [arXiv:0906.2087](#)
- Josan, A. S., Green, A. M. & Malik, K. A. 2009, *Phys. Rev. D*, **79**, 103520, [arXiv:0903.3184](#)
- Jungman, G., Kamionkowski, M. & Griest, K. 1996, *Phys. Rep.*, **267**, 195, [arXiv:hep-ph/9506380](#)
- Kang, J., Luty, M. A. & Nasri, S. 2008, *JHEP*, **9**, 86, [arXiv:hep-ph/0611322](#)
- Katz, B., Blum, K. & Waxman, E. 2009, [arXiv:0907.1686](#)
- Kim, J. E. & Carosi, G. 2008, [arXiv:0807.3125](#)
- Kippenhahn, R. & Weigert, A. 1991, *Stellar Structure and Evolution*, 1st edn. (Springer-Verlag, Berlin)
- Kolb, E. W., Chung, D. J. H. & Riotto, A. 1999, in *Proceedings of Dark matter in Astrophysics and Particle Physics: Dark 98*, ed. H. V. Klapdor-Kleingrothaus & L. Baudis, 592, [arXiv:hep-ph/9810361](#)
- Kolb, E. W. & Turner, M. S. 1990, *The Early Universe* (Frontiers in Physics, Addison-Wesley, Reading, MA)
- Komatsu, E., Dunkley, J., Nolte, M. R., Bennett, C. L., Gold, B., Hinshaw, G., Jarosik, N. & Larson, D. et al. 2009, *ApJS*, **180**, 330, [arXiv:0803.0547](#)

- Komatsu, E., Smith, K. M., Dunkley, J., Bennett, C. L., Gold, B., Hinshaw, G., Jarosik, N. & Larson, D. et al. 2010, [arXiv:1001.4538](#)
- Kowalski, M., Rubin, D., Aldering, G., Agostinho, R. J., Amadon, A., Amanullah, R., Balland, C. & Barbary, K. et al. 2008, *ApJ*, **686**, 749, [arXiv:0804.4142](#)
- Kuhlen, M., Diemand, J. & Madau, P. 2008, *ApJ*, **686**, 262, [arXiv:0805.4416](#)
- Kusenko, A. 2009, *Phys. Rep.*, **481**, 1, [arXiv:0906.2968](#)
- Kuster, M., Raffelt, G. & Beltrán, B., eds. 2008, *Lec. Notes in Physics*, Vol. 741, *Axions: Theory, Cosmology, and Experimental Searches* (Springer-Verlag, Berlin)
- Lacki, B. C. & Beacom, J. F. 2010, [arXiv:1003.3466](#)
- Larson, D., Dunkley, J., Hinshaw, G., Komatsu, E., Nolte, M. R., Bennett, C. L., Gold, B. & Halpern, M. et al. 2010, [arXiv:1001.4635](#)
- Lebedenko, V. N., Araújo, H. M., Barnes, E. J., Bewick, A., Cashmore, R., Chepel, V., Currie, A. & Davidge, D. et al. 2009, *Phys. Rev. D*, **80**, 052010, [arXiv:0812.1150](#)
- Lee, D. & Mohapatra, R. N. 1995, *Phys. Rev. D*, **51**, 1353, [arXiv:hep-ph/9406328](#)
- Lim, G. et al. 2009, in *Proceedings of the 31st International Cosmic Ray Conference, Lodz, Poland*, [arXiv:0905.2316](#)
- Linden, T. & Profumo, S. 2010, [arXiv:1003.0002](#)
- Liu, J., Yin, P. & Zhu, S. 2009, *Phys. Rev. D*, **79**, 063522, [arXiv:0812.0964](#)
- Loewenstein, M. & Kusenko, A. 2009, [arXiv:0912.0552](#)
- Lombardi, S., Aleksic, J., Barrio, J. A., Biland, A., Doro, M., Elsaesser, D., Gaug, M. & Mannheim, K. et al. 2009, in *Proceedings of the 31st International Cosmic Ray Conference, Lodz, Poland*, [arXiv:0907.0738](#)
- Lundberg, J. & Edsjö, J. 2004, *Phys. Rev. D*, **69**, 123505, [arXiv:astro-ph/0401113](#)
- Luty, M. A. 2005, *2004 TASI Lectures on Supersymmetry Breaking*, [arXiv:hep-th/0509029](#)
- Mandal, S. K., Buckley, M. R., Freese, K., Spolyar, D. & Murayama, H. 2010, *Phys. Rev. D*, **81**, 043508, [arXiv:0911.5188](#)
- Markevitch, M. 2006, in *ESA Special Publication*, Vol. 604, *Proceedings of The X-ray Universe 2005*, ed. A. Wilson, 723, [arXiv:astro-ph/0511345](#)
- Martin, S. P. 1997, in *Perspectives on supersymmetry*, ed. G. L. Kane, 1–98, [arXiv:hep-ph/9709356](#)
- Martinez, G. D., Bullock, J. S., Kaplinghat, M., Strigari, L. E. & Trotta, R. 2009, *JCAP*, **6**, 14, [arXiv:0902.4715](#)
- Massey, R., Rhodes, J., Ellis, R., Scoville, N., Leauthaud, A., Finoguenov, A., Capak, P. & Bacon, D. et al. 2007, *Nature*, **445**, 286, [arXiv:astro-ph/0701594](#)
- Maurin, D., Donato, F., Taillet, R. & Salati, P. 2001, *ApJ*, **555**, 585, [arXiv:astro-ph/0101231](#)
- McCullough, M. & Fairbairn, M. 2010, [arXiv:1001.2737](#)
- Merritt, D. 2010, in *Particle Dark Matter: Observations, Models and Searches*, ed. G. Bertone (Cambridge University Press), 83–98, [arXiv:1001.3706](#)
- Milgrom, M. 1983, *ApJ*, **270**, 365

- Morrissey, D. E., Tait, T. M. P. & Wagner, C. E. M. 2005, *Phys. Rev. D*, **72**, 095003, [arXiv:hep-ph/0508123](#)
- Moskalenko, I. V. & Strong, A. W. 1998, *ApJ*, **493**, 694, [arXiv:astro-ph/9710124](#)
- Moskalenko, I. V. & Wai, L. L. 2007, *ApJ*, **659**, L29, [arXiv:astro-ph/0702654](#)
- Natarajan, A. & Schwarz, D. J. 2008, *Phys. Rev. D*, **78**, 103524, [arXiv:0805.3945](#)
- Natarajan, A., Tan, J. C. & O'Shea, B. W. 2009, *ApJ*, **692**, 574, [arXiv:0807.3769](#)
- Navarro, J. F., Frenk, C. S. & White, S. D. M. 1996, *ApJ*, **462**, 563, [arXiv:astro-ph/9508025](#)
- Navarro, J. F., Hayashi, E., Power, C., Jenkins, A. R., Frenk, C. S., White, S. D. M., Springel, V. & Stadel, J. et al. 2004, *MNRAS*, **349**, 1039, [arXiv:astro-ph/0311231](#)
- Nomura, Y. & Thaler, J. 2009, *Phys. Rev. D*, **79**, 075008, [arXiv:0810.5397](#)
- Pacaud, F., Pierre, M., Adami, C., Altieri, B., Andreon, S., Chiappetti, L., Detal, A. & Duc, P. et al. 2007, *MNRAS*, **382**, 1289, [arXiv:0709.1950](#)
- Paczynski, B. 1986, *ApJ*, **304**, 1
- Peccei, R. D. 2008, in *Lec. Notes in Physics*, Vol. 741, *Axions: Theory, Cosmology, and Experimental Searches*, ed. M. Kuster, G. Raffelt & B. Beltrán (Springer-Verlag, Berlin), 3
- Peccei, R. D. & Quinn, H. R. 1977, *Phys. Rev. Lett.*, **38**, 1440
- Percival, W. J., Reid, B. A., Eisenstein, D. J., Bahcall, N. A., Budavari, T., Frieman, J. A., Fukugita, M. & Gunn, J. E. et al. 2010, *MNRAS*, **401**, 2148, [arXiv:0907.1660](#)
- Perlmutter, S., Aldering, G., Goldhaber, G., Knop, R. A., Nugent, P., Castro, P. G., Deustua, S. & Fabbro, S. et al. 1999, *ApJ*, **517**, 565, [arXiv:astro-ph/9812133](#)
- Peskin, M. E. & Schroeder, D. V. 1995, *An Introduction to Quantum Field Theory* (Westview Press)
- Peter, A. H. G. 2009, *Phys. Rev. D*, **79**, 103532, [arXiv:0902.1347](#)
- Pieri, L., Pizzella, A., Corsini, E. M., Dalla Bontà, E. & Bertola, F. 2009, *A&A*, **496**, 351, [arXiv:0812.1494](#)
- Piran, T., Shaviv, N. J. & Nakar, E. 2009, in *Proceedings of Rencontres de Moriond 2009 – Very High Energy Phenomena in the Universe*, [arXiv:0905.0904](#)
- Press, W. H. & Spergel, D. N. 1985, *ApJ*, **296**, 679
- Profumo, S. 2008, [arXiv:0812.4457](#)
- Profumo, S. & Jeltema, T. E. 2009, *JCAP*, **7**, 20, [arXiv:0906.0001](#)
- Pugnat, P., Duvillaret, L., Jost, R., Vitrant, G., Romanini, D., Siemko, A., Ballou, R. & Barbara, B. et al. 2008, *Phys. Rev. D*, **78**, 092003, [arXiv:0712.3362](#)
- Putze, A., Derome, L. & Maurin, D. 2010, [arXiv:1001.0551](#)
- Putze, A., Derome, L., Maurin, D., Perotto, L. & Taillet, R. 2009, *A&A*, **497**, 991, [arXiv:0808.2437](#)
- Raffelt, G. G. 2008, in *Lec. Notes in Physics*, Vol. 741, *Axions: Theory, Cosmology, and Experimental Searches*, ed. M. Kuster, G. Raffelt & B. Beltrán (Springer-Verlag, Berlin), 51
- Randall, L. & Sundrum, R. 1999, *Nucl. Phys. B*, **557**, 79, [arXiv:hep-th/9810155](#)

- Read, J. I., Mayer, L., Brooks, A. M., Governato, F. & Lake, G. 2009, *MNRAS*, **397**, 44, [arXiv:0902.0009](#)
- Regis, M. & Ullio, P. 2008, *Phys. Rev. D*, **78**, 043505, [arXiv:0802.0234](#)
- Ricotti, M. & Gould, A. 2009, *ApJ*, **707**, 979, [arXiv:0908.0735](#)
- Riess, A. G., Filippenko, A. V., Challis, P., Clocchiatti, A., Diercks, A., Garnavich, P. M., Gilliland, R. L. & Hogan, C. J. et al. 1998, *AJ*, **116**, 1009, [arXiv:astro-ph/9805201](#)
- Ripamonti, E., Mapelli, M. & Ferrara, A. 2007, *MNRAS*, **374**, 1067, [arXiv:astro-ph/0606482](#)
- Robilliard, C., Battesti, R., Fouché, M., Mauchain, J., Sautivet, A., Amiranoff, F. & Rizzo, C. 2007, *Phys. Rev. Lett.*, **99**, 190403, [arXiv:0707.1296](#)
- Rubin, V. C., Burstein, D., Ford, Jr., W. K. & Thonnard, N. 1985, *ApJ*, **289**, 81
- Rubin, V. C. & Ford, Jr., W. K. 1970, *ApJ*, **159**, 379
- Rubin, V. C., Thonnard, N. & Ford, Jr., W. K. 1978, *ApJ*, **225**, L107
- Ruiz de Austri, R., Trotta, R. & Roszkowski, L. 2006, *JHEP*, **5**, 2, [arXiv:hep-ph/0602028](#)
- Salati, P. & Silk, J. 1989, *ApJ*, **338**, 24
- Samtleben, D., Staggs, S. & Winstein, B. 2007, *Ann. Rev. Nuc. & Part. Sci.*, **57**, 245, [arXiv:0803.0834](#)
- Sandick, P., Spolyar, D., Buckley, M., Freese, K. & Hooper, D. 2009, [arXiv:0912.0513](#)
- Savage, C., Freese, K., Gondolo, P. & Spolyar, D. 2009a, *JCAP*, **9**, 36, [arXiv:0901.2713](#)
- Savage, C., Gelmini, G., Gondolo, P. & Freese, K. 2009b, *JCAP*, **4**, 10, [arXiv:0808.3607](#)
- Schwetz, T., Tórtola, M. & Valle, J. W. F. 2008, *New J. Phys.*, **10**, 113011, [arXiv:0808.2016](#)
- Scott, P., Asplund, M., Grevesse, N. & Sauval, A. J. 2009a, *ApJ*, **691**, L119, [arXiv:0811.0815](#), (Paper VIII)
- Scott, P., Edsjö, J. & Fairbairn, M. 2008, in *Proceedings of Dark Matter in Astroparticle and Particle Physics: Dark 2007*, ed. H. K. Klapdor-Kleingrothaus & G. F. Lewis (World Scientific, Singapore), 387–392, [arXiv:0711.0991](#), (Proceeding XIII)
- Scott, P., Edsjö, J. & Fairbairn, M. 2009b, in *Proceedings of Dark Matter in Astroparticle and Particle Physics: Dark 2009* (World Scientific, Singapore), [arXiv:0904.2395](#), (Proceeding XI)
- Scott, P. C., Asplund, M., Grevesse, N. & Sauval, A. J. 2006, *A&A*, **456**, 675, [arXiv:astro-ph/0605116](#), (Paper IX)
- Seckel, D., Stanev, T. & Gaisser, T. K. 1991, *ApJ*, **382**, 652
- Serpico, P. D. & Zaharijas, G. 2008, *Astropart. Phys.*, **29**, 380, [arXiv:0802.3245](#)
- Servant, G. & Tait, T. M. P. 2003, *Nucl. Phys. B*, **650**, 391, [arXiv:hep-ph/0206071](#)
- Sikivie, P. 2008, in *Lec. Notes in Physics*, Vol. 741, *Axions: Theory, Cosmology, and Experimental Searches*, ed. M. Kuster, G. Raffelt & B. Beltrán (Springer-Verlag, Berlin), 19
- Silk, J. 1968, *ApJ*, **151**, 459
- Slatyer, T. R., Padmanabhan, N. & Finkbeiner, D. P. 2009, *Phys. Rev. D*, **80**, 043526, [arXiv:0906.1197](#)

- Smith, D. & Weiner, N. 2001, *Phys. Rev. D*, **64**, 043502, [arXiv:hep-ph/0101138](#)
- Spite, F. & Spite, M. 1982, *A&A*, **115**, 357
- Spolyar, D., Bodenheimer, P., Freese, K. & Gondolo, P. 2009, *ApJ*, **705**, 1031, [arXiv:0903.3070](#)
- Spolyar, D., Freese, K. & Gondolo, P. 2008, *Phys. Rev. Lett.*, **100**, 051101, [arXiv:0705.0521](#)
- Springel, V., Wang, J., Vogelsberger, M., Ludlow, A., Jenkins, A., Helmi, A., Navarro, J. F. & Frenk, C. S. et al. 2008a, *MNRAS*, **391**, 1685, [arXiv:0809.0898](#)
- Springel, V., White, S. D. M., Frenk, C. S., Navarro, J. F., Jenkins, A., Vogelsberger, M., Wang, J. & Ludlow, A. et al. 2008b, *Nature*, **456**, 73, [arXiv:0809.0894](#)
- Springel, V., White, S. D. M., Jenkins, A., Frenk, C. S., Yoshida, N., Gao, L., Navarro, J. & Thacker, R. et al. 2005, *Nature*, **435**, 629, [arXiv:astro-ph/0504097](#)
- Starkman, G. D., Gould, A., Esmailzadeh, R. & Dimopoulos, S. 1990, *Phys. Rev. D*, **41**, 3594
- Steigman, G. 2007, *Ann. Rev. Nuc. & Part. Sci.*, **57**, 463, [arXiv:0712.1100](#)
- Steigman, G., Quintana, H., Sarazin, C. L. & Faulkner, J. 1978, *AJ*, **83**, 1050
- Stiff, D. & Widrow, L. M. 2003, *Phys. Rev. Lett.*, **90**, 211301, [arXiv:astro-ph/0301301](#)
- Stix, M. 2002, *The Sun: An Introduction*, 2nd edn. (Springer-Verlag, Berlin)
- Stoehr, F., White, S. D. M., Springel, V., Tormen, G. & Yoshida, N. 2003, *MNRAS*, **345**, 1313, [arXiv:astro-ph/0307026](#)
- Strong, A. W. & Moskalenko, I. V. 1998, *ApJ*, **509**, 212, [arXiv:astro-ph/9807150](#)
- Strong, A. W., Moskalenko, I. V. & Ptuskin, V. S. 2007, *Annual Review of Nuclear and Particle Science*, **57**, 285, [arXiv:astro-ph/0701517](#)
- Strong, A. W., Moskalenko, I. V. & Reimer, O. 2000, *ApJ*, **537**, 763, [arXiv:astro-ph/9811296](#)
- 't Hooft, G. 1976a, *Phys. Rev. D*, **14**, 3432
- . 1976b, *Phys. Rev. D*, **14**, 3432
- Taoso, M., Bertone, G. & Masiero, A. 2008, *JCAP*, **3**, 22, [arXiv:0711.4996](#)
- Tegmark, M., Blanton, M. R., Strauss, M. A., Hoyle, F., Schlegel, D., Scocimarro, R., Vogeley, M. S. & Weinberg, D. H. et al. 2004, *ApJ*, **606**, 702, [arXiv:astro-ph/0310725](#)
- Tegmark, M., Zaldarriaga, M. & Hamilton, A. J. 2001, *Phys. Rev. D*, **63**, 043007, [arXiv:astro-ph/0008167](#)
- Tisserand, P., Le Guillou, L., Afonso, C., Albert, J. N., Andersen, J., Ansari, R., Aubourg, É. & Bareyre, P. et al. 2007, *A&A*, **469**, 387, [arXiv:astro-ph/0607207](#)
- Tremaine, S. & Gunn, J. E. 1979, *Phys. Rev. Lett.*, **42**, 407
- Trotta, R., Feroz, F., Hobson, M., Roszkowski, L. & Ruiz de Austri, R. 2008, *JHEP*, **12**, 24, [arXiv:0809.3792](#)
- Tucker-Smith, D. & Weiner, N. 2005, *Phys. Rev. D*, **72**, 063509, [arXiv:hep-ph/0402065](#)
- Tully, R. B. & Fisher, J. R. 1977, *A&A*, **54**, 661
- Tyson, J. A., Kochanski, G. P. & Dell'Antonio, I. P. 1998, *ApJ*, **498**, L107, [arXiv:astro-ph/9801193](#)

- Ullio, P. & Bergström, L. 1998, *Phys. Rev. D*, **57**, 1962, [arXiv:hep-ph/9707333](#)
- Vikhlinin, A., Kravtsov, A., Forman, W., Jones, C., Markevitch, M., Murray, S. S. & Van Speybroeck, L. 2006, *ApJ*, **640**, 691, [arXiv:astro-ph/0507092](#)
- Visinelli, L. & Gondolo, P. 2009, *Phys. Rev. D*, **80**, 035024, [arXiv:0903.4377](#)
- Vitale, V., Morselli, A. & The *Fermi*-LAT Collaboration. 2009, in *Proceedings of the 2009 Fermi Symposium, eConf Proceedings*, Vol. C091122, [arXiv:0912.3828](#)
- White, M. J. 2007, *Proceedings of Rencontres de Moriond 2006 – Electroweak Interactions And Unified Theories, Int. J. Mod. Phys. A*, **22**, 5771, [arXiv:hep-ph/0605065](#)
- Wikström, G. & Edsjö, J. 2009, *JCAP*, **4**, 9, [arXiv:0903.2986](#)
- Wyrzykowski, Ł., Kozłowski, S., Skowron, J., Belokurov, V., Smith, M. C., Udalski, A., Szymański, M. K. & Kubiak, M. et al. 2009, *MNRAS*, **397**, 1228, [arXiv:0905.2044](#)
- Yüksel, H., Horiuchi, S., Beacom, J. F. & Ando, S. 2007, *Phys. Rev. D*, **76**, 123506, [arXiv:0707.0196](#)
- Yüksel, H., Kistler, M. D. & Stanev, T. 2009, *Phys. Rev. Lett.*, **103**, 051101, [arXiv:0810.2784](#)
- Zwicky, F. 1933, *Helvetica Physica Acta*, **6**, 110

Part II

Papers

Malcolm Fairbairn, Pat Scott & Joakim Edsjö
The zero age main sequence of WIMP burners
Phys. Rev. D **77**, 047301 (2008) arXiv:0710.3396.

The zero age main sequence of WIMP burners

Malcolm Fairbairn*

*PH-TH, CERN, Geneva, Switzerland
and King's College London, WC2R 2LS, United Kingdom*

Pat Scott† and Joakim Edsjö‡

*Cosmology, Particle Astrophysics and String Theory, Physics, Stockholm University
and High Energy Astrophysics and Cosmology Centre (HEAC), AlbaNova University Centre, SE-106 91 Stockholm, Sweden
(Received 5 November 2007; published 4 February 2008)*

We modify a stellar structure code to estimate the effect upon the main sequence of the accretion of weakly-interacting dark matter onto stars and its subsequent annihilation. The effect upon the stars depends upon whether the energy generation rate from dark matter annihilation is large enough to shut off the nuclear burning in the star. Main sequence weakly-interacting massive particles (WIMP) burners look much like proto-stars moving on the Hayashi track, although they are in principle completely stable. We make some brief comments about where such stars could be found, how they might be observed and more detailed simulations which are currently in progress. Finally we comment on whether or not it is possible to link the paradoxically hot, young stars found at the galactic center with WIMP burners.

DOI: 10.1103/PhysRevD.77.047301

PACS numbers: 95.35.+d

There is growing evidence that for each gram of baryonic matter in the universe, there are around five grams of dark matter which does not couple to the electromagnetic force [1]. One of the more convincing candidates for this dark matter are weakly-interacting massive particles (WIMPs). Because WIMPs have masses and couplings close to the weak scale, they naturally give rise to a relic abundance of dark matter close to that observed after freeze out in the early universe.

Because WIMPs couple weakly to standard model particles, there is a small but nonzero WIMP-nucleon cross section. The tightest constraints for the spin-independent cross section come from the XENON experiment [2]. The WIMP-nucleon interaction means that some WIMPs are gravitationally captured by stars, a process which has been well studied [3,4]. Usually the focus of such investigations is the possibility of dark matter annihilating into high energy neutrinos, which then escape the star to be potentially detected by neutrino experiments like IceCube. If the accretion of dark matter were large enough however, one might expect that the stars themselves could change.

The first way WIMPs can affect a star is by annihilating into standard model particles in its core, providing another energy source in addition to standard nuclear burning. We refer to stars where the energy produced by WIMP annihilations is greater than or comparable to that from nuclear burning as “WIMP burners.” Recent work has focused upon white dwarfs and neutron stars [5,6]. Here we instead focus on main sequence WIMP burners. Previous work in this direction was carried out by Salati and Silk [7] some years ago, in the context of cosmion dark matter. These authors used an $n = 3$ polytropic approximation to esti-

mate the influence of WIMP annihilation on the main sequence. We instead employ full numerical solutions to the hydrostatic equations of stellar structure and present results from a simple code, as well as supporting preliminary results from a more advanced code. We also update the discussion in the context of “modern WIMPs” rather than cosmions, as the nuclear scattering cross-sections and the WIMP mass are more constrained than in the past.

The second way WIMPs can influence stellar structure is by providing an additional mechanism of heat transport in the core. This could reduce the local temperature gradient [8], potentially inhibiting convection and enhancing the pulsation of horizontal branch stars [9,10]. At least for the Sun however, the values currently favored for the WIMP self-annihilation cross section [1] and the upper limit on the WIMP-nucleon cross section [2] indicate that this effect is not significant [11]. In this work, we neglect heat transport by WIMPs, but will in a later work include this effect in more detailed, time-dependent simulations [12]. For the current work, we have checked that this omission does not affect our results significantly.

Experiments give relatively weak constraints on the spin-dependent WIMP-nucleon cross section, so it may contribute far more to WIMP capture than the spin-independent one. For simplicity, we assume that the spin-dependent cross section dominates and is $\sigma_{SD} = 10^{-38} \text{ cm}^2$. For a Sun-like star with mass $1M_{\odot}$, a circular velocity of 220 km s^{-1} , a WIMP velocity dispersion of $\bar{v} = 270 \text{ km s}^{-1}$ and a WIMP mass of 100 GeV , the capture rate (as calculated with the full capture expressions [4] in DarkSUSY [13]) is then

$$\Gamma_0 = 2.90 \times 10^{24} \text{ s}^{-1}. \quad (1)$$

We assume a hydrogen mass fraction of 75%, uniformly distributed in the star. This is not a good approximation for

*malc@cern.ch
†pat@physto.se
‡edsjo@physto.se

the Sun, but reasonable for newly born stars. The capture rate on an arbitrary star is then approximately

$$\Gamma_c = \left(\frac{M_*}{M_\odot}\right) \left(\frac{v_{\text{esc}}}{618 \text{ km s}^{-1}}\right)^2 \left(\frac{270 \text{ km s}^{-1}}{\bar{v}}\right) \left(\frac{\rho_w}{0.3 \text{ GeV cm}^{-3}}\right) \times \left(\frac{100 \text{ GeV}}{m_w}\right) \left(\frac{\langle\phi\rangle}{\langle\phi\rangle_\odot}\right) \Gamma_\odot, \quad (2)$$

where M_* is the star's mass and v_{esc} its surface escape velocity, ρ_w is the ambient WIMP density and m_w is the WIMP mass. $\langle\phi\rangle = \langle v_{\text{esc}}^2(r)/v_{\text{esc}}^2 \rangle$ is the average potential at the height of the scattering nuclei (hydrogen in this case, for which $\langle\phi\rangle_\odot = 3.16$). For simplicity, we assume $\langle\phi\rangle/\langle\phi\rangle_\odot = 1$. Even if this approximation is not perfect, Eq. (2) is only necessary for converting between the ambient WIMP density ρ_w and the capture rate Γ_c , so it is easy to rescale if the reader wishes. We also assume $\bar{v} = 270 \text{ km s}^{-1}$, though for stars in very different environments to our own this must be adjusted. Throughout this paper, we use a WIMP mass of 100 GeV although to a first approximation the energy accreted by a star immersed in some fixed density of dark matter is only a function of the cross section, not the mass of the WIMP.

Once dark matter is captured by the star, it will form an approximately thermal (Gaussian) internal distribution, of characteristic radius [9,11,14]

$$r_w = \left[\frac{3kT_c}{2\pi G \rho_c m_w} \right]^{1/2}, \quad (3)$$

where ρ_c and T_c are the central density and temperature. Having been concentrated in the center of the star, the dark matter annihilates with itself, so the equation for the evolution of the number of WIMPs in the star over time is

$$\frac{dN}{dt} = \Gamma_c - 2\Gamma_a. \quad (4)$$

When $\Gamma_c = 2\Gamma_a$, the capture and annihilation rates are in equilibrium and any dark matter which accretes onto the star is instantly converted into additional luminosity. Here we assume that all of the annihilation products interact either electromagnetically or strongly, so that they have short mean free paths in the star and the energy thermalizes quickly. In reality, some fraction of the energy will be lost to neutrinos, but this is a small effect (typically on the order of 10% or less). The time scale for the steady state to be reached will be much less than the typical evolutionary time scale of a main sequence star, so we assume that this equilibrium has been achieved.

We studied the effect of this energy input upon stars by altering the FORTRAN code ZAMS [15], which looks for stable stellar solutions assuming a constant chemical composition and a simple equation of state. The code was modified by adding the energy generation due to WIMP annihilation to the nuclear energy generation rate.

Self-gravitating systems have negative specific heat, so as dark matter injects energy into the core of the star, the

temperature goes down. Since the nuclear reaction rates depend exponentially on temperature, they are significantly reduced for even a small drop in temperature. As the ambient density of dark matter is increased and the capture rate goes up, the injection of energy due to WIMP annihilations eventually reduces the temperature enough to shut off nuclear burning. WIMP annihilation is then the primary source of the star's luminosity.

Since WIMP annihilation occurs in a more centralized region than nuclear burning, the temperature gradient is much steeper in the core of the star than it would otherwise be, and the core becomes convective. Outside the core, less energy is generated per unit volume than if nuclear burning were proceeding normally, so the temperature gradient is less. The actual temperature is lower than in a normal star, but for small dark matter accretion rates it remains high enough to prevent any major increase in opacity, ensuring that energy transport in the region above the core remains radiative. The energy from the core is easily transmitted through this radiative zone to the surface layers of the star. The overall radius of the star remains approximately constant while the temperature decreases, so the luminosity also decreases.

As the WIMP accretion rate is raised, the star continues to cool until H^- ions are able to survive at increasingly large depths below the surface. If the star did not already have an appreciable surface convection zone, one develops. At high enough WIMP capture rates, the surface convection zone merges with the inner zone and the star becomes completely convective. The addition of more WIMPs and hence central luminosity beyond this point requires the star to grow in order to transport the additional energy to the surface. The two distinct stages of this "evolution" can clearly be seen in Fig. 1. This figure shows a black solid line corresponding to the zero age main sequence, along with "evolutionary tracks" plotted as the ambient density of WIMPs is increased. These tracks are strongly reminiscent of the Hayashi tracks which proto-stars travel along on the final stages of their evolution towards the main sequence. The difference is that such stars are shrinking in size on the Kelvin-Helmholtz time scale as they radiate away gravitational potential energy. In WIMP burners, there is constant energy generation in the core (provided the WIMP capture rate remains constant) and the stars can in principle remain at that position in the HR diagram for an arbitrarily long time.

The analysis of Salati and Silk [7] led to qualitatively similar conclusions about the backing up of the main sequence along the Hayashi track with increasing WIMP density. The shapes of the tracks are different in our more detailed analysis, and thus the actual positions of the resulting WIMP burners in the HR diagram differ. The effects require higher ambient WIMP densities also, as we have considered modern WIMPs rather than cosmions (i.e. with lower nuclear scattering cross-sections).

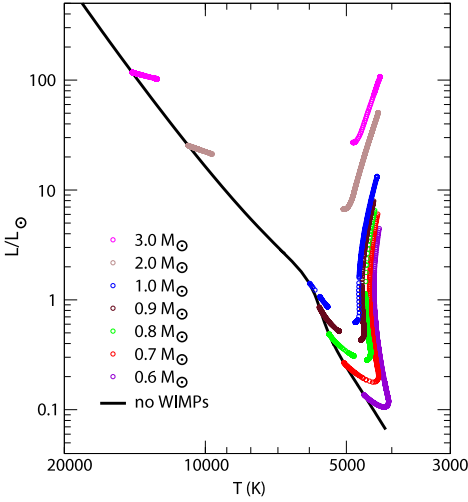


FIG. 1 (color online). The zero age main sequence of WIMP burners. The black solid line is the normal zero age main sequence for stars with solar metallicity. The points moving off the main sequence correspond to solutions where stars contain increasing amounts of dark matter in their cores. The gaps in the lines are addressed in the text.

In Fig. 1, tracks for stars of mass $0.8M_{\odot}$ are not complete, and show increasingly large gaps for larger masses. Using the modified ZAMS code, we could not find solutions corresponding to all temperatures between the main sequence stars and the cooler Hayashi-like WIMP burners. In Fig. 2 we plot temperature as a function of ambient WIMP density. The discontinuity occurs where the temperature of the star drops rapidly, shortly before the star becomes fully convective.

It was not initially clear whether this lack of solutions was a real effect or an artefact of the code. We have put

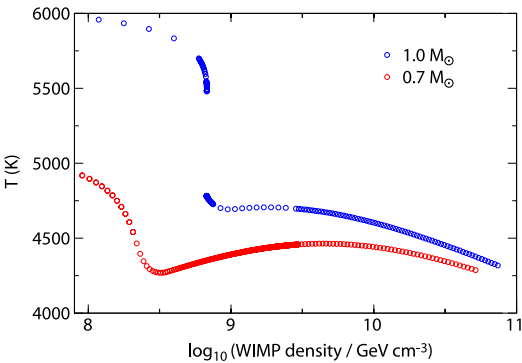


FIG. 2 (color online). The temperature of main sequence stars of mass $1M_{\odot}$ (upper curve) and $0.7M_{\odot}$ as a function of WIMP density. A spin-dependent WIMP-nucleon cross section of $\sigma = 10^{-38} \text{ cm}^2$ is assumed.

some effort into understanding whether some of the physical simplifications in the code (e.g. surface boundary conditions, a simplified equation of state and thus too rigid a criterion for the onset of surface convection, or the treatment of convective heat transport itself) are responsible for the lack of solutions. We could find no evidence to support this idea. Nonetheless, the gaps do not appear to have a physical basis. They seem to be a numerical artefact arising from the “shooting” technique used by the ZAMS code to solve the boundary-value problem of stellar structure. In the region of the gaps, small changes in the stellar radius cause large changes in the internal temperature. The surface defined by the discrepancy between the inwardly and outwardly integrated partial solutions employed in this technique then becomes a highly nontrivial function of the model parameters. Finding the global minimum of this function is then nearly impossible without an initial guess extremely close to the true solution, and the algorithm fails to converge.

To check that solutions do exist in this region, we investigated the gaps using a preliminary version of our next-generation WIMP burner code DarkStars. This code has been created from generalized versions of capture routines in DarkSUSY [13] which use the full capture rate expressions in [4], and the stellar evolution package EZ [16] derived from Eggleton’s STARS code [17]. The code is time-dependent, uses relaxation rather than shooting and includes WIMP energy transport, more detailed treatments of the WIMP distribution, capture rates, equation of state, nuclear reaction rates and opacities. DarkStars and results obtained with it will be described in full in an upcoming publication [12]. The results of the more detailed code (Fig. 3), while consistent with the ZAMS code close to the main sequence and in the fully convective regions on the right-hand side of the HR diagram, show that intermediate solutions do exist and that the gaps are

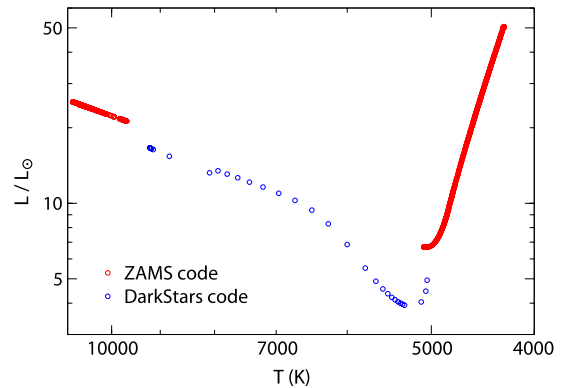


FIG. 3 (color online). Diagram for $M_* = 2M_{\odot}$ showing that solutions can be found corresponding to all temperatures when the more sophisticated DarkStars code is used.

not physical. This cross-check also shows that we can trust the solutions of the ZAMS code, but should not take the actual gaps in the curves seriously.

Figure 2 shows that for a spin-dependent WIMP-nucleon cross section of $\sigma = 10^{-38} \text{ cm}^2$, stars only start to change their behavior when immersed in a dark matter density of around 10^8 or 10^9 GeV cm^{-3} . This is much larger than the 0.3 GeV cm^{-3} which is thought to be the approximate density of dark matter in the solar system. Most modern simulations of galactic dark matter halos do suggest that the density of dark matter should be much higher in the center of the galaxy. This density should be made more pronounced by the phenomena of adiabatic contraction and dark matter spikes created around black holes, though tempered by self-annihilation of dark matter and gravitational heating due to the motion of stars. It is suggested [18] that densities larger than 10^8 GeV cm^{-3} can be found at radii closer than 10^{-2} pc from the galactic center. Observational challenges associated with constructing an HR diagram from stars in this crowded field are severe though, as the very center of the galaxy is shrouded in dust.

Finally, we comment upon the “paradox of youth” implied by what appear to be hot, young stars close to the central black holes of M31 and our own galaxy [19,20]. In our galaxy, these stars look like $\sim 15M_{\odot}$ main sequence stars with luminosities of the order $1000L_{\odot}$. Such a massive main sequence star should only be around 10 Myr old, so these objects would appear to have formed very recently. However, tidal forces close to the central black

hole are thought to be too large to be compatible with the collapse of a gas cloud to begin star formation. It is not easy to make normal UVB measurements of stellar temperatures at the galactic center due to extinction, but spectral lines found in the atmosphere of such stars appear to be consistent with a temperature of 30 000 K [19]. If this is the case, then it would be difficult to imagine that these are normal stars which have been converted into fully convective and highly luminous WIMP burners from the accretion of dark matter, as such stars would have a temperature of only a few thousand degrees.

A possible explanation for the “paradox of youth” is a combination of collisional stripping of red giant envelopes and merger events [20], owing to the high stellar densities near the centers of the two galaxies. If this is the case, then the anomalously hot stars in fact derive from an older population. Such a population should therefore also contain less luminous, unperturbed stars, including lower mass stars still on the main sequence. Provided that this explanation is correct, and if main sequence WIMP burners exist at all, then such lower mass stars should be examples of them. With upcoming observations of the galactic center expected to probe objects as faint as $1L_{\odot}$, a very real possibility exists for the detection of WIMP burners in the near future.

We thank Gianfranco Bertone, Torsten Bringmann and Georges Meynet for useful discussions. J.E. thanks the Swedish Research Council (VR) for support.

-
- [1] D. N. Spergel *et al.* (WMAP Collaboration), *Astrophys. J. Suppl. Ser.* **170**, 377 (2007).
 - [2] J. Angle *et al.* (XENON Collaboration), *Phys. Rev. Lett.* **100**, 021303 (2008).
 - [3] G. Steigman, C. L. Sarazin, H. Quintana, and J. Faulkner, *Astron. J.* **83**, 1050 (1978); W. H. Press and D. N. Spergel, *Astrophys. J.* **296**, 679 (1985); A. Gould, *Astrophys. J.* **321**, 560 (1987); K. Griest and D. Seckel, *Nucl. Phys.* **B283**, 681 (1987); **B296**, 1034(E) (1988).
 - [4] A. Gould, *Astrophys. J.* **321**, 571 (1987).
 - [5] I. V. Moskalenko and L. Wai, arXiv:astro-ph/0608535; *Astrophys. J.* **659**, L29 (2007).
 - [6] G. Bertone and M. Fairbairn, arXiv:0709.1485.
 - [7] P. Salati and J. Silk, *Astrophys. J.* **338**, 24 (1989).
 - [8] D. N. Spergel and W. H. Press, *Astrophys. J.* **294**, 663 (1985); A. Gould and G. Raffelt, *Astrophys. J.* **352**, 654 (1990); **352**, 669 (1990).
 - [9] A. Bouquet and P. Salati, *Astrophys. J.* **346**, 284 (1989).
 - [10] D. Dearborn, G. Raffelt, P. Salati, J. Silk, and A. Bouquet, *Astrophys. J.* **354**, 568 (1990).
 - [11] A. Bottino, G. Fiorentini, N. Fornengo, B. Ricci, S. Scopel, and F. L. Villante, *Phys. Rev. D* **66**, 053005 (2002).
 - [12] P. Scott, J. Edsjö, and M. Fairbairn, in *Proc. DARK2007*, edited by H. V. Klapdor-Kleingrothaus and I. V. Krivosheina (World Scientific, Singapore, 2008); (unpublished).
 - [13] P. Gondolo, J. Edsjo, P. Ullio, L. Bergstrom, M. Schelke, and E. A. Baltz, *J. Cosmol. Astropart. Phys.* **07** (2004) 008.
 - [14] A. Bouquet and P. Salati, *Astron. Astrophys.* **217**, 270 (1989).
 - [15] C. J. Hansen and S. D. Kawaler, *Stellar Interiors-Physical Principles, Structure, and Evolution* (Springer-Verlag, New York, 1994).
 - [16] B. Paxton, *Publ. Astron. Soc. Pac.* **116**, 699 (2004).
 - [17] P. P. Eggleton, *Mon. Not. R. Astron. Soc.* **151**, 351 (1971); **156**, 361 (1972); O. R. Pols, C. A. Tout, P. P. Eggleton, and Z. Han, *Mon. Not. R. Astron. Soc.* **274**, 964 (1995).
 - [18] G. Bertone and D. Merritt, *Phys. Rev. D* **72**, 103502 (2005).
 - [19] A. M. Ghez *et al.*, *Astrophys. J.* **586**, L127 (2003).
 - [20] P. Demarque and S. Virani, *Astron. Astrophys.* **461**, 651 (2007).

Pat Scott, Malcolm Fairbairn & Joakim Edsjö
Dark stars at the Galactic Centre – the main sequence
MNRAS **394**, 82–104 (2009) arXiv:0809.1871.

Dark stars at the Galactic centre – the main sequence

Pat Scott^{1*}, Malcolm Fairbairn^{2,3*} and Joakim Edsjö^{1*}

¹*Cosmology, Particle Astrophysics and String Theory, Department of Physics, Stockholm University & Oskar Klein Centre for Cosmoparticle Physics, AlbaNova University Centre, SE-106 91 Stockholm, Sweden*

²*Theory Division, CERN, CH-1211, Geneva 23, Switzerland*

³*Physics, Kings College London, Strand, London WC2R 2LS, UK*

Accepted 2008 November 19. Submitted 2008 November 17; in original form 2008 October 5.

ABSTRACT

In regions of very high dark matter density such as the Galactic centre, the capture and annihilation of WIMP dark matter by stars has the potential to significantly alter their evolution. We describe the dark stellar evolution code *DarkStars*, and present a series of detailed grids of WIMP-influenced stellar models for main sequence stars. We describe the changes in stellar structure and main sequence evolution which occur as a function of the rate of energy injection by WIMPs, for masses of $0.3\text{--}2.0\,M_{\odot}$ and metallicities $Z = 0.0003\text{--}0.02$. We show what rates of energy injection can be obtained using realistic orbital parameters for stars at the Galactic centre, including detailed consideration of the velocity and density profiles of dark matter. Capture and annihilation rates are strongly boosted when stars follow elliptical rather than circular orbits. If there is a spike of dark matter induced by the supermassive black hole at the Galactic centre, single solar-mass stars following orbits with periods as long as 50 years and eccentricities as low as 0.9 could be significantly affected. Binary systems with similar periods about the Galactic centre could be affected on even less eccentric orbits. The most striking observational effect of this scenario would be the existence of a binary consisting of a low-mass protostar and a higher-mass evolved star. The observation of low-mass stars and/or binaries on such orbits would either provide a detection of WIMP dark matter, or place stringent limits on the combination of the WIMP mass, spin-dependent nuclear-scattering cross-section, halo density and velocity distribution near the Galactic centre. In some cases, the derived limits on the WIMP mass and spin-dependent nuclear-scattering cross-section would be of comparable sensitivity to current direct-detection experiments.

Key words: dark matter, stars: evolution, stars: fundamental parameters, stars: interiors, Galaxy: centre, elementary particles

1 INTRODUCTION

Observations continue to support the existence of non-baryonic dark matter (DM; Bergström 2000; Bertone et al. 2005; Clowe et al. 2006; Komatsu et al. 2009) with a cosmological abundance around five times that of baryonic matter but of unknown composition. Weakly-interacting massive particles (WIMPs) are a popular and convenient class of dark matter candidates because their weak-scale masses and couplings naturally give rise to an appropriate thermal relic abundance in the early universe.

Typical WIMPs, such as the lightest neutralino in supersymmetry (Jungman et al. 1996), possess non-zero nuclear-scattering and self-annihilation cross-sections. The nuclear-scattering cross-section makes it possible for WIMPs to collide elastically with nuclei in massive bodies such as stars, obtain velocities less than the local escape velocity and become gravitationally bound (Press &

Spergel 1985; Griest & Seckel 1987; Gould 1987a,b). This population of WIMPs will continue to scatter off nuclei in the star, sinking down to the core and eventually annihilating with other captured WIMPs.

If enough WIMPs are captured, the structure of the host body may be altered by the energy produced in WIMP annihilations, or by energy transport caused by the WIMP-nucleus scattering events themselves. This was first realised over 30 years ago in the context of heavy neutrinos (Steigman et al. 1978). The potential for transport effects to modify the structure of stellar cores was initially developed by Spergel & Press (1985) and Faulkner & Gilliland (1985). Implications of annihilation for stellar evolution were first explored by Salati & Silk (1989) and Bouquet & Salati (1989b). A series of subsequent studies (Gilliland et al. 1986; Renzini 1987; Spergel & Faulkner 1988; Faulkner & Swenson 1988; Bouquet et al. 1989; Bouquet & Salati 1989a; Deluca et al. 1989; Salati 1990; Dearborn et al. 1990a,b; Giraud-Heraud et al. 1990; Christensen-Dalsgaard 1992; Faulkner & Swenson 1993) focused

* E-mail: pat@physto.se, malc@cern.ch, edsjo@physto.se

upon possible impacts of energy transport by ‘cosmion’ WIMPs designed to solve the solar neutrino problem. With the advent of neutrino oscillations this problem has of course disappeared. Furthermore, the existence of much more stringent limits upon the WIMP-nucleon scattering cross-sections (e.g. Desai et al. 2004; Angle et al. 2008; Ahmed et al. 2009; Behnke et al. 2008) and an improved understanding of the distribution of dark matter on galactic scales (e.g. Bertone & Merritt 2005; Diemand et al. 2007) mean that the likelihood of seeing changes induced purely by WIMP energy transport seems somewhat diminished. Indeed, later efforts to constrain WIMP physics via helioseismology have proven fruitless (Bottino et al. 2002).

Recent times have seen a resurgent interest in the impacts of WIMPs upon stars, now focussing almost exclusively upon the influence of annihilation. Moskalenko & Wai (2007) and Bertone & Fairbairn (2008) showed that it could be possible to see white dwarfs heated by WIMP annihilation, at the Galactic centre and in globular clusters respectively. Spolyar, Freese & Gondolo (2008) and Natarajan, Tan & O’Shea (2009) showed that WIMP annihilation might be able to partially inhibit the formation of PopIII stars, resulting in giant, cool, primordial stars supported entirely by annihilation energy. In previous letters the current authors presented the first numerical simulations of the structure and evolution of WIMP-burning main sequence stars, employing and comparing both a simple static structure code and a preliminary version of the evolutionary code we present here (Fairbairn, Scott & Edsjö 2008; Scott, Edsjö & Fairbairn 2008). We found that WIMP annihilation in stellar cores diminishes nuclear burning and causes them to re-ascend the Hayashi track, in agreement with the analytical estimates of Salati & Silk (1989).

Iocco (2008) and Freese et al. (2008) performed simplified capture calculations on models of ‘naturally-formed’ PopIII stars, showing that even if the stars were to form normally, they might later accrete sufficient dark matter to alter their appearance. The dark matter densities considered in these studies and in that of Spolyar et al. (2008) were confirmed as reasonable by Freese et al. (2009), using a more detailed treatment of the collapse of the primordial dark matter–gas halo. Both groups went on to consider different stages of the pre-main sequence evolution of WIMP-influenced PopIII stars: Freese et al. (2008) employed polytropic models in an attempt to understand the evolution of the stars postulated by Spolyar et al. (2008), and Iocco et al. (2008) followed the evolution from the tip of the Hayashi track using a full stellar evolution code. Both found stalling phases, but of different durations and at different stages of the stars’ formative evolution. Yoon, Iocco & Akiyama (2008) and Taoso et al. (2008) have now presented simulations of main sequence PopIII stars assumed to have formed normally, but then allowed to evolve with the effects of WIMP capture and annihilation. The last three studies show extended main sequence lifetimes and stalling on the Hayashi track, in agreement with our earlier conclusions at non-zero metallicity and the results we present here.

Those working on PopIII stars have referred to WIMP-burning stars as ‘dark stars’, whilst we and others working at non-zero metallicities have typically used the terms ‘WIMP burners’ or ‘dark matter burners’. In the interests of cohesiveness and simplicity, we will simply adopt the former term. We do acknowledge that the term ‘dark star’ is something of a misnomer, since stars burning dark matter are not strictly dark. As we shall see in the following pages, except for cases where the ambient dark matter density is extremely high, their luminosities are at least reduced relative to normal stars.

In this paper, we present a detailed analysis of the effects of dark matter capture, annihilation and energy transport upon the structure and evolution of main sequence stars, specifically those which might exist at the Galactic centre. In Sect. 2 we give the full description of the DarkStars code and its input physics alluded to in Fairbairn et al. (2008) and Scott et al. (2008). Sect. 3 presents the properties of main sequence dark stars, based upon a grid of stellar models covering a range of masses and metallicities. We take up the questions of the distribution of dark matter close to the Galactic centre in Sect. 4, and the properties of stellar orbits there in Sect. 5. In Sect. 6, we present results from further grids of evolutionary models computed with realistic treatments of the environment and orbits expected near the Galactic centre. We also discuss existing and potential observations in Sect. 6, then give some final remarks on the prospect of detecting or constraining the nature of dark matter through such observations in Sect. 7.

2 THEORY AND MODELLING

2.1 Capture, annihilation and energy injection

The total population of WIMPs $N(t)$ present in a star is given (Jungman et al. 1996) by the equation

$$\frac{dN(t)}{dt} = C(t) - 2A(t) - E(t), \quad (2.1)$$

where $C(t)$ is the rate at which WIMPs are captured, $A(t)$ is the rate at which annihilations occur and $E(t)$ is the evaporation rate. The factor of 2 in the annihilation term arises because each annihilation destroys two Majorana WIMPs. In many cases of interest evaporation is negligible, but we will return to this point later.

Many approximations to the full expression for $C(t)$ derived by Gould (1987a) have appeared in the literature, with widely varying accuracies. Here we attempt to present the full theory in a compact and usable form. We will also build upon the following in Sect. 4 when we consider alternative halo models. For a star capturing WIMPs from an infinitely distant halo, the capture rate is

$$C(t) = 4\pi \int_0^{R_*} r^2 \int_0^\infty \frac{f(u)}{u} w \Omega_v^-(w) du dr, \quad (2.2)$$

where r is the local height in the star, u is the incoming WIMP velocity before it is influenced by the star’s gravitational field and $f(u)$ is the WIMP velocity distribution in the halo. The local escape velocity at a height r is $v(r, t)$, and $w = w(u, r, t) \equiv \sqrt{u^2 + v(r, t)^2}$ is the velocity an incoming WIMP obtains by the time it reaches a height r . $\Omega_v^-(w)$ is the rate at which a WIMP with velocity w scatters to a velocity less than v , and thereby becomes captured. This formula does not apply to capture from an already-bound population of WIMPs, such as occurs in an adiabatically-contracting DM-gas cloud.

For a scattering nucleus of mass m_{nuc} and a WIMP mass m_χ , kinematics dictate that the only collisions able to scatter a WIMP to velocities less than v are those where the fraction Δ of the WIMP energy lost in the collision obeys

$$\frac{u^2}{w^2} \leq \Delta \leq \frac{\mu}{\mu_+}, \quad (2.3)$$

with

$$\mu \equiv \frac{m_\chi}{m_{\text{nuc}}}, \quad \mu_\pm \equiv \frac{\mu \pm 1}{2}. \quad (2.4)$$

This is clearly only possible for values of u that obey

$$\frac{u^2}{w^2} \leq \frac{\mu}{\mu_+^2}, \quad (2.5)$$

which is equivalent to

$$u^2 \leq \frac{\mu v^2}{\mu_-^2}. \quad (2.6)$$

The partial capture rate is then given by

$$\begin{aligned} \Omega_v^-(w) &= \sum_i \Omega_{v,i}^-(w) \\ &= \sum_i w \sigma_i n_i(r, t) \frac{\mu_i}{\mu_{+,i}^2} \theta\left(\frac{\mu_i v^2}{\mu_{-,i}^2} - u^2\right) \\ &\quad \times \int_{u^2/w^2}^{\mu_i/\mu_{+,i}^2} |F_i(\Delta)|^2 d\Delta. \end{aligned} \quad (2.7)$$

Here i denotes the i th nuclear species, n_i is its local number density in the star and $F_i(\Delta)$ is the i th nuclear form factor. θ is the Heaviside step function. The total cross-section σ_i for scattering of WIMPs on the i th nucleus can be approximated as (Jungman et al. 1996; Gondolo et al. 2004)

$$\sigma_i = \beta^2 \left[\sigma_{\text{SI}} A_i^2 + \sigma_{\text{SD}} \frac{4(J_i + 1)}{3J_i} |\langle S_{p,i} \rangle + \langle S_{n,i} \rangle|^2 \right], \quad (2.8)$$

where

$$\beta = \frac{m_{\text{nuc}}(m_\chi + m_p)}{m_p(m_\chi + m_{\text{nuc}})} \quad (2.9)$$

is the ratio of the reduced masses of the WIMP-nucleus and WIMP-proton systems. Here σ_{SI} and σ_{SD} are the hydrogen-normalised spin-independent and spin-dependent nuclear-scattering cross-sections respectively, A_i is the atomic number of the nucleus, J_i is its spin and $\langle S_{p,i} \rangle$ and $\langle S_{n,i} \rangle$ are the expectation values of the spins of its proton and neutron systems, respectively.

Assuming an exponential form factor

$$|F(\Delta)|^2 = \exp\left(-\frac{m_\chi w^2 \Delta}{2E_0}\right) \quad (2.10)$$

for heavy elements and a delta function for hydrogen, the integral in Eq. 2.7 can be performed analytically. Here E_0 is the coherence energy arising from the characteristic nuclear radius. When m_{nuc} is expressed in GeV/c^2 , it can be approximated as

$$E_0 \approx \frac{5.8407 \times 10^{-2}}{m_{\text{nuc}}(0.91m_{\text{nuc}}^{1/3} + 0.3)^2} \text{ GeV}. \quad (2.11)$$

Making the further assumption that WIMP velocities in the halo follow an isothermal distribution with dispersion \bar{v} , the velocity distribution in the rest frame of the dark matter halo is

$$f_0(u) = \frac{4}{\sqrt{\pi}} \left(\frac{3}{2}\right)^{3/2} \frac{\rho_\chi}{m_\chi} \frac{u^2}{\bar{v}^3} \exp\left(-\frac{3u^2}{2\bar{v}^2}\right), \quad (2.12)$$

with ρ_χ the ambient WIMP density. In the frame of a star moving with velocity v_* through the halo, this becomes

$$f_*(u) = f_0(u) \exp\left(-\frac{3v_*^2}{2\bar{v}^2}\right) \frac{\sinh(3uv_*/\bar{v}^2)}{3uv_*/\bar{v}^2}. \quad (2.13)$$

Using Eqs. 2.7, 2.10 and 2.13 it becomes possible to perform the velocity integral in Eq. 2.2 analytically. One converts the step function in Eq. 2.7 to a finite upper limit of integration $u_{\text{max},i}(r, t) = v(r, t)/\sqrt{\mu/\mu_-}$ and obtains

$$C(t) = 4\pi \int_0^{R_*} r^2 \sum_i [W_i(u_{\text{max},i}(r, t)) - W_i(0)] dr. \quad (2.14)$$

Here

$$\begin{aligned} W_i(u) &\equiv \int \frac{f_*(u)}{u} w \Omega_{v,i}^-(w) dw \\ &= \frac{\sigma_i n_i(r, t) \rho_\chi \mu_{+,i}^2 E_{0,i}}{m_\chi^2 \bar{v} v_* \mu_i} \sqrt{\frac{3}{2}} \left\{ (B+G)^{-\frac{1}{2}} \Upsilon(G) \right. \\ &\quad \times e^{-BGv_*^2/(B+G)} - (B+H)^{-\frac{1}{2}} \Upsilon(H) \\ &\quad \times e^{-\frac{H}{B+H} [B(v_*^2 + v(r, t)^2) + H v(r, t)^2]} \left. \right\}, \end{aligned} \quad (2.15)$$

$$G \equiv \frac{m_\chi}{2E_0}, \quad H \equiv G \frac{\mu}{\mu_+^2}, \quad B \equiv \frac{3}{2\bar{v}^2}, \quad (2.16)$$

$$\Upsilon(X) \equiv \Upsilon^-(X) - \Upsilon^+(X), \quad (2.17)$$

$$\Upsilon^\pm(X) \equiv \text{erf}\left\{ \frac{Xu + B(u \pm v_*)}{\sqrt{B+X}} \right\} \quad (2.18)$$

for heavier elements, and

$$\begin{aligned} W_{\text{H}}(u) &= \frac{\sigma_{\text{H}} n_{\text{H}}(r, t) \rho_\chi}{m_\chi \bar{v} v_*} \sqrt{\frac{3}{2\pi}} \left\{ \frac{v(r, t)^2 \Xi}{2\sqrt{B}} + \frac{\mu_{-, \text{H}}^2}{4\mu_{\text{H}} B^{3/2}} \right. \\ &\quad \times \left(2\sqrt{B}[(v_* - u)e^{-B(u+v_*)^2} + (v_* + u) \right. \\ &\quad \times e^{-B(u+v_*)^2 + 4Bv_* u}] - [1 + 2Bv_*^2] \Xi \left. \right) \left. \right\}, \end{aligned} \quad (2.19)$$

$$\Xi \equiv \sqrt{\pi} \left\{ \text{erf}[\sqrt{B}(u - v_*)] - \text{erf}[\sqrt{B}(u + v_*)] \right\} \quad (2.20)$$

for the special case of hydrogen.

The annihilation rate $A(t)$ is simply the integral of the local annihilation rate per unit volume $a(r, t)$

$$A(t) = 4\pi \int_0^{R_*} r^2 a(r, t) dr, \quad (2.21)$$

which is given by

$$a(r, t) = \frac{1}{2} \langle \sigma_a v \rangle_0 n_\chi(r, t)^2. \quad (2.22)$$

Here $n_\chi(r, t)$ is the local WIMP number density in the star and $\langle \sigma_a v \rangle_0$ is the non-relativistic limit of the velocity-averaged annihilation cross-section. The energy injected by WIMP annihilations ϵ_{ann} per unit mass of nuclear matter is

$$\epsilon_{\text{ann}}(r, t) = \frac{2a(r, t) m_\chi c^2}{\rho_*(r, t)} - \nu_{\text{loss}}(r, t), \quad (2.23)$$

where $\rho_*(r, t)$ is the local stellar density and $\nu_{\text{loss}}(r, t)$ accounts for the fraction of the WIMPs' rest-mass energy which escapes in the form of neutrinos. We assume that the WIMPs annihilate only into standard model particles which, apart from the neutrinos, very quickly deposit their energy in the surrounding gas. Together with the energy injection/removal rate ϵ_{trans} due to conductive transport by WIMPs, this gives the total local WIMP energy term

$$\epsilon_{\text{WIMP}}(r, t) = \epsilon_{\text{ann}}(r, t) + \epsilon_{\text{trans}}(r, t). \quad (2.24)$$

This acts as an additional source term in the standard stellar luminosity equation at every height in the star.

2.2 Conductive energy transport and distribution

The simplest way to describe the density of WIMPs in a star is to assume that they have thermalised with the stellar matter. We assume that thermalisation occurs instantaneously, as it would be too

cumbersome to allow for a non-thermalised evolution of the WIMP distribution at the same time as evolving a star (no formalism beyond explicit Monte Carlo simulations exists at this stage for doing such a thing). We expect this approximation to break down when capture rates change rapidly, such as during the short-term evolution of stars on elliptical orbits at the Galactic centre (Sec. 6.2). Our primary interest is in the longer-term behaviour of such stars, which should not be strongly effected by the thermalisation process.

Thermalisation can be local, such that the WIMP energies reflect the local temperature at every height in the star, or global, such that they reflect only a single overall characteristic temperature T_W . In the first case, WIMPs are in local thermodynamic equilibrium (LTE) with the stellar matter, whilst in the second case they are isothermally distributed. The isothermal assumption gives the Boltzmann distribution for particles in a gravitational well

$$n_{\chi, \text{iso}}(r, t) = N(t) \frac{g_j e^{-E_j/kT}}{\sum_{j'} g_{j'} e^{-E_{j'}/kT}} \quad (2.25)$$

$$= N(t) \frac{e^{-m_\chi \phi(r, t)/kT_W(t)}}{\int_0^{R_*} 4\pi r'^2 e^{-m_\chi \phi(r', t)/kT_W(t)} dr'},$$

where $\phi(r, t)$ is the local value of the gravitational potential, g_j is the statistical weight of the j th energy level (1 in this case) and $E_j = m_\chi \phi(r, t)$ is its gravitational potential energy. Because WIMPs cluster so strongly in the centre of a star, previous analyses typically assumed that the area in which they reside can be approximated by a sphere of uniform density $\rho_c(t)$, the central density. This sets $T_W(t)$ to the central temperature $T_c(t)$, and gives

$$\phi(r, t) \approx \frac{2\pi}{3} G \rho_c(t) r^2. \quad (2.26)$$

This takes Eq. 2.25 to

$$n_\chi(r, t) \approx N(t) \frac{e^{-\frac{r^2}{r_\chi^2}}}{\pi^{3/2} r_\chi^3}, \quad (2.27)$$

with

$$r_\chi(t) \equiv \left(\frac{3kT_c(t)}{2\pi G \rho_c(t) m_\chi} \right)^{1/2}. \quad (2.28)$$

In practice, there is no longer any real reason to prefer Eq. 2.27 to Eq. 2.25. The gravitational potential must be tabulated anyway at all heights in the star to obtain $v(r, t)$ for the capture calculation, and the integral in Eq. 2.25 can be evaluated quickly and easily using modern computers. Most importantly, a reasonable estimate for $T_W(t)$ can be directly calculated from the structure of the star (as we describe below).

The usefulness of the uniform sphere approximation lies in the length scale it defines, r_χ . This gives the approximate scale height of the WIMP distribution in the star, which can be compared with the WIMP mean free path

$$l(r, t) \equiv \left(\sum_i l_i(r, t)^{-1} \right)^{-1}, \quad l_i(r, t)^{-1} \equiv \sigma_i n_i(r, t) \quad (2.29)$$

at the centre of the star to give the Knudsen number of the system,

$$K(t) = \frac{l(0, t)}{r_\chi(t)}. \quad (2.30)$$

The Knudsen number indicates whether the WIMPs travel a distance less than the scale size on average and transport energy locally ($K < 1$), or typically travel out beyond r_χ before depositing energy non-locally ($K > 1$).

In the extreme limit $K \rightarrow 0$, the energy transport is completely local. In this case WIMPs scatter about so often that they are in LTE with the nuclei, and the energy transport is exactly the case of LTE conductive transport by a gas of massive particles. The exact form of the energy injection/removal rate at a given stellar radius (i.e. the contribution to the local luminosity), and the corresponding density structure for *LTE*-distributed (rather than isothermally-distributed) WIMPs has been calculated by Gould & Raffelt (1990b). These are

$$L_{\text{trans, LTE}}(r, t) = 4\pi r^2 \kappa(r, t) n_{\chi, \text{LTE}}(r, t) l(r, t) \times \left[\frac{kT_*(r, t)}{m_\chi} \right]^{1/2} k \frac{dT_*(r, t)}{dr} \quad (2.31)$$

and

$$n_{\chi, \text{LTE}}(r, t) = n_{\chi, \text{LTE}}(0, t) \left[\frac{T_*(r, t)}{T_c(t)} \right]^{3/2} \times \exp \left[- \int_0^r \frac{k\alpha(r', t) \frac{dT_*(r', t)}{dr'} + m_\chi \frac{d\phi(r', t)}{dr'} dr' \right], \quad (2.32)$$

where normalisation to $\int_0^{R_*} 4\pi r^2 n_{\chi, \text{LTE}}(r, t) dr = N(t)$ dictates the value of $n_{\chi, \text{LTE}}(0, t)$. Noting that in general

$$L(r, t) = 4\pi \int_0^r r'^2 \rho(r', t) \epsilon(r', t) dr', \quad (2.33)$$

we see that

$$\epsilon_{\text{trans, LTE}}(r, t) = \frac{1}{4\pi r^2 \rho(r, t)} \frac{dL_{\text{trans, LTE}}(r, t)}{dr} \quad (2.34)$$

Note that our sign convention differs from that of Gould & Raffelt (1990b); Eqs. 2.31 and 2.34 both refer to the energy *injection* rates, not the rate at which WIMPs remove energy (cf. the sign conventions in Eq. 2.24).

The factors α and κ are the dimensionless thermal diffusivity and conductivity, respectively. These vary throughout the star according to the relative abundances of the different atomic nuclei (and the distribution of WIMP-nucleus relative velocities, if the scattering cross-section is velocity-dependent due to a vector coupling to quarks; this is not the case for the neutralino). They are obtained through numerical solution of the Boltzmann collision equation for any given gas mixture. Gould & Raffelt (1990b) found and tabulated the values of α and κ for gases consisting of WIMPs and one other nucleus, varying the WIMP-to-nucleus mass ratio μ from 0 to 100. Whilst the rigorous thing to do for each physical mixture would be to re-solve the Boltzmann equation with a composite collisional operator given as a linear combination of the operators applicable to the single-nucleus case, a good approximation is to simply take a weighted mean of the tabulated α and κ values themselves. That is,

$$\alpha(r, t) = \sum_i \frac{\sigma_i n_i(r, t)}{\sum_j \sigma_j n_j(r, t)} \alpha_i(\mu_i) \quad (2.35)$$

and

$$\kappa(r, t) = \left\{ l(r, t) \sum_i [\kappa_i(\mu) l_i(r, t)]^{-1} \right\}^{-1}. \quad (2.36)$$

For $\mu < 100$, α and κ can be found by interpolation in the tables of Gould & Raffelt (1990b). For larger values of μ , the authors found the limiting behaviour $\alpha \rightarrow 2.5$ and $\kappa \rightarrow \frac{5}{32} \sqrt{2\pi\mu}$. To get a smooth curve for both α and κ , we set the final point of the interpolation table to the limiting values at $\mu = 120$, so that for $\mu > 120$ no interpolation is required and the analytical limits are used.

Notice that $L_{\text{trans,LTE}}(R_*, t)$ is always zero, as $\frac{dT_\star(r,t)}{dr}(R_*) \approx 0$; this reflects the fact that conduction by WIMPs never constitutes a net energy source nor sink in the star, and any energy the WIMPs remove from a hotter region is always returned in full to a cooler region. As shown in Fig. 1, $\epsilon_{\text{trans,LTE}}$ is negative in the inner part of the star, increases with radius until it becomes positive, peaks, then drops again to asymptotically approach zero as $r \rightarrow R_*$.

The statement that there is no net energy outflow due to WIMP-nucleon scatterings is equivalent to there being no evaporation of WIMPs from the star. That is, a captured WIMP never upscatters sufficiently energetically from a nucleus to become unbound and exit the system. That this is the case in the LTE regime is immediately apparent: WIMPs do not travel far from the centre before re-scattering and sinking back to the core. In the non-local regime, things are not so clear; when the WIMPs' mean free paths are much longer than the system scale height, evaporation could in principle be significant. In this case, the evaporation rate must be equivalent to the net outward energy flux due to WIMP conductive energy transport in the *isothermal (non-local) picture*. That is,

$$L_{\text{trans,iso}}(R_*, t) = m_\chi c^2 E(t) \equiv L_{\text{evap}}(R_*, t) \quad (2.37)$$

$$L_{\text{trans,iso}}(r, t) = 4\pi \int_0^r r^2 \rho(r, t) \epsilon_{\text{trans,SP}}(r, t, T_W) dr \quad (2.38)$$

$$L_{\text{evap}}(r, t) = 4\pi m_\chi c^2 \int_0^r r^2 R(r, t, T_W) dr, \quad (2.39)$$

where $R(r, t, T_W)$ is the local WIMP evaporation rate per unit volume from a shell at height r , discussed in detail by Gould (1987b). The theoretical rate of energy conduction in the isothermal regime,

$$\begin{aligned} \epsilon_{\text{trans,SP}}(r, t, T_W) &= \frac{8\sqrt{\frac{2}{\pi}} k^{3/2}}{\rho_\star(r, t)} n_{\chi, \text{iso}}(r, t) [T_\star(r, t) - T_W(t)] \\ &\times \sum_i \sigma_i n_i(r, t) \frac{m_\chi m_{\text{nuc}, i}}{(m_\chi + m_{\text{nuc}, i})^2} \left(\frac{T_\star(r, t)}{m_{\text{nuc}, i}} + \frac{T_W(t)}{m_\chi} \right)^{1/2} \end{aligned} \quad (2.40)$$

was developed by Spergel & Press (1985). The equality in Eq. 2.37 uniquely determines T_W , so given a value of $E(t)$ or a particular choice of function $R(r, t, T_W)$, one simply implements an appropriate root-finding algorithm to get T_W . Knowing T_W , one has all the information required to compute the isothermal density distribution (Eq. 2.25). Whilst the boundary condition itself (Eq. 2.37) arises from the consideration of evaporation, and is important to include in order to obtain T_W , in most cases of interest evaporation is negligible so $E(t) = 0$.

Treating conductive energy transport by WIMPs when $K > 1$, where the LTE conduction approximation breaks down entirely, is in general rather difficult. In a second paper, Gould & Raffelt (1990a) showed via explicit Monte Carlo solutions to the Boltzmann equation that there is no good way of analytically determining the WIMP energy transport for large K . One would naively expect that as $K \rightarrow \infty$, the WIMPs would behave essentially isothermally, following the isothermal density structure (Eq. 2.25) and transporting energy according to Eq. 2.40. Whilst they do get rather close to the isothermal density structure, the energy transport via Eq. 2.40 cannot be reconciled with the true Monte Carlo-derived ϵ_W in any systematic way. Eq. 2.40 should therefore not be used as a description of WIMP conductive energy transport in practice, even when $K \rightarrow \infty$. Its value is in providing a means of treating evaporation which is consistent with the isothermal density distribution, such that the characteristic temperature of the distri-

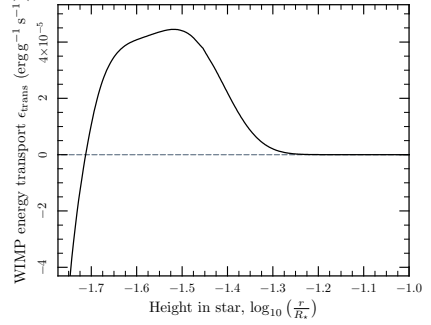


Figure 1. A snapshot of the energy deposited by WIMP conductive energy transport with height in an example star ($1 M_\odot$, $Z = 0.01$, evolved in an isothermal halo with $\rho_\chi = 10^{10} \text{ GeV cm}^{-3}$, $v_\star = 220 \text{ km s}^{-1}$ and $\bar{v} = 270 \text{ km s}^{-1}$). The snapshot was taken early in the star's evolution, before its structure had time to significantly adjust to the effects of WIMP annihilation. Conduction by WIMP-nucleus scattering consumes energy from the very centre of the core and redeposits it further out. The quantity shown here is the final form of ϵ_{trans} (Eq. 2.43), but it differs from $\epsilon_{\text{trans,LTE}}$ only by some correction factors given in Eqs. 2.41 and 2.44.

bution naturally results in the correct evaporation rate (even if that happens to be zero).

In their earlier paper, Gould & Raffelt (1990b) showed that as K increases, the true conductive luminosity is suppressed relative to their analytical prediction (Eq. 2.31). The breakdown occurs in a clearly quantifiable way for increasing K , so one way to treat conductive energy transport by WIMPs in the non-local regime is to adopt the local expression, but with a ‘semi-empirical’ luminosity suppression pre-factor in line with the suppression seen numerically. The suppression shows a sigmoidal shape on a log K scale in Gould & Raffelt’s results,

$$f(K) \approx 1 - \frac{1}{1 + e^{-(\ln K - \ln K_0)/\tau}}} = 1 - \frac{1}{1 + \left(\frac{K_0}{K}\right)^{1/\tau}}. \quad (2.41)$$

The relaxation scale must be about 0.4–0.5 to fit the numerical result well; with $\tau = 0.5$ this function agrees exactly with the suppression function chosen by Bottino et al. (2002), so we use this value. K_0 is the ‘crossing point’ from the local to non-local regimes, where WIMP energy transport is most effective; Gould & Raffelt found this to be $K_0 \approx 0.4$.

Gould & Raffelt (1990b) also showed a similar suppression of the LTE WIMP conductive luminosity with radius. This can be factored into the final expression for $L_T(r, t)$ as a further multiplicative suppression factor $h(r, t)$, such that

$$L_{\text{trans,final}}(r, t) = f(K) h(r, t) L_{\text{trans,LTE}}(r, t). \quad (2.42)$$

The final form of the term appearing in Eq. 2.24 and the stellar luminosity equation becomes

$$\epsilon_{\text{trans}} = \frac{1}{4\pi r^2 \rho(r, t)} \frac{d}{dr} [f(K) h(r, t) L_{\text{trans,LTE}}(r, t)], \quad (2.43)$$

in analogy with Eq. 2.34. The radial suppression function appears as a simple cubic polynomial

$$h(r, t) \approx \left(\frac{r - r_\chi(t)}{r_\chi(t)} \right)^3 + 1 \quad (2.44)$$

in Gould & Raffelt’s numerical results.

For any given K , the degree to which $L_{\text{trans}}(r)$ is suppressed relative to the LTE prediction can be thought of as a general indication of the goodness of the LTE approximation. Since the density structure in the extremely non-local regime is at least moderately well-described by the isothermal approximation (Eq. 2.25), the ‘goodness-of-LTE-assumption’ function $f(K)$ can also be used as a way of interpolating between the isothermal and LTE (Eq. 2.32) densities to give a semi-realistic density structure for all K :

$$n_{\chi,\text{final}}(r, t) = f(K)n_{\chi,\text{LTE}} + [1 - f(K)]n_{\chi,\text{iso}} \quad (2.45)$$

Since $0 \leq f(K) \leq 1$ and both the LTE and isothermal densities are individually normalised, $n_{\chi,\text{final}}(r, t)$ will stay correctly normalised for all K . Since it is only $n_{\chi,\text{LTE}}$ which enters into the expression for the final conductive energy transport, the density structure given by $n_{\chi,\text{final}}$ is important only for determining the radial distribution of injected annihilation energy.

Because no simple measure of the overall efficiency of conductive energy transport by WIMPs presently exists in the literature, we define such a quantity as

$$\mathfrak{E}(t) = \frac{\int_0^{R_*} r^2 \frac{\rho_*(r, t)}{\mu_*(r, t)} \left| \frac{\epsilon_{\text{trans}}}{\epsilon_{\text{other}}} \right| dr}{\int_0^{R_*} r^2 \frac{\rho_*(r, t)}{\mu_*(r, t)} dr}, \quad (2.46)$$

the dimensionless WIMP conductive effectiveness. Here $\mu_*(r, t)$ is the mean particle weight, ϵ_{other} refers to all other energy terms (nuclear, gravitational and annihilation), and the denominator is simply a normalisation factor. $\mathfrak{E}(t)$ is therefore the volume- and number-density-weighted, integrated ratio of WIMP-mediated energy transport to all other energy terms. The weighting by number density is appropriate because WIMP energy transport is presumably more relevant in areas of higher nuclear density. The absolute value arises because ϵ_{trans} is a transport rather than a net source term (i.e. takes on both positive and negative values). Roughly speaking, in a star where WIMP conductive energy transport is the most important local source of luminosity, \mathfrak{E} is greater than 1; where it is a sub-dominant contributor, \mathfrak{E} is less than 1. Whilst the weighting with local number density rightly biases $\mathfrak{E}(t)$ towards the stellar core, this means that it is possible for extremely effective, localised energy transport by WIMPs in the very centre of a star to dominate the overall stellar energetic effectiveness, without significantly altering the overall structure. This is because in such a case, the enhanced transport only occurs in the most central parts of the core.

2.3 The DarkStars code

DarkStars includes WIMP capture based on Eq. 2.2, generalised from the solar capture routines of DarkSUSY (Gondolo et al. 2004). Exponential form-factor suppression (Eq. 2.10) is assumed for scattering off nuclei heavier than hydrogen. In the basic version, the integral over incoming WIMP velocities can either be performed analytically assuming an isothermal velocity distribution (using Eqs. 2.15 and 2.19), or numerically over any arbitrary velocity distribution. In Sect. 4 we describe two additional velocity distributions which we have implemented in the code, one of which includes another analytical option for the velocity integral.

The capture routines are coupled to the EZ version (Paxton 2004) of the STARS stellar evolution code (Eggleton 1971, 1972; Pols et al. 1995), which uses relaxation to solve the hydrostatic equations of stellar structure over a 199-point adaptive

radial mesh at each timestep. We implement annihilation according to Eqs. 2.21–2.23. We determine the local WIMP density with Eqs. 2.25, 2.32 and 2.45, obtaining T_W as the solution to Eq. 2.37. We include conductive energy transport via Eqs. 2.31 and Eq. 2.43.

The WIMP population is advanced at each timestep by solving Eq. 2.1. We assume that since the stellar structure changes very slowly under the influence of the WIMPs in comparison to the evolution of $N(t)$, the evolution of the population between timesteps can be well described by the solution to Eq. 2.1 in the special case where $C(t)$ and $A_c(t) \equiv \frac{A(t)}{N(t)^2}$ are constant in time:

$$N(t + \Delta t) = \begin{cases} C(t)\tau_{\text{eq}}(t) \left[\tanh \left(\frac{\Delta t}{\tau_{\text{eq}}(t) + t_{\text{equiv}}} \right) \right]^\delta & \text{when } C(t) \neq 0, \\ \frac{N(t)}{1 + N(t)A_c(t)\Delta t} & \text{when } C(t) = 0, \end{cases} \quad (2.47)$$

$$\tau_{\text{eq}}(t) \equiv \frac{1}{\sqrt{C(t)A_c(t)}}, \quad (2.48)$$

$$t_{\text{equiv}} \equiv \tanh^{-1} \left(\left[\frac{N(t)}{C(t)\tau_{\text{eq}}(t)} \right]^\delta \right), \quad (2.49)$$

$$\delta \equiv \text{sign} \left(\frac{dN(t)}{dt} \right). \quad (2.50)$$

This is well-justified because both $C(t)$ and $A_c(t)$ depend only upon the stellar structure, not directly upon the absolute WIMP population. Here $\tau_{\text{eq}}(t)$ is the emergent time-scale of equilibration between capture and annihilation, and t_{equiv} is an equivalent earlier time from which the approximate solution needs to be evolved for the current values of C and A_c . Our approximation is an example of the general approach to solving stiff differential equations by separation into fast and slow subsystems known as coarse-graining, and allows a numerical solution to Eq. 2.1 with timesteps of the order of those typically required for stellar evolution.

This scheme constitutes an explicit solution to Eq. 2.1, where each new stellar model is converged with the WIMP population at the previous timestep, which is calculated with capture and annihilation rates computed using the stellar structure of the previous model. The models are therefore not completely self-consistent, as the WIMP population lags the stellar structure by one timestep. Implementing Eq. 2.1 in the internal implicit differencing scheme of the STARS code would have required extensive revision of the internal solver. As a consistency check, we have implemented a ‘reconvergence mode’ similar to that described by Dearborn et al. (1990b), where models are reconverged with the new WIMP population at every timestep, producing a fully self-consistent solution. We have also experimented with rescaling the automatically-chosen timesteps to smaller values. Except for some special cases which we describe in Sect. 3, the results do not change.

In general we limit timesteps to allow no more than a certain proportional change in the WIMP population per step. Typically we demand that the population does not change by more than the current value in one step, but for the more extreme situations in Sect. 6 we reduce this by a factor of ten. To aid initial convergence and prevent this prescription from demanding impossibly small timesteps early in the simulation, we begin simulations with populations of 10^{30-35} WIMPs. This is many orders of magnitude less than the population required to have an effect upon the stellar structure.

We calculate capture by the 22 most relevant nuclei: ^1H , ^3He , ^4He , ^{12}C , ^{13}C , ^{14}N , ^{16}O , ^{18}O , ^{20}Ne , ^{24}Mg , ^{23}Na , ^{27}Al , ^{28}Si , ^{32}S ,

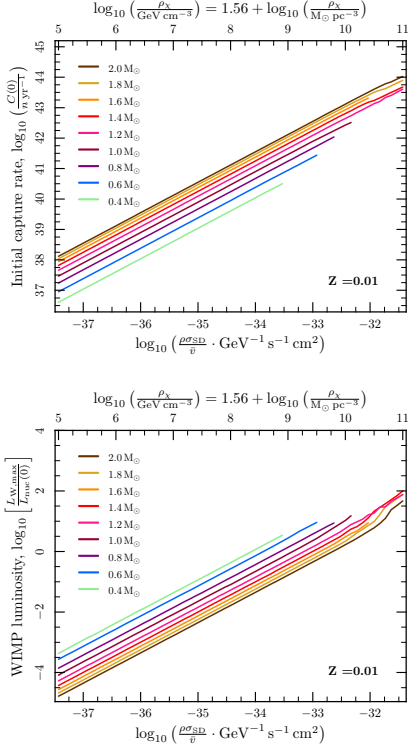


Figure 2. Initial capture rates (top) and annihilating-to-nuclear luminosity ratios (bottom) achieved by stars evolved in differing dark matter densities. Nuclear luminosities $L_{\text{nuc}}(0)$ are initial values, whilst annihilation luminosities $L_{W,\text{max}}$ are the maximum values achieved during a star's lifetime. The dark matter velocity structure is that typically assumed by direct detection experiments, where the distribution is isothermal with solar values $v_\star = 220$ and $\bar{v} = 270 \text{ km s}^{-1}$. We refer to this canonical example as the 'reference solar configuration' (RSC), where it should be understood that only the velocity structure, not the density, is reflective of the true solar situation. These plots provide a simple conversion mechanism between capture rates, WIMP luminosities and equivalent RSC dark matter densities.

^{40}Ar , ^{40}Ca , ^{56}Fe , ^{58}Ni , ^{60}Ni , ^{206}Pb , ^{207}Pb and ^{207}Pb . The stellar code follows the abundances of ^1H , ^4He , ^{12}C , ^{14}N , ^{16}O , ^{20}Ne and ^{24}Mg , and we assume that the remaining mass is distributed amongst the other 15 species according to their abundance ratios in the Sun. The data on inter-elemental ratios comes from Asplund, Grevesse & Sauval (2005, but with the Ni abundance from Scott et al. 2009), and on isotopic ratios from Heber et al. (2003, $^3\text{He}/^4\text{He}$), Scott et al. (2006, $^{12}\text{C}/^{13}\text{C}$ and $^{16}\text{O}/^{18}\text{O}$), preliminary results from work in progress ($^{58}\text{Ni}/^{60}\text{Ni}$) and Tatsumoto et al. (1976, via Anders & Grevesse 1989, $^{208}\text{Pb}/^{207}\text{Pb}/^{206}\text{Pb}$). Atomic and nuclear masses are sourced from Wapstra et al. (2003) and Audi et al. (2003). The present code allows total heavy-element mass fractions Z of 0.0001–0.03, which are paired with corresponding helium mass fractions of 0.24–0.30.

Since the annihilation rate goes as n_χ^2 whilst the evaporation

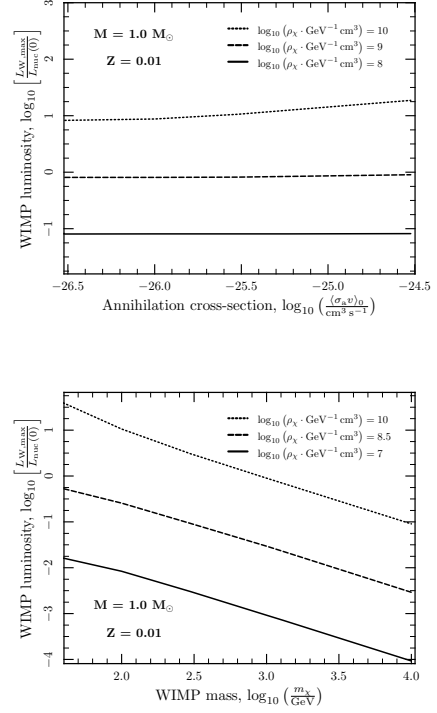


Figure 3. WIMP-to-nuclear luminosity ratios achieved by a $1 M_\odot$ star with different annihilation cross-sections (top) and WIMP masses (bottom). The dark matter halo configuration is the RSC. Since capture rates do not depend upon the annihilation cross-section, the WIMP luminosity is independent of the annihilation cross-section in stars where capture and annihilation are in equilibrium at the time of maximum annihilation luminosity. Because v_\star and \bar{v} are relatively large in the RSC, WIMP luminosities show a strong dependence upon the WIMP mass.

rate goes only as n_χ , the evaporation rate is much smaller for the high ambient WIMP densities and capture rates we are typically interested in. Even for the Sun, Gould (1987b) found that evaporation is insignificant unless the WIMP mass happens to be relatively closely matched with a nucleus found there in significant abundance. The heaviest such element is iron, so evaporation can be considered negligible in the Sun for $m_\chi \gtrsim 60 \text{ GeV}$, which is the case for most WIMPs considered interesting today. (The limit given by Gould was $m_\chi \gtrsim 4 \text{ GeV}$, but this assumed that elements heavier than helium could be neglected because, at the time, a WIMP mass higher than $\sim 10 \text{ GeV}$ was considered unlikely). We therefore simply obtain T_W with $E(t) = 0$, neglecting evaporation.

To estimate the factor ν_{loss} in Eq. 2.23, we carried out explicit Monte Carlo simulations of WIMP annihilation in the Sun, along the lines of Blennow et al. (2008). We considered a range of masses and annihilation channels, and included full three-flavour neutrino oscillations, neutrino interactions, stopping of muons and interactions of heavy mesons (e.g. B mesons) in the Sun's core. For

essentially all annihilation channels except $\tau^+\tau^-$, ν_{loss} for a 100 GeV WIMP is 5–15% of the rest-mass energy. For heavier WIMPs, ν_{loss} is reduced due to neutrino interactions in the star. For annihilation to $\tau^+\tau^-$, $\nu_{\text{loss}} \simeq 35\text{--}40\%$ for a 100 GeV WIMP (and drops for heavier WIMPs). Since the neutralino (our canonical WIMP) has very limited annihilation to $\tau^+\tau^-$, we assume a flat neutrino energy loss of $\nu_{\text{loss}} = 10\%$ for all annihilations. We also neglect the slight dependence upon stellar structure and mass.

Capture integrals in DarkStars are performed with QUADPACK (Piessens et al. 1983), whilst simple integrals are done by the users' choice of Simpson's rule, Romberg integration or fifth-order Runge-Kutta with an adaptive step size. Sufficiently well-behaved functions are interpolated using cubic splines. For the others, we found the tensional spline routines of Renka (1993) and Testa & Renka (1999), after a slight readjustment of the convergence parameters, invaluable.

Some provision has been made in the code for later allowing $R(r, t, T_W) \neq 0$, alternative form factors and metal-free evolution if required. DarkStars is available for public download from <http://www.fysik.su.se/~pat/darkstars/>.

Except where explicitly stated otherwise, we perform all simulations in this paper with a canonical WIMP mass of $m_\chi = 100$ GeV and an annihilation cross-section $\langle\sigma_a v\rangle_0 = 3 \times 10^{-26} \text{ cm}^3 \text{ s}^{-1}$, which arises from relic density considerations assuming WIMPs to be the dominant component of dark matter. We use nuclear-scattering cross-sections corresponding to the maximally-allowed experimental values $\sigma_{\text{SI}} = 10^{-44} \text{ cm}^2$ (Angle et al. 2008; Ahmed et al. 2009) and $\sigma_{\text{SD}} = 10^{-38} \text{ cm}^2$ (Desai et al. 2004; Behnke et al. 2008).

3 BENCHMARK IMPACTS ON MAIN SEQUENCE STARS

To understand the general effects of dark matter accretion and annihilation upon main-sequence stars, we start by considering a set of benchmark stars in a reference halo of WIMPs. In later sections, we will expand on these results for more realistic scenarios. For the benchmark stars, we evolved a grid of models with $0.3 M_\odot \leq M_* \leq 2 M_\odot$, $0.0003 \leq Z \leq 0.02$ and $5 \leq \log_{10}(\frac{\rho_\chi}{\text{GeV cm}^{-3}}) \leq 11$. The models were started from the zero-age main sequence (ZAMS), and evolved until one of the following stopping criteria was met:

- (i) The star left the main sequence (as indicated by the central hydrogen mass fraction X_c dropping below 10^{-6}).
- (ii) The star reached a stable equilibrium where all its energy was effectively provided by WIMP annihilation (as indicated by X_c , $\log_{10} \rho_c$ and $\log_{10} T_c$ changing by less than $10^{-14} \frac{M_*}{M_\odot}$, 10^{-10} and 10^{-10} respectively over four consecutive timesteps).
- (iii) The age of the star exceeded the age of the Universe.

Except for main-sequence lifetimes, we present results at $Z = 0.01$ and just give a brief discussion of the effects of metallicity in the text, since most of the properties we discuss did not show any major dependency upon metallicity.

For this grid we used the standard isothermal velocity distribution, with the default solar values of $v_* = v_\odot = 220 \text{ km s}^{-1}$ and $\bar{v} = \sqrt{3/2} v_\odot = 270 \text{ km s}^{-1}$. The resultant capture rates (at $t = 0$) and ratios of annihilation-to-nuclear luminosity are presented in Fig. 2. For the sake of comparison, nuclear luminosities L_{nuc} are taken at zero age, whilst WIMP annihilation luminosities $L_{W, \text{max}}$ are the maximum values the star achieves during its

evolution. Since stars start with almost no WIMPs, WIMP luminosity at zero age is essentially nil, and nuclear luminosity changes significantly after zero age as the WIMPs begin to influence the stellar structure. As expected, capture rates and WIMP-to-nuclear luminosity ratios increase linearly with ρ_χ , and lower-mass stars capture less but burn a greater ratio of WIMPs to nuclear fuel than their higher-mass counterparts. Significantly, WIMP annihilation outstrips nuclear burning in a large area of the parameter space. Capture rates increase slightly at lower metallicity because of the dominance of spin-dependent scattering and capture by hydrogen, but are outweighed by the increased nuclear luminosity, causing a small decrease in WIMP-to-nuclear burning ratios.

Because the primary factor governing the impact of WIMPs upon stellar evolution is simply $N(t)$, the benchmark results we present in this section will hold in general for other combinations of input particle and halo parameters, subject to an appropriate rescaling. In particular, all scenarios which result in the same product of the capture rate and WIMP mass map to roughly the same ratio of WIMP-to-nuclear burning, which in turn maps in an essentially one-to-one manner to all physical changes in a star's structure and evolution. (That is, ignoring 'higher-moment' factors like WIMP thermalisation, distribution, conductive energy transport and capture-annihilation equilibration). In this way, Fig. 2 acts as a conversion table between capture rates, WIMP luminosities and equivalent dark matter densities in the RSC. (We use the term 'WIMP luminosity' as shorthand for the ratio $\frac{L_{W, \text{max}}}{L_{\text{nuc}}(0)}$ when it is clear what we mean, or when the distinction is irrelevant).

Lines in Fig. 2 do not all extend to $\log_{10} \rho_\chi = 11$. This is because as WIMP luminosity becomes a more significant contributor to a star's energy generation, the stellar models become steadily more difficult to converge. In many cases, we had to very carefully adjust the initial timesteps in order to converge models near the ends of tracks in Fig. 2. In some cases we either could not obtain initial convergence or could not properly maintain it until one of the criteria above was met. Results from such models were discarded.

We performed control calculations on a single solar-mass star with different WIMP masses and annihilation cross-sections (Fig. 3). When capture and annihilation have equilibrated in a star, the WIMP luminosity effectively depends on the capture rate alone, which is independent of the annihilation cross-section (cf. Eqs. 2.14, 2.15 and 2.19), so we see that $\langle\sigma_a v\rangle_0$ makes no difference to the amount of energy generated. When equilibrium has not been achieved, this will not be the case. Such an effect can be seen in the slight upturn of the WIMP luminosity in the uppermost curve of the upper panel in Fig. 3. In this case the very high ρ_χ and very low $\langle\sigma_a v\rangle_0$ significantly change the stellar structure before equilibrium has been reached, causing L_W to peak prior to equilibrium. The dependence of L_W on m_χ in Fig. 3 shows roughly an inverse square relationship, which is a result of using the full capture expressions in the RSC. As can be seen from careful inspection of Eq. 2.19 for example, for small \bar{v} and v_* such as those used in the context of the early universe by e.g. Iocco (2008) and Freese et al. (2008), the dependence disappears.

In Figs. 4 and 5 we show evolutionary tracks in the HR and central equation-of-state diagrams of stars with different masses and WIMP luminosities. At low WIMP luminosities, the evolution is essentially normal. As WIMPs are allowed to provide more energy, the negative heat capacity of a star causes it to expand and cool. The central temperature and density drop, nuclear burning reduces and the star moves some distance back up the Hayashi track. The reduction in central temperatures and overall luminosities provided by pp-chain and CNO-process hydrogen burning are illus-

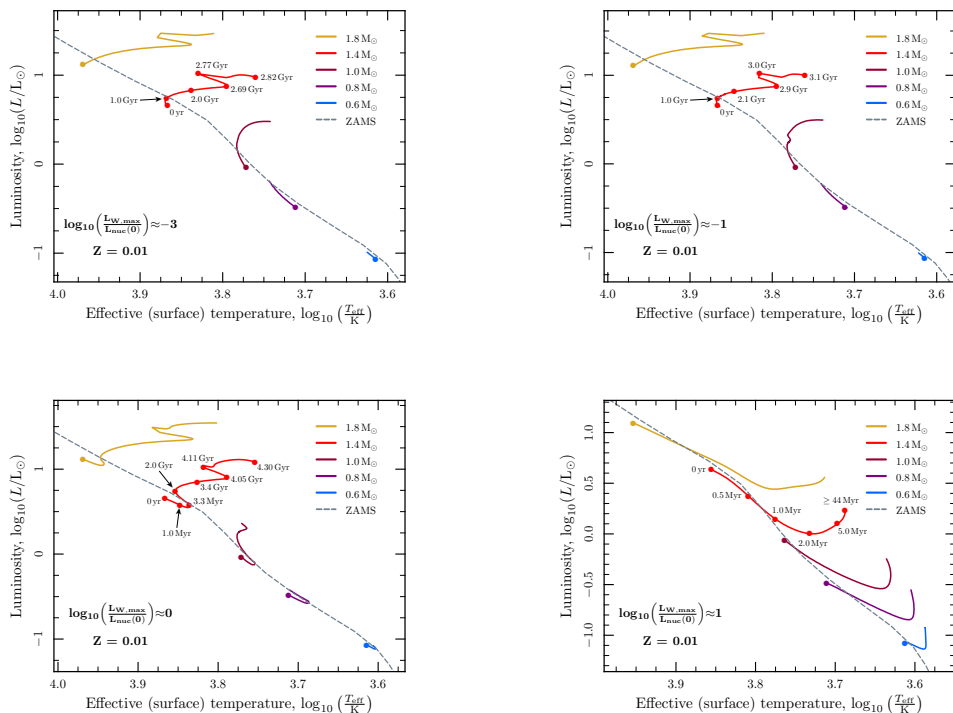


Figure 4. Evolutionary tracks followed in the HR diagram by stars of various masses, when WIMPs provide different fractions of their total energy budgets. Filled, unlabelled circles indicate the starting points of tracks, whilst labelled ones give indicative ages during the evolution of $1.4 M_{\odot}$ stars. Tracks have been halted when the star exhausts the supply of hydrogen in its core or reaches the current age of the universe. Stars with a greater luminosity contribution from WIMPs push further up the Hayashi track and spend longer there before returning to the main sequence. Stars which come to be entirely dominated by WIMP annihilation (*bottom right*) evolve quickly back up the Hayashi track and halt, holding their position in the HR diagram well beyond the age of the universe.

trated in Fig. 6. These values are taken at the time t_{adjust} when a star has completed its initial reaction to the presence of WIMPs, which corresponds to the central temperature and density reaching their minima and the star arriving at the bottom-leftmost point of its travels in Fig. 5. At very high WIMP luminosities, the stellar core expands and cools drastically, moving stars a long way back along the pre-main sequence and effectively shutting down nuclear burning all together. Such an object becomes a fully-fledged dark star, powered entirely and perpetually by WIMP annihilation.

At intermediate WIMP luminosities, nuclear burning is suppressed rather than completely extinguished. Its continued contribution to nuclear processing slowly raises the core temperature and density once more, in turn increasing the rate of nuclear reactions and accelerating the process. The star burns hydrogen alongside WIMPs, and goes on to evolve through a hybrid WIMP-hydrogen main sequence. Such evolution can be best seen in the bottom-left panel of Fig. 4. Thanks to the energy input from WIMP annihilation, the time it takes such a star to consume its core hydrogen is lengthened, so its effective main-sequence lifetime is extended (Fig. 7). The increase in main-sequence lifetime is notable at all metallicities, but most prominent at low Z , essentially because normal main-sequence lifetimes are shorter at lower metallicity. We

did not see changes with metallicity in the central temperatures, pp-chain or CNO luminosities of the stars in our grid.

We should point out here that in the extreme case of a very large WIMP luminosity, it is highly questionable whether a star would have ever reached the main sequence at all, or if it might have simply halted during its initial descent of the Hayashi track. The same might even be true of stars with intermediate WIMP luminosities, since it is not clear whether nuclear burning will win out over WIMP annihilation at exactly the same ages and capture rates when a star is evolved from the main sequence as when it is evolved from the pre-main sequence. This behaviour has been seen explicitly by Iocco et al. (2008). We strongly suspect that the solutions we find for high WIMP luminosities are the same as those obtained with models begun from the pre-main sequence by Iocco et al. (2008). We are currently investigating this question in detail.

The greater influence of WIMP capture and annihilation upon low-mass stars is strongly apparent in Fig. 7. Even if WIMPs supply only a tenth the energy of nuclear burning, the lifetime of a $0.8 M_{\odot}$ star is increased by almost a billion years. With the same ratio of WIMP-to-nuclear burning, the lifetime of a $2.0 M_{\odot}$ star is unchanged. Considering that according to Fig. 2, roughly an order of magnitude more dark matter is required for a $2.0 M_{\odot}$ star to even

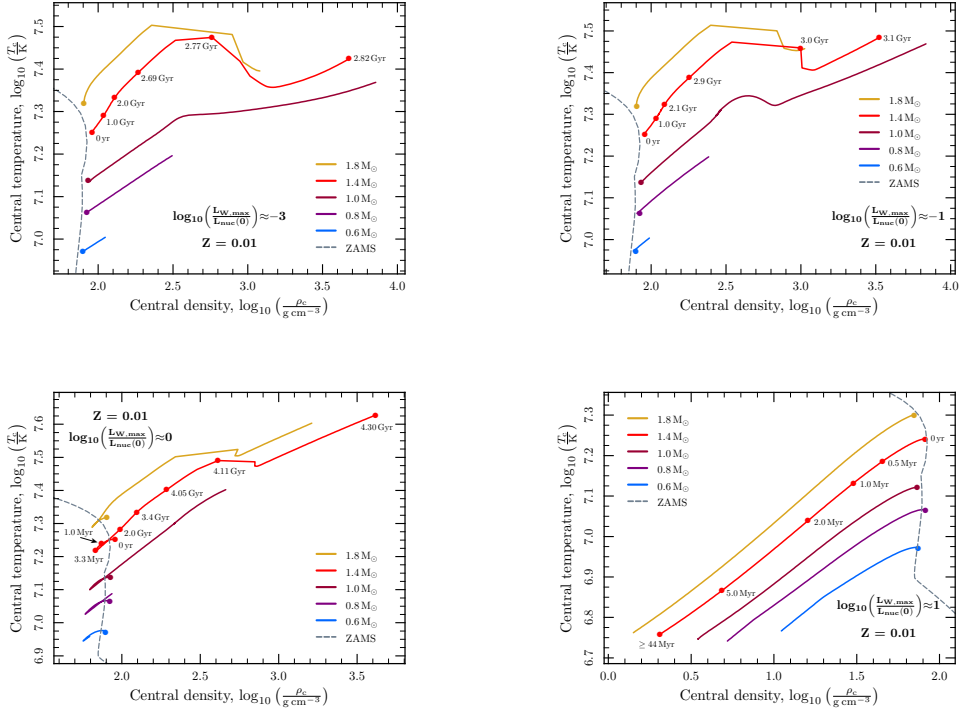


Figure 5. Evolutionary tracks followed in the central equation-of-state diagram by the stars of Fig. 4. Filled circles indicate the starting points of the tracks. Dashed lines show the location at which hydrogen burning becomes the dominant energy source, which defines the zero-age main sequence (ZAMS). To the bottom-left of this line, the core is too cool and diffuse to support the star by nuclear burning alone. Stars with a greater luminosity contribution from WIMPs push further into this region as they ascend the Hayashi track and their cores cool and expand, and thus take longer to recontract and return to the main sequence. The slight departure from smoothness apparent in some curves is simply due to finite temporal resolution of models.

achieve the same WIMP-to-nuclear burning ratio as a $0.8 M_{\odot}$ star, lower stellar mass is clearly a highly favourable property in the observational search for dark stars.

In Fig. 8 we show the extent of convection at $t = t_{\text{adjust}}$ in stars of various masses, as the WIMP luminosity is increased. Because WIMP annihilation is far more concentrated at the centre of a star than nuclear burning, stars with higher WIMP-to-nuclear burning ratios exhibit steeper radiative temperature gradients in their cores. This produces convective cores of increasing size, as the height over which the temperature gradient is superadiabatic increases. In parallel, the overall cooling and expansion of the star results in cooler surface layers, increasing the H^{-} concentration and opacity and resulting in progressively deeper surface convection zones. At high enough WIMP luminosities the two zones meet and the star becomes fully convective. At lower metallicities, the promotion of convection is deferred until significantly higher WIMP luminosities, with the effect strongest in higher-mass stars. As an example, a $0.4 M_{\odot}$ star at $Z = 0.02$ becomes fully convective at $\log_{10}[L_{W,\text{max}}/L_{\text{nuc}}(0)] \approx -0.1$, and requires $\log_{10}[L_{W,\text{max}}/L_{\text{nuc}}(0)] \approx 0.3$ at $Z = 0.0003$. A $1.4 M_{\odot}$ star on the other hand requires $\log_{10}[L_{W,\text{max}}/L_{\text{nuc}}(0)] \approx 0.8$ at $Z = 0.02$, but $\log_{10}[L_{W,\text{max}}/L_{\text{nuc}}(0)] > 2$ at $Z = 0.0003$.

We plot the dimensionless WIMP conductive effectiveness \mathcal{E} (Eq. 2.46) at $t = t_{\text{adjust}}$ for the full range of WIMP luminosities and stellar masses in Fig. 9. Due to the Knudsen-dependent and radial suppression factors (Eqs. 2.41 and 2.44), the contribution of WIMP conductive energy transport turns out to be small over most of the parameter space. Eq. 2.46 is, however, a rather coarse measure of the significance of conductive transport by WIMPs; a more detailed comparison would investigate its role in the effective opacity of nuclear matter in the star. At lower metallicities, the values of \mathcal{E} become slightly larger, with the effect increasing with stellar mass. WIMP energy transport might therefore be worth including in future studies of PopIII dark star evolution.

A number of numerical features complicate the interpretation of Figs. 6–9. To be able to simulate a grid of ~ 3500 stars and produce a manageable amount of output data, we chose only to save model data every tenth timestep. This meant the resolution available for choosing the points at which to define $L_{W,\text{max}}$ and t_{adjust} was not as high as it could have been. The effect upon t_{adjust} was greater than on $L_{W,\text{max}}$, as it was compounded by the fact that t_{adjust} is not as simply found as its definition would have one believe. In cases where the equilibration time-scale is long, t_{adjust} can be comparable to or longer than τ_{eq} . When this happens, t_{adjust} and

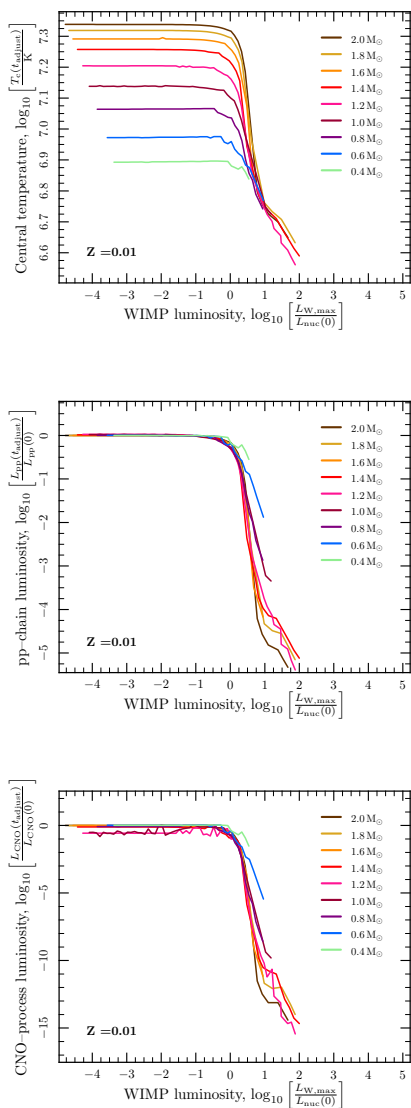


Figure 6. Central temperatures (top) and total luminosities provided by hydrogen fusion via the pp-chain (middle) and CNO-process (bottom), as a function of the luminosity provided by WIMP burning. Central temperatures and hydrogen-burning luminosities are as measured at t_{adjust} , the point at which a star has just completed its initial adjustment to the presence of WIMPs in its core. This corresponds to the time at which models' evolutionary paths have reached their bottom-leftmost points in Fig. 5. Rates of energy production from hydrogen burning are expressed as fractions of their initial values.

τ_{eq} begin to lose meaning, as the adjustment alters the capture rate, which feeds back on the adjustment. This only occurs when $C(t)$ and $A(t)$ are of intermediate size, because even though τ_{eq} is at its longest when $C(t)$ and $A(t)$ are very small, very little adjustment is necessary in this case so t_{adjust} is also very small. The upshot of all this is that a small amount of noise appears in Figs. 6, 8 and 9. For the sake of aesthetics, we recomputed individual evolutionary tracks in Figs. 4 and 5 with data saved every timestep.

For 1.0 and 1.2 M_{\odot} stars, the reference CNO-process luminosity extracted at $t = 0$ in Fig. 6 was somewhat overestimated, due to the initial relaxation of the stellar models. The CNO process is only just present in 1.0-1.2 M_{\odot} stars, and extremely temperature-sensitive, so is very likely to be significantly altered during numerical relaxation. The overestimation is the reason curves for 1.0 and 1.2 M_{\odot} do not tend properly to zero at low WIMP luminosities in the lower panel of Fig. 6.

Despite extensive prior testing, we found that our stopping criterion ii) was sometimes not quite stringent enough. Occasionally, models were halted which would have just managed to leave the main sequence in less than the age of the universe. We removed a small number of stars we suspected this of having influenced from the grid. As a result, the exact slopes of the steepest parts of the curves for higher masses in Fig. 7 are somewhat uncertain.

Some noise also exists in the plots of Fig. 7, simply due to the finite temporal resolution of the models. Timesteps typically become longer once a star nears the end of the main sequence, so some temporal 'overshoot' can occur before criterion i) is triggered. As always, our choice of the internal timestep scaling was a compromise between obtaining the smoothest results and being able to compute a reasonable number of models in a tractable timeframe (proper treatment of WIMP capture makes dark stellar evolution far more time-consuming than standard evolution).

For a small window of WIMP densities, we also found that stars underwent seemingly random expansion and recontraction events during their evolution on the hybrid WIMP-hydrogen main sequence. Suggestively, these windows correspond approximately to the areas where we were unable to find solutions using our static code (Fairbairn et al. 2008). The results of the static code suggest that this window can be thought of in the following way: for a particular ambient density of WIMPs, if one tries to obtain a static solution, one may find that two solutions exist for a WIMP-burning star. The first solution corresponds to a star where the central temperature is rather close to that of a normal star of the same mass, such that the WIMPs are spread over a larger volume according to equation 2.25. Because the WIMPs are spread over a larger volume, their annihilation is less centralised and the spatial distribution of their energy release into the star is closer to that of normal nuclear burning. The core temperature of the star is therefore not reduced very much and the solution is self-consistent. The second solution occurs when the WIMPs are localised in a small region in the centre of the star because the central temperature is low. The low central temperature is what would be expected if energy were input into a small region at the centre of the star, so this solution is also self-consistent. This situation arises primarily for larger mass stars, partially due to the extreme temperature-dependence of the CNO process which dominates nuclear burning in such stars.

The existence of two solutions with the static code suggests that we might expect evolution in this region of parameter space to be unpredictable when looked at with a time-dependent code. For example, stars might exhibit genuine periodic or chaotic variability, or could become numerically unstable. By reducing the internal timestep scaling and employing the reconvergence mode, we es-

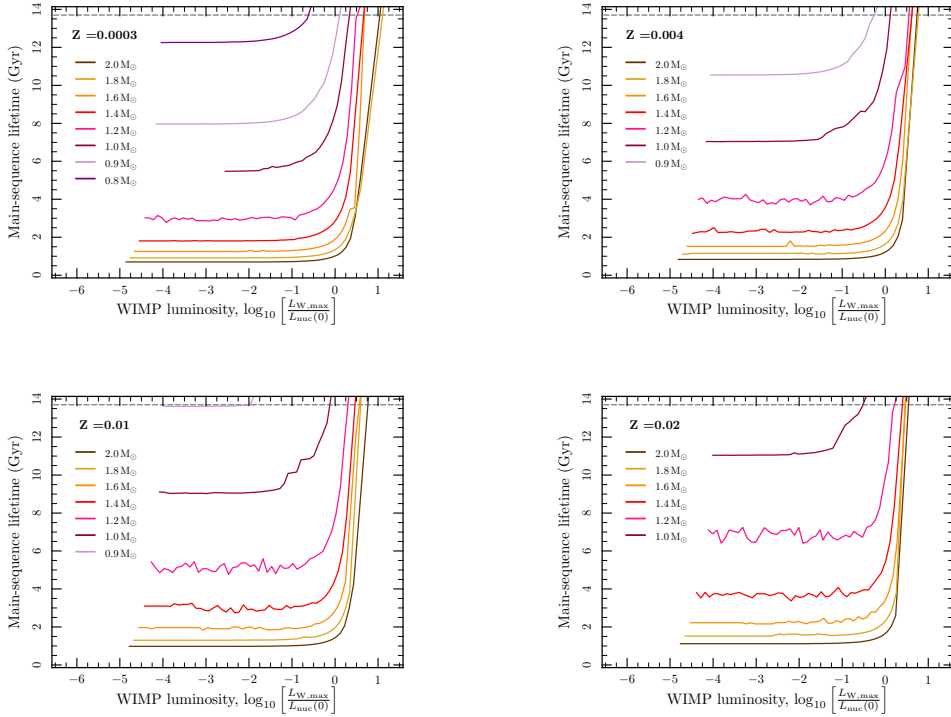


Figure 7. Main-sequence lifetimes of stars with differing masses, metallicities and WIMP luminosities. Dashed lines indicate the present age of the universe. Stars with a greater fraction of their energy provided by WIMPs consume hydrogen more slowly, so spend more time on the main sequence. For a given WIMP-to-nuclear burning ratio, the lifetimes of stars with lower masses and metallicities are more affected than their more massive, metal-rich counterparts.

tabulated that the apparently random expansions and contractions are numerical artefacts caused by insufficient temporal resolution; given sufficiently small timesteps, the time-dependent code seems to follow a path intermediate to the two solutions appearing in the basic static code. The borderline stability of the stellar structure in this region when treated with a code which assumes hydrostatic equilibrium (as *DarkStars* does) suggests that such stars might exhibit some true physical variability after all, but due to dynamical effects only captureable with a full hydrodynamic code. If there is interesting variable behaviour in this region then, it probably occurs on a timescale smaller than can be resolved by *DarkStars*.

The evolution of such stars over an entire lifetime seems largely unaffected by the excursions, so we are confident that the overall results of the grid still accurately reflect the general properties of main sequence dark stars. However, the excursions do further complicate the task of automatically choosing t_{adjust} , adding further noise to Figs. 6, 8 and 9.

4 THE GALACTIC DARK MATTER HALO

In order to simulate the accretion of dark matter by stars at the Galactic centre, one should understand its distribution in the Milky

Way. In particular, the density and velocity distribution of dark matter both play a role in determining the capture rate.

4.1 Density

Density profiles of dark matter halos have been a topic of computational study for over a decade (Navarro et al. 1996; Moore et al. 1999; Navarro et al. 2004; Diemand et al. 2007). As N -body simulations have been run on computers of ever-increasing speed, a standard lore for the expected distribution of dark matter in halos of all sizes has developed. Two conclusions that seem to be universally accepted are that dark matter is denser in the centre of halo simulations, and that the logarithmic gradient of the density $\gamma = d \ln \rho / d \ln r$ is more negative in the outer parts of simulated halos than the inner parts. A popular parametrisation is the ‘NFW profile,’ which interpolates smoothly between asymptotic values of $\gamma = -1$ in the inner regions of the halo and $\gamma = -3$ in the outer regions (Navarro et al. 1996). Navarro et al. (2004) have since suggested that a better profile would in fact be one where γ varies smoothly with radius, and does not asymptote to any particular value at large nor small radii; such a profile has been advocated by various authors since the 1960s (see Merritt et al. 2006, for an historical account).

Most simulations only include dark matter, since considering

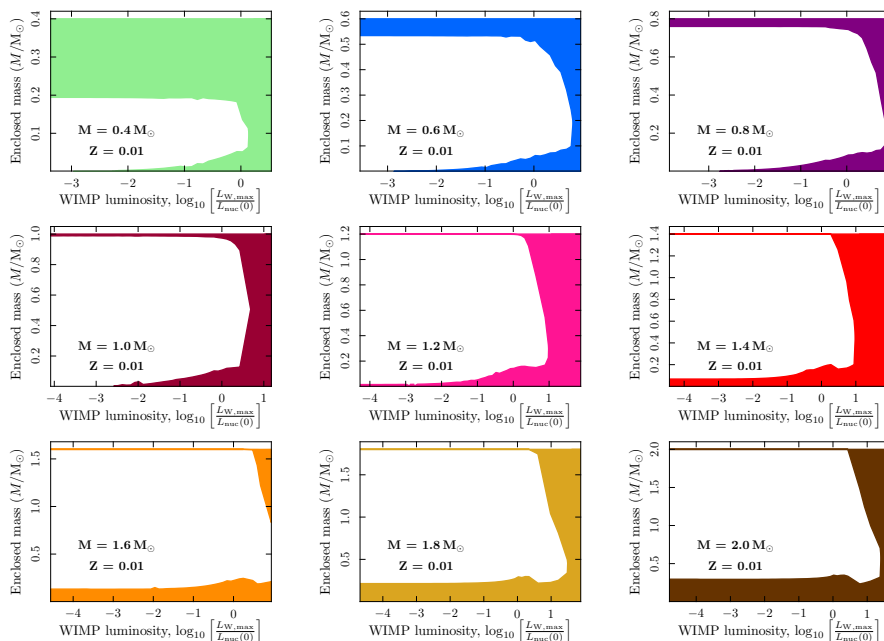


Figure 8. The extent of convection at $t = t_{\text{adjust}}$ in stars of different masses as the energy from WIMP annihilation in their cores is increased. Shaded areas indicate regions in which the stellar energy transport is convective; elsewhere, transport is radiative. Stars develop and extend their convective cores and envelopes as the WIMP luminosity is increased, eventually becoming fully convective at high values of $L_{W,\text{max}}$. Less massive stars require a smaller ratio of annihilation to fusion energy to alter their convective properties than heavier stars. Plots in different panels extend over slightly different ranges of the WIMP-to-nuclear burning ratio, according to which models we were able to converge. Not shown is the dependence upon metallicity: at lower metallicities, the onset of convection is deferred to higher WIMP luminosities, with effects greatest in higher-mass stars.

collisionless particles does not require the complicated hydrodynamics necessary to model baryons. The presence of baryons is expected to change the distribution of dark matter: since the baryons are able to lose energy and sink into the middle of a galaxy, they create a potential well which subsequently pulls the dark matter into the central region. This phenomenon of adiabatic contraction was first predicted by Zel'dovich et al. (1980), and formalised by Blumenthal et al. (1986). More recently, it has been realised that the non-circular nature of typical dark matter orbits reduces this effect, but does not remove it (Gnedin et al. 2004). In order to calculate the expected density profile of dark matter in a given galaxy, it is therefore necessary to take a dark matter halo from an N -body simulation of an appropriately-sized galaxy, then adiabatically contract it using the galaxy's observed baryonic profile. This should be done taking into account the non-circular nature of the dark matter orbits (Gnedin et al. 2004; Gustafsson et al. 2006).

This prescription gives a more realistic estimate of the expected dark matter density in the central regions of a real galaxy than the results of a collisionless N -body simulation (for a comparison of results obtained using this procedure with pure dark matter halos and those from simulations which also include baryons, see Gustafsson et al. 2006). The typical effect of such a contraction is to draw dark matter deeper into the central part of the galaxy, changing the inner slope of the density profile.

As one approaches the centre of a galaxy like the Milky Way

from a large distance, the gravitational potential is first dominated by the diffuse dark matter halo. Approaching the central bulge, the gravitational potential of the concentrated baryonic mass becomes more important. If the current understanding of the dark matter distribution in the Milky Way is correct, the changeover occurs at a radius of the same order of magnitude as the solar position. In the centremost regions, the supermassive black hole determines the gravitational dynamics. The density of dark matter is thought to rise continuously towards the centre of the galaxy, but at radii much less than the solar position, its gravitational influence is always dwarfed by that of baryons or the central black hole.

In the central parsec, where the black hole starts to dominate the gravitational potential, the dark matter profile depends upon a number of factors. One is simply the density of dark matter at larger radii, which forms an initial condition for the central density profile. If the black hole forms in situ, it may create a miniature adiabatic contraction of the local dark matter profile, leading to a central spike where the density gradient is steeper than in the rest of the galaxy. Immediately after its formation, the density of dark matter in such a spike can be extremely high (Gondolo & Silk 1999). The spike is expected to diffuse away over time due to dark matter self-annihilation, loss of dark matter as it falls into the black hole and heating of the dark matter by gravitational interactions with stars.

These different effects can be incorporated into a diffusion equation that gives rise to a final prediction for the density of

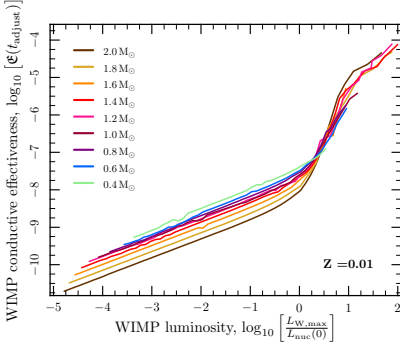


Figure 9. The significance of conductive energy transport by WIMPs, as measured by the dimensionless WIMP conductive effectiveness (Eq. 2.46). A value of 0 on the y-axis roughly indicates that conductive energy transport by WIMPs is as important as all other energy sources in the star combined. The importance of conduction by WIMPs is significantly less than that of actual energy sources. Not shown is the fact that Ξ becomes slightly larger at lower metallicity, with the effect increasing with stellar mass. This suggests that conductive energy transport should probably be taken into account when simulating massive metal-free stars.

Table 1. Parameters for the density profiles defined by Eqs. 4.1, which are approximations to the profiles presented by Bertone & Merritt (2005).

Profile	$\rho_\chi(100 \text{ pc})$	γ_1	γ_2	r_{out}	r_{in}
NFW+spike	25 GeV cm^{-3}	1	1.85	$7 \cdot 10^4 R_{\text{BH}}$	$10 R_{\text{BH}}$
AC+spike	360 GeV cm^{-3}	1.5	1.82	$7 \cdot 10^4 R_{\text{BH}}$	$10 R_{\text{BH}}$

dark matter near the central black hole (Bertone & Merritt 2005). In this work we will consider two dark matter density profiles, both approximations to the profiles presented by Bertone & Merritt (2005). These approximations correspond to profiles B and C used by Bergström et al. (2006). The ‘NFW+spike’ profile is a standard NFW $\gamma = 1$ profile with a central spike which has diffused away over time, considerably reducing its density. The ‘AC+spike’ profile has undergone adiabatic contraction on galactic scales due to the presence of baryons, and also has a central spike which was allowed to diffuse away over time. Both profiles can be parametrised by the expressions

$$\begin{aligned}
 \rho_\chi(r) &= \rho_\chi(100 \text{ pc}) \left(\frac{100 \text{ pc}}{r} \right)^{\gamma_1} & r > r_{\text{out}} \\
 \rho_\chi(r) &= \rho_\chi(r_{\text{out}}) \left(\frac{r_{\text{out}}}{r} \right)^{\gamma_2} & r_{\text{out}} > r > r_{\text{in}} \\
 \rho_\chi(r) &= \rho_\chi(r_{\text{in}}) & r_{\text{in}} > r,
 \end{aligned} \quad (4.1)$$

where parameters are listed in Table 1. Note that following adiabatic contraction, the smoothly varying profile advocated by Navarro et al. (2004) can become almost as steep in the central region as an equivalently-contracted NFW profile, depending upon the angular momentum of the dark matter particles.

4.2 Velocities

Having obtained some estimates of the possible densities of dark matter at the Galactic centre, we must also think about its velocity

distribution, which has a strong bearing upon the number of particles captured by stars.

Various estimates of the velocity distribution exist in the literature. For direct detection experiments such as CDMS, Xenon and COUPP to be able to easily compare results, the dark matter halo is typically assumed to be the isothermal RSC, with a radius-independent Keplerian velocity. In this case, the velocity dispersion is set by the Keplerian velocity at the solar position ($\bar{v} = \sqrt{3/2}v_\odot = 270 \text{ km s}^{-1}$), and acts as the width for a Gaussian distribution of velocities which is identical at every position.

As already mentioned, the highest resolution N -body simulations do not predict an isothermal halo, but rather one where the logarithmic density gradient close to the centre of the galaxy is much less than -2 . The Keplerian velocity in such a halo would therefore decrease to zero at the core, which would increase the rate at which dark matter would be accreted by stars. In a real galaxy however, the dark matter is a subdominant component at these small Galactic radii, and the presence of stars and the central black hole increases the gravitational potential there.

Our default assumption is that the velocity distribution of dark matter is isotropic, spherically symmetric, Gaussian and has a dispersion set by the Keplerian velocity in the solar vicinity. None of these assumptions are strictly correct, as we shall discuss shortly. Our simplest attempt to improve the realism of the velocity distribution is to exclude velocities above the local Galactic escape velocity, as WIMPs with such velocities would presumably already have left the Galaxy some time earlier. We therefore truncate the velocity distribution at the local escape velocity (in the rest frame of the Galaxy), which terminates the Maxwell tail of the distribution. Given a generic WIMP velocity distribution $g_0(u)$, seen in the rest frame of the galaxy, the equivalent truncated distribution will be

$$g_{\text{gal},0}(u) = \frac{\rho_\chi}{m_\chi} \frac{g_0(u)\theta(u_{\text{gal}} - u)}{\int_0^\infty g_0(u')\theta(u_{\text{gal}} - u') du'}, \quad (4.2)$$

where u_{gal} is the local escape velocity, and the integral ensures the new distribution remains correctly normalised. For a star at rest with respect to the Galactic halo, this then brings the capture rate (Eq. 2.2) to the form

$$C(t) = 4\pi D^{-1} \int_0^{R_*} r^2 \sum_i \int_0^{\min[u_{\text{gal}}, u_{\text{max},i}(r,t)]} \frac{g_0(u)}{u} \times w_{\Omega_{v,i}^-}(u) du dr. \quad (4.3)$$

The normalisation factor D is

$$D = \frac{m_\chi}{\rho_\chi} \int_0^{u_{\text{gal}}} g_0(u) du. \quad (4.4)$$

Working from Eq. 2.12, in the case of an isothermal velocity distribution this becomes

$$\begin{aligned}
 D &= \frac{4}{\sqrt{\pi}} \left(\frac{3}{2} \right)^{3/2} \int_0^{u_{\text{gal}}} \frac{u^2}{\bar{v}^3} \exp\left(-\frac{3u^2}{2\bar{v}^2}\right) du \\
 &= \text{erf}\left(\frac{u_{\text{gal}}}{\bar{v}} \sqrt{\frac{3}{2}}\right) - \sqrt{\frac{6}{\pi}} \frac{u_{\text{gal}}}{\bar{v}} \exp\left(-\frac{3u_{\text{gal}}^2}{2\bar{v}^2}\right).
 \end{aligned} \quad (4.5)$$

To find the capture rate in the frame of a star moving relative to the Galactic rest frame, we need to transform $g_{\text{gal},0}(u)$ to some equivalent $g_{\text{gal},*}(u)$ via an appropriate Galilean transform, in analogy with the step from Eq. 2.12 to Eq. 2.13, then consider what u_{gal} becomes in the frame of the star. The maximum velocity any WIMP from a distribution cut off at u_{gal} can have in the galactic frame is obviously u_{gal} . In the frame of the star though, WIMPs

coming from e.g. the direction in which the star is moving through the halo can appear with much greater speed than those coming from ‘behind’ the star. If an incoming WIMP has speed u_0 and velocity in the direction of the unit vector \mathbf{e}_W in the galactic frame, we see that its velocity \mathbf{u}_* in the star’s frame is

$$\begin{aligned}\mathbf{u}_* &= u_0 \mathbf{e}_W - \mathbf{v}_* \\ \Rightarrow u &\equiv |\mathbf{u}_*| = \sqrt{(u_0 \mathbf{e}_W - \mathbf{v}_*)^2} \\ \therefore u &< \sqrt{(u_{\text{gal}} \mathbf{e}_W - \mathbf{v}_*)^2} = (u_{\text{gal}}^2 + v_*^2 + 2u_{\text{gal}} v_* \cos \varphi)^{\frac{1}{2}}.\end{aligned}$$

So in the star’s frame, we have

$$u_{\text{gal}} \longrightarrow u_{\text{gal},*}(\varphi) = (u_{\text{gal}}^2 + v_*^2 + 2u_{\text{gal}} v_* \cos \varphi)^{\frac{1}{2}}, \quad (4.6)$$

where φ is the angle in the galactic frame between the motions of the WIMP and star, such that $\varphi = 0$ corresponds to a head-on collision. This then poses something of a problem, as in the analogous case of the isothermal distribution, φ had to be implicitly integrated over in the first place to obtain the integrand (Eq. 2.13) for which this new cut-off velocity is the limit. The solution to this is either to develop some sort of approximate averaging scheme, or to just do the integral over φ explicitly, *after* the integral over u . In this case, the expression for capture of a truncated isothermal distribution of WIMPs by a moving star is

$$\begin{aligned}C(t) &= 8\sqrt{\pi} \left(\frac{3}{2}\right)^{\frac{3}{2}} \frac{\rho_X}{m_X} D^{-1} \int_0^{R_*} r^2 \sum_i \int_{-1}^1 \int_0^{u_{\text{cut},i}} \frac{u}{v^3} \\ &\quad \times \omega \Omega_{v,i}^-(u) \exp\left(-\frac{3}{2v^2}(u^2 + v_*^2\right. \\ &\quad \left.+ 2uv_* \cos \varphi)\right) du d(\cos \varphi) dr,\end{aligned} \quad (4.7)$$

where

$$u_{\text{cut},i}(\varphi, r, t) \equiv \min[u_{\text{gal},*}(\varphi), u_{\text{max},i}(r, t)]. \quad (4.8)$$

As in the non-truncated case, the velocity integral in Eq. 4.7 can be performed analytically, yielding the truncated analogues of Eqs. 2.14–2.19

$$C(t) = 4\pi D^{-1} \int_0^{R_*} r^2 \int_{-1}^1 \sum_i [M_i(u_{\text{cut},i}(\varphi, r, t)) - M_i(0)] d(\cos \varphi) dr, \quad (4.9)$$

where

$$\begin{aligned}M_i(u) &= \frac{2\sigma_i n_i(r, t) \rho_X \mu_{+,i}^2 E_{0,i} K^{\frac{3}{2}}}{m_X^2 \mu_i \sqrt{\pi}} \left[\sqrt{\pi} K v_* \cos \varphi (\Psi(H) \right. \\ &\quad \times e^{K^2 v_*^2 \cos^2 \varphi / (K+H) - K v_*^2 - H v(r, t)^2} (K+H)^{-3/2} \\ &\quad - \Psi(G) e^{K^2 v_*^2 \cos^2 \varphi / (K+G) - K v_*^2} (K+G)^{-3/2}) \\ &\quad + e^{-2K u v_* \cos \varphi - K(u^2 + v_*^2) - H(u^2 + v(r, t)^2)} (K+H)^{-1} \\ &\quad \left. - e^{-2K u v_* \cos \varphi - K(u^2 + v_*^2) - G u^2} (K+G)^{-1} \right],\end{aligned} \quad (4.10)$$

$$\Psi(X) \equiv \text{erf}\left\{\frac{u(K+X) + K v_* \cos \varphi}{\sqrt{K+X}}\right\} \quad (4.11)$$

for heavier elements, and

$$\begin{aligned}M_H(u) &= \frac{\sigma_H n_H(r, t) \rho_X K^{-\frac{1}{2}}}{2m_X \sqrt{\pi}} \left[2 \left(\frac{\mu_{-,i}^2}{\mu_i} - K v(r, t)^2 \right) \right. \\ &\quad + K \frac{\mu_{-,i}^2}{\mu_i} [u^2 - u v_* \cos \varphi + v_*^2 \cos^2 \varphi] \\ &\quad \times e^{-2K u v_* \cos \varphi - K(u^2 + v_*^2)} + v_* \cos \varphi \sqrt{\pi K} \\ &\quad \times \left(3 \frac{\mu_{-,i}^2}{\mu_i} - 2K v(r, t)^2 + 2K v_*^2 \cos^2 \varphi \frac{\mu_{-,i}^2}{\mu_i} \right) \\ &\quad \left. \times \text{erf}\left[\sqrt{K}(u + v_* \cos \varphi)\right] e^{-v_*^2 K \sin^2 \varphi} \right] \quad (4.12)\end{aligned}$$

for hydrogen. This gives the machinery necessary to calculate the capture rate for a truncated isothermal (Gaussian) velocity distribution.

The fact that we *do not* expect the velocity distribution to be Gaussian in reality is related to the fact that one only expects a Gaussian distribution in the limit of an extensive distribution of particles, such as an ideal gas. For particles coupled to a long-range potential such as gravity, this is not the case. It has been suggested in the literature that the Tsallis distribution, one designed specifically to model the departure from extensivity, is a better fit to the data than a Gaussian (Hansen et al. 2006).

Furthermore, there are good reasons to believe that the radial distribution of dark matter will have a different width to the tangential distribution, since the orbits of dark matter particles are far from circular. For a star on a non-circular orbit around the centre of the Galaxy, this could have important consequences.

Finally, it is interesting to test the truth of the assumption that the velocity dispersion is fully determined by the Keplerian velocity at the solar position. The relationship between the Keplerian velocity, the velocity distribution and its anisotropy depends upon the shape of the potential well of the galaxy; the anisotropy in the velocity distribution can be obtained from the Jeans equations (Fairbairn & Schwetz 2009).

In order to quantify the departures from the isothermal halo model, we have examined data from the Via Lactea simulation (Diemand et al. 2007). This N -body simulation contains more than 2×10^8 dark matter particles, and is one of the largest simulations of a Milky Way-size dark matter halo to date. As suspected, the results do indeed show that all four of the simplifying assumptions involved in the isothermal halo model (isotropy, spherical symmetry, Gaussianity and a dispersion proportional to the Keplerian velocity at the solar position) are essentially incorrect. To obtain a new velocity distribution from the data, we looked at the velocities of particles at different radii. We attempted to fit the distributions with the Tsallis profile of Hansen et al. (2006), but found that although this does provide a better fit than a Gaussian, the following one-dimensional distribution is an even better fit:

$$h_{1D}(u_i) = \exp\left\{-\left[\frac{1}{2}\left(\frac{u_i}{\sigma_i}\right)^2\right]^{\alpha_i}\right\}, \quad (4.13)$$

where $i \in \{r, \theta, \phi\}$ and u_i is the velocity in the i th direction in Galactic coordinates. No normalisation prefactor has been included here. The parameter α measures the departure from Gaussianity and is distinctly different for the one-dimensional velocity distributions in the radial and angular directions. The values of α for the radial distribution (α_r) and a composite tangential distribution (α_T , where $u_T^2 \equiv u_\theta^2 + u_\phi^2$) can be found as a function of radius in Fairbairn & Schwetz (2009). The ratio of the velocity dispersion to the

local Keplerian velocity (v_{Kep} , or more precisely, the square root of the potential since the halo is not completely spherically symmetric) is also a function of radius and can be found in Fairbairn & Schwetz (2009).

These distributions become less Gaussian as one approaches the Galactic centre, with $\alpha \ll 1$ in the region we are most interested in. One should be careful not to take this result overly seriously though; not because the physics of the simulation is in doubt (above the ~ 0.1 kpc resolution scale), but rather because the simulation only includes dark matter. The velocity dispersion at the centre of an NFW profile goes to zero, whereas in a real galaxy, the presence of baryons and the central black hole would be expected to change the velocity distribution quite significantly. We do not make any strong claims as to the fitness of this non-Gaussian velocity distribution for modelling the very centre of the Galaxy; we employ it more with the goal of determining what degree of uncertainty exists in our capture results due to the velocity distribution.

In order to reasonably calculate the effect of the non-Gaussian distributions upon capture rates, we require a composite distribution of total velocity magnitudes in three dimensions. Since the fitted values of α and σ/v_{Kep} become almost isotropic at low Galactic radii, for this purpose we can set them to the same values in the radial and angular directions. We choose these values as the means of the fitted values in each spatial direction, for the smallest Galactic radius at which we fit the velocity distribution (1 kpc). This gives $\alpha = 0.35$ and $\sigma/v_{\text{Kep}} = 0.05$. At the Galactic centre, v_{Kep} is dominated by the black hole, so

$$\sigma = 56.8 \text{ km s}^{-1} \times \left(\frac{0.01 \text{ pc}}{r} \right)^{1/2}. \quad (4.14)$$

To obtain a three-dimensional distribution purely as a function of the velocity magnitude

$$u \equiv \sqrt{u_r^2 + u_\theta^2 + u_\phi^2}, \quad (4.15)$$

we take the product of the 3 one-dimensional distributions, convert to local spherical polar coordinates and integrate over the angular directions. This gives

$$h_{3D}(u_r, u_\theta, u_\phi) = 4\pi u^2 \exp \left[-\frac{1}{(2\sigma^2)^\alpha} (u_r^{2\alpha} + u_\theta^{2\alpha} + u_\phi^{2\alpha}) \right]. \quad (4.16)$$

When $\alpha = 1$, this clearly produces a Gaussian distribution of velocity magnitudes. For $\alpha \neq 1$, we can express u_r^2 , u_θ^2 and u_ϕ^2 in terms of one another and u^2 , then expand to second-order in a binomial series to produce

$$(u^2 - u_i^2 - u_j^2)^\alpha = u^{2\alpha} - \alpha u^{2(\alpha-1)}(u_i^2 + u_j^2), \quad (4.17)$$

where i and j are different members of the set $\{r, \theta, \phi\}$. This gives

$$u_r^{2\alpha} + u_\theta^{2\alpha} + u_\phi^{2\alpha} = (3 - 2\alpha) u^{2\alpha}. \quad (4.18)$$

Normalising over $u \in [0, \infty)$ gives the final three-dimensional ‘N-body’ velocity distribution

$$h_{3D}(u) = \frac{3(3-2\alpha)^{\frac{3}{2\alpha}}}{2^{\frac{3}{2}} \Gamma(1 + \frac{3}{2\alpha})} \frac{\rho_X}{m_X} \frac{u^2}{\sigma^3} \exp \left\{ -(3-2\alpha) \left[\frac{1}{2} \left(\frac{u}{\sigma} \right)^2 \right]^\alpha \right\}. \quad (4.19)$$

Whilst this expression breaks down at third order in the binomial expansion, we expect it to be a reasonable approximation given the level of uncertainty in choosing realistic values of α and σ/v_{Kep} . We now have a three-dimensional velocity distribution as a function

of the local Keplerian velocity, which can be inserted into Eq. 2.2 to obtain the capture rate. Putting Eq. 4.19 into Eq. 4.3 instead, one obtains the capture rate from an equivalent truncated distribution, which is also a function of the local escape velocity.

5 THE GALACTIC POTENTIAL

To calculate dark matter capture rates, it is extremely important to know the stellar velocity v_* through the dark matter halo. In order to correctly truncate the velocity distribution of the dark matter, one also needs to know the local Galactic escape velocity u_{max} .

The orbital velocities are rather simply obtained. Within a few tenths of a parsec, the Galactic potential is dominated by the central black hole. All the elliptical orbits we will consider lie within one fiftieth of a parsec, so they can be treated as exactly Keplerian about a point-mass black hole.

Calculating the escape velocities is more arduous, as we need to integrate the potential experienced by a test particle exiting the Galaxy. It is important to consider not only dark matter but also the presence of baryons, which dominate the potential from around 0.5 pc to several kpc. To model the baryon density of the Milky Way we use the same prescription as Gustafsson et al. (2006), assuming a central bulge of stars with density $\rho \propto r^{-\gamma} e^{-r/\lambda}$. We assume a thin disc of matter with surface density

$$\sigma_{\text{disc}}(r) = \frac{c M_{\text{disc}\infty}}{2\pi (r^2 + c^2)^{\frac{3}{2}}}. \quad (5.1)$$

We choose the free parameters to match observations of the Milky Way: $\gamma = 1.85$, $\lambda = 1$ kpc, $c = 5$ kpc and the total disc and bulge masses $M_{\text{disc}\infty} = 5M_{\text{bulge}} = 6.5 \times 10^{10} M_\odot$ (Kent et al. 1991; Zhao 1996; Dehnen & Binney 1998; Klypin et al. 2002). We assume that the extent of the disc is 15 kpc. We use an NFW profile with a scale radius of 20 kpc for the dark matter, normalised to 0.3 GeV cm^{-3} at the location of the solar system, and find the local escape velocity by integrating the energy loss along a radial path exiting the Galaxy.

6 IMPACTS ON STARS AT THE GALACTIC CENTRE

Armed with detailed estimates of the stellar orbits, local escape velocity, density of dark matter and its velocity distribution at the Galactic centre, we can now realistically evaluate the potential impact of WIMPs upon stellar evolution there. We ran two further grids of evolutionary models, both at $Z = 0.02$ and over $0.3 M_\odot \leq M_* \leq 1.5 M_\odot$. We computed models in both grids using the NFW+spike and AC+spike profiles from Sect. 4.

6.1 Circular orbits

The first grid covered single stars on circular orbits, with orbital radii extending from 10 pc to 10^{-6} pc. For this grid we used the standard, non-truncated version of the isothermal velocity distribution (Eq. 2.13). Results for models computed with the AC+spike density profile are shown in Fig. 10. As orbits are made smaller, capture rates rise because stars encounter higher densities of dark matter. This effect is balanced by a reduction in capture caused by stars’ increasing circular velocities as they orbit closer to the black hole. The capture rate and resultant WIMP luminosity peaks at an

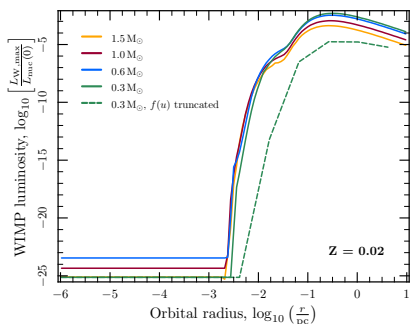


Figure 10. WIMP luminosities achieved by stars orbiting circularly about the central black hole. The dark matter velocity distribution is isothermal with dispersion $\bar{v} = 270 \text{ km s}^{-1}$, and the density profile follows the adiabatically contracted profile (AC+spike). The impact of instead using a velocity distribution truncated at the local Galactic escape velocity is shown with a dashed curve. Capture is maximised at a radius of approximately 0.3 pc, but no circular orbit produces capture rates high enough to translate into a WIMP luminosity which can produce any significant changes in stellar evolution. WIMP luminosities produced with the alternative density profile (NFW+spike) are even lower, so are not shown.

orbital radius of $\sim 0.3 \text{ pc}$. Inwards of this the velocity effect dominates and capture is highly suppressed. The constant WIMP luminosities at very small radii in Fig. 10 are entirely due to the initial populations of WIMPs that the models were started with.

We evolved some supplementary models (dashed curve in Fig. 10) with the truncated isothermal distribution (Eq. 4.2 applied to Eq. 2.12), to see if capture might be boosted to interesting levels by removing unphysical WIMP velocities. On the contrary, the truncation of the isothermal WIMP velocity distribution caused a strong reduction in capture rates. Stars moving as quickly as those on circular orbits near a black hole must capture predominantly from the Maxwell tail of the isothermal distribution, so truncation denies them many of their best capture candidates. The opposite is true of a star in the RSC, which captures from the centre of the distribution and benefits (slightly) in capture rate if the distribution is truncated and renormalised.

If it follows a circular orbit in an isothermal WIMP halo, even the lowest-mass single star, placed at the optimal radius in the most optimistic density profile, cannot accrete enough WIMPs to bring annihilation luminosity to within two orders of magnitude of its nuclear luminosity. We do not show WIMP luminosities resulting from the NFW+spike density profile, as they are even less interesting due to the profile's lower central density.

6.2 Elliptical orbits

The primary assumptions of the previous grid were that stars always follow circular orbits, and that the halo is isothermal. We know these to be untrue in reality, so in the second grid we considered the effects of elliptical orbits and a non-Gaussian velocity distribution.

This grid consisted of single stars on orbits with various ellipticities, within three classes: orbits with periods $P = 10 \text{ yr}$, orbits with $P = 50 \text{ yr}$ and orbits where the maximum star–black hole

Table 2. Orbits considered in Sect. 6.2, along which we evolved stars in Figs. 11–13.

Orbit class	e	r_{\min} (pc)	r_{\max} (pc)
$P = 50 \text{ yr}$	0	9.49×10^{-3}	9.49×10^{-3}
	0.5	4.74×10^{-3}	1.42×10^{-2}
	0.9	9.49×10^{-4}	1.80×10^{-2}
	0.99	9.49×10^{-5}	1.89×10^{-2}
	0.999	9.49×10^{-6}	1.90×10^{-2}
	0.9998	1.90×10^{-6}	1.90×10^{-2}
$P = 10 \text{ yr}$	0	3.24×10^{-3}	3.24×10^{-3}
	0.5	1.62×10^{-3}	4.87×10^{-3}
	0.9	3.25×10^{-4}	6.17×10^{-3}
	0.99	3.25×10^{-5}	6.46×10^{-3}
	0.999	3.25×10^{-6}	6.49×10^{-3}
	0.9995	1.62×10^{-6}	6.49×10^{-3}
$r_{\max} = 0.01 \text{ pc}$	0	1.00×10^{-2}	1.00×10^{-2}
	0.5	3.33×10^{-3}	1.00×10^{-2}
	0.9	5.26×10^{-4}	1.00×10^{-2}
	0.99	5.03×10^{-5}	1.00×10^{-2}
	0.99967	1.65×10^{-6}	1.00×10^{-2}

separation was 0.01 pc. The galactocentric distances at periaapsis and apoapsis (r_{\min} and r_{\max} respectively) of each of the orbits we considered for this grid are given in Table 6.2. The maximum eccentricity in each class was chosen so as to ensure that stars did not come within five Schwarzschild radii of the centre of the black hole, ensuring that relativistic corrections to the orbit were not critical.

The early evolution of one of the stars from the grid is shown in the left panel of Fig. 11. The initial flat sections of curves are where the star was held at a constant galactocentric radius for the first 3 timesteps to allow the model to properly relax. Capture and annihilation occur in punctuated stages, clearly correlated with the orbital period. Strikingly, the times of greatest capture are in fact when the star is *farthest* from the centre of the Galaxy, at apoapsis. This is because it has had a chance to slow down relative to the DM halo, and achieve a significant capture rate for a time before plummeting back down towards the black hole. By the time it reaches periaapsis, the star is moving so quickly that capture is essentially zero, regardless of how high the dark matter density is.

Because following the dark evolution of a star on such an orbit is extremely time-consuming, we evolved the models in this grid for just 5 full orbits each, then calculated the average capture rates achieved over this time. We explicitly assume that given identical initial mean capture rates, the long-term evolution of a star on a short-period elliptical orbit would be the same as the evolution of one which evolves on a circular orbit. That is, we assert that because of the one-to-one mapping between capture rate, WIMP luminosity and evolutionary effects discussed in Sect. 3, the evolution of stars on elliptical orbits in the Galactic centre can be predicted by assigning them an equivalent RSC star from the grid of models we presented earlier. Recall now our assumption in Sect. 2.2 that WIMPs instantaneously thermalise with the stellar material. This is almost certainly not a good approximation on the timescale of just 5 orbits. We therefore probably overestimate annihilation rates and how closely they track capture during such stars' early years, since annihilation takes longer to catch-up with capture when instantaneous thermalisation is not assumed. As our primary goal is to predict the long-term evolution on the basis of the initial capture rate, we don't expect this approximation to have a large impact here. We plan to directly test all these assumptions in later papers, using sin-

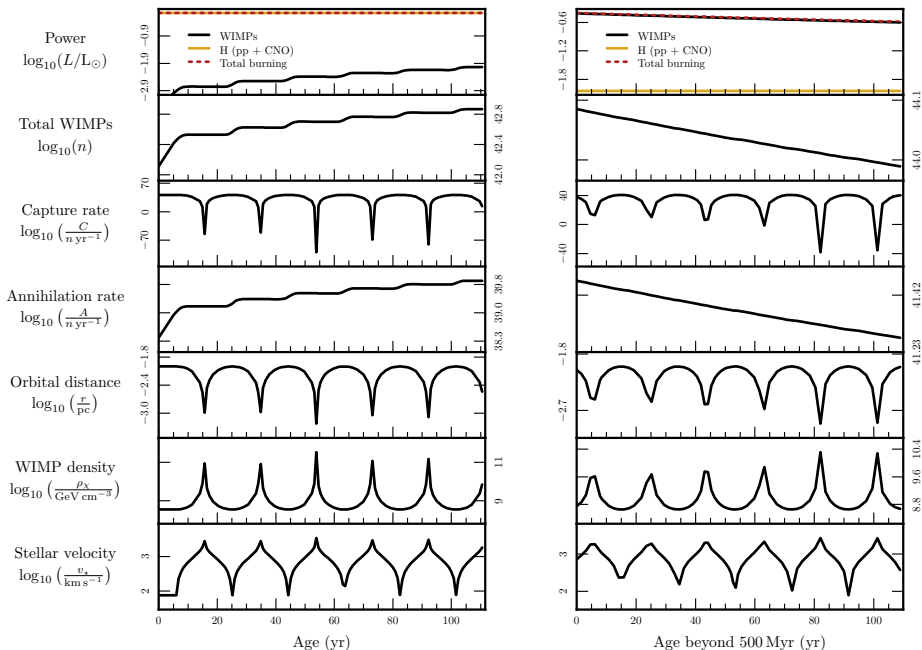


Figure 11. Evolution of a $1 M_{\odot}$, $Z = 0.02$ star on a highly elliptical orbit close to the central black hole, followed for 5 orbits in the beginning of its lifetime (left) and at an age of half a billion years (right). The orbit is that listed in the final line of Table 6.2. Dark matter velocities follow an isothermal distribution with $\bar{v} = 270 \text{ km s}^{-1}$, truncated at the local escape velocity, and densities follow the AC+spike profile. WIMP capture occurs exclusively around apoapsis despite this being the point at which the ambient WIMP density is lowest, thanks to the stars very low orbital velocity. Early in the evolution, before capture and annihilation have equilibrated and the WIMP population has stabilised, the total population, annihilation rate and resultant WIMP luminosity undergo punctuated increases each time the star goes through a period of capture. In the evolved star on the right, the equilibrium population of WIMPs provides a buffer against the transient nature of capture, and the evolution is essentially smooth. Because explicitly following the evolution on an elliptical orbit is highly time-consuming, between these two plots the star was allowed to evolve on an artificial circular orbit with the same initial mean capture rate as exhibited in the left panel. Because of the finite temporal resolution, some of the peaks at periapsis are not properly resolved; because capture here is effectively zero, this has no effect upon the evolution.

gle simulations with very long runtimes and explicitly simulating the thermalisation process.

Under these assumptions, we evolved the star of Fig. 11 for a further half a billion years with a constant equivalent RSC density of $3 \times 10^9 \text{ GeV cm}^{-3}$, to let it fully adjust to the effects of its captured WIMPs. We then put it back on the same elliptical orbit, where it was allowed to evolve for a further 5 orbits (right panel of Fig. 11). As an evolved dark star, it continues to capture in the same punctuated manner as during its early years. Now that the star has built up an equilibrium population of WIMPs though, its total population and annihilation rate are essentially immune to the transient nature of capture. The small decrease in the total population and annihilation rate over the 100 yr shown here is just due to a slight mismatch between the chosen equivalent RSC density and the actual mean capture rate on the elliptical orbit.

In an attempt to prevent very rapid changes in the capture rate, we limited timesteps to those which would prevent the ratio $\frac{\rho_{\text{WIMP}}}{v_{\text{WIMP}}}$ shifting by more than 30 per cent in a single step. Because the evolution code has trouble with convergence when timesteps are reduced too far, we also had to impose a *lower* limit to timesteps of 0.5–1.7 yr in order to prevent the above criterion breaking convergence as stars passed through periapsis. Luckily, periapsis turns

out to be the least important part of the orbit for the calculation of the mean capture rate and the actual evolution, so the only consequence of this is aesthetic: some of the peaks and troughs in Fig. 11 are not fully resolved.

Fig. 12 shows the mean capture rates achieved by all stars in this grid of models, assuming a truncated isothermal velocity distribution. Thanks to the additional capture window opened at apoapsis, stars following elliptical orbits have their capture rates boosted by up to 20 orders of magnitude beyond what they would have achieved on the equivalent circular orbit. The more elliptical the orbit, the slower the star is moving at apoapsis, so the more dark matter it is able to capture. Whilst stars in the two orbital classes with constant periods reach apoapsis further from the black hole with increasing orbital ellipticity, the reduction in capture rate caused by the resulting decrease in dark matter density at apoapsis is completely outweighed by the increase in capture brought on by the reduced star-WIMP relative velocities. The ellipticity boost is most marked for shorter orbital periods, as stars on shorter-period orbits have the most to lose by following circular orbits (due to their very high circular velocities), yet the most to gain by following elliptical orbits (because they sample regions of higher dark matter density).

Referring to Fig. 2, the stars of Fig. 12 evolved in the

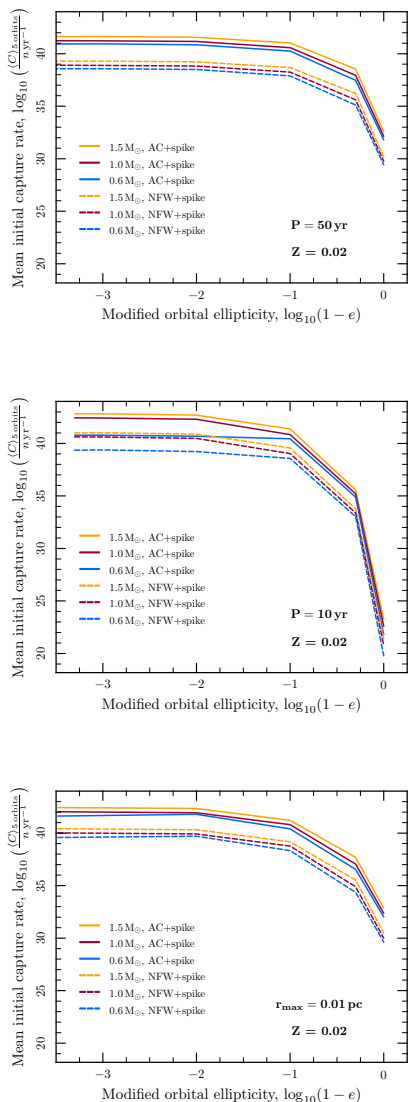


Figure 12. Mean capture rates achieved by stars on elliptical orbits with periods of 50 years (top) and 10 years (middle), as well as orbits where the star-black hole separation is 0.01 pc at apoapsis (bottom). Dark matter velocities follow an isothermal distribution with dispersion $\bar{v} = 270 \text{ km s}^{-1}$, truncated at the local Galactic escape velocity. Capture rates are boosted by up to 20 orders of magnitude when stars follow elliptical rather than circular orbits.

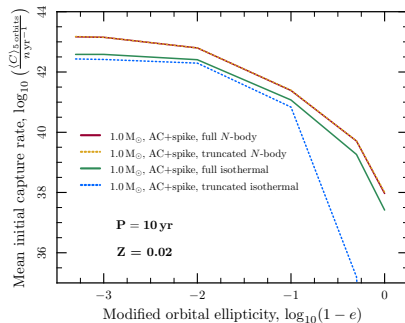


Figure 13. Mean capture rates achieved by a 1 M_{\odot} star on elliptical orbits through dark matter halos with different velocity distributions. All halos follow the AC+spike density profile. The N -body velocity distribution results in globally higher capture rates than the standard isothermal distribution. Truncating the velocity distribution at the local Galactic escape velocity decreases capture rates from the isothermal distribution, but has no impact upon capture from the N -body distribution.

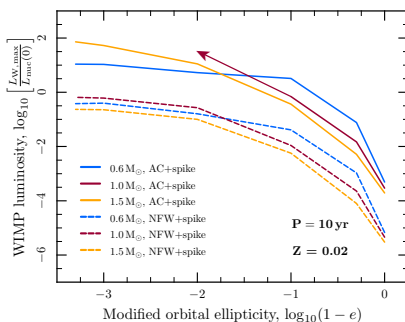


Figure 14. WIMP luminosities achieved by stars on orbits with 10-year periods around the Galactic centre. Annihilation can provide up to 100 times the power of nuclear fusion in stars on realistic orbits. If the Galactic halo has undergone adiabatic contraction (AC+spike), annihilation rivals nuclear fusion in stars on any orbit with an eccentricity greater than about $e = 0.9$, for all masses less than or equal to 1.5 M_{\odot} . If not (NFW+spike), stars of a solar mass or less approach break-even between fusion and annihilation energy on orbits with $e \gtrsim 0.99$. These curves have been obtained by applying the boosts seen in Fig. 13 to the capture rates of Fig. 12, and then interpolating within the results shown in Fig. 2 to obtain the resulting WIMP-to-nuclear burning ratios. The arrow indicates that the 1 M_{\odot} , AC+spike curve is expected to continue in this direction, but there is no reliable way to convert capture rates to WIMP luminosities in this region because the capture rates and implied WIMP luminosities are beyond the range of convergence of the benchmark models in Sect. 3. In the case of the least interesting orbits (circular orbits in an NFW+spike density profile), capture rates and WIMP luminosities are in fact below the limits of the grid in Sect. 3, so WIMP luminosities are extrapolations based on the assumption that the scaling with ambient WIMP density is the same at $e = 0$ as at $e = 0.5$.

AC+spike density profile can all achieve break-even between WIMP and nuclear luminosity if their orbits have a period of 10 yr and $e \gtrsim 0.99$. A $0.6 M_\odot$ star can achieve this goal even on a 50-year orbit, with ellipticity as low as $e = 0.9$, whilst a $1 M_\odot$ star can do the same for $e \gtrsim 0.99$. With the NFW+spike density profile and a truncated isothermal halo, stars will generally never achieve the same level of energy output from WIMP annihilation as nuclear burning (at least not if $m_\chi \geq 100$ GeV; cf. Fig. 3).

In Fig. 13, we show the impacts upon capture of going beyond the isothermal halo approximation. Here we illustrate the capture rates achieved by a $1 M_\odot$ star on 10-year orbits through both truncated and non-truncated versions of the N -body velocity distribution, and compare with the corresponding capture rates from isothermal distributions. Regardless of the orbital ellipticity, capture is at least a factor of 3 (i.e. half an order of magnitude) higher from the standard version of the N -body distribution than from the standard isothermal distribution. This difference blows significantly when the distributions are truncated at the local escape velocities and renormalised; whereas the truncation reduces capture from the isothermal distribution (particularly at low ellipticities), it leaves capture from the N -body halo entirely unaffected.

The truncated N -body distribution boosts capture rates at high ellipticities by a factor of 3–5 over the truncated isothermal distribution, significantly increasing the range of orbits over which we might expect to see dark stars. In Fig. 14 we estimate the long-term behaviour of stars on the 10-year orbits by combining the capture rates seen in Fig. 12, the boosts seen in Fig. 13 and the results from our benchmark simulations in Sec. 3. Here we have made the approximation that boosts do not depend upon the stellar mass or halo density profile; that is, we adjusted the capture rates of all stars by the difference between the truncated N -body and truncated isothermal curves in Fig. 13, depending only upon the orbits which stars followed. We then interpolated within the data of Fig. 2 to obtain WIMP luminosities from the adjusted capture rates, which included interpolating further amongst the curves of Fig. 2 to obtain data for $1.5 M_\odot$ stars.

Fig. 14 shows that the effects of WIMPs can be drastic, with the energy produced by WIMP annihilation outstripping that of nuclear fusion by up to a factor of 100. Indeed, some of the adjusted capture rates imply a WIMP luminosity even greater than that of any star we were able to reliably evolve in the grid of benchmark models (indicated by an arrow pointing in the direction one would expect the curve to continue in). We now see from Fig. 14 that even the NFW+spike density profile can actually produce stars where annihilation comes close to breaking even with nuclear burning ($P \approx 10$ yr, $e \gtrsim 0.99$ and $M_* \lesssim 1 M_\odot$). With the AC+spike profile, the same is true of stars with masses of up to $1.5 M_\odot$, following orbits with eccentricities $e \gtrsim 0.9$. If one were to perform the same conversion on capture rates achieved by stars on other orbits, postulating similar boosts as seen on 10-year orbits and assuming an AC+spike density profile, stars of $M_* \lesssim 1 M_\odot$ would also achieve break-even for $e \gtrsim 0.9$ with orbital periods of up to 50 years.

Finally, we point out that the magnitude of these results depends upon the chosen WIMP mass (Fig. 3). As such, one expects the final WIMP luminosities shown in Fig. 14 to be even further boosted for WIMPs lighter than 100 GeV, but suppressed for higher masses. The dependence of the capture rate and final WIMP-to-nuclear burning ratio upon the WIMP mass becomes weaker for smaller velocity dispersions, at least in an isothermal halo. Whilst we have not explicitly investigated how this picture changes in a halo with a non-Gaussian velocity distribution, we would expect similar behaviour. With velocity dispersions given by Eq. 4.14, we

therefore expect WIMP luminosities in the N -body distribution to have some dependence upon the WIMP mass, though not so pronounced as seen in Fig. 3. This dependence should theoretically allow one to place limits upon the WIMP mass in the event of either a positive or null detection of dark stars at the Galactic centre.

6.3 Binaries and higher-multiplicity stellar systems

Although we have not calculated the WIMP luminosities achievable by systems consisting of more than one star, our results with single stars make it easy to comment on this scenario. If a binary system's internal orbital plane was partially aligned with its gross orbit about the Galactic centre, the motions of its component stars would at various stages counteract the motion of the system about the central black hole. At certain times the component stars would have far smaller velocities relative to the WIMP halo than if they were orbiting as single stars on a similar orbit, resulting in increased capture rates. The systems most effective at achieving this boost would be those with the highest orbital speeds, as these would produce the greatest reduction in the relative velocity between stars and WIMPs. This effect would therefore be strongest in short-period, low-separation, higher-mass binary systems. Since the effects of WIMP annihilation are most marked in low-mass stars though, the optimal configuration would be a close binary with a maximal mass difference. A system consisting of $\sim 1 M_\odot$ and $\sim 4 M_\odot$ partners orbiting with a period of 5 hr would have an orbital velocity of ~ 700 km s $^{-1}$, enough to have a profound impact upon capture rates shown in Fig. 11, for example. In favourable cases, binary systems could mimic the effects of highly eccentric orbits upon capture rates, allowing stars on almost circular orbits to achieve significant capture rates, and further boosting capture rates from elliptical orbits. Similar effects could be expected in systems consisting of three or more stars, though their stability on orbits close to the Galactic Centre might be doubtful; indeed, even binaries might not survive for long near the central black hole (Perets 2009).

6.4 Observational constraints and prospects

Single stars on circular orbits capturing dark matter from an isothermal halo cannot achieve WIMP luminosities any greater than 1 per cent of their nuclear luminosities. Even if the WIMP velocities were not isothermal, but instead followed the N -body distribution, Fig. 13 indicates that capture would not be boosted by more than an additional factor of 5. From the results of Sect. 3, we know that $\log_{10}[L_{W,\max}/L_{\text{nuc}}(0)] \lesssim -1$ would not result in any significant change to a star's structure or evolution. Whilst this level of WIMP luminosity would create small convective cores in some stars, potentially interesting for asteroseismology of Galactic centre populations some time in the distant future, we find it very unlikely that main-sequence dark stars would exist outside binaries on any circular orbits in the Milky Way. Stars following elliptical orbits are not only far more likely to be dark stars, but are also considerably more common at the Galactic centre.

The central 30 pc of the Milky Way not only contains a $3 - 4 \times 10^6 M_\odot$ black hole, but also two of the densest star clusters in the Galaxy, including the Arches cluster. In the late 1980s, an unusual star with broad H I and He I emission lines was detected less than 0.5 pc from the central compact radio source, Sgr A*, which is thought to be associated with the central black hole (Forrest et al. 1986; Allen et al. 1990). Because the centre of the Galaxy

is shrouded with dust, observations can only take place in the infrared, so the normal spectral information used to identify stars is not available. Over the next few years, an increasing number of such stars were discovered, appearing to be helium-rich blue supergiants and Wolf-Rayet stars, with masses of up to $100 M_{\odot}$ (Krabbe et al. 1991, 1995). The presence of such young stars close to the Galactic centre was difficult to understand, as it was unclear how a gas cloud could condense to form a star in a region so close to the central black hole due to the extreme tidal forces there. This problem came to be known as the ‘Paradox of Youth’ (Sanders 1992; Morris 1993). Recent work has increased the number of known OB stars in the central parsec of the Galaxy to close to 100, excluding the central square arcsecond (Paumard et al. 2006). These young stars appear to form two counter rotating discs, suggesting that they are possibly associated with different star formation events in dense accreting matter (Levin & Beloborodov 2003; Genzel et al. 2003; Paumard et al. 2006).

The very fact that we know the mass of the central black hole itself is due to the discovery and subsequent tracking of stars even closer than the young He I stars: a cluster of stars was discovered in the 1990s within the central square arcsecond, and dubbed the ‘SgrA* stellar cluster’ (Genzel et al. 1997). The stars in this cluster (referred to as S stars, E stars or SO stars apparently depending upon the native language of the lead researcher) move extremely close to the central black hole. The star which has been observed moving closest to the central black hole is called S14, E2 or SO-16, and was seen within 45 AU, or only 600 Schwarzschild radii, of the black hole (Ghez et al. 2005). The kinematics of the SgrA* cluster is such that stars are on randomly oriented, highly elliptical orbits, rather than circular ones confined to a single disc.

Near-infrared observations of the S stars made with the Keck telescope and VLT revealed that their atmospheres did not contain CO (Genzel et al. 1997), setting a lower bound on their surface temperatures. Further work led to the conclusion that the S stars are in fact simply $10\text{--}15 M_{\odot}$ main-sequence stars (Ghez et al. 2005; Martins et al. 2008). The short main-sequence lifetimes of such high-mass stars ($\sim 10^7$ yr) presents a further Paradox of Youth at the Galactic centre, not explainable by star formation in an accretion disc due to the random orientation of the S-star orbits.

Many have tried to explain the presence of the S stars. One idea is that they formed far from the Galactic centre (perhaps in the Arches cluster) and subsequently migrated inwards (Gerhard 2001). Another is that they formed in situ during an earlier era when the density was much larger than it is today (Levin & Beloborodov 2003). They could also be old stars which look young because they have collided with other stars (Genzel et al. 2003), a scenario reminiscent of the blue straggler phenomenon in globular clusters. A rather convincing explanation is that they were originally members of binaries belonging to one of the outer discs, which were perturbed either by interactions between the discs (Löckmann et al. 2008) or by interactions with other massive objects (Perets et al. 2007). The three-body interaction then caused one star from each binary to become tightly bound to the black hole, and the other to be ejected as a hypervelocity star.

What implications might dark stars have for this picture? We have already seen that stars burning dark matter have significantly increased main-sequence lifetimes. One might then imagine a scenario whereby stars are created elsewhere and migrate to the Galactic centre, where the presence of dark matter extends their lifetimes. This might provide an alternative explanation for either the S stars or the outer stellar discs of OB-type stars. However, such an explanation is incomplete. The problem with models where stars are

created elsewhere and migrate to the centre of the Galaxy is that the inspiralling timescale is typically very large compared to their main sequence lifetime. One would therefore expect that stars should have left the main sequence by the time they arrive at the central region. Furthermore, we have shown that more massive stars require higher dark matter densities than low mass ones to experience any structural changes; it is highly unlikely that a star as massive as $10 M_{\odot}$ could capture enough WIMPs to significantly alter its main-sequence evolution on any realistic orbit near the Galactic centre. One possibility is that such a star could reach the end of its main sequence lifetime during the migration, arrive at the Galactic centre and then begin capturing large numbers of WIMPs. If burning WIMPs during its post-main-sequence evolution made such a star begin to resemble an OB or Wolf-Rayet star, or revert to looking outwardly like a main sequence star, this could provide an additional explanation for the dense stellar discs or the S stars, respectively. We will consider the prospect of post-main-sequence dark stars in a later paper.

Whilst such an explanation for the Paradox of Youth must be considered improbable, it is interesting to remember that the S stars are indeed on more elliptical orbits than other stars at the Galactic centre, which would be consistent with them having accreted far more dark matter than others (Zhu et al. 2008).

More promising is the possibility that future observations of the Galactic centre will reveal fainter, lower-mass stars (although there is some suggestion that the initial mass function within the central parsec could be top heavy; Maness et al. 2007). If the binary disruption scenario is indeed the source of the S stars, one would expect that the bursts of star formation which created them in the outer discs would also have produced lower-mass stars. Some such stars would form in binaries, and could conceivably follow the same path to the Galactic centre as the S stars. This would produce a population of low-mass stars in the central square arcsecond with randomly-oriented, highly elliptical orbits similar to those of the S stars. Likewise, most of the other explanations for the origin of the S stars could also involve formation and subsequent migration/disruption of a lower-mass population alongside the S stars, also leading to a population of potential low-mass dark stars.

Finally, the prospect of dark stars forming in binary systems opens a very promising channel through which they might be observed. Stars within a binary can be compared photometrically if they have similar brightness, allowing their masses and evolutionary states to be determined. In some cases, binaries might consist of a low-mass star which is significantly affected by WIMP capture and annihilation, and a high-mass partner which is too massive to show any effects whatsoever. The most striking example of this would be a binary consisting of a low-mass star ‘frozen’ by WIMP burning (resembling a protostar) and a higher-mass companion which had evolved all the way into a white dwarf, though such a system would be difficult to observe at the Galactic centre because of the faintness of the white dwarf.

7 CONCLUSIONS

When the energy injected due to the annihilation of WIMPs approaches that of nuclear burning, the capture of weakly interacting dark matter will significantly alter the structure and evolution of stars on the main sequence. Stars on circular orbits in the Milky Way are extremely unlikely to achieve sufficient capture rates for this to occur unless they are present in binaries. Stars orbiting close to the Galactic centre on elliptical orbits have their capture rates

strongly boosted in comparison to those on circular orbits. The velocity distribution of dark matter near the Galactic centre may be highly non-Gaussian, further boosting capture rates on elliptical orbits by nearly an order of magnitude. Assuming that the nuclear-scattering cross-sections are equal to their current experimental limits, that dark matter forms a spike around the supermassive black hole at the Galactic centre, and that the dark matter distribution on larger scales has undergone adiabatic contraction, stars of $1 M_{\odot}$ and below will reach break-even between annihilation and fusion energy on orbits with periods of up to 50 years and eccentricities as low as 0.9. $1.5 M_{\odot}$ stars can achieve the same goal with comparable orbital eccentricities if they orbit the central black hole in 10 years or less. Without adiabatic contraction of the galactic halo, orbits at least as short as this and eccentricities of about 0.99 are required for stars of a solar mass and below to become dark stars.

These requirements are likely to be significantly relaxed for stars in binary systems. A binary consisting of a low-mass protostar and a highly-evolved massive star would make the impact of WIMP annihilation very hard to deny.

The observation of one or more stars at the Galactic centre exhibiting the properties we have described would strongly suggest the influence of WIMP dark matter. Conversely, since we have assumed scattering cross-sections compatible with the current experimental limits, the observation of even a single completely normal star or binary on the orbits we have discussed would allow one to place stringent limits on the properties of dark matter and its density at the Galactic centre. If one instead assumed a particular halo model for dark matter at the Galactic centre, the dependence of the capture rate upon the WIMP mass and spin-dependent scattering cross-section would allow one to derive limits on these parameters which are highly competitive with current direct-detection sensitivities. If a star were seen on an orbit where we expect effects even without adiabatic contraction of the Galactic halo on large scales (i.e. $M \lesssim 1 M_{\odot}$, $P \lesssim 10$ yr, $e \gtrsim 0.99$), then the derived limits could be made mostly independent of the halo model.

ACKNOWLEDGMENTS

We thank the referee David Dearborn for strengthening the conclusions of this paper by pointing out the capacity of binaries to further boost capture rates. We are very grateful to Jürg Diemand for making the raw results of the Via Lactea simulation available, and Ross Church, Melvyn Davies, Fabio Iocco and Paolo Gondolo for helpful discussions on this work. P.S. thanks the European Network of Theoretical Astroparticle Physics ILIAS/N6 under contract number RII3-CT-2004-506222 for enabling a visit to CERN, where some of this work was performed, and J.E. thanks the Swedish Research Council (VR) for funding support. This work has made use of NASA's Astrophysics Data System and SPIRES.

REFERENCES

Ahmed Z., et al., 2009, *Phys. Rev. Lett.*, 102, 011301
 Allen D. A., Hyland A. R., Hillier D. J., 1990, *MNRAS*, 244, 706
 Anders E., Grevesse N., 1989, *Geochim. Cosmochim. Acta*, 53, 197
 Angle J., et al., 2008, *Phys. Rev. Lett.*, 100, 021303

Asplund M., Grevesse N., Sauval A. J., 2005, in Barnes III T. G., Bash F. N., eds, *ASP Conf. Ser. 336 Astron. Soc. Pac.*, San Francisco, p. 25
 Audi G., Wapstra A. H., Thibault C., 2003, *Nucl. Phys. A*, 729, 337
 Behnke E., et al., 2008, *Science*, 319, 933
 Bergström L., 2000, *Rep. Prog. Phys.*, 63, 793
 Bergström L., Fairbairn M., Pieri L., 2006, *Phys. Rev. D*, 74, 123515
 Bertone G., Fairbairn M., 2008, *Phys. Rev. D*, 77, 043515
 Bertone G., Hooper D., Silk J., 2005, *Phys. Rep.*, 405, 279
 Bertone G., Merritt D., 2005, *Phys. Rev. D*, 72, 103502
 Blennow M., Edsjö J., Ohlsson T., 2008, *JCAP*, 1, 21
 Blumenthal G. R., Faber S. M., Flores R., Primack J. R., 1986, *ApJ*, 301, 27
 Bottino A., Fiorentini G., Fornengo N., Ricci B., Scopel S., Villante F. L., 2002, *Phys. Rev. D*, 66, 053005
 Bouquet A., Kaplan J., Martin F., 1989, *A&A*, 222, 103
 Bouquet A., Salati P., 1989a, *ApJ*, 346, 284
 Bouquet A., Salati P., 1989b, *A&A*, 217, 270
 Christensen-Dalsgaard J., 1992, *ApJ*, 385, 354
 Clowe D., Bradač M., Gonzalez A. H., Markevitch M., Randall S. W., Jones C., Zaritsky D., 2006, *ApJ*, 648, L109
 Dearborn D., Raffelt G., Salati P., Silk J., Bouquet A., 1990a, *Nature*, 343, 347
 Dearborn D., Raffelt G., Salati P., Silk J., Bouquet A., 1990b, *ApJ*, 354, 568
 Dehnen W., Binney J., 1998, *MNRAS*, 294, 429
 Deluca E. E., Griest K., Rosner R., Wang J., 1989, *FERMILAB-Pub-89/49-A*, NASA STI/Recon Technical Report N, 89, 20880
 Desai S., et al., 2004, *Phys. Rev. D*, 70, 083523
 Diemand J., Kuhlen M., Madau P., 2007, *ApJ*, 657, 262
 Eggleton P. P., 1971, *MNRAS*, 151, 351
 Eggleton P. P., 1972, *MNRAS*, 156, 361
 Fairbairn M., Schwetz T., 2009, *JCAP*, 1, 37
 Fairbairn M., Scott P., Edsjö J., 2008, *Phys. Rev. D*, 77, 047301
 Faulkner J., Gilliland R. L., 1985, *ApJ*, 299, 994
 Faulkner J., Swenson F. J., 1988, *ApJ*, 329, L47
 Faulkner J., Swenson F. J., 1993, *ApJ*, 411, 200
 Forrest W. J., Pipher J. L., Stein W. A., 1986, *ApJ*, 301, L49
 Freese K., Bodenheimer P., Spolyar D., Gondolo P., 2008, *ApJ*, 685, L101
 Freese K., Gondolo P., Sellwood J. A., Spolyar D., 2009, *ApJ*, 693, 1563
 Freese K., Spolyar D., Aguirre A., 2008, *JCAP*, 11, 14
 Genzel R., Eckart A., Ott T., Eisenhauer F., 1997, *MNRAS*, 291, 219
 Genzel R., et al., 2003, *ApJ*, 594, 812
 Gerhard O., 2001, *ApJ*, 546, L39
 Ghez A. M., Salim S., Hornstein S. D., Tanner A., Lu J. R., Morris M., Becklin E. E., Duchêne G., 2005, *ApJ*, 620, 744
 Gilliland R. L., Faulkner J., Press W. H., Spergel D. N., 1986, *ApJ*, 306, 703
 Giraud-Heraud Y., Kaplan J., de Volnay F. M., Tao C., Turck-Chieze S., 1990, *Sol. Phys.*, 128, 21
 Gnedin O. Y., Kravtsov A. V., Klypin A. A., Nagai D., 2004, *ApJ*, 616, 16
 Gondolo P., Edsjö J., Ullio P., Bergström L., Schelke M., Baltz E. A., 2004, *JCAP*, 7, 8
 Gondolo P., Silk J., 1999, *Phys. Rev. Lett.*, 83, 1719
 Gould A., 1987a, *ApJ*, 321, 571
 Gould A., 1987b, *ApJ*, 321, 560

- Gould A., Raffelt G., 1990a, *ApJ*, 352, 669
- Gould A., Raffelt G., 1990b, *ApJ*, 352, 654
- Griest K., Seckel D., 1987, *Nucl. Phys. B*, 283, 681
- Gustafsson M., Fairbairn M., Sommer-Larsen J., 2006, *Phys. Rev. D*, 74, 123522
- Hansen S. H., Moore B., Zemp M., Stadel J., 2006, *JCAP*, 0601, 014
- Heber V. S., Baur H., Wieler R., 2003, *ApJ*, 597, 602
- Iocco F., 2008, *ApJ*, 677, L1
- Iocco F., Bressan A., Ripamonti E., Schneider R., Ferrara A., Marigo P., 2008, *MNRAS*, 390, 1655
- Jungman G., Kamionkowski M., Griest K., 1996, *Phys. Rep.*, 267, 195
- Kent S. M., Dame T. M., Fazio G., 1991, *ApJ*, 378, 131
- Klypin A., Zhao H., Somerville R. S., 2002, *ApJ*, 573, 597
- Komatsu E., et al., 2009, *ApJS*, 180, 330
- Krabbe A., Genzel R., Drapatz S., Rotaciuc V., 1991, *ApJ*, 382, L19
- Krabbe A., Genzel R., Eckart A., Najarro F., Lutz D., Cameron M., Kroker H., Tacconi-Garman L. E., Thatte N., Weitzel L., Drapatz S., Geballe T., Sternberg A., Kudritzki R., 1995, *ApJ*, 447, L95
- Levin Y., Beloborodov A. M., 2003, *ApJ*, 590, L33
- Löckmann U., Baumgardt H., Kroupa P., 2008, *ApJ*, 683, L151
- Maness H., et al., 2007, *ApJ*, 669, 1024
- Martins F., Gillessen S., Eisenhauer F., Genzel R., Ott T., Trippe S., 2008, *ApJ*, 672, L119
- Merritt D., Graham A. W., Moore B., Diemand J., Terzić B., 2006, *AJ*, 132, 2685
- Moore B., Quinn T., Governato F., Stadel J., Lake G., 1999, *MNRAS*, 310, 1147
- Morris M., 1993, *ApJ*, 408, 496
- Moskalenko I. V., Wai L. L., 2007, *ApJ*, 659, L29
- Natarajan A., Tan J. C., O'Shea B. W., 2009, *ApJ*, 692, 574
- Navarro J. F., et al., 2004, *MNRAS*, 349, 1039
- Navarro J. F., Frenk C. S., White S. D. M., 1996, *ApJ*, 462, 563
- Paumard T., et al., 2006, *J. Phys. Conf. Ser.*, 54, 199
- Paxton B., 2004, *PASP*, 116, 699
- Perets H. B., 2009, *ApJ*, 690, 795
- Perets H. B., Hopman C., Alexander T., 2007, *ApJ*, 656, 709
- Piessens R., de Doncker-Kapenga E., Ueberhuber C. W., 1983, *Quadpack. A subroutine package for automatic integration. Springer Series in Computational Mathematics*, Springer, Berlin
- Pols O. R., Tout C. A., Eggleton P. P., Han Z., 1995, *MNRAS*, 274, 964
- Press W. H., Spergel D. N., 1985, *ApJ*, 296, 679
- Renka R. J., 1993, *ACM Trans. Math. Softw.*, 19, 81
- Renzini A., 1987, *A&A*, 171, 121
- Salati P., 1990, *ApJ*, 348, 738
- Salati P., Silk J., 1989, *ApJ*, 338, 24
- Sanders R. H., 1992, *Nature*, 359, 131
- Scott P., Asplund M., Grevesse N., Sauval A. J., 2009, *ApJ*, 691, L119
- Scott P., Edsjö J., Fairbairn M., 2008, in *Klapdor-Kleingrothaus H. K., Lewis G. F., eds, Dark Matter in Astroparticle and Particle Physics: Dark 2007*. World Scientific, Singapore, pp 387–392, arXiv:0711.0991
- Scott P. C., Asplund M., Grevesse N., Sauval A. J., 2006, *A&A*, 456, 675
- Spergel D. N., Faulkner J., 1988, *ApJ*, 331, L21
- Spergel D. N., Press W. H., 1985, *ApJ*, 294, 663
- Spolyar D., Freese K., Gondolo P., 2008, *Phys. Rev. Lett.*, 100, 051101
- Steigman G., Quintana H., Sarazin C. L., Faulkner J., 1978, *AJ*, 83, 1050
- Taoso M., Bertone G., Meynet G., Ekström S., 2008, *Phys. Rev. D*, 78, 123510
- Tatsumoto M., Unruh D. M., Desborough G. A., 1976, *Geochim. Cosmochim. Acta*, 40, 617
- Testa F. J., Renka R. J., 1999, *ACM Trans. Math. Softw.*, 25, 95
- Wapstra A. H., Audi G., Thibault C., 2003, *Nucl. Phys. A*, 729, 129
- Yoon S.-C., Iocco F., Akiyama S., 2008, *ApJ*, 688, L1
- Zel'dovich Y. B., Klypin A. A., Khlopov M. Y., Chechetkin V. M., 1980, *Soviet J. Nuc. Phys.*, 31, 664
- Zhao H. S., 1996, *MNRAS*, 283, 149
- Zhu Q., Kudritzki R. P., Figer D. F., Najarro F., Merritt D., 2008, *ApJ*, 681, 1254

This paper has been typeset from a \LaTeX file prepared by the author.

Paper III

Pat Scott & Sofia Sivertsson

Gamma-rays from ultracompact primordial dark matter minihalos

Phys. Rev. Lett. **103**, 211301 (2009) arXiv:0908.4082.

Gamma Rays from Ultracompact Primordial Dark Matter Minihalos

Pat Scott^{1,2} and Sofia Sivertsson^{1,3}

¹*Oskar Klein Centre for Cosmoparticle Physics, AlbaNova, SE-10691 Stockholm, Sweden*

²*Department of Physics, Stockholm University, AlbaNova, SE-10691 Stockholm, Sweden*

³*Department of Theoretical Physics, Royal Institute of Technology (KTH), AlbaNova, SE-10691 Stockholm, Sweden*

(Received 2 September 2009; published 20 November 2009)

Ultracompact minihalos have been proposed as a new class of dark matter structure. They would be produced by phase transitions in the early Universe or features in the inflaton potential, and constitute nonbaryonic massive compact halo objects today. We examine the prospects of detecting these minihalos in gamma rays if dark matter can self-annihilate. We compute present-day fluxes from minihalos produced in the e^+e^- annihilation epoch and the QCD and electroweak phase transitions. Even at a distance of 4 kpc, minihalos from the e^+e^- epoch would be eminently detectable today by the Fermi satellite or air Čerenkov telescopes, or even in archival *EGRET* data. Within 2 kpc, they would appear as extended sources to Fermi. At 4 kpc, minihalos from the QCD transition have similar predicted fluxes to dwarf spheroidal galaxies, so might also be detectable by present or upcoming experiments.

DOI: 10.1103/PhysRevLett.103.211301

PACS numbers: 95.35.+d, 98.70.Rz, 98.80.Cq

The identity of dark matter remains one of the key outstanding problems in physics. Weakly interacting massive particles (WIMPs) provide a compelling solution [1] because their weak-scale masses and cross sections make for a natural explanation of the observed abundance of dark matter. As most proposed WIMPs are their own antiparticles, high WIMP densities would also lead to high rates of self-annihilation. Annihilation products might then provide indirect evidence of the nature of dark matter. Gamma rays are particularly attractive in this respect, as they do not suffer the same problems of deflection and attenuation as massive, charged species.

It was proposed [2] that dark matter could be massive compact halo objects (MACHOs) of condensed baryons, e.g., brown dwarfs or faint stars. These are ruled out as the dominant component of dark matter by the cosmic microwave background (CMB; [3]), Big Bang nucleosynthesis [4], and microlensing searches [5]. Primordial black holes (PBHs) are an alternative, disfavored by their energetic evaporation, gravitational influence [6], and the large primordial density perturbations required for their production ($\delta \gtrsim 30\%$). For comparison, the initial density perturbations from inflation were $\delta \sim 10^{-5}$.

Ricotti and Gould [7] proposed a nonbaryonic MACHO that avoids these constraints and presents a promising new target for microlensing searches. Formation proceeds similarly to PBHs, whereby small-scale density perturbations in the early Universe collapse to a compact body. A small-scale power spectrum that is the same as observed on large scales [3] provides insufficient power for this to occur. Perturbations could however be enhanced by features in the inflaton potential, or phase transitions in the early Universe [8]. If a perturbation is small, matter will not be sufficiently compressed to form a black hole, leaving only a compact cloud of gas and dark matter. This mechanism requires density contrasts of just $\delta \gtrsim 10^{-3}$ to proceed so is

far more viable than PBH formation. If such ultracompact minihalos (UCMHs) exist, they will be ultradense and excellent targets for indirect detection of WIMPs [9].

Here, we investigate gamma-ray signals expected from UCMHs containing WIMP dark matter. We consider UCMHs produced in three phase transitions in the early Universe: electroweak symmetry breaking ($T_{EW} \approx 200$ GeV), QCD confinement ($T_{QCD} \approx 200$ MeV), and e^+e^- annihilation ($T_{ee} \approx 0.51$ MeV). We first discuss the masses, density profiles, and primordial abundance of UCMHs, then WIMP models and annihilation channels. We present predicted fluxes and discuss prospects for detection with satellite missions and Air Čerenkov telescopes (ACTs). In an appendix, we also give explicit predictions from a supersymmetric framework with a neutralino WIMP [10].

Following matter-radiation equality, ultracompact minihalos accrete matter by radial infall [7] as

$$M_h(z) = \delta m \left(\frac{1 + z_{eq}}{1 + z} \right), \quad (1)$$

where $M_h(z)$ is the total mass of the UCMH at redshift z , and z_{eq} is the redshift of matter-radiation equality. We assume that UCMHs at $z = 0$ grew only until $z = 10$, because by this time structure formation would have progressed sufficiently far to prevent further accretion [11]. The initial mass of the overdensity is $\delta m \equiv \delta \times M_H(z_X)$, where $M_H(z_X)$ is the horizon mass at the time of phase transition X , and in this case, $\delta = 10^{-3}$. We take $z_{eq} + 1 = 2.32 \times 10^4 \Omega_m h^2$ [12], giving $z_{eq} = 3160$ with $\Omega_m h^2 = 0.136$ from the current best fit to the CMB, large-scale structure and Type Ia supernovae [3].

During radiation domination, the horizon mass is [13]

$$M_H(z) \approx M_H(z_{eq}) \left(\frac{1 + z_{eq}}{1 + z} \right)^2. \quad (2)$$

As $T(z) \propto g_{*S}(z)^{-1/3} R(z)^{-1} \propto g_{*S}(z)^{-(1/3)}(1+z)$ [12], with R the scale factor of the Universe and g_{*S} the number of effective entropic degrees of freedom, this becomes

$$M_H(T) \approx M_H(T_{\text{eq}}) \left(\frac{g_{*S}(T_{\text{eq}})^{1/3} T_{\text{eq}}}{g_{*S}(T)^{1/3} T} \right)^2. \quad (3)$$

The horizon mass, temperature, and effective entropic degrees of freedom at equality can be estimated as $M_H(T_{\text{eq}}) = 6.5 \times 10^{15} (\Omega_m h^2)^{-2} = 3.5 \times 10^{17} M_\odot$ [6], $T_{\text{eq}} = 5.5 \Omega_m h^2 = 0.75$ eV and $g_{*S}(z_{\text{eq}}) = 3.91$ [12]. At the phase transitions, $g_{*S}(T_{\text{EW}}) = 107$, $g_{*S}(T_{\text{QCD}}) \approx 55$ and $g_{*S}(T_{\text{ee}}) = 10.8$ [12], giving $\delta m_{\{\text{EW}, \text{QCD}, \text{ee}\}} = \{5.4 \times 10^{-10}, 8.4 \times 10^{-4}, 3.9 \times 10^{23}\} M_\odot$.

The dark matter density profile in an ultracompact minihalo is [7]

$$\rho_\chi(r, z) = \frac{3f_\chi M_h(z)}{16\pi R_h(z)^{3/4} r^{9/4}}, \quad (4)$$

in the radial infall approximation. Here, the dark matter fraction is $f_\chi = \Omega_{\text{CDM}}/\Omega_m = 0.834$ [3], and

$$\left(\frac{R_h(z)}{\text{pc}} \right) = 0.019 \left(\frac{1000}{z+1} \right) \left(\frac{M_h(z)}{M_\odot} \right)^{1/3} \quad (5)$$

is the maximum extent of the UCMH at redshift z .

The dark matter in an ultracompact minihalo could be further concentrated if baryons collapse and contract the gravitational potential. We calculated the density profile after adiabatic contraction using the method of Blumenthal *et al.* [14]. This assumes that $rM(r)$ is conserved at all r , where $M(r)$ is the mass within radius r , and that orbits of the dissipationless WIMPs do not cross. We assumed that a fraction F of the total halo mass condenses to a constant-density baryonic core of radius r_{core} . We considered $F = 10^{-2}$, 10^{-3} , and $r_{\text{core}}/R_h = 5 \times 10^{-2}$, 10^{-3} . The effect of the contraction is small for the larger core radius, so we show results only for $r_{\text{core}}/R_h = 10^{-3}$. Because the induced contraction at r is given by the increase in the baryonic mass within r , the contraction caused by a constant-density baryonic core is most pronounced around the core's edge. This is in contrast to the contraction of halos around adiabatically formed black holes, where the baryons collapse to a central point, steepening the dark matter density profile at all radii. The dark matter density in the very center of a halo does not rise significantly in the contraction unless the new baryonic distribution also has a pronounced spike at the very center.

UCMHs also erode over time as dark matter annihilates away; being ultracompact and ancient, this effect is highly significant. A simple way to estimate the maximum density ρ_{max} at time t in a halo born at t_i is [15]

$$\rho(r_{\text{cut}}) \equiv \rho_{\text{max}} = \frac{m_\chi}{\langle \sigma v \rangle (t - t_i)}, \quad (6)$$

where m_χ is the WIMP mass and $\langle \sigma v \rangle$ is the annihilation cross section (multiplied by the collisional velocity and

taken in the zero-velocity limit). We truncate the density profiles at $r = r_{\text{cut}}$, setting the density within this radius equal to ρ_{max} . For UCMHs seen today, $t = 13.7$ Gyr [3]. For noncontracted UCMHs, $t_i = t(z_{\text{eq}}) = 59$ Myr [16] because they have existed since the time of equality. For contracted profiles, $t_i = t(10) = 0.49$ Gyr [16], as they were concentrated at $z = 10$.

To estimate the cosmological abundance of UCMHs, one integrates the probability distribution of primordial density perturbations between the UCMH formation threshold ($\delta \sim 10^{-3}$) and the PBH threshold ($\delta \sim 0.3$). We approximate the distribution as Gaussian [17], giving a relic density at matter-radiation equality of

$$\Omega_{\text{UCMH}}(M_H) = \int_{10^{-3}}^{0.3} \frac{\delta}{\sqrt{2\pi}\sigma(M_H)} \exp\left(-\frac{\delta^2}{2\sigma(M_H)^2}\right) d\delta. \quad (7)$$

Here, $\sigma(M_H)^2$ is the variance of perturbations at M_H . Assuming a scale-independent perturbation spectrum of index n , and normalizing to the perturbations observed in the CMB, σ can be approximated as [17]

$$\sigma(M_H) = 9.5 \times 10^{-5} (M_H/10^{56} \text{ g})^{(1-n)/4}. \quad (8)$$

On CMB scales, $n \sim 1$ [3]. However, the CMB probes only a limited number of modes. A different power law could plausibly dominate at the small scales relevant to UCMH formation; indeed, many inflationary models give a running spectral index [6], and phase transitions could produce scale-dependent features in the power spectrum [8]. The present limit at the scale of PBH/UCMH formation is $n \lesssim 1.25$ [17]. As they grow by a further factor of 290 [Eq. (1)] between equality and $z = 10$, UCMHs formed in the e^+e^- annihilation epoch could account for, e.g., $\sim 1\%$ of today's dark matter if $n = 1.15$. For the QCD and electroweak phase transitions, similar abundances could be obtained for $n = 1.09$ – 1.11 .

The gamma-ray flux from WIMP annihilation, in a solid angle $\Delta\Omega$ and integrated above energy E_{th} , is

$$\Phi(E_{\text{th}}, \Delta\Omega) = \frac{1}{8\pi m_\chi^2} \sum_f \int_{E_{\text{th}}}^{m_\chi} \frac{dN_f}{dE} dE \langle \sigma_f v \rangle \times \int_{\Delta\Omega} \int_{\text{l.o.s.}} \rho^2(\Omega, l) dl d\Omega, \quad (9)$$

where dN_f/dE is the differential photon yield from the f th annihilation channel. The final integral runs over the line of sight to the halo. For a spherically symmetric halo appearing as a point source at distance d , this is

$$\Phi(E_{\text{th}}) = \frac{1}{2d^2 m_\chi^2} \sum_f \int_{E_{\text{th}}}^{m_\chi} \frac{dN_f}{dE} dE \langle \sigma_f v \rangle \int_0^{R_h} r^2 \rho^2(r) dr. \quad (10)$$

We use $d = 4$ kpc as our canonical value because the best UCMHs for microlensing searches lie towards the Galactic bulge [7], but our results can be rescaled to any d . With a

mass fraction of 1% and $2.1 \times 10^9 M_\odot$ of dark matter within 4 kpc of Earth [assuming a Navarro–Frenk–White (NFW) halo [18]], we expect 1×10^{14} electroweak, 9×10^7 QCD or 200 e^+e^- UCMHs within 4 kpc. At 4 kpc, all UCMHs are point sources to current experiments, though below we discuss situations where they might be seen as extended objects.

In Fig. 1, we show gamma-ray fluxes from UCMHs containing WIMPs annihilating into either $b\bar{b}$ or $\mu^+\mu^-$. We computed these with parton-shower photon yields from PYTHIA 6.4 [19] in Darksusy 5.05 [20]. The $b\bar{b}$ channel is common in supersymmetric models, and the $\mu^+\mu^-$ channel is prominent in models which fit the PAMELA and Fermi electron excesses [21,22]. For the $b\bar{b}$ channel, we use the canonical cross section $\langle\sigma v\rangle = 3 \times 10^{-26} \text{ cm}^3 \text{ s}^{-1}$ implied by the relic density. For $\mu^+\mu^-$, we apply a boost

factor of 100, corresponding to the Sommerfeld enhancement necessary to explain the electron data in many models. If a UCMH were situated sufficiently nearby, however, its compactness might provide the required boost factor without needing any Sommerfeld enhancement.

Despite the increased density, adiabatic contraction does not greatly increase the gamma-ray flux. This is because the flux profile is dominated by the central region, which is not strongly contracted. The Sommerfeld enhancement we used for the $\mu^+\mu^-$ channel increases r_{cut} , making the flux profile less concentrated at the center and therefore more responsive to increases in density near r_{core} . If $r_{\text{core}} \ll r_{\text{cut}}$ or $r_{\text{core}} \gg r_{\text{cut}}$, this effect is absent.

In Fig. 1, we show representative point-source sensitivities of EGRET [23] and Fermi [24] above 100 MeV. Figure 2 gives the expected fluxes as a function of threshold energy, allowing for a direct comparison with the sensitivities of current and upcoming ACTs [25,26].

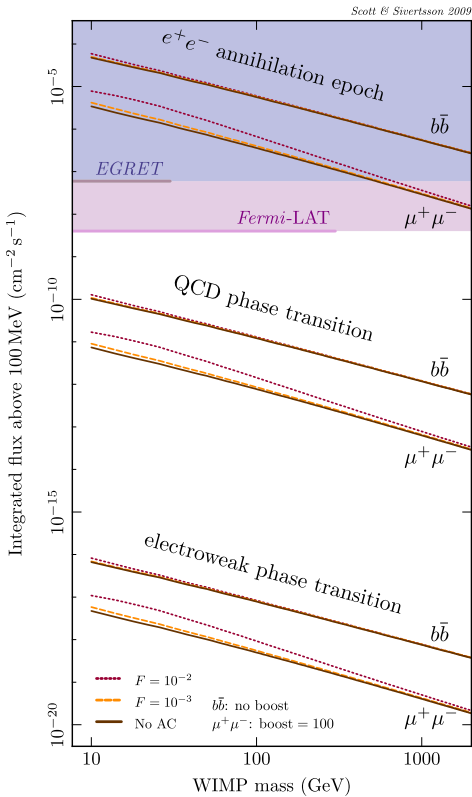


FIG. 1 (color online). Integrated fluxes above 100 MeV for UCMHs annihilating into either $b\bar{b}$ or $\mu^+\mu^-$ pairs at a distance $d = 4$ kpc. Curves are shown for different phase transitions and degrees of adiabatic contraction. Adiabatically contracted UCMHs are assumed to have a fraction F of their mass collapsed into a constant-density baryonic core of radius $10^{-3}R_h$. Also shown are approximate 5σ , power-law, high-latitude, point-source sensitivities for 2 weeks of pointed EGRET [23] and 1 yr of all-sky Fermi-LAT [24] observations. Solid limits indicate instruments' nominal energy ranges; see also note [26].

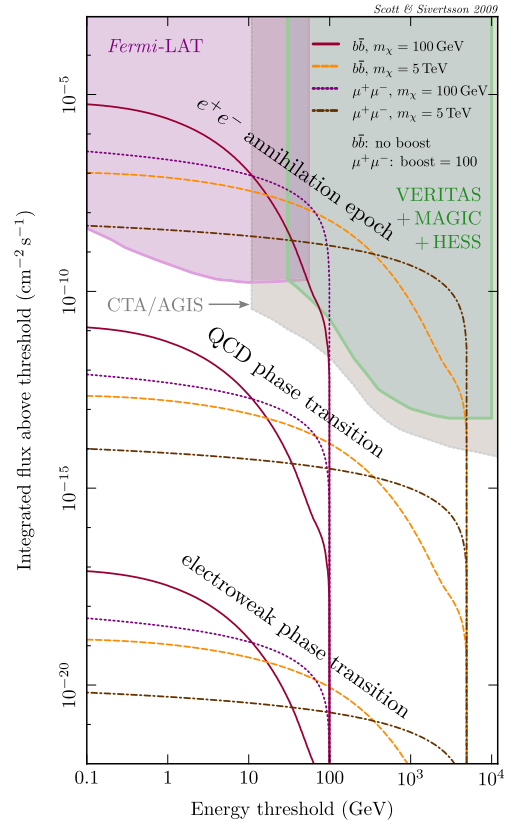


FIG. 2 (color online). Fluxes from uncontracted UCMHs at $d = 4$ kpc, as a function of the energy threshold of the observing experiment. Shaded areas show the regions accessible after a 1 yr survey by the Fermi-LAT [24], and 50 hr of observation by existing and planned Air Čerenkov Telescopes [25]. See also note [26].

UCMHs formed in the e^+e^- annihilation epoch should be observable by either *Fermi*, MAGIC, or HESS, depending upon the WIMP mass. They could have already been seen by *EGRET* in some cases, effectively ruling out the $b\bar{b}$ channel up to multi-TeV masses. Given their radial flux profiles, UCMHs from the e^+e^- epoch within $d \sim 2$ kpc should even appear as extended sources to *Fermi*. The nondiscovery to date of a point source with the spectral characteristics of annihilating dark matter suggests that the amplitude of perturbations generated by e^+e^- annihilation in the early Universe was $\delta < 10^{-3}$. A dedicated analysis of the *EGRET* and *Fermi* catalogues (particularly unidentified sources) is required for this statement to be made more definite. Such a study might even reveal some UCMH candidates. Limits from ACTs are more difficult to obtain, as UCMHs could have simply been missed by observing the wrong parts of the sky. On the other hand, if microlensing searches towards the Galactic bulge detect a UCMH from the e^+e^- transition, it can be definitively followed up by ACTs.

UCMHs from the QCD phase transition are not yet visible at $d = 4$ kpc, but their predicted fluxes are comparable to those of dwarf galaxies (e.g., [27]). If their abundance and the distance of the nearest example from Earth were favorable, they might be seen by *Fermi* or future instruments like the Čerenkov Telescope Array (CTA). UCMHs from the electroweak phase transition will probably not be detectable soon unless some lie within ~ 1 ly; in any case, light UCMHs might face formation problems from kinetic coupling of dark matter and free-streaming.

These results have important implications. Because of Eq. (6), the microlensing profiles of UCMHs containing WIMPs could differ from those of Ref. [7]. The additional annihilation products generated by UCMHs early in their lives could have an impact upon the ionization history of the Universe, and photons from the extra annihilation might modify the extragalactic gamma-ray background. If models explaining the *Fermi* and *PAMELA* electron excesses are accurate, UCMHs would also inject more electrons into the intergalactic medium and increase inverse Compton scattering of the CMB at all wavelengths.

We thank Joakim Edsjö, Joachim Ripken, Dave Thomson, and the anonymous referees for helpful comments, and the Swedish Research Council for funding support.

-
- [1] L. Bergström, Rep. Prog. Phys. **63**, 793 (2000); G. Bertone, D. Hooper, and J. Silk, Phys. Rep. **405**, 279 (2005); L. Bergström New J. Phys. **11**, 105006 (2009).
 - [2] B. Paczynski, Astrophys. J. **304**, 1 (1986).
 - [3] E. Komatsu *et al.*, Astrophys. J. Suppl. Ser. **180**, 330 (2009).
 - [4] F. Iocco, G. Mangano, G. Miele, O. Pisanti, and P.D. Serpico, Phys. Rep. **472**, 1 (2009).

- [5] P. Tisserand *et al.*, Astron. Astrophys. **469**, 387 (2007); Ł. Wyrzykowski, S. Kozłowski, J. Skowron, V. Belokurov, M. C. Smith, A. Udalski, M. K. Szymański, M. Kubiak, G. Pietrzyński, and I. Soszyński *et al.*, Mon. Not. R. Astron. Soc. **397**, 1228 (2009).
- [6] A. S. Josan, A. M. Green, and K. A. Malik, Phys. Rev. D **79**, 103520 (2009).
- [7] M. Ricotti and A. Gould, arXiv:0908.0735.
- [8] C. Schmid, D. J. Schwarz, and P. Widerin, Phys. Rev. Lett. **78**, 791 (1997).
- [9] Ricotti & Gould [7] also discuss ultracompact minihalos containing PBHs, but these require similar amplitude density perturbations as PBHs, so are less appealing.
- [10] See EPAPS Document No. E-PRLTAO-103-016948 for supersymmetric (CMSSM) predictions. For more information on EPAPS, see <http://www.aip.org/pubservs/epaps.html>.
- [11] Using, e.g., $z = 30$ instead has little impact on results.
- [12] E. W. Kolb and M. S. Turner, *The Early Universe* Frontiers in Physics (Addison-Wesley, Reading, MA, 1990).
- [13] P. Coles and F. Lucchin, *Cosmology: The Origin and Evolution of Cosmic Structure* (Wiley & Sons, West Sussex, UK, 2002).
- [14] G. R. Blumenthal, S. M. Faber, R. Flores, and J. R. Primack, Astrophys. J. **301**, 27 (1986).
- [15] P. Ullio, L. Bergström, J. Edsjö, and C. Lacey, Phys. Rev. D **66**, 123502 (2002).
- [16] E. L. Wright, Publ. Astron. Soc. Pac. **118**, 1711 (2006).
- [17] A. M. Green and A. R. Liddle, Phys. Rev. D **56**, 6166 (1997).
- [18] G. Battaglia, A. Helmi, H. Morrison, P. Harding, E. W. Olszewski, M. Mateo, K. C. Freeman, J. Norris, and S. A. Shectman, Mon. Not. R. Astron. Soc. **370**, 1055 (2006).
- [19] T. Sjöstrand, S. Mrenna, and P. Skands, J. High Energy Phys. **05** (2006) 026.
- [20] P. Gondolo, J. Edsjö, P. Ullio, L. Bergström, M. Schelke, and E. A. Baltz, J. Cosmol. Astropart. Phys. **7** (2004) 8.
- [21] O. Adriani, G. C. Barbarino, G. A. Bazilevskaya, R. Bellotti, M. Boezio, E. A. Bogomolov, L. Bonechi, M. Bongi, V. Bonvicini, and S. Bottai *et al.*, Nature (London) **458**, 607 (2009).
- [22] A. A. Abdo *et al.*, Phys. Rev. Lett. **102**, 181101 (2009).
- [23] R. C. Hartman, D. L. Bertsch, S. D. Bloom, A. W. Chen, P. Deines-Jones, J. A. Esposito, C. E. Fichtel, D. P. Friedlander, S. D. Hunter, and L. M. McDonald *et al.*, Astrophys. J. Suppl. Ser. **123**, 79 (1999).
- [24] http://fermi.gsfc.nasa.gov/ssc/data/analysis/documentation/Cicerone_/Cicerone_LAT_IRFs/LAT_sensitivity.html.
- [25] (The CTA Consortium), arXiv:0908.1410.
- [26] The sensitivities in Fig. 1 are not so accurate outside the nominal energy ranges, as heavier WIMPs in principle produce some flux outside the observable windows. The same is so for the 5 TeV lines in Fig. 2; the flux accessible to *Fermi* is probably less than shown for this mass, as part of the signal falls outside its nominal energy range. Properly extending sensitivities above the stated energy range requires a detailed spectral analysis.
- [27] G. D. Martinez, J. S. Bullock, M. Kaplinghat, L. E. Strigari, and R. Trotta, J. Cosmol. Astropart. Phys. **6** (2009) 14.

Gamma rays from ultracompact primordial dark matter minihalos

Pat Scott^{1,2} and Sofia Sivertsson^{1,3}¹*Oskar Klein Centre for Cosmoparticle Physics*²*Department of Physics, Stockholm University, AlbaNova, SE-10691 Stockholm, Sweden*³*Department of Theoretical Physics, Royal Institute of Technology (KTH), AlbaNova, SE-10691 Stockholm, Sweden*

(Dated: October 23, 2009)

APPENDIX: FLUX PREDICTIONS IN THE CMSSM

Fig. 3 shows neutralino annihilation fluxes predicted in the Constrained Minimal Supersymmetric Standard Model (CMSSM), for UCMHs formed in the e^+e^- epoch. We performed a global CMSSM fit using SuperBayeS [1], including CMB constraints on the relic density, accelerator searches for sparticles and the Higgs boson, the muon $g-2$, the $\bar{B}_s - B_s$ mass difference, and limits on rare B -decays. Details can be found in Ref. 1. Fluxes show a familiar band of high probability from points in the focus point region, due to clustering around the canonical annihilation cross-section compatible with the relic density. A lower-probability region is also seen, corresponding to models where stau co-annihilation is significant. The entirety of the allowed CMSSM parameter space should be accessible by current instruments if UCMHs were formed in the e^+e^- epoch. Predictions for UCMHs arising in the QCD and electroweak transitions look similar, but are shifted to lower fluxes as in Figs. 1 and 2.

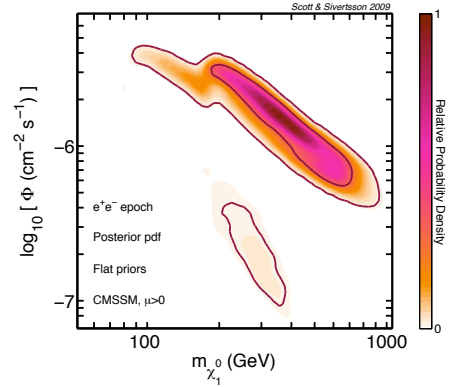


FIG. 3: Expected fluxes in the context of the CMSSM, for UCMHs formed in the e^+e^- annihilation epoch, integrated above 100 MeV. Contours indicate 1 and 2σ confidence intervals. Fits included a range of experimental data, and required that the neutralino is the only component of dark matter. Predictions from the QCD and electroweak transitions look similar, but are ~ 5.5 and ~ 12 orders smaller, respectively.

[1] R. Trotta, F. Feroz, M. Hobson, L. Roszkowski, and R. Ruiz de Austri, JHEP **12**, 24 (2008), arXiv:0809.3792.

Paper IV

Pat Scott, Jan Conrad, Joakim Edsjö, Lars Bergström, Christian Farnier & Yashar Akrami

Direct constraints on minimal supersymmetry from Fermi-LAT observations of the dwarf galaxy Segue 1

JCAP **01**, 031 (2010) [arXiv:0909.3300](#).

Direct constraints on minimal supersymmetry from Fermi-LAT observations of the dwarf galaxy Segue 1

Pat Scott,^a Jan Conrad,^a Joakim Edsjö,^a Lars Bergström,^a
Christian Farnier^b and Yashar Akrami^a

^aOskar Klein Centre for Cosmoparticle Physics and Department of Physics,
Stockholm University,
AlbaNova University Centre, SE-10691 Stockholm, Sweden

^bLaboratoire de Physique Thorique et Astroparticules, CNRS/IN2P3,
Université Montpellier II, CC 70,
Place Eugene Bataillon, F-34095 Montpellier Cedex 5, France

E-mail: pat@fysik.su.se, conrad@fysik.su.se, edsjo@fysik.su.se, lbe@fysik.su.se,
farnier@in2p3.fr, yashar@fysik.su.se

Received September 17, 2009

Revised December 15, 2009

Accepted December 24, 2009

Published January 26, 2010

Abstract. The dwarf galaxy Segue 1 is one of the most promising targets for the indirect detection of dark matter. Here we examine what constraints 9 months of FERMI-LAT gamma-ray observations of Segue 1 place upon the Constrained Minimal Supersymmetric Standard Model (CMSSM), with the lightest neutralino as the dark matter particle. We use nested sampling to explore the CMSSM parameter space, simultaneously fitting other relevant constraints from accelerator bounds, the relic density, electroweak precision observables, the anomalous magnetic moment of the muon and B -physics. We include spectral and spatial fits to the FERMI observations, a full treatment of the instrumental response and its related uncertainty, and detailed background models. We also perform an extrapolation to 5 years of observations, assuming no signal is observed from Segue 1 in that time. Results marginally disfavour models with low neutralino masses and high annihilation cross-sections. Virtually all of these models are however already disfavoured by existing experimental or relic density constraints.

Keywords: dark matter theory, dwarfs galaxies, supersymmetry and cosmology, gamma ray theory

ArXiv ePrint: [0909.3300](https://arxiv.org/abs/0909.3300)

Contents

1	Introduction	1
2	Analysis	4
2.1	Gamma-rays from neutralino annihilation in dwarf galaxies	4
2.2	Observations and instrumental considerations	5
2.3	Likelihoods from Segue 1	5
2.3.1	Extrapolation to 5 years of observations	7
2.4	CMSSM scans	8
3	Results and discussion	9
3.1	Fits to FERMI data only	9
3.2	Global fits	11
4	Conclusions	15

1 Introduction

The identity of dark matter is one of the most compelling problems facing modern physics. A wealth of viable theoretical candidates have been put forward (see e.g. [1–4]), with the majority based on extensions to the standard model (SM) of particle physics. One of the more durable suggestions is that dark matter consists of weakly-interacting massive particles (WIMPs), thermally produced in the early universe and therefore naturally present in approximately the right cosmological abundance. Models of supersymmetry (SUSY) where R -parity is conserved provide a prototypical WIMP candidate in the lightest neutralino. Low-energy SUSY is also highly attractive because it generically solves the SM hierarchy problem whilst simultaneously providing a favourable framework for gauge-coupling unification and electroweak symmetry breaking [5, 6].

Because the neutralino is a Majorana particle, its self-annihilation opens a potential channel for discovery via the observation of annihilation products like photons, hadrons and leptons. Self-annihilation rates are proportional to the square of the particle density, so any environment with a high density of dark matter is a good prospective target. In practice, expected backgrounds from different targets strongly influence their suitability for such indirect detection. Dwarf spheroidal galaxies have recently emerged as leading targets for gamma-ray detection of dark matter [7–11], thanks to their high mass-to-light ratios [7, 12–14] and small expected astrophysical backgrounds.

Segue 1 is probably the most promising object in this respect [15, 16], due to its extreme dark matter domination ($M/L \approx 1320$), relative proximity (23 kpc) and high latitude [14]. As with other dwarf galaxies, constraining the density profile of dark matter in Segue 1 is difficult; being small and faint, very few stars are available to act as kinematic tracers of the gravitational potential. Its spatial superimposition upon the leading arm of the Sagittarius stream [17] complicates matters further, as do the partially degenerate impacts of dark matter, bulk rotation and magnetic fields upon the stellar velocity dispersion [18]. Indeed, the status of Segue 1 as a dwarf galaxy rather than a star cluster, and therefore its domination by dark matter, have been called into question [17, 19]. We will assume here that it is indeed

a galaxy, an assertion strongly supported by further recent (but as yet unpublished) spectroscopic data [20]. These new data should also significantly reduce the uncertainty associated with the density profile of dark matter within Segue 1. As of the time of writing, the best available estimate of this profile comes from Markov-Chain Monte Carlo (MCMC) scans of halo parameters and corresponding solutions to the Jeans equation, based on line-of-sight velocities of 24 stars in Segue 1 [15].

The Large Area Telescope (LAT; [21]), aboard the FERMI satellite, is a high-energy, pair-conversion gamma-ray space telescope. The LAT is designed to operate predominantly in survey mode, and has been doing so since August 4, 2008. With its energy range (20 MeV to over 300 GeV) and high spatial and spectral resolution ($\Delta E/E \approx 12\%$, point-spread function $< 0.1^\circ$ at 100 GeV), the LAT is well-suited to gamma-ray searches for dark matter annihilation. A major undertaking within the LAT collaboration has been to try to discover or place limits upon theories of dark matter using FERMI observations of Milky Way dwarf galaxies and satellites, the Galactic centre, the Galactic halo and extragalactic sources [22–26]. The detector design also facilitates direct observation of cosmic-ray electrons [27], another possibly relevant channel for dark matter indirect detection.

By any measure, SUSY is an extensive and highly developed addition to the SM, giving rise to a wealth of potential experimental signatures beyond dark matter. Any explanation of dark matter as a neutralino must therefore satisfy a host of other phenomenological constraints. Even within the minimal supersymmetric extension of the SM (the MSSM), the low-energy phenomenology of the theory strongly depends upon the particular parameterisation employed in the soft SUSY-breaking sector, and the specific values of the chosen parameters. Given that the most general soft SUSY-breaking Lagrangian in the MSSM has over a hundred free parameters, one must choose some reduced parameterisation in order to make any progress in fitting experimental data. One approach is to employ a low-energy effective Lagrangian for the soft breaking terms, with various parameters set to zero or made equal for computational convenience (and in order to avoid experimental constraints on e.g. flavour-changing neutral currents). The alternative is to choose a specific breaking scheme, such as gravity mediation in minimal supergravity (mSUGRA) [28], gauge mediation (GMSB) [29] or anomaly mediation (AMSB) [30], where a small number of breaking parameters are defined and unified at some high energy, and the masses and couplings are run down to low energy using the renormalisation group equations (RGEs) in order to obtain phenomenological predictions.

In this paper we focus on the Constrained MSSM (CMSSM) as a convenient example of one such high-energy parameterisation. This scheme is defined at the gauge coupling unification scale ($\sim 10^{16}$ GeV) in terms of 4 free continuous parameters and one sign:

$$\{m_0, m_{\frac{1}{2}}, A_0, \tan \beta, \text{sgn } \mu\}. \quad (1.1)$$

Here m_0 is the universal scalar mass, $m_{\frac{1}{2}}$ the gaugino mass parameter, A_0 the trilinear coupling between Higgs bosons, squarks and sleptons, $\tan \beta$ the ratio of vacuum expectation values of up-type and down-type Higgs bosons, and $\text{sgn } \mu$ the sign of the Higgs mixing parameter in the superpotential. We choose μ to be positive throughout this paper. The magnitude of μ is set by the requirement that SUSY breaking radiatively induces electroweak symmetry breaking; in this sense the CMSSM differs slightly from mSUGRA (where electroweak symmetry breaking is not strictly part of the definition and $\tan \beta$ is swapped for the parameter B — see e.g. [5]), but for nearly all intents and purposes the two can be considered equivalent.

The CMSSM possesses a number of distinct regions where the relic density of the lightest neutralino matches the observed dark matter abundance (see e.g. [31, 32] and references therein). The majority of the CMSSM parameter space results in too high a relic density; regions producing the correct amount of dark matter are those where some channel of neutralino destruction is especially efficient. Until recently, most analyses focused on the so-called bulk region at low m_0 and $m_{\frac{1}{2}}$, where neutralino annihilation proceeds efficiently by exchange of light sleptons. This region is now mostly ruled out by collider limits on sparticle masses and difficulty in meeting Higgs mass limits when both m_0 and $m_{\frac{1}{2}}$ are small. The stau coannihilation region occurs at low m_0 , where the stau is almost degenerate in mass with the lightest neutralino. Here the correct relic density is achieved via co-annihilations between the two sparticles rather than any increase in the neutralino self-annihilation cross-section. A similar situation occurs in the stop coannihilation region, which exists at large negative A_0 . The stau coannihilation region is still viable, but stop coannihilation is disfavoured by low-energy experiments and Higgs constraints. In the focus point region at large m_0 , the lightest neutralino picks up a significant Higgsino component, opening new annihilation channels and boosting certain coannihilations. Finally, small ‘funnels’ of parameter space exist where neutralino annihilation can be increased by a mass resonance with one of the MSSM Higgs particles (i.e. where the Higgs in question has roughly twice the mass of the lightest neutralino). The focus point and funnel regions are still allowed by present experimental constraints.

Scanning of MSSM parameter spaces is nowadays a highly developed art. Starting from simple grid and random scans [33–37] within slices of the mSUGRA parameter space, efforts expanded to MCMC searches of the full CMSSM/mSUGRA space [38], later also including the most important SM uncertainties [32, 39]. As nested sampling [40, 41] has come to replace the MCMC as the scanning technique of choice, hope has risen that MSSM scans might now finally be globally convergent [42, 43]. New results with genetic algorithms [44], however, suggest that current scanning techniques may yet have some distance to go in this respect. Some authors have begun to focus on higher-dimensional low-energy effective MSSM parameterisations [43, 45, 46], which provide for a broader range of phenomenological consequences but are almost impossible to scan effectively without sophisticated algorithms and substantial supercomputing resources. Explorations of SUSY-breaking schemes beyond mSUGRA have also been carried out lately using similar parameter scans [47–50], as have investigations of next-to-minimal SUGRA [51–53]. SUSY scans are generally either based on the Bayesian posterior probability [39, 42, 43, 47], the direct use of the frequentist likelihood [32, 36, 49] (usually by a χ^2 analysis), or a simple ‘in-or-out’ approach to individual points being permitted by experimental data [33–35, 38].

MSSM scans have thus far focused on the constraints provided by particle experiments and the dark matter relic density determined from the microwave background, sometimes to produce corresponding predictions for astronomical observations (e.g. [15, 54–56]). To our knowledge, none have so far included actual constraints from searches for annihilating dark matter; this is no doubt because such constraints have only recently come within a reasonable distance of model predictions.

In this paper, we include the first 9 months of the search for dark matter annihilation in Segue 1 with FERMI in explicit CMSSM parameter scans. We use spectrally and spatially resolved photon counts observed by the LAT to directly assess the likelihood of the different regions in the CMSSM parameter space, then combine these with laboratory and cosmological data to perform global fits to the model parameters. We also provide a predicted impact on the parameter space after 5 years of observations. In section 2 we describe our analysis techniques, before presenting results in section 3 and conclusions in section 4.

2 Analysis

2.1 Gamma-rays from neutralino annihilation in dwarf galaxies

The expected differential gamma-ray flux per unit solid angle from a source of neutralino annihilations is (see e.g. [57])

$$\frac{d\Phi}{dE d\Omega} = \frac{1 + BF}{8\pi m_\chi^2} \sum_f \frac{dN_f^\gamma}{dE} \sigma_f v \int_{\text{l.o.s.}} \rho_\chi^2(l) dl. \quad (2.1)$$

Here m_χ is the neutralino mass, BF is the boost factor due to any unresolved substructure in the source, f labels different annihilation final states, dN_f^γ/dE is the differential photon yield from any particular final state, σ_f is the cross-section for annihilation into that state, v is the relative velocity between neutralinos, and the integral runs over the line of sight to the source. In the absence of any bound states (i.e. Sommerfeld enhancements), massive neutralinos move so slowly that they can effectively be considered to collide at rest, allowing $\sigma_f v$ to be replaced with the velocity-averaged term in the zero-velocity limit, $\langle \sigma_f v \rangle_0$.

Three main channels contribute to the spectrum of neutralino annihilation. Through loop processes, annihilation can proceed directly into two photons [58, 59]

$$\frac{dN_{\gamma\gamma}^\gamma}{dE} = 2\delta(E - m_\chi), \quad (2.2)$$

or into a Z boson and a photon [60]

$$\frac{dN_{Z\gamma}^\gamma}{dE} = \delta\left(E - m_\chi + \frac{m_Z^2}{4m_\chi}\right), \quad (2.3)$$

giving a monochromatic gamma-ray line. A hard spectrum can also be produced by the so-called internal bremsstrahlung (consisting of final-state radiation and virtual internal bremsstrahlung), generated when a photon is emitted from a virtual particle participating in the annihilation diagram [61]. Finally, continuum gamma-rays can be produced by annihilation into quarks, leptons and heavy gauge bosons (including the Z from the $Z\gamma$ line), which subsequently decay via π^0 to softer photons. The cross-sections and resultant spectral yields for each of these processes are directly calculable from the SUSY parameters which define a point in e.g. the CMSSM parameter space (after appropriate RGE running). We use DarkSUSY [62] for this calculation.

The integral and boost factor in eq. (2.1) are determined by the dark matter distribution in the astrophysical source. We use the Einasto profile [63]

$$\rho(r) = \rho_s \exp \left\{ -2n \left[\left(\frac{r}{r_s} \right)^{\frac{1}{n}} - 1 \right] \right\} \quad (2.4)$$

to describe the average dark matter content of Segue 1, where n is the Einasto index and r_s and ρ_s are the scale radius and density, respectively. This profile is somewhat more conservative than the traditional NFW [64], in the sense that it is less steep in the central regions, leading to generally better agreement with observations of various dark matter halos [63, 65, 66]. It is also slightly more dense at intermediate radii. The adopted form of the density profile actually makes little overall difference to the expected flux. This is because

in general, dwarf galaxies will appear either as point sources or very close to pointlike to the LAT, meaning that observations mostly probe the full halo rather than just the central cusp.

We use the best-fit values of the scale radius and scale density found by Martinez et al. [15] in their recent fits to stellar kinematic data ($r_s = 0.07$ kpc, $\rho_s = 3.8 \text{ GeV cm}^{-3}$). Since Martinez et al. found no preference for a particular Einasto index, we adopt the central value considered in their scans, $n = 3.3$. We note that the fits were not only influenced by the kinematic data, but also by a theoretical prior imposed by assuming the same correlation between r_s and ρ_s as seen in subhalo populations of theoretical N -body simulations of cold dark matter structure formation. Whilst this presents no real problem, it is encouraging to see that additional kinematic data [20] largely dominate the prior in more recent fits. The same authors performed an extensive investigation of the possible substructure boosts in Segue 1, showing that all BF values between 0 and ~ 70 are compatible with kinematic data and small-scale structure predictions within the CMSSM, with the most likely value depending strongly on the particular model employed for the concentration-mass relation. We therefore employ two indicative values for the boost factor: a rather pessimistic case, $BF = 1$, and an optimistic case, $BF = 50$. It is important to note that $BF = 0$ has a very low probability in the results of Martinez et al.

2.2 Observations and instrumental considerations

We considered photon events observed in a 10 square degree, stereographically-projected section of the sky centred on Segue 1 (RA, Dec. = $151.763^\circ, 16.074^\circ$ [14]). We applied cuts on event zenith angles ($\theta < 105^\circ$), energies ($100 \text{ MeV} < E < 300 \text{ GeV}$) and identifications (only ‘diffuse class’ events — see [21]). All data were processed using the same reconstruction algorithms and instrument response functions (IRFs) as the publicly-released first-year data. Counts and corresponding exposures were placed into 64×64 spatial and 14 logarithmic energy bins. The resultant energy-integrated map of photon counts is shown in figure 1.

The FERMI-LAT IRFs consist of the effective area, point-spread function (PSF) and energy dispersion. We factored the effective area of the telescope into our calculations of the exposure for each bin of observed photon counts, using the standard analysis tools available from HEASARC, specifically ScienceTools 9.11.¹ We convolved our modelled gamma-ray fluxes with the PSF and energy dispersion of the LAT using the publicly-available Fortran90 library FLATlib [67], which was designed specifically for performing this task quickly enough to be useful in MSSM scans. Full FERMI-LAT IRFs are defined not only as a function of photon energy, but impact angle with respect to the telescope zenith (and even azimuthal angle, though the dependence is weak). FLATlib achieves its fast convolution by averaging the IRFs over impact angles, allowing the integral over the PSF to be cast as a true convolution and performed by fast spectral methods. The energy integral cannot be performed in a similar way, because all three IRFs remain energy-dependent. FLATlib performs this integral explicitly, using a fast importance-sampling technique which utilises the rough resemblance of the energy dispersion function to a Gaussian. For the sake of computational speed, we truncated the PSF at a width of 3.2° in the scans we present in this paper. With the present IRF set, this is well beyond the LAT’s 95% containment resolution at e.g. 100 GeV ($\approx 0.3^\circ$) or even 1 GeV ($\approx 2^\circ$).

2.3 Likelihoods from Segue 1

The expected spatial extent of Segue 1 in the gamma-ray sky, if it shines with dark matter annihilation, is comparable to the width of the LAT PSF. This puts Segue 1 on the borderline

¹Available at <http://fermi.gsfc.nasa.gov/ssc/data/analysis/software/>.

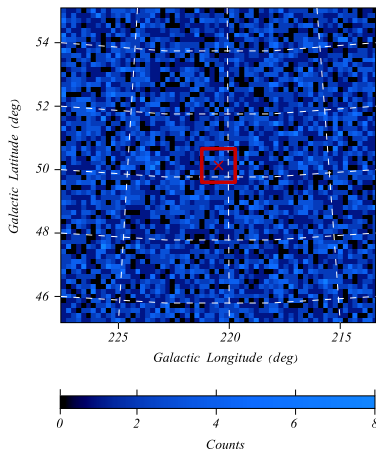


Figure 1. Photon counts observed by FERMI in the region around Segue 1 during the first 9 months of LAT operation in all-sky survey mode. Counts are integrated over all energies between 100 MeV and 300 GeV. The red cross shows the exact location of the centre of Segue 1, and the red box shows the region included in our likelihood calculations.

between a predicted point source and a predicted extended source. For every set of CMSSM parameters, we computed model spectra at each pixel in the inner 6×6 square shown in red in figure 1. We took care to explicitly integrate the density profile over the innermost 2×2 pixels as a whole, so as to correctly capture the contribution of the very centre of the galaxy (located at their vertex). We compared the predicted spectra with the observed ones in each of the 36 pixels to obtain a likelihood based on 504 data points, which we then included in the total likelihood for that point in our CMSSM scan. We chose only to include the inner 36 pixels in the CMSSM likelihood simply because these are the only pixels where there is a predicted signal at any significant level.

All modelled spectra explicitly included contributions from gamma-ray lines, internal bremsstrahlung and continuum radiation. To properly model the observed event counts in the region around Segue 1, we also took the Galactic and isotropic diffuse emissions into account. We used a preliminary form of the GALPROP fit to the emission observed by FERMI [68] to describe the Galactic diffuse emission. The contribution of the isotropic diffuse emission, presumably originating from extragalactic sources, is much weaker and depends on the Galactic diffuse model adopted. To describe this, we adopted an isotropic power law model with index -2.1 , derived from EGRET observations by Sreekumar et al. [69]. The models recommended by the LAT team were updated recently, and released to the Fermi Science Support Centre. At the $\sim 50^\circ$ latitude of Segue 1, the differences between the old and new models are not important for this analysis. The normalisations for both backgrounds were set to the best-fit values obtained in the preliminary 9-month LAT dwarf upper-limit analysis [24, 70], based on the full 10 square degree region of interest rather than just the inner 36 pixels included in our likelihoods. No sources were detected in this region in the first 9 months of LAT operation.

Because of the very low statistics observed in LAT photon counts towards Segue 1, a χ^2 estimation of the likelihood is inappropriate in this case. We calculated the likelihood using a binned Poissonian measure

$$\mathcal{L} = \prod_j \frac{\theta_j^{n_j} e^{-\theta_j}}{n_j!}, \quad (2.5)$$

or, recast in the more familiar minus log-likelihood form (analogous to half the χ^2),

$$-\ln \mathcal{L} = \sum_j [\theta_j + \ln(n_j!) - n_j \ln(\theta_j)]. \quad (2.6)$$

Here n_j and θ_j are the observed and predicted number of counts respectively, in the j th bin. This prescription clearly accounts for statistical errors by definition, but including systematic errors is less obvious. To do so, one can marginalise over an assumed probability density function (PDF) of a systematic error in a semi-Bayesian manner, treating it as a nuisance parameter. If we consider a systematic error that has the impact of consistently rescaling the observed number of counts as $n_j \rightarrow \epsilon n_j$ (i.e. a constant percentage systematic error $|1 - \epsilon|$), and assume a Gaussian form with width σ_ϵ for the PDF of ϵ , the marginalised log-likelihood is (see e.g. [71])

$$-\ln \mathcal{L} = -\sum_j \ln \left\{ \frac{1}{\sqrt{2\pi}\sigma_\epsilon} \int_0^\infty \frac{(\epsilon\theta_j)^{n_j} e^{-\epsilon\theta_j} \exp\left[-\frac{1}{2}\left(\frac{1-\epsilon}{\sigma_\epsilon}\right)^2\right]}{n_j!} d\epsilon \right\} \quad (2.7)$$

$$= -\sum_j \ln \left\{ \frac{\theta_j^{n_j}}{\sqrt{2\pi}\sigma_\epsilon n_j!} \int_0^\infty \epsilon^{n_j} \exp\left[-\epsilon\theta_j - \frac{1}{2}\left(\frac{1-\epsilon}{\sigma_\epsilon}\right)^2\right] d\epsilon \right\}. \quad (2.8)$$

The integral is only analytically soluble for $\theta_j < \sigma_\epsilon^{-2}$, which is not generally true when dealing with small statistics; we performed it numerically for each likelihood evaluation.

We included estimated systematic errors from the LAT effective area (f) and our modelled spectra (τ) by combining them in quadrature, i.e. $\sigma_\epsilon(E_j) = \sqrt{f(E_j)^2 + \tau^2}$. Note the explicit energy dependence of f ; for the present IRF set, $f(E_j)$ ranges from 10% at 100 MeV, to 5% at 562 MeV, to 20% at 10 GeV. We interpolated between these values linearly, and assumed the edge values outside this range. We tuned the importance sampling algorithm used by FLATlib using slower, more accurate standard numerical integration schemes, choosing a sampling efficiency for our specific problem that would introduce an overall systematic theoretical error τ of no more than 5% in the normalisation of flux predictions. Other systematic errors are no doubt also present in the theoretical predictions, but we expect the term from the fast integration to dominate.

2.3.1 Extrapolation to 5 years of observations

To make predictions about the impact of 5 years of LAT observations, we explicitly assume that no excess events will have been observed after this time. There is no correct way to rescale Poissonian counts to longer timescales, so the Poissonian likelihood above cannot be used when extrapolating to longer observing times. We instead set the ‘observed’ number of photons equal to the number predicted by the background model, using rescaled 9-month exposures. This prescription also avoids the erroneous shifts which confidence intervals based

on Poissonian statistics can sometimes experience due to a downward statistical fluctuation of the background. In this case the observed counts become a continuous instead of a discrete variable, so the problem of small statistics disappears. The appropriate likelihood measure is then once more the χ^2

$$\chi^2 = \sum_j \frac{(\Phi_{\text{model},j} - \Phi_{\text{observed},j})^2}{\sigma_j^2} = \sum_j \frac{\left(\frac{\theta_j - n_j}{\mathcal{E}_j}\right)^2}{\sigma_{\text{model},j}^2 + \sigma_{\text{observed},j}^2}, \quad (2.9)$$

where $\Phi_{\text{model},j}$ and $\Phi_{\text{observed},j}$ are the predicted and observed fluxes, $\sigma_{\text{model},j}$ and $\sigma_{\text{observed},j}$ are their standard deviations, and \mathcal{E}_j is the exposure. The exposure is itself the product of the effective area and observing time. The standard deviation of the predicted flux can be estimated as simply the product of the predicted flux and the percentage systematic theoretical uncertainty τ (5% in our case — see above), $\sigma_{\text{model},j} = \tau \Phi_{\text{model},j}$. The standard deviation in the observed flux can be estimated from the standard deviation of the observed counts σ_{n_j} , and the uncertainty on the exposure $\sigma_{\mathcal{E}_j}$, giving

$$\sigma_{\text{observed},j}^2 = \left(\frac{n_j}{\mathcal{E}_j}\right)^2 \left(\frac{\sigma_{n_j}^2}{n_j^2} + \frac{\sigma_{\mathcal{E}_j}^2}{\mathcal{E}_j^2}\right). \quad (2.10)$$

Since the underlying physical process is still Poissonian, the best estimate of σ_{n_j} is in fact $\sigma_{n_j} = \sqrt{\theta_j}$. Furthermore, since the uncertainty in the observing time is negligible, $\sigma_{\mathcal{E}_j}$ can be estimated as simply the percentage systematic error of the effective area $f(E_j)$ times the actual exposure, $\sigma_{\mathcal{E}_j} = f(E_j)\mathcal{E}_j$. We then have

$$\sigma_{\text{observed},j}^2 = \left(\frac{n_j}{\mathcal{E}_j}\right)^2 \left(\frac{\theta_j}{n_j^2} + f(E_j)^2\right) \quad (2.11)$$

$$= \frac{\Phi_{\text{model},j}^2}{\mathcal{E}_j} + \Phi_{\text{observed},j}^2 f(E_j)^2, \quad (2.12)$$

giving

$$\chi^2 = \sum_j \frac{(\Phi_{\text{model},j} - \Phi_{\text{observed},j})^2}{\frac{\Phi_{\text{model},j}^2}{\mathcal{E}_j} + \Phi_{\text{observed},j}^2 f(E_j)^2 + \tau^2 \Phi_{\text{model},j}^2}. \quad (2.13)$$

We hasten to point out that constraints based on this extrapolation are probably overly conservative, as we assume the same background rejection, systematic errors and background model for both the 9-month analysis and the 5-year extrapolation. Our overall understanding of the instrument will improve over time, as will our understanding of the background as FERMI accumulates better statistics on the Galactic diffuse and extragalactic components, leading to correspondingly better constraints on the annihilation cross-section. Kinematic constraints upon the dark matter density profile of Segue 1 will also improve in time [20, 25], which may impact constraints on CMSSM parameters.

2.4 CMSSM scans

We scanned the CMSSM parameter space using a modified version of SuperBayeS 1.35 [42], employing the MultiNest [41] nested sampling algorithm with 4000 live points. In the plots we show, all parameters except those shown on figure axes have been marginalised over in some way. In the case of the frequentist profile likelihood, this is simply a matter of maximising

the likelihood in the other dimensions of the parameter space. In the case of the Bayesian posterior, the total posterior (prior times likelihood) is integrated over the other dimensions of the space (for a review see e.g. [72]). Because we are somewhat more interested in the prior-independent profile likelihood than the marginalised posterior,² we prefer linear priors on the CMSSM parameters because they are flat relative to the likelihood, causing the sampling algorithm to proceed strictly according to the frequentist likelihood function. The effects of alternative priors have already been discussed in detail for previous CMSSM scans [42].

We used **DarkSUSY 5.04** for the relic density and indirect detection computations. This allowed us to calculate internal bremsstrahlung spectra, and improved the continuum spectrum and relic density calculations. We also improved the interface between **SuperBayeS** and **DarkSUSY**, most notably pertaining to the energies at which some particle masses were defined.

Apart from the **FERMI** data, the experimental data and nuisance parameters which we included in scans were identical to those in [42] and [44]. SM nuisance parameters were the top and bottom quark masses and strong and electromagnetic coupling constants. Experimental data were precision electroweak measurements of SM parameters from the Large Electron-Positron collider (LEP), the relic density from 5-year Wilkinson Microwave Anisotropy Probe (WMAP) fits ($\Omega_{\text{DM}} h^2 = 0.1099 \pm 0.0062$ [73]), LEP constraints on sparticle masses, LEP constraints on the Higgs mass, the anomalous magnetic moment of the muon ($g - 2$), the $\bar{B}_s - B_s$ mass difference, and branching fractions of rare processes $b \rightarrow s\gamma$, $\bar{B}_u \rightarrow \nu\tau^-$ and $\bar{B}_s \rightarrow \mu^+\mu^-$. Details can be found in [42].

In our chosen configuration, completing the integration over the LAT IRFs for a given point in the CMSSM parameter space required a similar order of magnitude in processing time as a relic density calculation. Since the relic density computation is the main bottleneck in MSSM scans, this meant that scans took roughly twice as much total processor time to complete as a standard **SuperBayeS** run. One advantage of **FLATlib**, however, is that it can employ the multi-threaded version of the FFTW library [74], allowing the IRF integration to be performed with a considerably greater degree of parallelisation than the present relic density routines.

3 Results and discussion

3.1 Fits to **FERMI** data only

In figure 2 we show results of scans where the likelihood function only included **FERMI** data, LEP measurements of nuisance parameters and the requirements of physicality (the absence of tachyons, that the neutralino is the lightest SUSY particle, and that electroweak symmetry breaking is induced by SUSY breaking). Preferred values of the neutralino self-annihilation cross-section and mass are shown for scans including 9 months of data, scans including the extrapolation to 5 years of data, and a control case without any **FERMI** data. Preferred regions are also given for both the pessimistic and optimistic boost factors discussed in section 2.1.

One apparent feature of figure 2 is the lack of viable models with large annihilation cross sections for large neutralino masses. This feature is present simply because the annihilation cross section goes as m_χ^{-2} , causing it to fall off at higher masses.

Given the absence of any observed signal from Segue 1, **FERMI** data clearly disfavors models with the highest cross-sections and lowest masses. This is expected, since higher

²We make the point, however, that both should be considered if one wants to gain as complete a picture as possible of the preferred regions in an insufficiently-constrained parameter space like the CMSSM.

cross-sections and lower masses lead to a larger predicted signal. That constraints are best at lower neutralino masses is also consistent with the falling sensitivity of the LAT with energy above about 50 GeV, and the reduced source statistics at higher energies. The improvement in constraints when moving from the current 9 months of data to the 5-year predictions is also roughly what would be expected from a \sqrt{t} improvement in sensitivity. This shows that the two different likelihood estimators we employ give consistent results (we also checked this explicitly for 9 months of data, finding very good agreement).

Predictably, the adopted boost factor plays a large role in determining the extent of constraints brought to bear on the CMSSM by Segue 1. In the most pessimistic scenario, 9 months of LAT observations have no impact on confidence regions, as all disfavoured cross-sections are larger than allowed by physicality arguments. In the most optimistic scenario, the data disfavours all models with cross-sections greater than $\sim 3 \times 10^{-25} \text{ cm}^3 \text{ s}^{-1}$. Improvements in constraints when moving from $BF = 1$ to $BF = 50$ are consistent with the factor of 51/2 improvement in sensitivity expected from eq. (2.1), as the most pessimistic constraints lie above the extent of contours in the upper middle panel of figure 2. Extrapolating to 5 years of observations, all values above $10^{-25} \text{ cm}^3 \text{ s}^{-1}$ would be disfavoured, as would a region extending down below $10^{-26} \text{ cm}^3 \text{ s}^{-1}$ at the lowest masses. Once again, we caution the reader that this extrapolation does not take into account systematic improvements in the background and dark matter profile modelling after 5 years, nor in the LAT reconstruction algorithms (see section 2.3.1).

For comparison, in figure 2 we also show the previously-presented, preliminary 95% confidence level upper limit from 9 months of LAT observations [70]. This limit was derived assuming annihilation proceeds only into $b\bar{b}$ pairs. Apart from the obvious difference in overall strategy (upper limits from an assumed final state versus inclusion in explicit model scans), our analysis differs from the upper limit one in a number of ways. The upper limit was derived assuming a point source for Segue 1, whereas we perform spatial fits; the upper limit is based upon an NFW rather than Einasto density profile, and does not include systematic errors nor a treatment of the energy dispersion.

Nonetheless, the areas disfavoured in our scans are broadly consistent with the 9 month upper limit, a positive comment on the reliability of both analyses. Our corresponding exclusions do however occur at somewhat higher cross-sections than in the upper limit analysis (i.e. our exclusion region is above both the extent of coloured contours and the black line in the upper middle panel of figure 2). This is to be expected, as our ability to exclude models is degraded relative to the upper limit analysis by properly accounting for the systematic error in the effective area. Because this error is energy-dependent, our exclusions also have a slightly different energy-dependence than the 95% upper limit.

It should be noted that the degree of substructure apparent in the confidence regions of figure 2 is unlikely to be physical, and is indeed probably something of an artefact of the scanning technique (i.e. ‘scanning noise’). In the absence of any constraint on the annihilation cross-section from the relic density, the vast majority of points providing a good fit to the included data lie at much lower cross-sections. This prompts the scanning algorithm to concentrate its efforts there, leaving the region in which we are most interested somewhat poorly sampled. From a Bayesian point of view, one would say that when the relic density is not included, this region sits well above the most likely annihilation cross-sections in the CMSSM, so is not meant to be very well sampled by the nested sampling technique.

Because only a small number of models are disfavoured by including just Segue data in the likelihood function, there is little overall impact on the favoured values of m_0 , $m_{\frac{1}{2}}$, A_0

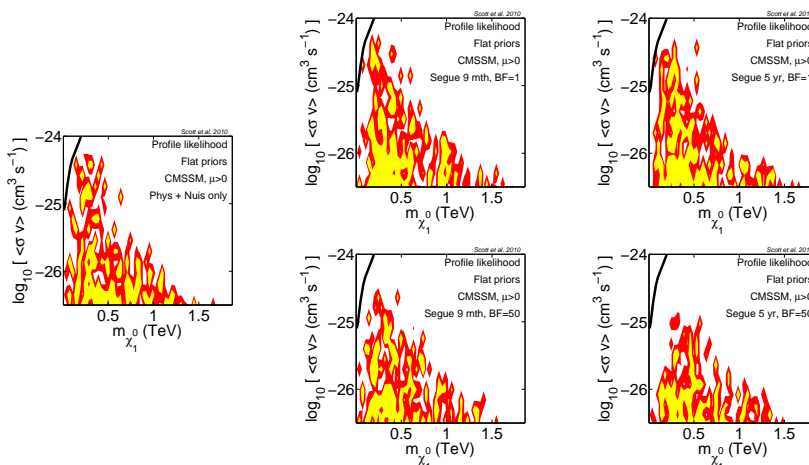


Figure 2. Neutralino self-annihilation cross-sections in the CMSSM, in the zero-velocity limit. *Left:* with no constraining experimental data except measurements of SM nuisance parameters and physicality requirements. *Middle:* constraints provided by 9 months of FERMI data on Segue 1, under the most pessimistic (*top*) and optimistic (*bottom*) assumptions about the substructure boost factor. *Right:* projected constraints after 5 years of FERMI observations. Colours indicate 68% (yellow) and 95% (red) confidence regions. The preliminary 95% confidence level upper limit on the annihilation cross-section from 9 months of FERMI data, assuming 100% WIMP annihilation into $b\bar{b}$ [70], is given for comparison (black curve).

and $\tan\beta$ beyond what is allowed purely on physicality grounds. We will show confidence regions from global fits only for these parameters.

3.2 Global fits

In figure 3 we show the result of including the relic density constraint from the WMAP 5-year data, along with all other experimental bounds. The effect is to favour models populating two distinct regions: a broad strip around the canonical WIMP annihilation cross-section at $3 \times 10^{-26} \text{ cm}^3 \text{ s}^{-1}$, and a low-mass region at smaller cross-sections, corresponding to models where stau co-annihilations reduce the relic density to the observed level despite the very low self-annihilation rates. The models disfavoured by FERMI observations of Segue 1 in figure 2 are here already strongly disfavoured by the relic density constraint, so the additional data from the LAT appears to have little impact upon the preferred cross-sections and masses. A slight reduction in the profile likelihoods of the lowest mass, highest cross-section corner of the preferred region appears to be present in the extrapolation to 5 years of data.

The best-fit point is however rather different in the 9-month scan as compared to scans without Fermi data, or with 5 years of mock observations (where we assumed that no excess above background will be seen in 5 years). In the 9-month scan, the best fit occurs in the focus point region, at a high annihilation cross-section and a low neutralino mass ($\langle\sigma v\rangle = 1.8 \times 10^{-26} \text{ cm}^3 \text{ s}^{-1}$, $m_\chi = 95 \text{ GeV}$), whereas the best fits in the other cases are for stau coannihilation models. This difference appears to be the result of a very small statistical excess above the modelled background in the 9-month data. Because the corresponding

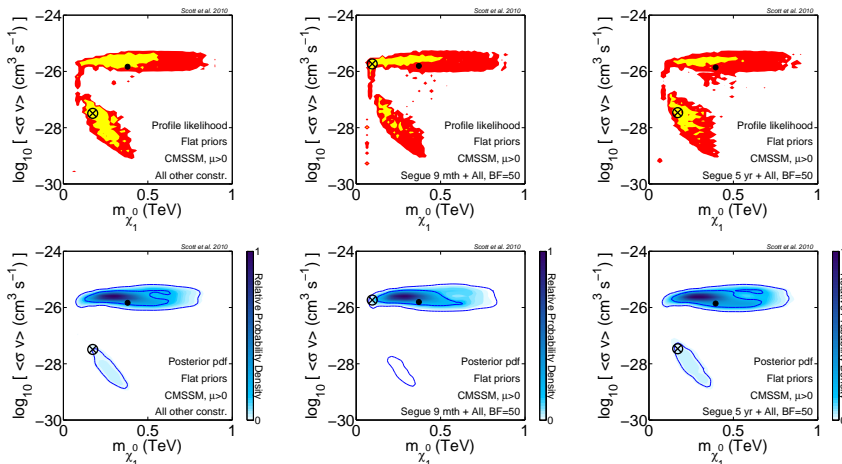


Figure 3. Annihilation cross-sections in the CMSSM which fit all experimental constraints, assuming the neutralino to be the dominant component of dark matter. Favoured regions are as implied by existing experimental data only (*left*), and with the addition of 9 months of Segue 1 observations by FERMI (*middle*). We also show the extrapolated impact of a non-observation of Segue 1 after 5 years (*right*). Upper plots show profile likelihoods (where yellow and red indicate 68% and 95% confidence regions respectively), while lower plots show marginalised posterior PDFs (where solid blue contours give 68% and 95% credible regions). Solid dots indicate posterior means, whereas crosses indicate best-fit points.

confidence regions are not substantially altered despite the movement of the best fit, the excess would appear to be consistent with observational (statistical) noise. Given the range of FERMI’s sensitivity, it is thus not at all surprising that the best-fit would appear at this location, falling right on the edge of the instrument’s sensitivity. This point may however be an interesting one to watch as statistics improve.

It is instructive to note the difference in how the co-annihilation region is represented in figure 3 by the profile likelihood and the marginalised posterior. Because the range of CMSSM parameters spanned by the co-annihilation region is quite narrow (i.e. fine-tuned), the total number of points in this region found by the scans is not particularly high, leading to a relatively low posterior PDF. This is despite the fact that very good fits can be found with a reasonably broad range of neutralino masses and cross-sections in this region, as evidenced by its size in the profile likelihood plots. In this sense, the Bayesian posterior PDF can be seen to penalise the co-annihilation region to a certain degree for being fine-tuned. Whether this is a desirable characteristic or not is of course a matter of opinion. It is, however, important to recognise that such information is only accessible by comparing the posterior PDF and the profile likelihood; the information in their combination is greater than the sum of the parts.

A natural question to ask might be whether more interesting constraints could be obtained from Segue 1 by allowing the neutralino to be a sub-dominant component of dark matter. Unfortunately, this generally does not add a lot to the discussion when considering constraints from indirect detection with gamma-rays. Even though the relic density is essentially inversely proportional to the annihilation cross-section, in mixed dark matter

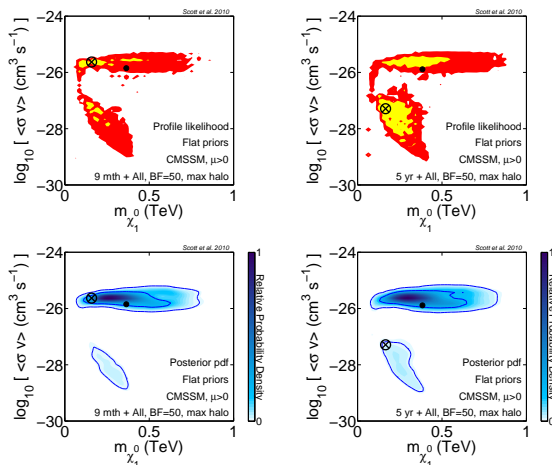


Figure 4. Annihilation cross-sections in the CMSSM which fit all experimental constraints, assuming a ‘maximally dense’ dark matter halo profile for Segue 1. In this case, the halo scale radius and density were chosen $\sim 2\sigma$ away from the best-fit values derived from stellar kinematic data. Here we again assume the neutralino to be the dominant component of dark matter. Favoured regions are as implied by 9 months of Segue 1 observations by FERMI (*left*), and extrapolations to 5 years of data assuming no signal from Segue 1 (*right*). Shadings and markings are as per figure 3.

scenarios the density of neutralinos in Segue 1 becomes directly proportional to the relic density. The expected signal is then increased due to the larger annihilation cross-sections permitted by sub-dominant relic densities, but reduced by the reduction in signal due to the reduced galactic densities. The net result is a reduction in the expected signal, since the flux (eq. (2.1)) depends upon the first power of the annihilation cross-section, but the square of the density. Thus for a decrease in the relic density such that $\Omega_\chi \rightarrow \Omega_\chi/X$, the flux is modified as $\Phi \rightarrow X/X^2\Phi = \Phi/X$. The result is that the favoured cross-sections move to higher values, but the constraints from Segue 1 move even further, providing less constraining power than when the neutralino is assumed to be the only component of dark matter. This argument of course may not hold for points in the parameter space where the relic density is not strictly inversely proportional to the annihilation cross-section, such as strong co-annihilation or resonant annihilation scenarios. The former certainly are not probed by the Segue 1 observations in any case, since they lie at very low annihilation cross-sections. In principle though, highly fine-tuned points in the latter scenario could slightly modify the impact of the Segue constraints in subdominant situations. As discussed below however, our scans do not uncover a significant number of models where such a mechanism occurs.

In figure 4 we investigate whether variations in the dark matter profile of Segue 1, within the errors of Martinez et al. [15], might also produce more interesting constraints. Here we again take an Einasto profile (eq. (2.4)), but instead use parameters corresponding to the most dark-matter-rich profile allowed at $\sim 2\sigma$ ($r_s = 10$ pc, $\rho_s = 70$ GeV cm $^{-3}$). The corresponding constraints on annihilation cross-sections are indeed stronger than in figure 3, but are still largely dominated by the relic density. This is not surprising, as even though the scale density is a factor of 18 higher in this case, the smaller scale radius means that

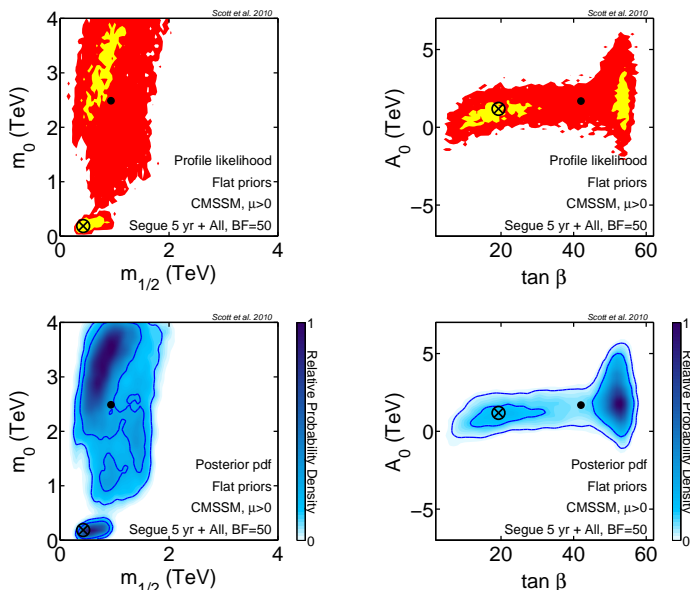


Figure 5. Preferred CMSSM parameter regions including FERMI-LAT observations of Segue 1 and all other observables. Shadings and markings are as per figure 3. Preferred regions are very similar whether one considers the existing 9 months of LAT data or extrapolates to 5 years of observations.

the higher density occurs at a smaller radius. In this sense the two parameters are partially degenerate; because FERMI probes essentially the whole dwarf halo (as Segue 1 should appear almost as a point source), and the total mass of Segue 1 is not substantially altered by the change in halo parameters, the corresponding constraints are not massively improved. The constraints coming from 9 months of data can be seen to cluster more tightly around the best-fit point at low mass and high cross-section, but not to the point where significant parts of the rest of the parameter space are excluded. This is consistent with our assertion above that any excess can be explained in terms of statistical fluctuations.

The preferred CMSSM parameter regions including all constraints are shown in figure 5. Given the marginal impact of Segue 1 observations on scans including the relic density, it is not surprising that the regions are very similar to those shown in [42], even when using the extrapolation to 5 years of observations. The stau co-annihilation region is clearly visible at low m_0 and $m_{1/2}$, separated from the focus point region at larger m_0 . Scans indicate that both regions are equally well-favoured, though the co-annihilation region tends to return the best-fit point in most cases. The bulk region is mostly disfavoured by relic density and LEP constraints [32], but persists at low masses in our scans, overlapping the co-annihilation region in the m_0 - $m_{1/2}$ plane. The high-probability region at low $\tan\beta$ in the A_0 - $\tan\beta$ plane favoured by the co-annihilation region shows up as a much smoother peak in our scans than in some previous works [32, 39, 42]. We suspect that this is due to our use of the upgraded version of DarkSUSY for the relic density calculation.

The ‘funnel’ region, where resonant annihilation can become important at very low $m_{1/2}$,

does not show up in our scans here. This is unsurprising, as the nested sampling algorithm is designed to sample according to the total posterior mass, and the linear prior places a very small scanning weight upon such fine-tuned regions at low mass. Nested sampling routines only find this region when using logarithmic priors on m_0 and $m_{\frac{1}{2}}$ [42], though normal MCMC scans can find it a little more easily (e.g. [32, 39]). On the other hand, standard MCMCs and nested sampling implemented with logarithmic priors sample the focus point region less densely, causing them to sometimes miss the highest-likelihood points important for a profile likelihood analysis. These difficulties are typical consequences of using scanning algorithms designed for Bayesian analyses to compute the frequentist profile likelihood; a more promising path for frequentist scans appears to be to use genetic algorithms [44]. Using genetic algorithms, it seems possible to find all high-likelihood regions in a prior-independent way, but the ability to effectively map their surroundings and produce reliable confidence regions lags behind other techniques.

Some recent MCMC scans [49, 50] have not found large focus-point regions which fit all experimental constraints well, leading the authors to claim that the co-annihilation region is favoured by present data. In these cases, the reduced likelihood in the focus point region relative to the co-annihilation region was almost entirely due to the fact that it is virtually impossible to produce a good fit to the muon $g - 2$ with large values of m_0 in the CMSSM. Using nested sampling with linear priors however, and the physics and likelihood routines within *SuperBayes*, one can find points in the focus point region where this effect is essentially offset by a correspondingly better fit to other observables [42].

4 Conclusions

We have incorporated fits to 9 months of FERMI-LAT observations of the dwarf galaxy Segue 1 into explicit global CMSSM parameter scans. We included gamma-ray lines, internal bremsstrahlung and secondary decay, as well as detailed characterisations of the detector response, its uncertainties and the observed background. We have also presented scans illustrating the estimated impact of a non-observation of dark matter annihilation in Segue 1 after 5 years of LAT operation.

The LAT data disfavour a small number of physically-viable CMSSM models with low neutralino masses and high annihilation cross-sections, but results depend strongly upon the assumed substructure boost factor in Segue 1. Such models are already strongly disfavoured by relic density constraints. Extrapolating to 5 years of operation and assuming the most optimistic boost factor presently allowed by astronomical data, the absence of any annihilation signal from Segue 1 would disfavour all models with cross sections higher than $10^{-25} \text{ cm}^3 \text{ s}^{-1}$, as well as a number at low mass with cross-sections as low as $10^{-26} \text{ cm}^3 \text{ s}^{-1}$. Even at this level however, the CMSSM models disfavoured by FERMI would already be essentially excluded by existing data from the microwave background and terrestrial experiments.

Acknowledgments

We are grateful to our colleagues in the FERMI-LAT Dark Matter & New Physics group for many helpful comments and discussions, and to Riccardo Rando for advice on the LAT IRFs. We also thank Roberto Trotta for comments on an earlier version of the manuscript. Through *DarkSUSY*, *FLATlib* and *SuperBayes* we also drew upon a number of other publicly-available scientific codes, including *CUBPACK* [75], *FeynHiggs* [76], *SLHALib* [77], *SoftSUSY* [78] and

WCSLIB [79]. PS, JC, JE, LB and YA are grateful to the Swedish Research Council (VR) for financial support. JC is a Royal Swedish Academy of Sciences Research Fellow supported by a grant from the Knut and Alice Wallenberg Foundation.

A number of agencies and institutes have supported both the development and the operation of the LAT as well as scientific data analysis. These include the National Aeronautics and Space Administration and the Department of Energy in the United States, the Commissariat à l’Energie Atomique and the Centre National de la Recherche Scientifique / Institut National de Physique Nucléaire et de Physique des Particules in France, the Agenzia Spaziale Italiana and the Istituto Nazionale di Fisica Nucleare in Italy, the Ministry of Education, Culture, Sports, Science and Technology (MEXT), High Energy Accelerator Research Organisation (KEK) and Japan Aerospace Exploration Agency (JAXA) in Japan, and the K. A. Wallenberg Foundation, the Swedish Research Council and the Swedish National Space Board in Sweden. Additional support for science analysis during the operations phase is gratefully acknowledged from the Istituto Nazionale di Astrofisica in Italy and the and the Centre National d’Études Spatiales in France.

References

- [1] G. Jungman, M. Kamionkowski and K. Griest, *Supersymmetric dark matter*, *Phys. Rept.* **267** (1996) 195 [[hep-ph/9506380](#)] [[SPIRES](#)].
- [2] L. Bergström, *Non-baryonic dark matter: observational evidence and detection methods*, *Rept. Prog. Phys.* **63** (2000) 793 [[hep-ph/0002126](#)] [[SPIRES](#)].
- [3] G. Bertone, D. Hooper and J. Silk, *Particle dark matter: evidence, candidates and constraints*, *Phys. Rept.* **405** (2005) 279 [[hep-ph/0404175](#)] [[SPIRES](#)].
- [4] L. Bergström, *Dark matter candidates*, *New J. Phys.* **11** (2009) 105006 [[arXiv:0903.4849](#)] [[SPIRES](#)].
- [5] H. Baer and X. Tata, *Weak scale supersymmetry*, Cambridge University Press, Cambridge U.K. (2006).
- [6] I. Aitchison, *Supersymmetry in particle physics*, Cambridge University Press, Cambridge U.K. (2007).
- [7] L.E. Strigari et al., *The most dark matter dominated galaxies: predicted gamma-ray signals from the faintest Milky Way dwarfs*, *Astrophys. J.* **678** (2008) 614 [[arXiv:0709.1510](#)] [[SPIRES](#)].
- [8] T. Bringmann, M. Doro and M. Fornasa, *Dark matter signals from Draco and Willman 1: prospects for MAGIC II and CTA*, *JCAP* **01** (2009) 016 [[arXiv:0809.2269](#)] [[SPIRES](#)].
- [9] L. Pieri, A. Pizzella, E.M. Corsini, E.D. Bontà and F. Bertola, *Could the Fermi-LAT detect gamma-rays from dark matter annihilation in the dwarf galaxies of the local group?*, *Astron. Astrophys.* **496** (2009) 351 [[arXiv:0812.1494](#)] [[SPIRES](#)].
- [10] R. Essig, N. Sehgal and L.E. Strigari, *Bounds on cross-sections and lifetimes for dark matter annihilation and decay into charged leptons from gamma-ray observations of dwarf galaxies*, *Phys. Rev. D* **80** (2009) 023506 [[arXiv:0902.4750](#)] [[SPIRES](#)].
- [11] S. Lombardi et al., *Search for dark matter signatures with MAGIC-I and prospects for MAGIC phase-II*, [arXiv:0907.0738](#) [[SPIRES](#)].
- [12] J.D. Simon and M. Geha, *The kinematics of the ultra-faint Milky Way satellites: solving the missing satellite problem*, *Astrophys. J.* **670** (2007) 313 [[arXiv:0706.0516](#)] [[SPIRES](#)].

- [13] V. Belokurov et al., *The discovery of Segue 2: a prototype of the population of satellites*, *Mon. Not. Roy. Astron. Soc.* **397** (2009) 1748 [[arXiv:0903.0818](#)] [[SPIRES](#)].
- [14] M. Geha et al., *The least luminous galaxy: spectroscopy of the Milky Way satellite Segue 1*, *Astrophys. J.* **692** (2009) 1464 [[arXiv:0809.2781](#)] [[SPIRES](#)].
- [15] G.D. Martinez, J.S. Bullock, M. Kaplinghat, L.E. Strigari and R. Trotta, *Indirect dark matter detection from dwarf satellites: joint expectations from astrophysics and supersymmetry*, *JCAP* **06** (2009) 014 [[arXiv:0902.4715](#)] [[SPIRES](#)].
- [16] M. Kuhlen, *The dark matter annihilation signal from dwarf galaxies and subhalos*, [arXiv:0906.1822](#) [[SPIRES](#)].
- [17] SDSS collaboration, V. Belokurov et al., *Cats and dogs, hair and a hero: a quintet of new Milky Way companions*, *Astrophys. J.* **654** (2007) 897 [[astro-ph/0608448](#)] [[SPIRES](#)].
- [18] M. Xiang-Gruss, Y.-Q. Lou and W.J. Duschl, *Dark matter dominated dwarf disc galaxy Segue 1*, *Mon. Not. Roy. Astron. Soc.* **400** (2009) L52 [[arXiv:0909.3496](#)] [[SPIRES](#)].
- [19] M. Niederste-Ostholt et al., *The origin of Segue 1*, [arXiv:0906.3669](#) [[SPIRES](#)].
- [20] M. Geha, *Ultra-faint satellites of the Milky Way*, presentation at *TeV particle astrophysics V*, Stanford U.S.A. July 14 2009.
- [21] FERMI-LAT collaboration, W.B. Atwood et al., *The Large Area Telescope on the Fermi gamma-ray space telescope mission*, *Astrophys. J.* **697** (2009) 1071 [[arXiv:0902.1089](#)] [[SPIRES](#)].
- [22] E.A. Baltz et al., *Pre-launch estimates for GLAST sensitivity to dark matter annihilation signals*, *JCAP* **07** (2008) 013 [[arXiv:0806.2911](#)] [[SPIRES](#)].
- [23] FERMI-LAT collaboration, C. Meurer, *Dark matter searches with the Fermi Large Area Telescope*, *AIP Conf. Proc.* **719** (2009) 1085 [[arXiv:0904.2348](#)] [[SPIRES](#)].
- [24] FERMI-LAT collaboration, C. Farnier, E. Nuss and J. Cohen-Tanugi, *Dark matter annihilations search in dwarf spheroidal galaxies with Fermi*, in *Proceedings of the 2nd Roma International Conference on Astro-Particle Physics*, (2009). *Nucl. Instr. Meth. A* in press.
- [25] FERMI-LAT collaboration, *Observations of dwarf spheroidal galaxies with the Fermi-LAT detector and constraints on dark matter models*, in preparation (2009).
- [26] FERMI-LAT collaboration, P. Wang, *The search for dark matter Galactic satellites with Fermi-LAT*, presentation at *TeV Particle Astrophysics V*, Stanford U.S.A. July 14 2009.
- [27] FERMI-LAT collaboration, A.A. Abdo et al., *Measurement of the cosmic ray e^+ plus e^- spectrum from 20 GeV to 1 TeV with the Fermi Large Area Telescope*, *Phys. Rev. Lett.* **102** (2009) 181101 [[arXiv:0905.0025](#)] [[SPIRES](#)].
- [28] A.H. Chamseddine, R.L. Arnowitt and P. Nath, *Locally supersymmetric grand unification*, *Phys. Rev. Lett.* **49** (1982) 970 [[SPIRES](#)].
- [29] G.F. Giudice and R. Rattazzi, *Theories with gauge-mediated supersymmetry breaking*, *Phys. Rept.* **322** (1999) 419 [[hep-ph/9801271](#)] [[SPIRES](#)].
- [30] L. Randall and R. Sundrum, *Out of this world supersymmetry breaking*, *Nucl. Phys. B* **557** (1999) 79 [[hep-th/9810155](#)] [[SPIRES](#)].
- [31] S.P. Martin, *A supersymmetry primer*, in *Perspectives on supersymmetry*, G.L. Kane ed., (1997), pg. 1 [[hep-ph/9709356](#)] [[SPIRES](#)].
- [32] B.C. Allanach and C.G. Lester, *Multi-dimensional mSUGRA likelihood maps*, *Phys. Rev. D* **73** (2006) 015013 [[hep-ph/0507283](#)] [[SPIRES](#)].
- [33] M. Drees and M.M. Nojiri, *The neutralino relic density in minimal $N = 1$ supergravity*, *Phys. Rev. D* **47** (1993) 376 [[hep-ph/9207234](#)] [[SPIRES](#)].

- [34] H. Baer and M. Brhlik, *Cosmological relic density from minimal supergravity with implications for collider physics*, *Phys. Rev. D* **53** (1996) 597 [[hep-ph/9508321](#)] [[SPIRES](#)].
- [35] J.R. Ellis, T. Falk, G. Gani, K.A. Olive and M. Srednicki, *The CMSSM parameter space at large $\tan\beta$* , *Phys. Lett. B* **510** (2001) 236 [[hep-ph/0102098](#)] [[SPIRES](#)].
- [36] J.R. Ellis, K.A. Olive, Y. Santoso and V.C. Spanos, *Likelihood analysis of the CMSSM parameter space*, *Phys. Rev. D* **69** (2004) 095004 [[hep-ph/0310356](#)] [[SPIRES](#)].
- [37] L. Roszkowski, R. Ruiz de Austri and T. Nihei, *New cosmological and experimental constraints on the CMSSM*, *JHEP* **08** (2001) 024 [[hep-ph/0106334](#)] [[SPIRES](#)].
- [38] E.A. Baltz and P. Gondolo, *Markov chain Monte Carlo exploration of minimal supergravity with implications for dark matter*, *JHEP* **10** (2004) 052 [[hep-ph/0407039](#)] [[SPIRES](#)].
- [39] R. Ruiz de Austri, R. Trotta and L. Roszkowski, *A Markov chain Monte Carlo analysis of the CMSSM*, *JHEP* **05** (2006) 002 [[hep-ph/0602028](#)] [[SPIRES](#)].
- [40] J. Skilling, *Nested sampling*, in *AIP Conf. Proc.* **735** (2004) 395, R. Fischer, R. Preuss and U.V. Toussaint eds., U.S.A. (2004).
- [41] F. Feroz, M.P. Hobson and M. Bridges, *MultiNest: an efficient and robust Bayesian inference tool for cosmology and particle physics*, [arXiv:0809.3437](#) [[SPIRES](#)].
- [42] R. Trotta, F. Feroz, M.P. Hobson, L. Roszkowski and R. Ruiz de Austri, *The impact of priors and observables on parameter inferences in the constrained MSSM*, *JHEP* **12** (2008) 024 [[arXiv:0809.3792](#)] [[SPIRES](#)].
- [43] S.S. AbdusSalam, B.C. Allanach, F. Quevedo, F. Feroz and M. Hobson, *Fitting the phenomenological MSSM*, [arXiv:0904.2548](#) [[SPIRES](#)].
- [44] Y. Akrami, P. Scott, J. Edsjö, J. Conrad and L. Bergström, *A profile likelihood analysis of the constrained MSSM with genetic algorithms*, [arXiv:0910.3950](#) [[SPIRES](#)].
- [45] R.C. Cotta, J.S. Gainer, J.L. Hewett and T.G. Rizzo, *Dark matter in the MSSM*, *New J. Phys.* **11** (2009) 105026 [[arXiv:0903.4409](#)] [[SPIRES](#)].
- [46] C.F. Berger, J.S. Gainer, J.L. Hewett and T.G. Rizzo, *Supersymmetry without prejudice*, *JHEP* **02** (2009) 023 [[arXiv:0812.0980](#)] [[SPIRES](#)].
- [47] L. Roszkowski, R. Ruiz de Austri, R. Trotta, Y.-L.S. Tsai and T.A. Varley, *Some novel features of the non-universal Higgs model*, [arXiv:0903.1279](#) [[SPIRES](#)].
- [48] S.S. AbdusSalam, B.C. Allanach, M.J. Dolan, F. Feroz and M.P. Hobson, *Selecting a model of supersymmetry breaking mediation*, *Phys. Rev. D* **80** (2009) 035017 [[arXiv:0906.0957](#)] [[SPIRES](#)].
- [49] O. Buchmueller et al., *Predictions for supersymmetric particle masses in the CMSSM using indirect experimental and cosmological constraints*, *JHEP* **09** (2008) 117 [[arXiv:0808.4128](#)] [[SPIRES](#)].
- [50] O. Buchmueller et al., *Likelihood functions for supersymmetric observables in frequentist analyses of the CMSSM and NUHM1*, *Eur. Phys. J. C* **64** (2009) 391 [[arXiv:0907.5568](#)] [[SPIRES](#)].
- [51] C. Balázs and D. Carter, *Discovery potential of the next-to-minimal supergravity motivated model*, *Phys. Rev. D* **78** (2008) 055001 [[arXiv:0808.0770](#)] [[SPIRES](#)].
- [52] C. Balázs and D. Carter, *Likelihood analysis of the next-to-minimal supergravity motivated model*, *AIP Conf. Proc.* **1178** (2009) 23 [[arXiv:0906.5012](#)] [[SPIRES](#)].
- [53] D.E. Lopez-Fogliani, L. Roszkowski, R.R. de Austri and T.A. Varley, *A Bayesian analysis of the constrained NMSSM*, *Phys. Rev. D* **80** (2009) 095013 [[arXiv:0906.4911](#)] [[SPIRES](#)].

- [54] L. Roszkowski, R. Ruiz de Austri, J. Silk and R. Trotta, *On prospects for dark matter indirect detection in the constrained MSSM*, *Phys. Lett. B* **671** (2009) 10 [[arXiv:0707.0622](#)] [[SPIRES](#)].
- [55] R. Trotta, R. Ruiz de Austri and C. Pérez de los Heros, *Prospects for dark matter detection with IceCube in the context of the CMSSM*, *JCAP* **08** (2009) 034 [[arXiv:0906.0366](#)] [[SPIRES](#)].
- [56] P. Scott and S. Sivertsson, *Gamma-rays from ultracompact primordial dark matter minihalos*, *Phys. Rev. Lett.* **103** (2009) 211301 [[arXiv:0908.4082](#)] [[SPIRES](#)].
- [57] L. Bergström, P. Ullio and J.H. Buckley, *Observability of gamma rays from dark matter neutralino annihilations in the Milky Way halo*, *Astropart. Phys.* **9** (1998) 137 [[astro-ph/9712318](#)] [[SPIRES](#)].
- [58] L. Bergström and H. Snellman, *Observable monochromatic photons from cosmic photino annihilation*, *Phys. Rev. D* **37** (1988) 3737 [[SPIRES](#)].
- [59] L. Bergström and P. Ullio, *Full one-loop calculation of neutralino annihilation into two photons*, *Nucl. Phys. B* **504** (1997) 27 [[hep-ph/9706232](#)] [[SPIRES](#)].
- [60] P. Ullio and L. Bergström, *Neutralino annihilation into a photon and a Z boson*, *Phys. Rev. D* **57** (1998) 1962 [[hep-ph/9707333](#)] [[SPIRES](#)].
- [61] T. Bringmann, L. Bergström and J. Edsjö, *New gamma-ray contributions to supersymmetric dark matter annihilation*, *JHEP* **01** (2008) 049 [[arXiv:0710.3169](#)] [[SPIRES](#)].
- [62] P. Gondolo et al., *DarkSUSY: computing supersymmetric dark matter properties numerically*, *JCAP* **07** (2004) 008 [[astro-ph/0406204](#)] [[SPIRES](#)].
- [63] J.F. Navarro et al., *The inner structure of Λ CDM halos III: universality and asymptotic slopes*, *Mon. Not. Roy. Astron. Soc.* **349** (2004) 1039 [[astro-ph/0311231](#)] [[SPIRES](#)].
- [64] J.F. Navarro, C.S. Frenk and S.D.M. White, *The structure of cold dark matter halos*, *Astrophys. J.* **462** (1996) 563 [[astro-ph/9508025](#)] [[SPIRES](#)].
- [65] A.W. Graham, D. Merritt, B. Moore, J. Diemand and B. Terzić, *Empirical models for dark matter halos. I. Nonparametric construction of density profiles and comparison with parametric models*, *Astron. J.* **132** (2006) 2685 [[astro-ph/0509417](#)] [[SPIRES](#)].
- [66] L. Gao et al., *The redshift dependence of the structure of massive Λ CDM halos*, *Mon. Not. Roy. Astron. Soc.* **387** (2008) 536 [[arXiv:0711.0746](#)] [[SPIRES](#)].
- [67] P. Scott, *FLATlib*, <http://www.fysik.su.se/~pat/flatlib>. We intend to describe FLATlib in greater detail in a forthcoming technical note.
- [68] FERMI-LAT collaboration, *Large-scale Galactic gamma rays with Fermi-LAT: implications for cosmic rays and the interstellar medium*, in preparation (2009).
- [69] EGRET collaboration, P. Sreekumar et al., *EGRET observations of the extragalactic gamma ray emission*, *Astrophys. J.* **494** (1998) 523 [[astro-ph/9709257](#)] [[SPIRES](#)].
- [70] FERMI-LAT collaboration, T. Jeltema, *Searching for dark matter annihilation in dwarf spheroidal galaxies with Fermi*, presentation at *TeV Particle Astrophysics V*, Stanford U.S.A. July 14 2009.
- [71] J. Conrad, O. Botner, A. Hallgren and C. Pérez de los Heros, *Including systematic uncertainties in confidence interval construction for Poisson statistics*, *Phys. Rev. D* **67** (2003) 012002 [[hep-ex/0202013](#)] [[SPIRES](#)].
- [72] R. Trotta, *Bayes in the sky: bayesian inference and model selection in cosmology*, *Contemp. Phys.* **49** (2008) 71 [[arXiv:0803.4089](#)] [[SPIRES](#)].
- [73] WMAP collaboration, J. Dunkley et al., *Five-year Wilkinson Microwave Anisotropy Probe (WMAP) observations: likelihoods and parameters from the WMAP data*, *Astrophys. J. Suppl.* **180** (2009) 306 [[arXiv:0803.0586](#)] [[SPIRES](#)].

- [74] M. Frigo and S.G. Johnson, *The design and implementation of FFTW3*, *IEEE Proc.* **93** (2005) 216.
- [75] R. Cools and A. Haegemans, *Algorithm 824: Cubpack: a package for automatic cubature; framework description*, *ACM Trans. Math. Software* **29** (2003) 287.
- [76] S. Heinemeyer, W. Hollik and G. Weiglein, *FeynHiggs: a program for the calculation of the masses of the neutral CP-even Higgs bosons in the MSSM*, *Comput. Phys. Commun.* **124** (2000) 76 [[hep-ph/9812320](#)] [[SPIRES](#)].
- [77] T. Hahn, *SUSY Les Houches Accord 2 I/O made easy*, *Comput. Phys. Commun.* **180** (2009) 1681 [[hep-ph/0605049](#)] [[SPIRES](#)].
- [78] B.C. Allanach, *SOFTSUSY: a C++ program for calculating supersymmetric spectra*, *Comput. Phys. Commun.* **143** (2002) 305 [[hep-ph/0104145](#)] [[SPIRES](#)].
- [79] M.R. Calabretta and E.W. Greisen, *Representations of celestial coordinates in FITS*, *Astron. Astrophys.* **395** (2002) 1077 [[astro-ph/0207413](#)] [[SPIRES](#)].

Paper V

Yashar Akrami, Pat Scott, Joakim Edsjö, Jan Conrad & Lars Bergström
A profile likelihood analysis of the Constrained MSSM with genetic algorithms
JHEP in press, arXiv:0910.3950 (2010).

A Profile Likelihood Analysis of the Constrained MSSM with Genetic Algorithms

Yashar Akrami, Pat Scott, Joakim Edsjö, Jan Conrad and Lars Bergström

Oskar Klein Centre for Cosmoparticle Physics

Department of Physics, Stockholm University

AlbaNova, SE-10691 Stockholm, Sweden

E-mails: [yashar](#), [pat](#), [edsjo](#), [conrad](#), [lbe@fysik.su.se](#)

ABSTRACT: The Constrained Minimal Supersymmetric Standard Model (CMSSM) is one of the simplest and most widely-studied supersymmetric extensions to the standard model of particle physics. Nevertheless, current data do not sufficiently constrain the model parameters in a way completely independent of priors, statistical measures and scanning techniques. We present a new technique for scanning supersymmetric parameter spaces, optimised for frequentist profile likelihood analyses and based on Genetic Algorithms. We apply this technique to the CMSSM, taking into account existing collider and cosmological data in our global fit. We compare our method to the MultiNest algorithm, an efficient Bayesian technique, paying particular attention to the best-fit points and implications for particle masses at the LHC and dark matter searches. Our global best-fit point lies in the focus point region. We find many high-likelihood points in both the stau co-annihilation and focus point regions, including a previously neglected section of the co-annihilation region at large m_0 . We show that there are many high-likelihood points in the CMSSM parameter space commonly missed by existing scanning techniques, especially at high masses. This has a significant influence on the derived confidence regions for parameters and observables, and can dramatically change the entire statistical inference of such scans.

KEYWORDS: [Supersymmetry Phenomenology](#), [Supersymmetric Standard Model](#), [Cosmology of Theories beyond the SM](#).

Contents

1. Introduction	1
2. Model and analysis	6
2.1 CMSSM likelihood	6
2.1.1 Parameters and ranges	6
2.1.2 Constraints: physicality, observables, and uncertainties	7
2.2 Genetic Algorithms and profile likelihoods of the CMSSM	9
2.2.1 Main strategy	10
2.2.2 Our specific implementation	12
3. Results and discussion	15
3.1 Best-fit points and high-likelihood regions	15
3.2 Implications for the LHC	23
3.3 Implications for dark matter searches	25
3.4 Technical comparison with nested sampling	28
3.4.1 Dependence on priors and parameterisation	28
3.4.2 Speed and convergence	30
4. Summary and conclusions	34

1. Introduction

New physics beyond the Standard Model (SM) is broadly conjectured to appear at TeV energy scales. Particular attention has been paid to supersymmetric (SUSY) extensions of the SM, widely hoped to show up at the Large Hadron Collider (LHC). One of the strongest motivations for physics at the new scale is the absence of any SM mechanism for protecting the Higgs mass against radiative corrections; this is known as the hierarchy or fine-tuning problem [1]. Softly-broken weak-scale supersymmetry (for an introduction, see Ref. 2) provides a natural solution to this problem via the cancellation of quadratic divergences in radiative corrections to the Higgs mass. The natural connection between SUSY and grand unified theories (GUTs) also offers extensive scope for achieving gauge-coupling unification in this framework [3]. Supersymmetry has even turned out to be a natural component of many string theories, so it may be worth incorporating into extensions of the SM anyway (though in these models it is not at all necessary for SUSY to be detectable at low energies).

Another major theoretical motivation for supersymmetry is that most weak-scale versions contain a viable dark matter (DM) candidate [4]. Its stability is typically achieved via a conserved discrete symmetry (R -parity) which arises naturally in some GUTs, and

makes the lightest supersymmetric particle (LSP) stable. Its ‘darkness’ is achieved by having the LSP be a neutral particle, such as the lightest neutralino or sneutrino. These are both weakly-interacting massive particles (WIMPs), making them prime dark matter candidates [4]. The sneutrino is strongly constrained due to its large nuclear-scattering cross-section, but the neutralino remains arguably the leading candidate for DM.

Describing the low-energy behaviour of a supersymmetric model typically requires adding many new parameters to the SM. This makes phenomenological analyses highly complicated. Even upgrading the SM to its most minimal SUSY form, the Minimal Supersymmetric Standard Model (MSSM; for a recent review, see Ref. 5), introduces more than a hundred free parameters. All but one of these come from the soft terms in the SUSY-breaking sector. Fortunately, extensive regions of the full MSSM parameter space are ruled out phenomenologically, as generic values of many of the new parameters allow flavour changing neutral currents (FCNCs) or CP violation at levels excluded by experiment.

One might be able to relate many of these seemingly-free parameters theoretically, dramatically reducing their number. This requires specification of either the underlying SUSY-breaking mechanism itself, or a mediation mechanism by which SUSY-breaking would be conducted from some undiscovered particle sector to the known particle spectrum and its SUSY counterparts. Several mediation mechanisms (for recent reviews, see e.g. Refs. 5 and 6) have been proposed which relate the MSSM parameters in very different ways, but so far no clear preference has been established for one mechanism over another. For a comparison of some mediation models using current data, see Ref. 7. Gravity-mediated SUSY breaking, based on supergravity unification, naturally leads to the suppression of many of the dangerous FCNC and CP-violating terms. Its simplest version is known as minimal supergravity (mSUGRA) [8, 9].

An alternative approach is to directly specify a phenomenological MSSM reduction at low energy. Here one sets troublesome CP-violating and FCNC-generating terms to zero by hand, and further reduces the number of parameters by assuming high degrees of symmetry in e.g. mass and mixing matrices.

A hybrid approach is to construct a phenomenological GUT-scale model, broadly motivated by the connection between SUSY and GUTs. Here one imposes boundary conditions at the GUT scale ($\sim 10^{16}$ GeV) and then explores the low-energy phenomenology by means of the Renormalisation Group Equations (RGEs). One of the most popular schemes is the Constrained MSSM (CMSSM) [10], which incorporates the phenomenologically-interesting parts of mSUGRA. The CMSSM includes four continuous parameters: the ratio of the two Higgs vacuum expectation values ($\tan \beta$), and the GUT-scale values of the SUSY-breaking scalar, gaugino and trilinear mass parameters (m_0 , $m_{1/2}$ and A_0). The sign of μ (the MSSM Higgs/higgsino mass parameter) makes for one additional discrete parameter; its magnitude is determined by requiring that SUSY-breaking induces electroweak symmetry-breaking. Despite greatly curbing the range of possible phenomenological consequences, the small number of parameters in the CMSSM has made it a tractable way to explore basic low-energy SUSY phenomenology.

Before drawing conclusions about model selection or parameter values from experimen-

tal data, one must choose a statistical framework to work in. There are two very different fundamental interpretations of probability, resulting in two approaches to statistics (for a detailed discussion, see e.g. Ref. 11). Frequentism deals with relative frequencies, interpreting probability as the fraction of times an outcome would occur if a measurement were repeated an infinite number of times. Bayesianism deals with subjective probabilities assigned to different hypotheses, interpreting probability as a measure of the degree of belief that a hypothesis is true. The former is used for assigning statistical errors to measurements, whilst the latter can be used to quantify both statistical and systematic uncertainties. In the Bayesian approach one is interested in the probability of a set of model parameters given some data, whereas in the frequentist approach the only quantity one can discuss is the probability of some dataset given a specific set of model parameters, i.e. a likelihood function.

In a frequentist framework, one simply maps a model's likelihood as a function of the model parameters. The point with the highest likelihood is the best fit, and uncertainties upon the parameter values can be given by e.g. iso-likelihood contours in the model parameter space. To obtain joint confidence intervals on a subset of parameters, the full likelihood is reduced to a lower-dimensional function by maximising it along the unwanted directions in the parameter space. This is the profile likelihood procedure [12, and references therein]. In the Bayesian picture [13], probabilities are directly assigned to different volumes in the parameter space. One must therefore also consider the state of subjective knowledge about the relative probabilities of different parameter values, independent of the actual data; this is a prior. In this case, the statistical measure is not the likelihood itself, but a prior-weighted likelihood known as the posterior probability density function (PDF). Because this posterior is nothing but the joint PDF of all the parameters, constraints on a subset of model parameters are obtained by marginalising (i.e. integrating) it over the unwanted parameters. This marginalised posterior is then the Bayesian counterpart to the profile likelihood. Bayesians report the posterior mean as the most-favoured point (given by the expectation values of the parameters according to the marginalised posterior), with uncertainties defined by surfaces containing set percentages of the total marginalised posterior, or 'probability mass'.

One practically interesting consequence of including priors is that they are a powerful tool for estimating how robust a fit is. If the posterior is strongly dependent on the prior, the data are not sufficient to constrain the model parameters. It has been shown that the prior still plays a large role in Bayesian inferences in the CMSSM [14]. If an actual detection occurs at the LHC, this dependency should disappear [44].

Clearly the results of frequentist and Bayesian inferences will not coincide in general. This is especially true if the model likelihood has a complex dependence on the parameters (i.e. not just a simple Gaussian form), and if insufficient experimental data is available. Note that this is true even if the prior is taken to be flat; a flat prior in one parameter basis is certainly not flat in every such basis. In the case of large sample limits both approaches give similar results, because the likelihood and posterior PDF both become almost Gaussian; this is why both are commonly used in scientific data analysis.

The first CMSSM parameter scans were performed on fixed grids in parameter space [15,

16]. Predictions of e.g. the relic density of the neutralino as a cold dark matter candidate or the Higgs/superpartner masses were computed for each point on the grid, and compared with experimental data. In these earliest papers, points for which the predicted quantities were within an arbitrary confidence level (e.g. 1σ , 2σ) were deemed “good”. Because all accepted points are considered equivalently good, this method provides no way to determine points’ relative goodnesses-of-fit, and precludes any deeper statistical interpretation of results.

The first attempts at statistical interpretation were to perform (frequentist) χ^2 analyses with grid scans [17]. Limited random scans were also done in some of these cases. Despite some advantages of grid scans, their main drawback is that the number of points sampled in an N -dimensional space with k points for each parameter grows as k^N , making the method extremely inefficient. This is even true for spaces of moderate dimension like the CMSSM. The lack of efficiency is mainly due to the complexity and highly non-linear nature of the mapping of the CMSSM parameters to physical observables; many important features of the parameter space can be missed by not using a high enough grid resolution.

Another class of techniques that has become popular in SUSY analyses is based on more sophisticated scanning algorithms. These are techniques designed around the Bayesian requirement that a probability surface be mapped in such a way that the density of the resultant points is proportional to the actual probability. However, the points they return can also be used in frequentist analyses. Foremost amongst these techniques is the Markov Chain Monte Carlo (MCMC) method [18–37], which has also been widely used in other branches of science, in particular cosmological data analysis [38]. The MCMC method provides a greatly improved scanning efficiency in comparison to traditional grid searches, scaling as kN instead of k^N for an N -dimensional parameter space. More recently, the framework of nested sampling [39] has come to prominence, particularly via the publicly-available implementation **MultiNest** [40]. A handful of recent papers have explored the CMSSM parameter space or its observables using this technique [14, 32, 41–46], as well as the higher-dimensional spaces of the Constrained Next-to-MSSM (CNMSSM) [47] and phenomenological MSSM (pMSSM) [48]. **MultiNest** was also the technique of choice in the supersymmetry-breaking study of Ref. 7. A CMSSM scan with **MultiNest** takes roughly a factor of ~ 200 less computational effort than a full MCMC scan, whilst results obtained with both algorithms are identical (up to numerical noise) [14].

Besides improved computational efficiency, MCMCs and nested sampling offer other convenient features for both frequentist and Bayesian analyses. In a fully-defined statistical framework, all significant sources of uncertainty can be included, including theoretical uncertainties and our imperfect knowledge of the relevant SM parameters. These can be introduced as additional ‘nuisance’ parameters in the scans, and resultant profile likelihoods and posterior PDFs profiled/marginalised over them. In a similar way, one can profile and marginalise over all parameters at once to make straightforward statistical inferences about any arbitrary function of the model parameters, like neutralino annihilation fluxes [27, 32, 46] or cross-sections [45]. The profiling/marginalisation takes almost no additional computational effort: profiling simply requires finding the sample with the highest likelihood in a list, whereas marginalisation, given the design of MCMCs and nested

sampling, merely requires tallying the number of samples in the list. Finally, it is straightforward to take into account all priors when using these techniques for Bayesian analyses.

Although the prior-dependence of Bayesian inference can be useful for determining the robustness of a fit, it may be considered undesirable when trying to draw concrete conclusions from the fitting procedure. This is because the prior is a subjective quantity, and most researchers intuitively prefer their conclusions not to depend on subjective assessments. In this case, the natural preference would be to rely on a profile likelihood analysis rather than one based on the posterior PDF. The question then becomes: how does one effectively and efficiently explore a parameter space like the CMSSM, with its many finely-tuned regions, in the context of the profile likelihood?

As a first attempt to answer this question, the profile likelihood of the CMSSM was recently mapped with MCMCs [25] and MultiNest [14]. Despite the improved efficiency of these Bayesian methods with respect to grid searches by several orders of magnitude, they are not optimised to look for isolated points with large likelihoods. They are thus very likely to entirely miss high-likelihood regions occupying very tiny volumes in the parameter space. Such regions might have a strong impact on the final results of the profile likelihood scan¹, since the profile likelihood is normalised to the best-fit point and places all regions, no matter how small, on an equal footing. It appears that in the case of the CMSSM there are many such fine-tuned regions. This is seen in e.g. CMSSM profile likelihood maps with different MultiNest scanning priors [14]. Given that the profile likelihood is independent of the prior by definition, these results demonstrate that many high-likelihood regions are missed when using a scanning algorithm optimised for Bayesian statistics. In order to make valid statistical inferences in the context of the profile likelihood, the first (and perhaps most crucial) step is to correctly locate the best-fit points. Setting confidence limits and describing other statistical characteristics of the parameter space makes sense only if this first step is performed correctly.

If one wishes to work confidently in a frequentist framework, some alternative scanning method is clearly needed. The method should be optimised for calculating the profile likelihood, rather than the Bayesian evidence or posterior. Even if the results obtained with such a method turn out to be consistent with those of MCMCs and nested sampling, the exercise would greatly increase the utility and trustworthiness of those techniques.

In this paper, we employ a particular class of optimisation techniques known as Genetic Algorithms (GAs) to scan the CMSSM parameter space, performing a global frequentist fit to current collider and cosmological data. GAs and other evolutionary algorithms have not yet been widely used in high energy physics or cosmology; to our knowledge, their only prior use in SUSY phenomenology [49] has been for purposes completely different to ours². There are two main reasons GAs should perform well in profile likelihood scans. Firstly, the sole design purpose of GAs is to maximise or minimise a function. This is exactly what is required by the profile likelihood; in the absence of any need to marginalise (i.e. integrate) over dimensions in the parameter space, it is more important that a search

¹Missing fine-tuned regions could even modify the posterior PDF if they are numerous or large enough.

²See e.g. Refs. 50–52 for their use in high energy physics, Ref. 53 for uses in cosmology and general relativity, and Ref. 54 for applications to nuclear physics.

algorithm finds the best-fit peaks than accurately maps the likelihood surface at lower elevations. Secondly, the ability of GAs to probe global extrema excels most clearly over other techniques when the parameter space is very large, complex or poorly understood; this is precisely the situation for SUSY models. We focus exclusively on the CMSSM as our test-bed model, but the algorithms could easily be employed in higher-dimensional SUSY parameter spaces without considerable change in the scanning efficiency (as they scale as kN for an N -dimensional parameter space). We compare our profile likelihood results directly with those of the **MultiNest** scanning algorithm. This means that we also compare indirectly with MCMC scans, because **MultiNest** and MCMCs give essentially identical results [14]. We find that GAs uncover many better-fit points than previous **MultiNest** scans.

This paper proceeds as follows: in Sec. 2 we briefly review the parameters of the CMSSM, the predicted observables, constraints and bounds on them from collider and cosmological observations. We then introduce GAs as our specific scanning technique of choice. We present and discuss results in Sec. 3, comparing those obtained with GAs to those produced by **MultiNest**. We include the best-fit points and the highest-likelihood regions of the parameter space, as well as the implications for particle discovery at the LHC and in direct and indirect dark matter searches. We draw conclusions and comment on future prospects in Sec. 4.

2. Model and analysis

2.1 CMSSM likelihood

Our goal is to compare the results of a profile likelihood analysis of the CMSSM performed with GAs to those obtained using Bayesian scanning techniques, in particular **MultiNest**. For this reason, we work with the same set of free parameters and ranges, the same observables (measurable physical quantities predicted by the model) and the same constraints (the observed values of observables, as well as physicality requirements) as in Ref. 14. We also perform the theoretical calculations and construct the full likelihood function of the model based on these variables and data in the same way as in Ref. 14. We limit ourselves to just a brief review of these quantities and constraints here. For a detailed discussion, the reader is referred to previous papers [14, 21, 24].

2.1.1 Parameters and ranges

As pointed out in Sec. 1, there are four new continuous parameters $m_{1/2}$, m_0 , A_0 and $\tan\beta$, which are the main free parameters of the model to be fit to the data. There is also a new discrete parameter, the sign of μ , which we fix to be positive.³

³The choice of positive μ is motivated largely by constraints on the CMSSM from the anomalous magnetic moment of the muon $\delta a_\mu^{\text{SUSY}}$. The branching fraction $BR(\bar{B} \rightarrow X_s \gamma)$ actually prefers negative μ (see, for example, Ref. 41 and the references therein). $\mu > 0$ was apparently chosen in earlier work [14] to stress the seeming inconsistency between the SM predictions for $\delta a_\mu^{\text{SUSY}}$ and experimental data. We employ the same fixed sign in the present work for consistency, although it is of course possible to leave this a free discrete parameter in any global fit.

We add four additional nuisance parameters to the set of free parameters in our scans. These are the SM parameters with the largest uncertainties and strongest impacts upon CMSSM predictions: m_t , the pole top quark mass, $m_b(m_b)^{\overline{MS}}$, the bottom quark mass evaluated at m_b , $\alpha_{\text{em}}(m_Z)^{\overline{MS}}$, the electromagnetic coupling constant evaluated at the Z -boson pole mass m_Z , and $\alpha_s(m_Z)^{\overline{MS}}$, the strong coupling constant, also evaluated at m_Z . These last three quantities are computed in the modified minimal subtraction renormalisation scheme \overline{MS} .

The set of CMSSM and SM parameters together constitute an 8-dimensional parameter space

$$\Theta = (m_0, m_{1/2}, A_0, \tan \beta, m_t, m_b(m_b)^{\overline{MS}}, \alpha_{\text{em}}(m_Z)^{\overline{MS}}, \alpha_s(m_Z)^{\overline{MS}}), \quad (2.1)$$

to be scanned and constrained according to the available experimental data. The ranges over which we scan the parameters are $m_0, m_{1/2} \in (50 \text{ GeV}, 4 \text{ TeV})$, $A_0 \in (-7 \text{ TeV}, 7 \text{ TeV})$, $\tan \beta \in (2, 62)$, $m_t \in [167.0 \text{ GeV}, 178.2 \text{ GeV}]$, $m_b(m_b)^{\overline{MS}} \in [3.92 \text{ GeV}, 4.48 \text{ GeV}]$, $1/\alpha_{\text{em}}(m_Z)^{\overline{MS}} \in [127.835, 128.075]$ and $\alpha_s(m_Z)^{\overline{MS}} \in [0.1096, 0.1256]$.

2.1.2 Constraints: physicsity, observables, and uncertainties

In order to compare the predictions of each point in the parameter space with data, one has to first derive some quantities which are experimentally measurable. For a global fit, one needs to take into account all existing (and upcoming) data, such as collider and cosmological observations, and direct and indirect dark matter detection experiments. This is indeed the ultimate goal in any attempt to constrain a specific theoretical model like the CMSSM. Because our main goal in this paper is to assess how powerful GAs are compared to conventional methods (in particular the MultiNest algorithm), we restrict our analysis to the same set of observables and constraints as in the comparison paper [14]. These include the collider limits on Higgs and superpartner masses, electroweak precision measurements, B -physics quantities and the cosmologically-measured abundance of dark matter. These quantities and constraints are given in Table 1.

The observables are of three types:

- The SM nuisance parameters. Although they are considered free parameters of the model along with the CMSSM parameters, these are rather well-constrained by the data, and therefore used in constructing the full likelihood function.
- Observables for which positive measurements have been made. These are the W -boson pole mass (m_W), the effective leptonic weak mixing angle ($\sin^2 \theta_{\text{eff}}$), anomalous magnetic moment of the muon ($\delta a_\mu^{\text{SUSY}}$), branching fraction $BR(\overline{B} \rightarrow X_s \gamma)$, \overline{B}_s - B_s mass difference (ΔM_{B_s}), branching fraction $BR(\overline{B}_s \rightarrow \tau \nu)$, and dark matter relic density ($\Omega_\chi h^2$) assuming the neutralino is the only constituent of dark matter.
- Observables for which at the moment only (upper or lower) limits exist, i.e. the branching fraction $BR(\overline{B}_s \rightarrow \mu^+ \mu^-)$, the lightest MSSM Higgs boson mass m_h (assuming its coupling to the Z -boson is SM-like), and the superpartner masses.

Our sources for these experimental data are indicated in the table. Note that there are no theoretical uncertainties associated with the SM parameters, because they are simultaneously observables and free input parameters. For details about these quantities,

Observable	Mean value	Uncertainties (standard deviations)		Reference
		experimental	theoretical	
SM nuisance parameters				
m_t	172.6 GeV	1.4 GeV	-	[55]
$m_b(m_b)^{\overline{MS}}$	4.20 GeV	0.07 GeV	-	[56]
$\alpha_s(m_Z)^{\overline{MS}}$	0.1176	0.002	-	[56]
$1/\alpha_{\text{em}}(m_Z)^{\overline{MS}}$	127.955	0.03	-	[57]
measured				
m_W	80.398 GeV	25 MeV	15 MeV	[58]
$\sin^2 \theta_{\text{eff}}$	0.23153	16×10^{-5}	15×10^{-5}	[58]
$\delta a_\mu^{\text{SUSY}} \times 10^{10}$	29.5	8.8	1.0	[59]
$BR(\overline{B} \rightarrow X_s \gamma) \times 10^4$	3.55	0.26	0.21	[60]
ΔM_{B_s}	17.77 ps ⁻¹	0.12 ps ⁻¹	2.4 ps ⁻¹	[61]
$BR(\overline{B}_u \rightarrow \tau \nu) \times 10^4$	1.32	0.49	0.38	[60]
$\Omega_\chi h^2$	0.1099	0.0062	$0.1 \Omega_\chi h^2$	[62]
limits only (95% CL)				
$BR(\overline{B}_s \rightarrow \mu^+ \mu^-)$	$< 5.8 \times 10^{-8}$		14%	[63]
m_h	> 114.4 GeV (SM-like Higgs)		3 GeV	[64]
ζ_h^2	$f(m_h)$ (see Ref. 21)		negligible	[64]
$m_{\tilde{\chi}_1^0}$	> 50 GeV		5%	[65]
$m_{\tilde{\chi}_1^\pm}$	> 103.5 GeV (> 92.4 GeV)		5%	[66] ([67, 68])
$m_{\tilde{e}_R}$	> 100 GeV (> 73 GeV)		5%	[66] ([67, 68])
$m_{\tilde{\mu}_R}$	> 95 GeV (> 73 GeV)		5%	[66] ([67, 68])
$m_{\tilde{\tau}_1}$	> 87 GeV (> 73 GeV)		5%	[66] ([67, 68])
$m_{\tilde{\nu}}$	> 94 GeV (> 43 GeV)		5%	[69] ([67, 68])
$m_{\tilde{t}_1}$	> 95 GeV (> 65 GeV)		5%	[66] ([67, 68])
$m_{\tilde{b}_1}$	> 95 GeV (> 59 GeV)		5%	[66] ([67, 68])
$m_{\tilde{q}}$	> 375 GeV		5%	[56]
$m_{\tilde{g}}$	> 289 GeV		5%	[56]

Table 1: List of all physical observables used in the analysis. These are: collider limits on Higgs and superpartner masses, electroweak precision measurements, B -physics quantities and the dark matter relic density. For the sake of comparability, these are the same quantities and values as used in Ref. 14. The upper sub-table gives measurements of SM nuisance parameters. The central panel consists of observables for which a positive measurement has been made, and the lower panel shows observables for which only limits exist at the moment. The numbers in parenthesis are more conservative bounds applicable only under specific conditions. For details and arguments, see Refs. 14, 21 and 24. Table adapted mostly from Ref. 42.

experimental values and errors, particularly the reasoning behind theoretical uncertainties, see Refs. 14, 21 and 24.

In order to calculate all observables and likelihoods for different points in the CMSSM parameter space, we have used **SuperBayeS** 1.35 [70], a publicly available package which combines **SoftSusy** [71], **DarkSusy** [72], **FeynHiggs** [73], **Bdecay** and **MicrOMEGAs** [74] in a statistically consistent way. The public version of the package offers three different scanning algorithms: MCMCs, **MultiNest**, and fixed-grid scanning. We have modified the code to also include GAs. Other global-fit packages are also available: **Fittino** [36], for MCMC scans of the CMSSM, **SFitter** [28], for MCMC scans of the CMSSM and also weak-scale

MSSM, and *Gfitter* [75], for Standard Model fits to electroweak precision data (SUSY fits will soon be included as well). Amongst other search strategies, *Gfitter* can make use of GAs.

In *SuperBayeS*, the likelihoods of observables for which positive measurements exist (indicated in the upper and central panels of Table 1), are modeled by a multi-dimensional Gaussian function. The variance of this Gaussian is given by the sum of the experimental and theoretical variances associated with each observable; the corresponding standard deviations are shown in Table 1. For observables where only upper or lower limits exist (indicated in the lower panel of Table 1), a smeared step-function likelihood is used, constructed taking into account estimated theoretical errors in calculating the predicted values of the observables. For details on the exact mathematical forms of these likelihood functions, see Ref. 21.

In addition to experimental constraints from collider and cosmological observations, one must also ensure that each point is physically self-consistent; those that are not should be discarded or assigned a very low likelihood value. Unphysical points are ones where no self-consistent solutions to the RGEs exist, the conditions of electroweak symmetry-breaking are not satisfied, one or more masses become tachyonic, or the theoretical assumption that the neutralino is the LSP is violated. This is done in *SuperBayeS* by assigning an extremely small (almost zero) likelihood to the points that do not fulfil the physicality conditions.

2.2 Genetic Algorithms and profile likelihoods of the CMSSM

GAs [76–78] are a class of adaptive heuristic search techniques that draw on the evolutionary ideas of natural selection and survival of the fittest to solve optimisation problems. According to these principles, individuals in a breeding population which are better adapted to their environment generate more offspring than others.

GAs were invented in early 1970s, primarily by John Holland and colleagues for solving optimisation problems [79], although the idea of evolutionary computing had been introduced as early as the 1950s. Holland also introduced a formal mathematical framework, known as *Holland’s Schema Theorem*, which is commonly considered to be the theoretical explanation for the success of GAs. Now, about thirty years after their invention, GAs have amply demonstrated their practical usefulness (and robustness) in a variety of complex optimisation problems in computational science, economics, medicine and engineering [77].

The idea is very simple: in general, solving a problem means nothing more than finding the one solution most compatible with the conditions of the problem amongst many candidate solutions, in an efficient way. In most cases, the quality of different candidate solutions can be formulated in terms of a mathematical ‘fitness function’, to be maximised by some algorithm employed to solve the problem. With a GA, one repeatedly modifies a population of individual candidate solutions in such a way that after several iterations, the fittest point in the population evolves towards an optimal solution to the problem.

These iterative modifications are designed to imitate the reproductive behaviour of living organisms. At each stage, some individuals are selected randomly or semi-randomly from the current population to be parents. These parents produce children, which become

the next generation of candidate solutions. If parents with larger fitness values have more chance to recombine and produce children, over successive generations the best individual in the population should approach an optimal solution.

Because GAs are based only on fitness values at each point, and are insensitive to the function's gradients, they can also be applied to problems for which the fitness function has many discontinuities, is stochastic, highly non-linear or non-differentiable, or possesses any other special features which make the optimisation process extremely difficult. GAs are generally prescribed when the traditional optimisation algorithms either fail entirely or give substandard results. These properties make GAs ideal for our particular problem, as the CMSSM has exactly those unruly properties.

In what follows, we describe the general algorithmic strategy employed in a GA, followed by our particular implementation for a profile likelihood analysis of the CMSSM.

2.2.1 Main strategy

Denote the full model likelihood by $\mathcal{L}(\Theta)$, where Θ is the set of free parameters introduced in Eq. 2.1. This function, as a natural proxy for the goodness-of-fit given a fixed number of degrees of freedom, indicates how fit each particular Θ , or individual, is. It is thus a good choice for the genetic fitness function. We now want to find a specific individual, say Θ_{max} , for which the fitness function $\mathcal{L}(\Theta)$ is globally maximised.

Consider a population of I candidate individuals Θ_i ($i = 1, \dots, I$). Denote this entire population by P . This population is operated on K times by a semi-random *genetic operator* \mathbb{G} to produce a series of new populations P^k , where ($k = 1, \dots, K$) and $P^k = \mathbb{G}P^{k-1}$. The i th individual in the k th generation is Θ_i^k . For the general fitness of individuals to improve from one generation to the next, \mathbb{G} must clearly depend upon $\mathcal{L}(\Theta)$.

The search must be initialised with some starting population P^0 , which is then evolved under the action of \mathbb{G} until some convergence criterion \mathbb{T} is met. At this stage, the algorithm returns its best estimate of Θ_{max} as the individual Θ where $\mathcal{L}(\Theta_i^k)$ is maximised. If \mathbb{G} and \mathbb{T} have been chosen appropriately, this should occur at $k = K$, i.e. in the last generation. This algorithm can be summarised as follows:

```

initialisation:
 $P^0 := \{\Theta_i^0\}, \forall i \in [1, I]$ 
 $k := 0$ 
reproduction loop:
do while not  $\mathbb{T}$ 
     $k := k + 1$ 
    generating new population through genetic operators:
     $P^k := \mathbb{G}P^{k-1}$ 
end do
reading the best-fit point:
 $\Theta_{max} := \Theta_i^m$  where  $\mathcal{L}(\Theta_i^m) = \max \{\mathcal{L}(\Theta_i^k)\}, \forall i \in [1, I], \forall k \in [1, K]$ 

```

Three main properties define a GA. Firstly, \mathbb{G} operates on a population of points rather than a single individual. This makes GAs rather different from conventional Monte Carlo

search techniques such as the MCMC, though the nested sampling algorithm does also act on a population of points. The parallelism of a GA means that if appropriate measures of population diversity are incorporated into the algorithm, local maxima in the likelihood surface can be dealt with quite effectively; if a population is required to maintain a certain level of diversity, concentrations of individuals clustering too strongly around local maxima will be avoided by the remaining members of the population. This parallelism increases the convergence rate of the algorithm remarkably.

Secondly, \mathbb{G} does not operate directly on the real values of the parameters Θ_i (the phenotype), but acts on their encoded versions (the chromosomes, or genotype). Depending on the problem, individuals can be encoded as a string of binary or decimal digits, or even more complex data structures. \mathbb{G} then acts on the chromosomes in the current generation based only on their fitnesses, i.e. the likelihood function in our case. No further information is required for the GA to work; this means discontinuities in the likelihood function or its derivatives have virtually no affect on the performance of the algorithm.

Finally, the transition rules used in \mathbb{G} are probabilistic, not deterministic. The constituent genetic operators contained within \mathbb{G} are the key elements of the algorithm, and how they act on different populations defines different types of GAs. In our case

$$\mathbb{G} = \mathbb{R}\mathbb{M}\mathbb{C}\mathbb{S}, \quad (2.2)$$

where \mathbb{S} is the selection procedure (how parents are selected for breeding from a source population), \mathbb{C} is the crossover (how offspring are to inherit properties from their parents), \mathbb{M} is the mutation process (random changes made to the properties of newly-created offspring), and \mathbb{R} is the reproduction scheme used to place offspring into a broader population. \mathbb{C} and \mathbb{M} are stochastic processes defined at the genotype level, whereas \mathbb{S} and \mathbb{R} are phenotype-level processes, semi-random and essentially deterministic in nature, respectively.

The randomised operators of GAs are strongly distinct from simple random walks. This is because every new generation of individuals inherits some desirable characteristics from the present generation. Crossover (or recombination) rules play a crucial role in determining how the parents create the children of the next generation. The children are not copied directly to the next population; mutation rules specify that a certain degree of random modification should be applied to the newly-produced offsprings' chromosomes. Mutation is very important at this stage, since it is often the only mechanism preventing the algorithm from getting stuck in local maxima; its strength is typically linked dynamically to some measure of population diversity.

The reproduction loop is terminated whenever \mathbb{T} is fulfilled. In our case, whenever a predefined number of generations N have been produced (i.e. $K \equiv N$). The termination parameter (i.e. the number of generations N) and the chosen termination criterion itself depend upon the particular problem at hand and how accurate a solution is required. The fittest individual in the final population is then accepted as the best-fit solution to the problem. If one is also interested in mapping the likelihood function in the vicinity of the best-fit points, so as to be able to plot e.g. 1 and 2σ confidence regions for different CMSSM parameters, then it is useful to also retain all the individuals produced during the iterations of the algorithm.

2.2.2 Our specific implementation

Although any algorithm with the basic features described above ensures progressive improvement over successive generations, to guarantee absolute maximisation one usually needs to implement additional strategies and techniques, depending on the particular problem at hand. To implement a GA for analysing the CMSSM parameter space, we have taken advantage of the public GA package PIKAIA [80, 81]. Here we briefly describe the options and ingredients from PIKAIA 1.2 that we used in our GA implementation; the majority of these were the default choices.

- **Fitness function:** A natural fitness function to choose is the log-likelihood of the model, $\ln \mathcal{L}(\Theta)$. This function is however always negative (or zero). Since PIKAIA internally seeks to maximise a function, and this function must be positive definite, we chose the inverse chi-square (i.e. $\frac{1}{\chi^2}$) as the simplest appropriate fitness function. Except for the way we adjust the mutation rate for different generational iterations (see below), all the other genetic operators implemented in our algorithm are functions only of the ranking of individuals in the population; the actual values of the fitness function at these points do not matter as long as the ranking is preserved.

- **Encoding:** We encode individuals in the population (i.e. points in the CMSSM parameter space) using a decimal alphabet. That is, a string of base 10 integers, such that every normalised parameter θ_i is encoded into a string $d_1 d_2 \dots d_{n_d}$, where the $d_i \in [0, 9]$ are positive integers. This is different from many other public-domain GAs which usually make use of binary encoding. We use 5 digits to encode each parameter. This means that every individual chromosome is a decimal string of length $m \times n_d = 8 \times 5 = 40$.

- **Initialisation and population size:** We use completely random points in the parameter space for the initial population. We choose a population size of $n_p = 100$ (the typical number usually used in GAs), keeping it fixed throughout the entire evolutionary process.

- **Selection:** In order to select parents in any given iteration, a stochastic mechanism is used. The probability of an individual to be selected for breeding is determined based on its fitness in the following way: first, we assign to each individual Θ_i a rank r_i based on its fitness f_i such that $r = 1$ corresponds to the fittest individual and $r = n_p$ to the most unfit. Then a ranking fitness f'_i is defined in terms of this rank:

$$f'_i = n_p - r_i + 1.$$

The sum of all ranking fitness values in the population is computed as

$$F = \sum_{i=1}^{n_p} f'_i,$$

and n_p running sums are defined as

$$S_j = \sum_{i=1}^j f'_i, \quad j = 1, \dots, n_p.$$

Obviously $S_{j+1} \geq S_j$ (since f'_i are all positive), and $S_{n_p} = F$. As the next step, a random number $R \in [0, F]$ is generated and the element S_j is located for which $S_{j-1} \leq R < S_j$. The corresponding individual is one of the parents selected for breeding; the other one is also chosen in the same manner. This selection procedure is called the Roulette Wheel Algorithm (see Ref. 80 and references therein for more on this procedure and the motivation for using the ranking fitness in place of the true fitness).

- **Crossover:** When a pair of parent chromosomes have been chosen, a pair of offspring are produced via the crossover operator \mathcal{C} . We use two different types of operators for this purpose, namely, uniform one-point and two-point crossovers (see Ref. 82 for a comprehensive review of existing crossover operators). Table 2 illustrates how these two processes work. In our case, parents are encoded as 40-digit strings. The one-point crossover begins by randomly selecting a cutting point along the chromosomes' length, and dividing each parent string into two sub-strings. This is done by generating a random integer $K \in [1, 40]$. According to the crossover scheme, the strings located in identical parts of the two strings are then swapped to give the two children chromosomes. It is clear that even though the information encoded in the parent chromosomes is transferred to the offspring chromosomes, the latter are in general different from the former, corresponding to a different set of model parameters in the parameter space. In the two-point crossover scheme, two slicing points are selected randomly by generating two random integers $K_1, K_2 \in [1, 40]$, and the string segments between these two cutting points are exchanged.

uniform one-point crossover		
initial parent chromosomes	6739...8451	4394...0570
selecting a random cutting point	6739...84 51	4394...05 70
swapping the sub-strings	6739...84 70	4394...05 51
final offspring	6739...8470	4394...0551
uniform two-point crossover		
initial parent chromosomes	6739...8451	4394...0570
selecting two random cutting points	67 39...845 1	43 94...057 0
swapping the sub-strings	67 94...057 1	43 39...845 0
final offspring	6794...0571	4339...8450

Table 2: Schematic description of the uniform one-point and two-point crossover operators employed in our analysis.

In our algorithm, for each pair of parent chromosomes, either one-point or two-point crossover is chosen with equal probability. This combination of the one-point and two-point crossovers is proposed to avoid the so-called “end-point bias” problem produced by using only the one-point crossover. This happens when, for example, a combination of two sub-strings situated at opposite ends of a parent string are advantageous when decoded back to the phenotypic level (in the sense that they give a high fitness), *but only when they are expressed simultaneously*. Such a feature is impossible to pass on to offspring when using a uniform one-point crossover, as cutting the string at any single point always destroys this combination. This is much less of a problem for sub-strings located more centrally in the parent string (see Ref. 80 again for more details on this issue).

Once two parents have been selected for breeding, the crossover operation is applied only with a preset probability. This probability is usually taken to be large but not 100%. We use 85% in our analysis, meaning that there is a 15% chance that any given breeding pair will be passed on intact to the next stage, where they will be affected by mutation.

- **Mutation:** We employ the so-called uniform one-point mutation operator. Different genes in the offspring’s chromosomes (i.e. decimal digits in the 40-digit strings) are replaced with a predefined probability (the ‘mutation rate’), by a random integer in the interval $[0, 9]$. Like the crossover operator, mutation preserves the parameter bounds. The choice of mutation rate is highly important, and very problem-dependent; in general it cannot be chosen *a priori*. If too large, it can destroy a potentially excellent offspring and, in the extreme case, make the whole algorithm behave effectively as an entirely random search. If too small, it can endanger the variability in the population and cause the whole population to become trapped in local maxima; a large enough mutation rate is often the only mechanism to escape premature convergence at local maxima. Therefore, instead of using a fixed mutation rate we allow it to vary dynamically throughout the run, such that the degree of ‘biodiversity’ is monitored and the mutation rate is adjusted accordingly. When the majority of individuals in a population (as estimated by the median individual) are very similar to the best individual, the population is probably clustered around a local maximum and the mutation rate should increase. The converse is also true: a high degree of diversity indicates that the mutation rate should be kept low. The degree of clustering and the subsequent amount of adjustment in our algorithm are assessed based on the difference between the actual fitness values of the best and median points. This is done by defining the quantity $\Delta f = (f_{r=1} - f_{r=n_p/2}) / (f_{r=1} + f_{r=n_p/2})$ in which $f_{r=1}$ and $f_{r=n_p/2}$ correspond to the fitnesses of the best and median individuals, respectively. The mutation rate is then increased (decreased) by a fixed multiplicative factor whenever Δf is smaller (larger) than a preset lower (upper) bound. We choose the lower and upper critical values of Δf to be 0.05 and 0.25 respectively, and the multiplicative factor to be 1.5. We bound the mutation rate to lie between the typical values of 0.0005 and 0.25. We use an initial mutation rate of 0.005.

- **Reproduction plans:** After selecting parents and producing offspring by acting on them with the crossover and mutation operators, the newly bred individuals must somehow be incorporated into the population. The strategy which controls this process is called a reproduction plan. Although there are several advanced reproduction plans on the market, we utilise the simplest off-the-shelf option: full generational replacement. This means that the whole parent population is replaced by the newly-created children in each iteration, all in a single step.

- **Elitism:** There is always a possibility that the fittest individual is not passed on to the next generation, since it may be destroyed under the action of the crossover and mutation operations on the parents. To guarantee survival of this individual, we use an elitism feature in our reproduction plan. Under full generational replacement, elitism simply means that the fittest individual in the offspring population is replaced by the fittest parent, if the latter has a higher fitness value.

- **Termination and number of generations:** There are several termination criteria

one could use for a GA. Rather than evolving the population generation after generation until some tolerance criterion is met, we perform the evolution over a fixed and predetermined number of generations. This is because the former strategy is claimed to be potentially dangerous when approaching a new problem, in view of the usual convergence trends exhibited by GA-based optimisers (see Ref. 80 for more details). In our analysis, we used 10 separate runs of the algorithm with different initial random seeds, and a fixed number of likelihood evaluations ($\sim 3 \times 10^5$) for each. We then compiled all points into a single list, and used it to map the profile likelihood of the CMSSM.

3. Results and discussion

We now present and analyse the results of our global profile likelihood fit of the CMSSM using GAs. We compare results with a similar global fit using the state-of-the-art Bayesian algorithm **MultiNest** [40]. In Sec. 3.1 we give the best-fit points and high-likelihood regions in the CMSSM parameter space. In Sec. 3.2 we discuss and compare implications of both methods for the detection of supersymmetric and Higgs particles at the LHC. Sec. 3.3 is devoted to an investigation of dark matter in the CMSSM and the prospects for its direct and indirect detection. Throughout this section we compare our GA profile likelihood results mainly with those of the **MultiNest** algorithm implemented with linear (flat) priors. The reasons for this are outlined in Sec. 3.4, along with a comparison of the two scanning techniques in terms of the computational speed and convergence.

3.1 Best-fit points and high-likelihood regions

The χ^2 at our best-fit point is 9.35. This is surprisingly better than the values of 13.51 and 11.90 found by **MultiNest** with linear and logarithmic priors, respectively, for the same problem. This improvement in the best fit can in principle have a drastic impact on the statistical inference drawn about the model parameters.

To demonstrate these effects, let us start with two-dimensional (2D) plots for the principal parameters of the CMSSM, i.e. m_0 , $m_{1/2}$, A_0 and $\tan\beta$, shown in Figs. 1 and 2. These figures show 2D profile likelihood maps. In the first figure, the full likelihood is maximised over all free (CMSSM plus SM nuisance) parameters except m_0 and $m_{1/2}$. Similar diagrams are shown in Fig. 2, but now for the 2D profile likelihoods in terms of the parameters A_0 and $\tan\beta$.

Figs. 1a and 2a show the 2D profile likelihood maps obtained by taking into account all the sample points in the parameter space resulting from the GA scan. The inner and outer contours indicate 68.3% (1σ) and 95.4% (2σ) confidence regions based on the GA best-fit point of $\chi^2 = 9.35$. That is, points with $\chi^2 \leq 11.65$ fall into the 1σ region, and points with $\chi^2 \leq 15.52$ fall into the 2σ region. Similar plots are presented for the **MultiNest** results in Figs. 1d and 2d, where the 1σ and 2σ contours are drawn based on the **MultiNest** best-fit of $\chi^2 = 13.51$ (1 and 2σ regions are given by $\chi^2 \leq 15.81$ and $\chi^2 \leq 19.68$, respectively). These panels reflect the outcomes of each scanning algorithm in the absence of any information from the other. The sample points have been divided into 75×75 bins in all plots and no smoothing is applied.

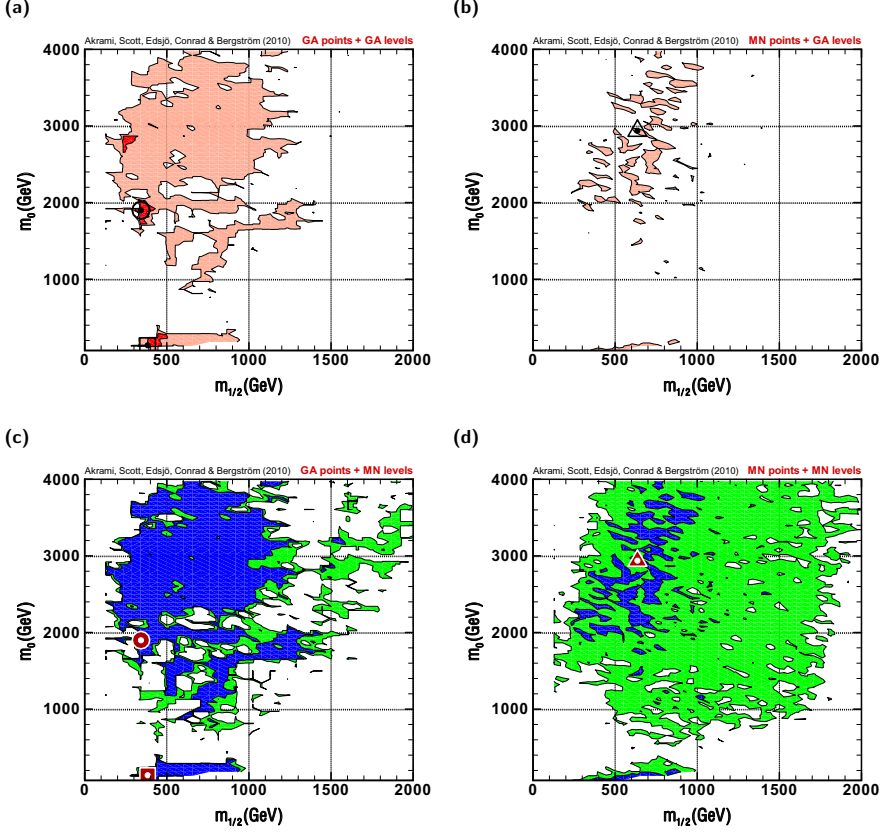


Figure 1: Two-dimensional profile likelihoods in the m_0 - $m_{1/2}$ plane for CMSSM scans with GAs (a) and MultiNest (d). These two panels show the statistically-consistent results of each scan. The inner and outer contours represent 68.3% (1σ) and 95.4% (2σ) confidence regions respectively, for each scan. The dotted circle, square and triangle show respectively the GA global best-fit point with a χ^2 of 9.35 (located in the focus point region), the GA best-fit point in the stau co-annihilation region ($\chi^2 = 11.34$), and the best-fit point found by linear-prior MultiNest ($\chi^2 = 13.51$). Panels (b) and (c) are given for comparative purposes only. Panel (b) shows the same MultiNest sample points as in (d), but with iso-likelihood contour levels drawn as in (a), based on the GA best-fit likelihood value. Panel (c) shows the same GA sample points as in (a), but with iso-likelihood contours as in (d), based on the MultiNest best-fit likelihood value. The sample points have been divided into 75×75 bins in all plots. Here we see that the GA uncovers a large number of points with much higher likelihoods than MultiNest, across large sections of the m_0 - $m_{1/2}$ plane.

It is important to realise that although both the 1 and 2σ confidence regions in the GA results seem to be rather smaller in size than the corresponding regions in the MultiNest scan (especially the 1σ region), this is by no means an indication that MultiNest has found more high-likelihood points in the parameter space. The situation is in fact the exact opposite.

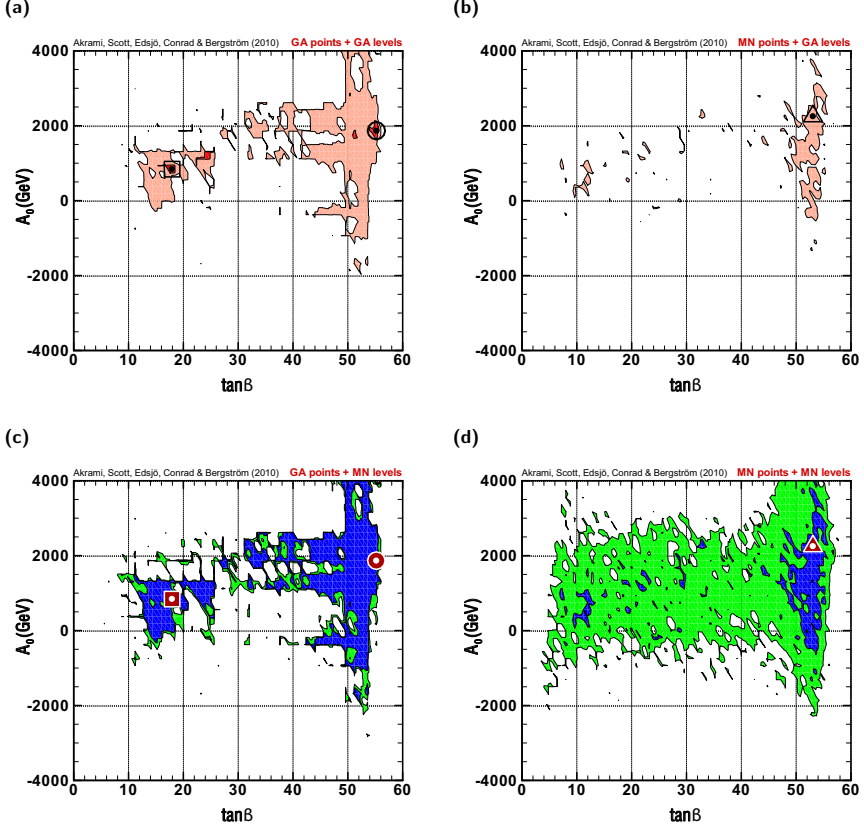


Figure 2: As in Fig. 1, but in the A_0 - $\tan \beta$ plane.

This is clear when we recall that the best-fit likelihood values are very different in the two cases giving rise to two completely different sets of iso-likelihood contours. To make this point clear, suppose for the sake of argument that the GA best-fit likelihood value is indeed the absolute global maximum we were looking for. If so, we can now check how well the MultiNest algorithm has sampled the parameter space, by looking at Figs. 1b and 2b. These show how many of the MultiNest samples are located in the correct confidence regions set by the absolute maximum; the contours are drawn based on this best-fit value rather than the one found by MultiNest itself. The plots show that MultiNest has discovered no points in the 1σ region and only a small fraction of the 2σ region. In particular, it is interesting to notice that the MultiNest best-fit point, i.e. the one with $\chi^2 = 13.51$ (marked as dotted triangles in Figs. 1b,d and 2b,d) now sits in the 2σ region. These all come from the fact that only points with $\chi^2 \leq 11.65$ and $\chi^2 \leq 15.52$ fall in the 1σ and 2σ regions,

respectively, and there are not many points found by **MultiNest** with such low χ^2 s. The same statement holds for the log-prior **MultiNest** best-fit point with $\chi^2 = 11.90$.

It is obvious from these plots that the GA has found many points in the parameter space with rather high likelihood (or equivalently, low χ^2) which were missed (or skipped) by **MultiNest**. This indicates that the use of **MultiNest** scans in the context of the frequentist profile likelihood is rather questionable. This is not really surprising, given that **MultiNest** is designed to sample the Bayesian posterior PDF, not map the profile likelihood.

We can also use the resultant GA samples in a different way to clarify this result. In Figs. 1c and 2c, the GA samples are plotted with the same contours as in Figs. 1d and 2d, i.e. based on the **MultiNest** best-fit likelihood value. Compared to 1d and 2d, we see that there are many high-likelihood points in the **MultiNest** 1σ region found by the GA and missed by **MultiNest**. In the sense of the profile likelihood, it appears that **MultiNest** has converged prematurely; we see a much larger and more uniform pseudo- 1σ region with the GA data. Here we see that most of the region labeled as being within the 2σ confidence level in the **MultiNest** scan is actually part of its 1σ confidence region.

Our results confirm the complexity of the CMSSM parameter space, showing that much care should be taken in making any statistical statement about it. This is especially true when using a frequentist approach, as this complication plays a crucial role in the final conclusions. It is of course true that the convergence criterion for **MultiNest** is defined on the basis of the Bayesian evidence, and the algorithm may have (indeed, probably has) converged properly in this context. The point we want to emphasise is that even if **MultiNest** is converged for a Bayesian posterior PDF analysis of the model, this convergence is far from acceptable for a profile likelihood analysis. The same is also very likely to be true of other less sophisticated Bayesian methods, such as the MCMC; this is the case at least for MCMC scans performed with the same physics and likelihood calculations as in our analysis (since MCMCs and **MultiNest** give almost identical results in this case [14]).

The aforementioned comparison does also suggest, however, that even the Bayesian posterior PDF obtained from **MultiNest** and MCMC scans might not yet be quite properly mapped. This is because in principle, a significant amount of probability mass could be contained in the regions found by the GA but missed or skipped by **MultiNest**. Given the absence of any definition of a measure on the parameter space in profile likelihood analyses such as the one we perform, we are unfortunately not in a position to make any conclusive statement about the actual contribution of these regions to the Bayesian probability mass. Nevertheless, the difference in size between the blue regions in Figs. 1c and 1d is intriguing. We discuss these convergence questions further in Sec. 3.4.

Our GA scan has found high-likelihood points in many of the CMSSM regions known to be consistent with data, in particular the relic abundance of dark matter [83]. These include the stau ($\tilde{\tau}$) *co-annihilation* (COA) region [84] usually at small m_0 where the lightest stau is close in mass to the neutralino, the *focus point* (FP) region [85] at large m_0 where a large Higgsino component causes neutralino annihilation into gauge boson pairs, and the light Higgs boson *funnel* region [15, 86] at small $m_{1/2}$. We have not found any high-likelihood points in the stop (\tilde{t}) *co-annihilation* region [87–89] at large negative A_0 , where the lightest stop is close in mass to the neutralino. This could be interpreted as

confirmation of the claim that this region, although compatible with the WMAP constraint on the relic density of dark matter, is highly disfavoured when other observables are also taken into account [19].

It is important to make the point that although our method does find some points in the funnel region, it does not spread out very well around those points to map the whole region. Finding this very fine-tuned region is a known challenge for any scanning strategy, including nested sampling. The failure of the GA to map other points in the funnel region can be understood. We believe that this behaviour is caused by the specific crossover scheme employed in our analysis (i.e. one/two-point crossover), and could probably be cured by using a more advanced algorithm. Alternatively, a different parameterisation of the model, such as a logarithmic scaling of the mass parameters (or equivalently, genetic encoding in terms of the logarithms of these parameters), would probably find the funnel region much more effectively (in the same way as it does when **MultiNest** is implemented with logarithmic priors). In any case, it is important to realise that these types of regions are findable by our method (although not very well), even without taking into account any ad hoc change in the model parameterisation (or choosing a non-linear prior such as the logarithmic one in the Bayesian language). See Sec. 3.4 for more discussions about the priors and parameterisation.

Returning to the best-fit points, it is visible from the plots that the global best-fit point is located in the FP region (dotted circles in Figs. 1a,c and 2a,c). This has a very interesting phenomenological implication, which we return to later in this section when we discuss contributions to the total likelihood of the best-fit model from different observables. For comparison, we have also marked the best-fit point located in the COA region, which has $\chi^2 = 11.34$ (dotted squares in Figs. 1a,c and 2a,c). This point is situated inside the 1σ confidence level contour (Figs. 1a and 2a) and is well-favoured by our analysis. It is interesting to notice that the χ^2 for this point, although worse than the global best-fit χ^2 , is still better than the best value found by the **MultiNest** scan, even when implemented with a log prior ($\chi^2 = 11.90$), which also corresponds to a point in the COA region. This result is important as **MultiNest** scans with logarithmic priors are usually considered a good way to probe low-mass regions such as the COA. Our algorithm, even working with effectively linear priors (because the genome featured a linear encoding to the parameters), appears to have found a better point in this region as well.

As another exhibition of the consequences of our results compared to the Bayesian nested sampling technique, it is interesting to look at the 1D profile likelihoods for the CMSSM parameters (Fig. 3). The horizontal axes in the plots indicate the CMSSM parameters and the vertical axes show the corresponding profile likelihoods, normalised to the best-fit GA value (i.e. with $\chi^2 = 9.35$). Green and grey bars show the GA and **MultiNest** 1D profile likelihoods respectively. We sorted points into 50 bins for these plots. We have also included the global (FP) and COA best-fit points in the plots, indicated by solid and dashed red lines, respectively.

The very different results in Fig. 3 from the two different algorithms are yet another confirmation that existing sampling techniques are probably still not sufficiently reliable for the exploration and mapping of SUSY likelihoods, at least in a frequentist framework.

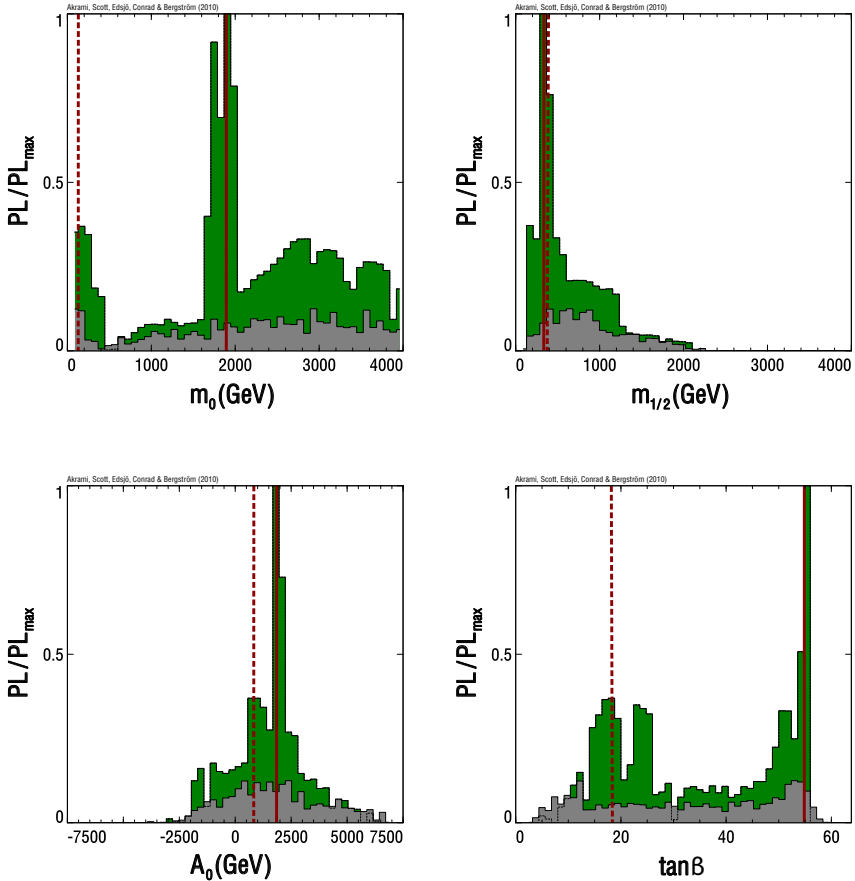


Figure 3: One-dimensional profile likelihoods (PL) of CMSSM parameters, normalised to the global GA best fit (PL_{max}). The green and grey bars show results from GA and MultiNest scans, respectively. Solid and dashed red lines represent the GA global best-fit point ($\chi^2 = 9.35$, located in the focus point region) and the GA best-fit point in the tau co-annihilation region ($\chi^2 = 11.34$), respectively. Samples are divided into 50 bins.

These plots show that by employing a different scanning algorithm, it is quite possible to find many important new points in the parameter space. This can in principle affect the whole inference about the model, especially when we are interested not only in drawing a general statement about the high-likelihood regions, but also in performing a more detailed exploration of the model likelihood around the best-fit points. It also shows that the GA technology we made use of in this paper seems a better choice for frequentist analyses than conventional tools, which are typically optimised for Bayesian searches; we have found

model (+nuisance) parameters		
	GA global BFP (located in FP region)	GA COA BFP
m_0	1900.5 GeV	133.9 GeV
$m_{1/2}$	342.8 GeV	383.1 GeV
A_0	1873.9 GeV	840.6 GeV
$\tan \beta$	55.0	17.9
m_t	172.9 GeV	173.3 GeV
$m_b(m_b)^{\overline{MS}}$	4.19 GeV	4.20 GeV
$\alpha_s(m_Z)^{\overline{MS}}$	0.1172	0.1183
$1/\alpha_{\text{em}}(m_Z)^{\overline{MS}}$	127.955	127.955
observables		
	GA global BFP (located in FP region)	GA COA BFP
m_W	80.366 GeV	80.371 GeV
$\sin^2 \theta_{\text{eff}}$	0.23156	0.23153
$\delta a_\mu^{\text{SUSY}} \times 10^{10}$	5.9	14.5
$BR(\overline{B} \rightarrow X_s \gamma) \times 10^4$	3.58	2.97
ΔM_{B_s}	17.37 ps ⁻¹	19.0 ps ⁻¹
$BR(\overline{B}_u \rightarrow \tau \nu) \times 10^4$	1.32	1.46
$\Omega_\chi h^2$	0.10949	0.10985
$BR(\overline{B}_s \rightarrow \mu^+ \mu^-)$	4.34×10^{-8}	3.87×10^{-8}

Table 3: Parameter and observable values at the best-fit points (BFPs) found using Genetic Algorithms. These quantities are shown for both the global best-fit point (located in the focus point (FP) region) and the best-fit point in the stau co-annihilation (COA) region. Higgs and sparticle masses will be given in Table 5, when talking about implications for the LHC.

higher likelihood values for almost all the regions within the interesting range of model parameters. Whilst this certainly favours this technique over others, it should also serve as a warning. We can by no means be sure that the GA has actually found the true global best-fit point. Clearly this concern should be taken much more seriously when one is dealing with more complicated models than the CMSSM, with more parameters and more complex theoretical structures.

Listed in Tables 3 and 4 are all properties of the two GA best-fit points. The upper part of the first table gives values of the CMSSM principal parameters and SM nuisance parameters, whereas the lower part shows all physical observables employed in our calculation of model likelihood. These are the same quantities as given in Table 1 except for the Higgs and sparticle masses, which will be presented in the upcoming section on implications for the LHC. To make the differences between the properties of these two “good” points more clear, in the second table we have indicated the individual contributions from different observables to the total χ^2 at each point. These quantities are also given for MultiNest best-fit points found using flat and logarithmic priors.

One interesting fact seen in Table 4 is the apparent tension between $\delta a_\mu^{\text{SUSY}}$ and the other observables, in particular $BR(\overline{B} \rightarrow X_s \gamma)$. This has been widely discussed in the past [14, 31, 37, 42]. While most of the discrepancy between the model and the experimental data at our global best-fit point (living in the FP region) comes from $\delta a_\mu^{\text{SUSY}}$ ($\sim 76\%$), and $BR(\overline{B} \rightarrow X_s \gamma)$ contributes only about 0.1% to the total χ^2 , these two observables partially switch roles at the COA point. This confirms that $BR(\overline{B} \rightarrow X_s \gamma)$ in general favours large

observable	partial χ^2 (fractional contribution to the total χ^2 in %)			
	GA global BFP located in FP region	GA COA BFP	MN global BFP with flat priors	MN global BFP with log priors
nuisance parameters	0.12 (1.27%)	0.35 (3.10%)	0.48 (3.56%)	0.81 (6.78%)
m_W	1.21 (12.95%)	0.83 (7.29%)	1.48 (10.92%)	0.69 (5.83%)
$\sin^2 \theta_{\text{eff}}$	0.024 (0.26%)	$\sim 10^{-4}$ (0.001%)	0.07 (0.49%)	0.0040 (0.034%)
$\delta a_\mu^{\text{SUSY}}$	7.09 (75.79%)	2.86 (25.21%)	9.21 (68.20%)	2.40 (20.18%)
$BR(\overline{B} \rightarrow X_s \gamma)$	0.010 (0.11%)	3.03 (26.76%)	0.10 (0.74%)	3.83 (32.20%)
ΔM_{B_s}	0.028 (0.30%)	0.26 (2.31%)	0.09 (0.66%)	0.29 (2.41%)
$BR(\overline{B}_u \rightarrow \tau \nu)$	$\sim 10^{-5}$ ($10^{-4}\%$)	0.050 (0.44%)	1.91 (14.14%)	0.043 (0.36%)
$\Omega_\chi h^2$	0.0011 (0.012%)	$\sim 10^{-5}$ ($10^{-4}\%$)	0.03 (0.2%)	0.13 (1.07%)
$BR(\overline{B}_s \rightarrow \mu^+ \mu^-)$	0.016 (0.17%)	0.00 (0.00%)	0.00 (0.00%)	0.00 (0.00%)
m_h	0.85 (9.14%)	3.96 (34.88%)	0.15 (1.09%)	3.70 (31.13%)
sparticles	0.00 (0.00%)	0.00 (0.00%)	0.00 (0.00%)	0.00 (0.00%)
all	9.35 (100 %)	11.34 (100 %)	13.51 (100 %)	11.90 (100 %)

Table 4: Contributions to the total χ^2 by different observables employed in the scans (Table 1). Contributions are shown for the GA global best-fit point (BFP) located in the focus point (FP) region and the GA best-fit point in the stau co-annihilation (COA) region. Fractional contributions are also given in percent. Similar quantities for both MultiNest scans with flat (linear) and logarithmic priors are also listed for comparison, where the former is in the FP region and the latter is in the COA region.

m_0 (the FP region), while $\delta a_\mu^{\text{SUSY}}$ favours smaller masses (the COA region). A similar feature is also visible in the two MultiNest best-fit points for flat and log priors, as they reside in the FP and COA regions, respectively.

In the case where our best-fit point is placed in the FP region, the total χ^2 from all observables except $\delta a_\mu^{\text{SUSY}}$ and $BR(\overline{B} \rightarrow X_s \gamma)$ is a remarkably smaller fraction ($\sim 24\%$) of the total than in the COA region ($\sim 48\%$) (this is also the case if we compare the two MultiNest points in the table, with contributions of $\sim 31\%$ and $\sim 47.5\%$). This can be qualitatively interpreted as yet another reflection of the fact that in the absence of any constraint from $\delta a_\mu^{\text{SUSY}}$, the data is largely consistent with the global best-fit point being in the FP region. That is, if one ignores $\delta a_\mu^{\text{SUSY}}$, it is much easier to fulfil all the experimental constraints on the CMSSM by moving towards larger m_0 . If one wants to satisfy also the extra constraint coming from $\delta a_\mu^{\text{SUSY}}$, this might be possible by moving back towards lower masses (the COA region), but at the price of reducing the total likelihood.

It is important to stress that our global best-fit point is in fact part of the FP region, with high m_0 (i.e. ~ 1900 GeV). This means that even taking into account the constraint from $\delta a_\mu^{\text{SUSY}}$, the FP is still favoured over the COA region in our analysis, in clear contradiction with some recent claims [31, 37] that the latter is favoured by existing data. These analyses were performed in a frequentist framework, and based on MCMC scans. However, the large discrepancy with our findings probably comes more from differences in the likelihood functions themselves than the scanning algorithms, i.e. in the calculations of physical observables and their contributions to the likelihood. A direct comparison with these works would only be possible if we were to also work with exactly the same routines for the calculation of the likelihood as in Refs. 31 and 37, changing only the scanning algorithm (as we have here in comparing with Ref. 14). The difference we see in this case

mostly reflects the discrepancy between the results of Ref. 14 and Refs. 31 and 37.

Nonetheless, it is important to note that some differences could be due to the scanning technique. We have shown in this paper that at least for the specific physics setup implemented in **SuperBayeS**, GAs find better-fit points than nested sampling, which in turn is known to find essentially the same points as MCMCs. It is therefore quite reasonable to expect that GAs could find many points missed by MCMCs. There are even some other FP points found by GAs with masses of about 2800 GeV and located in the 1σ region (see Fig. 1a), supporting the conclusion that although low masses are favoured over high masses in the previous **MultiNest** and MCMC scans using **SuperBayeS**, the opposite holds in our GA scans. This means that there exist many high-likelihood points in the FP region entirely missed by **MultiNest** and MCMC scans performed in the **SuperBayeS** analyses. It seems that those algorithms do not sample this region of the parameter space very well, at least when **SuperBayeS** routines are used for physics and likelihood calculations. We see no reason why a similar situation could not also occur when different codes are used to evaluate the likelihood function.

Since we have not used exactly the same physics and likelihood setup, nor the same numerical routines for calculating different quantities as employed in Refs. 31 and 37 (and we cannot do that in a consistent way as the code employed in those studies is not publicly available), we cannot make a definitive statement as to the overall impact of the scanning algorithm in the discrepancy we see with their results. One should however be very cautious in general when attempting to draw strong conclusions about e.g. the FP being excluded by existing data. The complex structure of the CMSSM parameter space makes the corresponding likelihood surface very sensitive to small changes in the codes and experimental data used to construct the full likelihood, which in turn can introduce a significant dependence upon the scanning algorithm.

3.2 Implications for the LHC

We showed in the previous section that compared to the state-of-the-art Bayesian algorithm **MultiNest**, GAs are a very powerful tool for finding high-likelihood points in the CMSSM parameter space. It is therefore interesting to examine how strongly these results impact predictions for future experimental tests at e.g. the LHC. We have calculated the 1D profile likelihoods corresponding to the gluino mass $m_{\tilde{g}}$ (as a popular representative of the sparticles) and the lightest Higgs mass m_h , both of which will be searched for at the LHC. The resultant plots are given in Fig. 4. These plots are generated in the same way as those in Fig. 3, indicating the differences between the two scanning strategies. Here, we once again see that the GA has found much better fits in the mass ranges covered by **MultiNest**.

Looking first at the gluino mass prediction (left-hand plot of Fig. 4), we confirm earlier findings [14, 37] that the LHC will probe all likely CMSSM gluino masses if its reach extends beyond ~ 3 TeV. The FP and COA best-fit points are both located at relatively low masses with quite similar values (~ 900 GeV). These values are well within the reach of even the early operations of the LHC. The detailed CMSSM mass spectra computed at both of these points are presented in Table 5. It can be seen from these spectra that our global best-fit

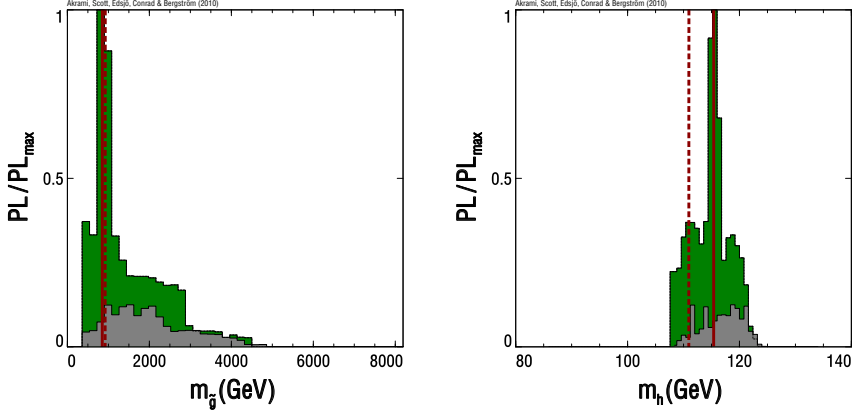


Figure 4: As in Fig. 3, but for the gluino mass $m_{\tilde{g}}$ and the lightest Higgs mass m_h .

(GeV)	GA global BFP located in FP region	GA COA BFP	(GeV)	GA global BFP located in FP region	GA COA BFP
$m_{\tilde{e}_L}$	1908	294.1	$m_{\tilde{d}_R}$	1994	798.1
$m_{\tilde{e}_R}$	1903	202	$m_{\tilde{s}_L}$	2000	832.4
$m_{\tilde{\mu}_L}$	1907	294.1	$m_{\tilde{s}_R}$	1994	798.1
$m_{\tilde{\mu}_R}$	1901	201.9	$m_{\tilde{b}_1}$	1354	765
$m_{\tilde{\tau}_1}$	1100	160.1	$m_{\tilde{b}_2}$	1492	793.4
$m_{\tilde{\tau}_2}$	1560	289.2	$m_{\tilde{\chi}_1^0}$	140.4	152.6
$m_{\tilde{\nu}_e}$	1906	283.3	$m_{\tilde{\chi}_2^0}$	269.9	285.4
$m_{\tilde{\nu}_\mu}$	1905	283.3	$m_{\tilde{\chi}_3^0}$	519.7	451.1
$m_{\tilde{\nu}_\tau}$	1560	272.5	$m_{\tilde{\chi}_4^0}$	529.7	469.6
$m_{\tilde{u}_L}$	1998	826.1	$m_{\tilde{\chi}_1^\pm}$	270.4	286.9
$m_{\tilde{u}_R}$	1996	805.4	$m_{\tilde{\chi}_2^\pm}$	530.3	468.5
$m_{\tilde{c}_L}$	1998	826.1	m_h	115.55	111.11
$m_{\tilde{c}_R}$	1996	805.4	m_H	179.93	504.24
$m_{\tilde{t}_1}$	1194	672.8	m_A	179.83	504.04
$m_{\tilde{t}_2}$	1364	803	m_{H^\pm}	201.14	510.67
$m_{\tilde{d}_L}$	2001	832.4	$m_{\tilde{g}}$	877.1	898.8

Table 5: Mass spectra of the GA global best-fit point (BFP) located in the focus point (FP) region and the GA best-fit point in the stau co-annihilation (COA) region.

point favours rather high masses for the sfermions, while the COA best-fit point favours low masses.

Looking at the right-hand plot of Fig. 4, corresponding to the likelihood of different values of m_h , we notice that although a large number of good points have Higgs masses higher than the SM limit from the Large Electron-Positron Collider (LEP; i.e. $m_h \geq 114.4$ GeV), including the global best-fit point (with $m_h = 115.55$ GeV), there are also

many other important ones which violate this limit, including the best-fit COA point (with $m_h = 111.11$ GeV). These points with low-mass Higgs bosons have been allowed by the smoothed likelihood function that we employed for the LEP limit (cf. Sec. 2.1). Instead of this treatment of the Higgs sector, one could use a more sophisticated method, such as implemented by **HiggsBounds** [90]. This would apply the collider bounds on the Higgs mass in a SUSY-appropriate manner, and give more accurate likelihoods at low masses around the 114.4 GeV bound.

Looking again at Table 4, the contribution from m_h as a percentage of the total χ^2 is considerably larger in the COA case than the FP. This becomes clear when we compare their corresponding values for m_h (i.e. 115.55 GeV and 111.11 GeV, respectively) with the LEP limit. The lower Higgs mass in the COA region is a reflection of the correlation between m_0 and m_h in the CMSSM, confirming once more that moving to low m_0 (i.e. approaching the COA region) causes models to become less compatible with all experimental data except $\delta a_\mu^{\text{SUSY}}$.

3.3 Implications for dark matter searches

As a natural continuation of our discussion of the consequences of our results for present and upcoming experiments, we turn now to dark matter, beginning with direct detection (DD) experiments. One interesting quantity for these experiments is the spin-independent scattering cross-section σ_p^{SI} of the neutralino and a proton. This cross-section is often plotted against the neutralino mass $m_{\tilde{\chi}_1^0}$ when comparing limits from different direct detection experiments. Predictions are given in this plane from both the **MultiNest** and GA scans in Fig. 5, drawn similarly to Figs. 1 and 2. σ_p^{SI} is shown in units of pb (i.e. 10^{-36}cm^2). Contours shown in the upper (lower) panels are generated according to the GA (**MultiNest**) best-fit point, and the points with highest likelihoods are marked as before. Although no constraints from direct detection measurements have been used in forming the model likelihood in this paper (mainly in order to work with the same set of quantities and constraints as employed in Ref. 14), we have also included the current best DD limits for comparison. These are limits at the 90% confidence level from CDMS-II [91] and XENON10 [92].

Looking at Fig. 5, we first notice that all the conclusions we made earlier are reconfirmed here: there are many important points in the parameter space that have appeared by the use of GAs, having a strong impact on the statistical conclusions. For example, instead of a rather spread and sparse 1σ confidence region produced by **MultiNest** (Fig. 5d), GAs (Fig. 5a) reveal a more compact region, sharply peaked around the best-fit points. It is interesting to see that in the latter case, most of the 1σ FP region around the dotted circle, including the point itself, is already excluded by CDMS-II and XENON10 under standard halo assumptions. The global best-fit point has quite a large cross-section ($\sigma_p^{SI} \sim 2 \times 10^{-7}$ pb) compared to the **MultiNest** global best-fit point ($\sigma_p^{SI} \sim 1.7 \times 10^{-8}$ pb), making it much more easily probed by direct detection (Table 6). On the contrary, the best-fit COA point has a much lower σ_p^{SI} ($\sim 2.2 \times 10^{-9}$ pb), and is still well below these experimental limits. With future experiments planned to reach cross-sections as low as 10^{-10} pb, this point will eventually be tested as well. Even if we do not consider the highest-likelihood point found by the GA, and just compare the two lower panels in Fig. 5,

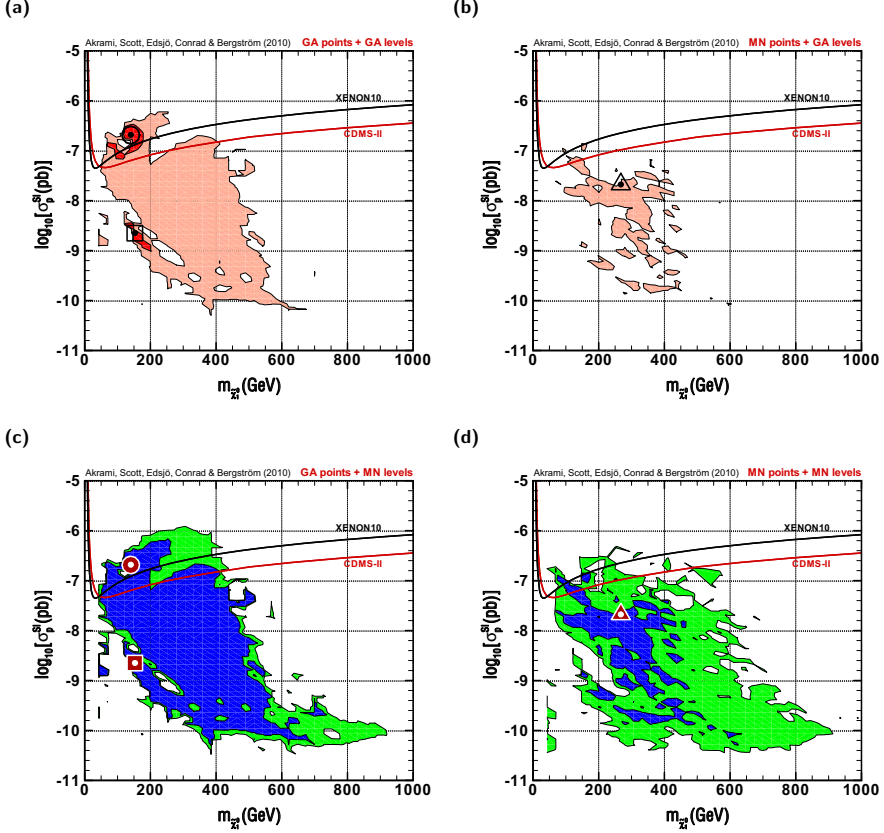


Figure 5: As in Fig. 1 and Fig. 2, but representing the best-fit points and high-likelihood regions for the spin-independent scattering cross-section of the neutralino and a proton σ_p^{SI} versus the neutralino mass $m_{\tilde{\chi}_1^0}$. Panels (a) and (d) show the statistically-consistent results of the GA and MultiNest scans, respectively. Panels (b) and (c) are given for comparative purposes only. The latest experimental limits from CDMS-II [91] and XENON10 [92] are also shown, plotted as red and black curves respectively. These curves are exclusion limits at the 90% confidence level under the assumption of a standard local halo configuration.

MultiNest has obviously only explored a small fraction of its 1σ high-likelihood region in the parameter space. It has also missed most of its 1σ and 2σ points in the region $\sigma_p^{SI} > 10^{-7}$ pb. This is a particularly interesting area, being within the reach of current dark matter DD experiments.

In Table 6, we also give the calculated values for the spin-dependent scattering cross-sections of the neutralino with a proton (σ_p^{SD}) and a neutron (σ_n^{SD}), for both the FP and COA best-fit points.

Considering implications for indirect detection (ID) of dark matter, one is often in-

direct detection		
	GA global BFP	GA BFP in COA region
σ_p^{SI}	2.057×10^{-7} pb	2.236×10^{-9} pb
σ_p^{SD}	2.435×10^{-6} pb	4.231×10^{-6} pb
σ_n^{SD}	1.644×10^{-6} pb	3.142×10^{-6} pb
indirect detection		
	GA global BFP	GA BFP in COA region
$\langle\sigma v\rangle$	$2.260 \times 10^{-26} \text{cm}^3 \text{s}^{-1}$	$5.385 \times 10^{-28} \text{cm}^3 \text{s}^{-1}$

Table 6: Dark matter direct and indirect detection observables. These are the spin-independent and spin-dependent scattering cross-sections of the neutralino with nucleons in pb (10^{-36}cm^2), and the velocity-averaged neutralino self-annihilation cross-section. These are calculated at the global best-fit point (BFP) located in the focus point (FP) region, and at the best-fit point in the stau co-annihilation (COA) region.

terested in a plot very similar to the one presented for the DD case, but now for the velocity-averaged neutralino self-annihilation cross-section $\langle\sigma v\rangle$ (instead of the scattering cross-section in the previous case), again versus the neutralino mass $m_{\tilde{\chi}_1^0}$. Such plots are shown in Fig. 6 for all different cases in the same style as in Fig. 5. Their general characteristics resemble very much those we enumerated for the DD case.

We first notice the strong correlation between the DD and ID plots, such as the generic similarities between the corresponding high-likelihood regions and the best-fit points. One interesting feature visible in these plots is the existence of a new, considerably large, high-likelihood region spanned by the approximate ranges of $350 \text{ GeV} < m_{\tilde{\chi}_1^0} < 500 \text{ GeV}$ and $-27.5 < \log_{10}(\langle\sigma v\rangle) < -26.5$ and almost completely missed by *MultiNest*. To our knowledge, this region has not been introduced so far by any other Bayesian or frequentist analysis. Further investigations show that these points are located in the stau co-annihilation region, but with very high m_0 (up to $\sim 1750 \text{ GeV}$). The very existence of such a high mass COA region compatible with all data indicates again that one should be very careful in drawing any conclusion that low masses in the parameter space are favoured over high masses by existing data. This point was emphasised earlier, in Sec. 3.1, with regards to the high-mass, high-likelihood points in the FP region.

Looking again at the high-likelihood regions and the best-fit points in Fig. 6, it is interesting to realise how likely these different points and regions are to be tested by the current and upcoming ID instruments. For example, depending on how much its sensitivity improves in future years, it might be possible for the Large Area Telescope (LAT) [93] aboard the *Fermi* gamma-ray space telescope to cover part of the high-likelihood FP region, including the global best-fit point with $\langle\sigma v\rangle \sim 2.3 \times 10^{-26} \text{cm}^3 \text{s}^{-1}$ (Table 6). It is in fact expected from pre-launch estimates [94] that the instrument will cover some fraction of the parameter space below $\langle\sigma v\rangle \sim 10^{-26} \text{cm}^3 \text{s}^{-1}$, depending on the neutralino mass. A detailed *MultiNest* global fit of the CMSSM parameter space using 9 months of *Fermi* data has already been performed [45], using the dwarf spheroidal galaxy Segue 1 as a target; constraints are already quite close to becoming interesting. A similar analysis can also be done using GAs. The other best-fit (COA) point, however, has $\langle\sigma v\rangle \sim 5.4 \times 10^{-28} \text{cm}^3 \text{s}^{-1}$, which is well below what is realistically detectable by *Fermi*.

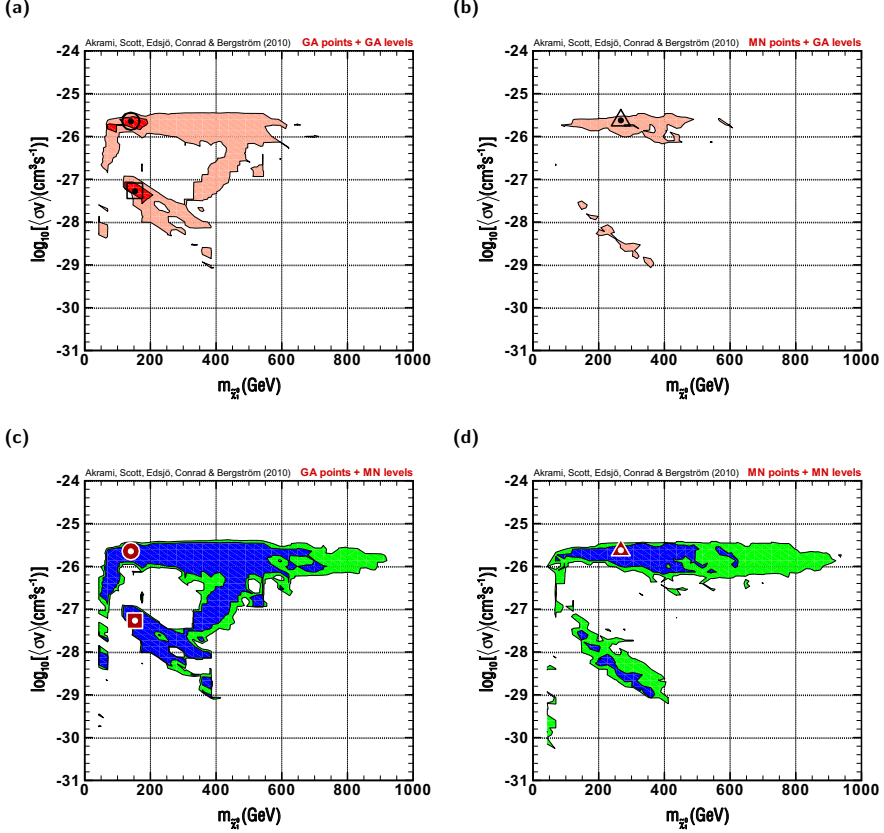


Figure 6: As in Fig. 1, Fig. 2 and Fig. 5 but representing the best-fit points and high-likelihood regions for the velocity-averaged neutralino self-annihilation cross-section $\langle\sigma v\rangle$ versus the neutralino mass $m_{\tilde{\chi}_1^0}$. Again, panels (a) and (d) show the statistically-consistent GA and MultiNest results, respectively, and panels (b) and (c) are given for comparative purposes only.

Finally, we have shown in Fig. 7 the 1D profile likelihood for the neutralino mass $m_{\tilde{\chi}_1^0}$. The plot is produced in the same way as Figs. 3 and 4, and compares the results of both GA and MultiNest scans. It is again important to notice the higher-likelihood points found by the GA almost everywhere in the interesting mass range. We also observe that both the FP and COA best-fit points have quite similar and low neutralino masses (~ 150 GeV), similar to what was seen for $m_{\tilde{g}}$ in Fig. 4.

3.4 Technical comparison with nested sampling

3.4.1 Dependence on priors and parameterisation

Throughout the previous sections, we compared our GA results mostly with those of the

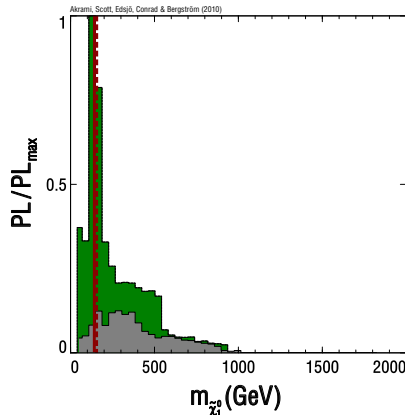


Figure 7: As in Fig. 3 and Fig. 4, but for the neutralino mass $m_{\tilde{\chi}_1^0}$.

linear-prior MultiNest scan of the CMSSM, especially when we discussed the resultant 1D and 2D profile likelihoods. We mentioned several times that MultiNest implemented with log priors gives a better value of 11.90 for the best-fit χ^2 , compared to the best fit when implemented with linear priors (13.51). It is true that one can achieve better fits in certain regions of the parameter space by utilising e.g. a logarithmic prior in the search algorithm (see e.g. Ref. 14 and references therein for a discussion of the effects of priors on best-fit points and high-likelihood regions, as well as Bayesian posterior means and high-probability regions). However, there are good reasons not to use the log-prior MultiNest results for the main performance comparisons in this paper.

Firstly, in order to make any comparison of the two algorithms reasonable, one should put both on the same footing. On the one hand, the likelihood function, as defined in terms of the original model parameters, is the only statistical measure employed in any frequentist study. Our genetic analysis is no exception. Our GA scans the parameter space according to the likelihood, as a function of the original model parameters. On the other hand, MultiNest, similarly to every other sampling technique optimised for Bayesian scans, performs the scan based on the posterior PDF (i.e. likelihood times prior) rather than the likelihood alone. Consequently, a very natural way of comparing the two is to make the latter sampling algorithm also proceed according to the likelihood function only. This can be achieved by choosing a flat prior in this case.

Imposing any other nontrivial prior (or equivalently, changing the scanning metric), although entirely justified in the Bayesian framework, is a very ad hoc approach in a frequentist framework. In the Bayesian case, this simply means that the algorithm samples the regions containing larger prior volumes better, producing more sample points in these regions. This is exactly what one requires for a Bayesian scan in which the density of

samples reflects the posterior density at different points in the parameter space. In the profile likelihood analysis however, we are interested in having reasonable maps of the likelihood function in terms of the given model parameters. Imposing any prior in this case means nothing but giving different scanning weights to different parts of the parameter space, i.e. forcing the algorithm to scan some regions with higher resolutions than the others; this can make the algorithm miss important points in some regions.

In the frequentist language, the effect of imposing a non-flat prior is the same as reparameterising the model. This for example means that, in the case of the log-prior scan, the likelihood function is redefined in terms of the logarithmically-scaled parameters rather than the original model parameters. Results of a profile likelihood analysis should in principle be independent of the specific parameterisation of the model; it should not matter if one works with e.g. one set of coordinates or another. This statement is however correct only if one has perfect knowledge of the likelihood function. No numerical scanning algorithm provides this perfect knowledge, as its resolution is always limited. This means that different parameterisations of the model do give different results until the limit of ‘perfect sampling’ has been reached. Any specific choice should then be justified ‘a priori’. One can for example argue that a specific scaling is theoretically better justified compared to others (e.g. that a log prior is geometrically preferred to a flat one). In principle this is a Bayesian statement, as it places an implicit measure on the parameter space, but it does have a practical impact upon frequentist profile likelihood scans. If one wanted to explore the effects of such reparameterisations, it would be entirely possible to do this by way of a GA, implemented in terms of genomes encoding the rescaled parameters. We suspect that by using a logarithmically-encoded genome, we would for example find the funnel region properly and probably even some better-fitting points than our current best-fit. Since our primary intention in the current work has been to look at the CMSSM model as it is, we have therefore adhered to the likelihood function defined in terms of the original parameters (and thus employed a linearly-encoded genome). We leave the investigation of logarithmically-encoded genomes for future work, where we intend to compare results with those of log-prior MultiNest scans.

3.4.2 Speed and convergence

The results presented in this work are based on 3 million sample points in total, corresponding to the same number of likelihood evaluations. The samples have been generated through 10 separate runs with different initial populations and 3000 generations each. The resultant samples were then combined to obtain the final set of points. Compared to a typical number of likelihood evaluations required in a MultiNest scan (around 500,000), the computational effort here is larger by a factor of 6. We have however chosen the number of runs and generations entirely by hand, not by any advanced convergence criteria; it may be possible to achieve similar (or better) results with less likelihood evaluations, using a more carefully tuned GA and/or a suitable stopping criterion.

There is in fact no way of checking whether or not our present implementation of the algorithm, although giving better results compared to MultiNest, has globally converged; there are indeed several reasons making us believe that it probably has not.

	m_0 (GeV)	$m_{1/2}$ (GeV)	A_0 (GeV)	$\tan\beta$	m_t (GeV)	$m_b(m_b)^{MS}$ (GeV)	$\alpha_s(m_Z)^{MS}$	$1/\alpha_{em}(m_Z)^{MS}$	χ^2_{min}
Run 1	1900.5	342.8	1873.9	55.0	172.9	4.20	0.1172	127.955	9.35
Run 2	133.9	383.1	840.6	17.9	173.3	4.20	0.1183	127.955	11.34
Run 3	198.8	426.3	1059.4	22.6	173.3	4.20	0.1183	127.955	11.45
Run 4	2817.3	244.6	1712.9	51.2	172.9	4.20	0.1179	127.954	11.55
Run 5	2693.1	240.0	1706.0	51.0	172.6	4.20	0.1179	127.954	11.61
Run 6	2737.8	238.7	1692.6	51.0	172.6	4.20	0.1176	127.954	11.63
Run 7	2775.1	248.2	1780.2	51.1	172.6	4.20	0.1179	127.954	11.65
Run 8	3102.3	287.3	1976.8	51.2	172.8	4.20	0.1176	127.954	11.76
Run 9	3158.9	276.6	1901.2	51.1	173.1	4.21	0.1174	127.955	11.78
Run 10	3159.3	317.0	2136.8	51.2	172.7	4.20	0.1180	127.955	11.86

Table 7: Parameter and χ^2 values at the best-fit points found by Genetic Algorithms in each of 10 runs. The final inference is based on all points found in all runs.

One way of seeing this is to look at the results for each of the 10 runs separately. To illustrate this, we have given in Fig. 8 the corresponding two-dimensional profile likelihoods in the m_0 - $m_{1/2}$ plane.⁴ The iso-likelihood contours in each panel show the statistically-consistent 1σ and 2σ confidence regions, based on the best-fit point found in that specific scan. Panels are sorted according to the best-fit χ^2 values. The values of all model and nuisance parameters at the best-fit points for all 10 runs are also given in Table 7, together with the best-fit χ^2 values.

Our global best-fit point ($\chi^2 = 9.35$) is found only in one run. The other 9 runs have not found best-fit points better than $\chi^2 = 11.34$. However, all these other best-fit values ($\chi^2 = 11.34, 11.45, 11.55, 11.61, 11.63, 11.65, 11.76, 11.78$, and 11.86) are also significantly better than the one found by MultiNest with linear priors ($\chi^2 = 13.51$). Although some of these best fits in individual runs are very similar to the value found by MultiNest with logarithmic priors ($\chi^2 = 11.90$), they are still at least slightly better in every single case.

The plots in Fig. 8 indicate that none of our individual GA runs have been able to cover all the interesting high-likelihood regions on their own. It seems for example that in runs 2 and 3, the algorithm has become trapped in local minima in the COA region. In runs 4-10, the same has happened at high masses, including the focus point region. However, if the individual GAs continued to run, they may have escaped these minima. In runs 6 and 7 for example, although the 1σ region does not include the global best-fit region of run 1, is very likely to extend and eventually uncover that region if the run continues. The other difficulty is that if the current version of the algorithm finds the global best-fit point (or some high-likelihood points in its vicinity) relatively quickly, the chance that it will then scan other points with lower likelihoods within the interesting confidence regions is dramatically reduced. This indicates a drawback of the algorithm in correctly mapping confidence intervals around the global best-fit point. This problem is not unexpected, as the primary purpose of GAs is to find global maxima or minima for a specific function as quickly as possible; if they succeed in this, there is no reason for them to start mapping the other less important surrounding points. This issue obviously becomes more serious

⁴Other two- and also one-dimensional profile likelihood plots for the parameters and observables exhibit similar features, so add little to the discussion.

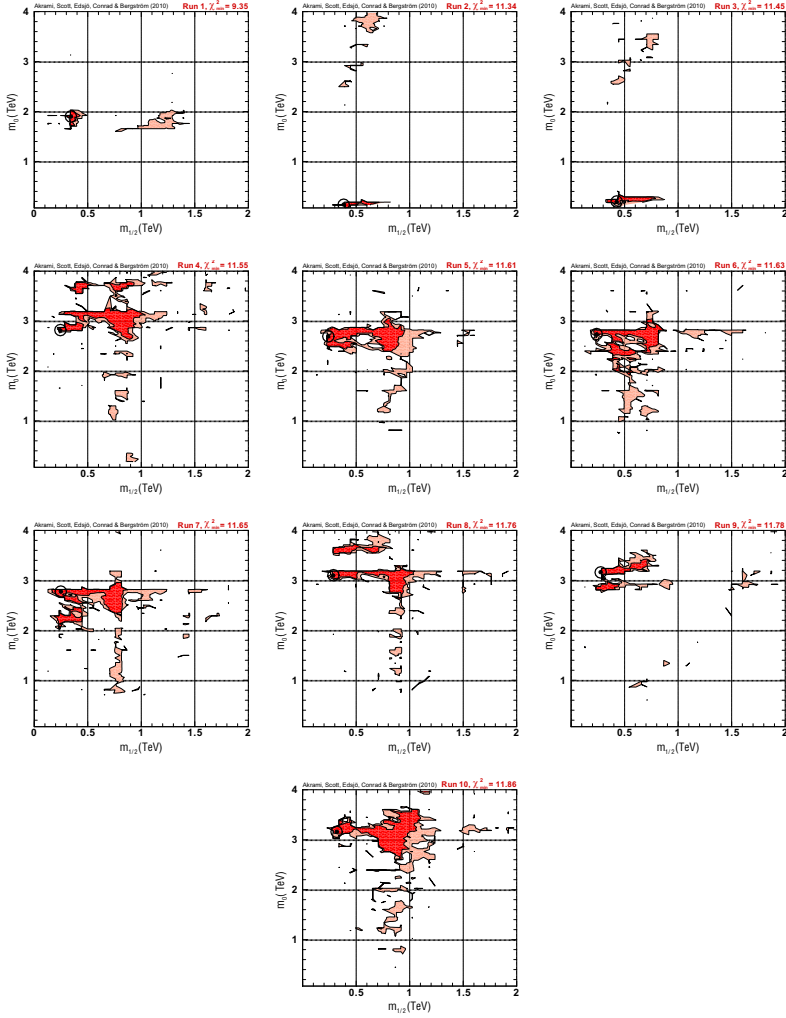


Figure 8: Individual two-dimensional profile likelihoods in the m_0 - $m_{1/2}$ plane for each of the 10 runs employed in our analysis. Each panel shows the statistically-consistent results of each scan based on the best-fit point found in that scan. As in previous figures, the inner and outer contours represent 68.3% (1σ) and 95.4% (2σ) confidence regions, respectively. The dotted circles show the best-fit points of each run. The sample points have been divided into 75×75 bins in all plots. Panels are sorted according to the values for the best-fit χ^2 . The final two-dimensional profile likelihood in Fig. 1a is obtained by combining all 10 scans and drawing iso-likelihood contours relative to the global best fit, i.e. $\chi^2 = 9.35$.

when spike-like best-fit regions exist, a characteristic which appears to be the case for the CMSSM. For example, the existence of relatively large high-likelihood regions in panels

4,5,6,7,8 and 10 is probably due to the fact that there are many points with likelihood values very close to the highest one, distributed in a large area; this is not the case for runs 1,2, or 3. This means that if the GAs continue to run in those cases and it so happens that the global best-fit point of run 1 is found at some stage, their mapping of the interesting regions will be much better than the present case in run 1. This is again an indication that there is a trade-off between how quickly we want the algorithm to find the actual global best-fit point and how accurately it is supposed to map the confidence regions; employing more advanced operators and strategies in the algorithms might improve the situation.

As far as our current implementation of GAs is concerned, all the above imply that the algorithms have not converged properly in every individual run. Firstly, they have not been able to find the actual global best-fit point in all (or even necessarily any) of the scans, and secondly, in the run with the highest-likelihood best-fit point (run 1), the mapping of the confidence regions around that point is rather unsatisfactory. On the other hand, most of the unwanted features discussed here are alleviated by combining the results of all 10 runs. This demonstrates the important role that parallelisation could play in improving the efficiency of GAs. Although our full set of sample points seems to provide better results than **MultiNest**, we are still not sure that this parallel version of the algorithm has converged either. This is again because the number of separate runs employed in our analysis is chosen rather arbitrarily. The arbitrariness in both the number of runs and the termination criteria in each run means that no result-driven convergence condition exists in our GAs. One could possibly utilise more sophisticated criteria in the termination condition, giving rise to better estimates of the convergence in each run, but to our knowledge no problem-independent such alternatives exist; we leave the investigation of such possibilities for future work.

As discussed in Sec. 3.1, even though such a convergence condition does exist for the **MultiNest** scans, making the algorithm terminate after less total likelihood evaluations than our GAs, it still misses many points that are important in the frequentist framework. The convergence criterion for **MultiNest** is defined in terms of the Bayesian evidence; even if a run is properly converged in terms of the evidence, this convergence makes sense only in the context of the Bayesian posterior PDF, not a frequentist profile likelihood analysis. That is, many isolated spikes might have been missed, and consequently the likelihood might not have been mapped effectively. Even tuning the convergence parameters (such as the tolerance) may not help. This is because if the **MultiNest** algorithm does not find a high-likelihood point on its first approach to a region, it is given no chance to go back and find it at a later stage. This means that even if the convergence parameter for **MultiNest** is tuned in such a way that the algorithm runs for the same number of likelihood evaluations as a GA (i.e. 3 million here), this does not help in finding better-fit points. One should thus be very careful in introducing convergence criteria to any scanning techniques (including GAs and **MultiNest**) dealing with a complex model such as the CMSSM; the criteria should be carefully defined depending on which statistical measure is employed.

We also point out that the isolated likelihood spikes missed by Bayesian algorithms will only fail to affect the posterior mass if a limited number of them exist. If there are a significant number of spikes, they could add up to a large portion of the posterior mass, and

affect even the Bayesian inference. Our GA results indicate that many such missed points actually exist, hinting that **MultiNest** might not have even mapped the entire posterior PDF correctly. Given the frequentist framework of this paper, this must unfortunately remain mere speculation, as our results do not allow any good estimate to be made of the posterior mass contained in the extra points.

We conclude this section by emphasising the role of parallelisation in terms of required computational power. Not only does the parallelisation enhance the scanning efficiency of GAs by reducing the probability of premature convergence and trapping in local maxima, it also increases the speed significantly. This can be done in different ways. Firstly, GAs work with a population of points instead of a single individual, providing extensive opportunity for treating different individuals in parallel. As an immediate consequence, the required time in a typical simple GA run with full generational replacement (the scheme we have used) can in principle decrease by a factor of n_p , the number of individuals in each population (100 in our case). The other way to parallelise GAs is to have separate populations evolve in parallel. By employing more advanced genetic operators and strategies such as ‘immigration’, individuals in different populations can even interact with each other. Although we have not employed such advanced parallel versions of the algorithm in our analysis, the samples have been generated in a parallel manner, i.e. through 10 separate runs with 3000 generations each.

4. Summary and conclusions

Constraining the parameter space of the MSSM using existing data is under no circumstances an easy or straightforward task. Even in the case of the CMSSM, a highly simplified and economical version of the model, the present data are not sufficient to constrain the parameters in a way completely independent of computational and statistical techniques.

There have been several efforts to study properties and predictions of different versions of the MSSM. Many recent activities in this field have used scanning methods optimised for calculating the Bayesian evidence and posterior PDF. Those analyses have been highly successful in revealing the complex structure of SUSY models, demonstrating that some patience will be required before we can place any strong constraints on their parameters. The same Bayesian scanning methods have also been employed for frequentist analyses of the problem, particularly in the framework of the profile likelihood. These methods are not optimised for such frequentist analyses, so care should be taken in applying them to such tasks.

We have employed a completely new scanning algorithm in this paper, based on Genetic Algorithms (GAs). We have shown GAs to be a powerful tool for frequentist approaches to the problem of scanning the CMSSM parameter space. We compared the outcomes of GA scans directly with those of the state-of-the-art Bayesian algorithm **MultiNest**, in the framework of the CMSSM. For this comparison, we mostly considered **MultiNest** scans with flat priors, but kept in mind that e.g. logarithmic priors give rise to higher-likelihood points at low masses in the CMSSM parameter space; we justified this choice of priors.

Our results are very promising and quite surprising. We found many new high-likelihood CMSSM points, which have a strong impact on the final statistical conclusions of the study. These not only influence considerably the inferred high-likelihood regions and confidence levels on the parameter values, but also indicate that the applicability of the conventional Bayesian scanning techniques is highly questionable in a frequentist context. Although our initial motivation in using GAs was to gain a correct estimate of the likelihood at the global best-fit point, which is crucial in a profile likelihood analysis, we also realised that they can find many new and interesting points in almost all the relevant regions of parameter space. These points strongly affect the inferred confidence regions around the best-fit point. Even though we cannot be confident of exactly how completely our algorithm is really mapping these high-likelihood regions, it has certainly covered large parts of them better than any previous algorithm.

We think that by improving the different ingredients of GAs, such as the crossover and mutation schemes, this ability might even be enhanced further. We largely employed the standard, simplest versions of the genetic operators in our analysis, as well as very typical genetic parameters. These turned out to work sufficiently well for our purposes. Although we believe that tuning the algorithm might produce even more interesting results, it is good news that satisfactory results can be produced even with a very generic version. This likely means that one can apply the method to more complicated SUSY models without extensive fine-tuning.

One interesting outcome of our scan is that the global best-fit point is found to be located in the focus point region, with a likelihood significantly larger than the best-fit point in the stau co-annihilation region (which in turn actually still has a higher likelihood than the global best-fit value obtained with **MultiNest**, even with logarithmic priors). The focus point region is favoured in our analysis over the co-annihilation region, in contrast to findings from some recent MCMC studies [31, 37], where the opposite was strongly claimed. We also found a rather large part of the stau co-annihilation region, consistent with all experimental data, located at high m_0 . This part of the co-annihilation region seems to have been missed in other recent scans. All these results show that, at least in our particular setup, high masses, corresponding either to the FP or the COA regions, are by no means disfavoured by current data (except perhaps direct detection of dark matter). The discrepancy between this finding and those of some other authors that the FP is disfavoured might originate in the different scanning algorithms employed, or in the different physics and likelihood calculations performed in each analysis. We have however shown, by comparing our results with others produced using exactly the same setup except for the scanning algorithm, that one should not be at all confident that all the relevant points for a frequentist analysis can be found by scanning techniques optimised for Bayesian statistics, such as nested sampling and MCMCs.

We have also calculated some of the quantities most interesting in searches for SUSY at the LHC, and in direct and indirect searches for dark matter. We showed that GAs found much better points compared to **MultiNest** almost everywhere in the interesting mass ranges of the lightest Higgs boson, gluino and neutralino. We confirmed previous conclusions that the LHC is in principle able to investigate a large fraction of the high-likelihood points

in the CMSSM parameter space if it explores sparticle masses up to around 3 TeV. As far as the Higgs mass is concerned, there are many points with rather low masses that, although sitting just below the low mass limit given by LEP, are globally very well fit to the experimental data. In the context of dark matter searches, we noticed that the global best-fit point and much of the surrounding 1σ confidence level region at high cross-sections are actually already mostly ruled out by direct detection limits, if one assumes the standard halo model to be accurate. We also argued that some of these points may be tested by upcoming indirect detection experiments, in particular the *Fermi* gamma-ray space telescope. Finally, we realised that the high-likelihood stau co-annihilation region at large m_0 introduces a new allowed region in the combination of the neutralino mass and self-annihilation cross-section, which (to our knowledge) has not been observed previously.

We also compared our algorithm with **MultiNest** in terms of speed and convergence, and argued that GAs are no worse than **MultiNest** in this respect. GAs have a large potential for parallelisation, reducing considerably the time required for a typical run. This property, as well as the fact that the computational effort scales linearly (i.e. as kN for an N -dimensional parameter space), also makes GAs an excellent method for the frequentist exploration of higher-dimensional SUSY parameter spaces.

Finally, perhaps the bottom line of the present work is that we once again see that even the CMSSM, despite its simplicity, possesses a highly complex and poorly-understood structure, with many small, fine-tuned regions. This makes investigation of the model parameter space very difficult and still very challenging for modern statistical scanning techniques. Although the method proposed in this paper seems to outperform the usual Bayesian techniques in a frequentist analysis, it is important to remember that it may by no means be the final word in this direction. Dependence of the results on the chosen statistical framework, measure and method calls for caution in drawing strong conclusions based on such scans. The situation will of course improve significantly with additional constraints provided by forthcoming data.

Acknowledgments

The authors are grateful to the Swedish Research Council (VR) for financial support. YA was also supported by the Helge Axelsson Johnson foundation. JC is a Royal Swedish Academy of Sciences Research Fellow supported by a grant from the Knut and Alice Wallenberg Foundation. We thank Roberto Trotta for helpful discussions. We are also thankful to the authors of Ref. 31 for useful comments on a previous version of the manuscript.

References

- [1] See e.g. S. P. Martin, *A Supersymmetry Primer*, arXiv:hep-ph/9709356.
- [2] I. Aitchison, *Supersymmetry in Particle Physics: An Elementary Introduction*, Cambridge University Press (2007); H. Baer and X. Tata, *Weak Scale Supersymmetry: From Superfields to Scattering Events*, Cambridge University Press (2006).

- [3] J. R. Ellis, S. Kelley and D. V. Nanopoulos, *Probing the desert using gauge coupling unification*, *Phys. Lett.* **B 260** (1991) 131.
- [4] See e.g. G. Jungman, M. Kamionkowski and K. Griest, *Supersymmetric dark matter*, *Phys. Rep.* **267** (1996) 195 [arXiv:hep-ph/9506380]; L. Bergström, *Non-baryonic dark matter: Observational evidence and detection methods*, *Rept. Prog. Phys.* **63** (2000) 793 [arXiv:hep-ph/0002126]; G. Bertone, D. Hooper and J. Silk, *Particle dark matter: Evidence, candidates and constraints*, *Phys. Rep.* **405** (2005) 279 [arXiv:hep-ph/0404175]; L. Bergström, *Dark Matter Candidates*, arXiv:0903.4849.
- [5] D. J. H. Chung, L. L. Everett, G. L. Kane, S. F. King, J. D. Lykken and L. T. Wang, *The soft supersymmetry-breaking Lagrangian: Theory and applications*, *Phys. Rep.* **407** (2005) 1 [arXiv:hep-ph/0312378].
- [6] M. A. Luty, *2004 TASI lectures on supersymmetry breaking*, arXiv:hep-th/0509029.
- [7] S. S. AbdusSalam, B. C. Allanach, M. J. Dolan, F. Feroz and M. P. Hobson, *Selecting a Model of Supersymmetry Breaking Mediation*, *Phys. Rev.* **D 80** (2009) 035017 [arXiv:0906.0957].
- [8] A. Chamseddine, R. Arnowitt and P. Nath, *Locally Supersymmetric Grand Unification*, *Phys. Rev. Lett.* **49** (1982) 970.
- [9] R. Barbieri, S. Ferrara and C. Savoy, *Gauge Models With Spontaneously Broken Local Supersymmetry*, *Phys. Lett.* **B 119** (1982) 343; N. Ohta, *Grand Unified Theories Based On Local Supersymmetry*, *Prog. Theor. Phys.* **70** (1983) 542; L. J. Hall, J. Lykken and S. Weinberg, *Supergravity As The Messenger Of Supersymmetry Breaking*, *Phys. Rev.* **D 27** (1983) 2359; P. Nath, R. L. Arnowitt and A. H. Chamseddine, *Gauge Hierarchy In Supergravity Guts*, *Nucl. Phys.* **B 227** (1983) 121; And for some reviews, see e.g. H. P. Nilles, *Supersymmetry, Supergravity and Particle Physics*, *Phys. Rep.* **110** (1984) 1; A. Brignole, L. E. Ibañez and C. Muñoz, *Soft supersymmetry breaking terms from supergravity and superstring models*, published in *Perspectives on Supersymmetry*, ed. G. L. Kane, 125 [arXiv:hep-ph/9707209].
- [10] L. Alvarez-Gaume, J. Polchinski and M. B. Wise, *Minimal Low-Energy Supergravity*, *Nucl. Phys.* **B 221** (1983) 495; R. Arnowitt and P. Nath, *Supersymmetric mass spectrum in $SU(5)$ supergravity grand unification*, *Phys. Rev. Lett.* **69** (1992) 725; P. Nath and R. Arnowitt, *Radiative breaking, proton stability and the viability of no-scale supergravity models*, *Phys. Lett.* **B 287** (1992) 89; P. Nath and R. Arnowitt, *Top quark mass and Higgs mass limits in the standard $SU(5)$ supergravity unification*, *Phys. Lett.* **B 289** (1992) 368; G. G. Ross and R. G. Roberts, *Minimal supersymmetric unification predictions*, *Nucl. Phys.* **B 377** (1992) 571; P. Nath and R. Arnowitt, *Predictions in $SU(5)$ supergravity grand unification with proton stability and relic density constraints*, *Phys. Rev. Lett.* **70** (1993) 3696 [arXiv:hep-ph/9302318]; R. L. Arnowitt and P. Nath, *Cosmological constraints and $SU(5)$ supergravity grand*

- unification, *Phys. Lett. B* **299** (1993) 58 [Erratum-ibid. **307** (1993) 403] [arXiv:hep-ph/9302317]; V. Barger, M. S. Berger and P. Ohmann, *Supersymmetric particle spectrum*, *Phys. Rev. D* **49** (1994) 4908 [arXiv:hep-ph/9311269]; G. L. Kane, C. F. Kolda, L. Roszkowski and J. D. Wells, *Study of constrained minimal supersymmetry*, *Phys. Rev. D* **49** (1994) 6173 [arXiv:hep-ph/9312272].
- [11] G. Cowan, *Statistical data analysis*, Oxford University Press (1998).
- [12] W. A. Rolke, A. M. Lopez and J. Conrad, *Confidence Intervals with Frequentist Treatment of Statistical and Systematic Uncertainties*, *Nucl. Instrum. Methods A* **551** (2005) 493 [arXiv:physics/0403059].
- [13] For an introduction to general applications of Bayesian statistics in physics, see e.g. G. D’Agostini, *Probability and Measurement Uncertainty in Physics - a Bayesian Primer*, arXiv:hep-ph/9512295; For reviews of its applications in cosmology, see, R. Trotta, *Applications of Bayesian model selection to cosmological parameters*, *Mon. Not. Roy. Astron. Soc.* **378** (2007) 72 [arXiv:astro-ph/0504022]; R. Trotta, *Bayes in the sky: Bayesian inference and model selection in cosmology*, *Contemp. Phys.* **49** (2008) 71 [arXiv:0803.4089]; A. R. Liddle, *Statistical methods for cosmological parameter selection and estimation*, arXiv:0903.4210; M. Hobson, A. Jaffe, A. Liddle, P. Mukherjee, *Bayesian Methods in Cosmology*, Cambridge University Press (2008).
- [14] R. Trotta, F. Feroz, M.P. Hobson, L. Roszkowski and R. Ruiz de Austri, *The impact of priors and observables on parameter inferences in the Constrained MSSM*, *JHEP* **12** (2008) 024 [arXiv:0809.3792].
- [15] M. Drees and M. Nojiri, *The neutralino relic density in minimal $N=1$ supergravity*, *Phys. Rev. D* **47** (1993) 376 [arXiv:hep-ph/9207234].
- [16] H. Baer and M. Brhlik, *Cosmological relic density from minimal supergravity with implications for collider physics*, *Phys. Rev. D* **53** (1996) 597 [arXiv:hep-ph/9508321]; J. R. Ellis, T. Falk, K. A. Olive and M. Srednicki, *Calculations of neutralino–stau coannihilation channels and the cosmologically relevant region of MSSM parameter space*, *Astropart. Phys.* **13** (2000) 181 [Erratum-ibid. **15** (2001) 413] [arXiv:hep-ph/9905481]; J. R. Ellis, T. Falk, G. Ganis, K. A. Olive and M. Srednicki, *The CMSSM parameter space at large $\tan \beta$* , *Phys. Lett. B* **510** (2001) 236 [arXiv:hep-ph/0102098]; T. Nihei, L. Roszkowski and R. Ruiz de Austri, *New Cosmological and Experimental Constraints on the CMSSM*, *JHEP* **08** (2001) 024 [arXiv:hep-ph/0106334]; A. Lahanas and V. Spanos, *Implications of the pseudo–scalar Higgs boson in determining the neutralino dark matter*, *Euro. Phys. Journ. C* **23** (2002) 185 [arXiv:hep-ph/0106345].
- [17] J. R. Ellis, T. Falk, G. Ganis, K.A. Olive and M. Srednicki, *The CMSSM parameter space at large $\tan \beta$* , *Phys. Lett. B* **510** (2001) 236 [arXiv:hep-ph/0102098]; J. R. Ellis, K. A. Olive, Y. Santoso and V. C. Spanos, *Likelihood analysis of the CMSSM parameter space*, *Phys. Rev. D* **69** (2004) 095004 [arXiv:hep-ph/0310356]; J. R. Ellis,

- S. Heinemeyer, K. A. Olive and G. Weiglein, *Indirect sensitivities to the scale of supersymmetry*, *JHEP* **02** (2005) 013 [arXiv:hep-ph/0411216]; J. R. Ellis, S. Heinemeyer, K. A. Olive and G. Weiglein, *Phenomenological indications of the scale of supersymmetry*, *JHEP* **05** (2006) 005 [arXiv:hep-ph/0602220]; O. Buchmueller *et al.*, *Prediction for the Lightest Higgs Boson Mass in the CMSSM using Indirect Experimental Constraints*, *Phys. Lett. B* **657** (2007) 87 [arXiv:0707.3447].
- [18] E. A. Baltz and P. Gondolo, *Markov chain monte carlo exploration of minimal supergravity with implications for dark matter*, *JHEP* **10** (2004) 052 [arXiv:hep-ph/0407039].
- [19] B. C. Allanach and C. G. Lester, *Multi-dimensional mSUGRA likelihood maps*, *Phys. Rev. D* **73** (2006) 015013 [arXiv:hep-ph/0507283].
- [20] B. C. Allanach, *Naturalness priors and fits to the constrained minimal supersymmetric standard model*, *Phys. Lett. B* **635** (2006) 123 [arXiv:hep-ph/0601089].
- [21] R. Ruiz de Austri, R. Trotta and L. Roszkowski, *A Markov Chain Monte Carlo analysis of the CMSSM*, *JHEP* **05** (2006) 002 [arXiv:hep-ph/0602028].
- [22] R. Trotta, R. Ruiz de Austri and L. Roszkowski, *Prospects for direct dark matter detection in the Constrained MSSM*, *New Astron. Rev.* **51** (2007) 316 [arXiv:astro-ph/0609126].
- [23] B. C. Allanach, C. G. Lester and A. M. Weber, *The dark side of mSUGRA*, *JHEP* **12** (2006) 065 [arXiv:hep-ph/0609295].
- [24] L. Roszkowski, R. Ruiz de Austri and R. Trotta, *On the detectability of the CMSSM light Higgs boson at the Tevatron*, *JHEP* **04** (2007) 084 [arXiv:hep-ph/0611173].
- [25] B. C. Allanach, K. Cranmer, C. G. Lester, and A. M. Weber, *Natural Priors, CMSSM Fits and LHC Weather Forecasts*, *JHEP* **08** (2007) 023 [arXiv:0705.0487].
- [26] L. Roszkowski, R. Ruiz de Austri and R. Trotta, *Implications for the Constrained MSSM from a new prediction for $b \rightarrow s\gamma$* , *JHEP* **07** (2007) 075 [arXiv:0705.2012].
- [27] L. Roszkowski, R. Ruiz de Austri, J. Silk and R. Trotta, *On prospects for dark matter indirect detection in the Constrained MSSM*, *Phys. Lett. B* **671** (2009) 10 [arXiv:0707.0622].
- [28] R. Lafaye, T. Plehn, M. Rauch and D. Zerwas, *Measuring Supersymmetry*, *Euro. Phys. Journ. C* **54** (2008) 617 [arXiv:0709.3985].
- [29] B. C. Allanach, M. J. Dolan and A. M. Weber, *Global Fits of the Large Volume String Scenario to WMAP5 and Other Indirect Constraints Using Markov Chain Monte Carlo*, *JHEP* **08** (2008) 105 [arXiv:0806.1184].
- [30] B. C. Allanach and D. Hooper, *Panglossian Prospects for Detecting Neutralino Dark Matter in Light of Natural Priors*, *JHEP* **10** (2008) 071 [arXiv:0806.1923].

- [31] O. Buchmueller *et al.*, *Predictions for Supersymmetric Particle Masses in the CMSSM using Indirect Experimental and Cosmological Constraints*, *JHEP* **09** (2008) 117 [arXiv:0808.4128].
- [32] G. D. Martinez, J. S. Bullock, M. Kaplinghat, L. E. Strigari and R. Trotta, *Indirect Dark Matter Detection from Dwarf Satellites: Joint Expectations from Astrophysics and Supersymmetry*, *JCAP* **06** (2009) 014 [arXiv:0902.4715].
- [33] L. Roszkowski, R. R. de Austri, R. Trotta, Y. L. Tsai and T. A. Varley, *Some novel features of the Non-Universal Higgs Model*, arXiv:0903.1279.
- [34] C. Balazs and D. Carter, *Likelihood analysis of the next-to-minimal supergravity motivated model*, arXiv:0906.5012.
- [35] G. Belanger, F. Boudjema, A. Pukhov and R. K. Singh, *Constraining the MSSM with universal gaugino masses and implication for searches at the LHC*, arXiv:0906.5048.
- [36] P. Bechtle, K. Desch, M. Uhlenbrock and P. Wienemann, *Constraining SUSY models with Fittino using measurements before, with and beyond the LHC*, arXiv:0907.2589.
- [37] O. Buchmueller *et al.*, *Likelihood Functions for Supersymmetric Observables in Frequentist Analyses of the CMSSM and NUHM1*, arXiv:0907.5568.
- [38] See e.g. A. Lewis and S. Bridle, *Cosmological parameters from CMB and other data: a Monte-Carlo approach*, *Phys. Rev. D* **66** (2002) 103511 [arXiv:astro-ph/0205436].
- [39] J. Skilling, *Nested sampling*, in *Bayesian inference and maximum entropy methods in science and engineering*, R. Fischer, R. Preuss and U. von Toussaint eds., Springer Verlag, U.S.A., *AIP Conf. Proc.* **735** (2004) 395; J. Skilling, *Nested sampling for general bayesian computation*, *Bayesian Anal.* **C1** (2006) 833.
- [40] F. Feroz and M. P. Hobson *Multimodal nested sampling: an efficient and robust alternative to MCMC methods for astronomical data analysis*, *Mon. Not. Roy. Astron. Soc.* **384** (2008) 449 [arXiv:0704.3704]; F. Feroz, M. P. Hobson and M. Bridges, *MultiNest: an efficient and robust Bayesian inference tool for cosmology and particle physics*, arXiv:0809.3437.
- [41] F. Feroz, B. C. Allanach, M. Hobson, S. S. AbdusSalam, R. Trotta and A. M. Weber, *Bayesian Selection of $\text{sign}(\mu)$ within $mSUGRA$ in Global Fits Including WMAP5 Results*, *JHEP* **10** (2008) 064 [arXiv:0807.4512].
- [42] F. Feroz, M. P. Hobson, L. Roszkowski, R. R. de Austri, and R. Trotta, *Are $BR(\bar{B} \rightarrow X_s \gamma)$ and $(g-2)_\mu$ consistent within the Constrained MSSM?*, arXiv:0903.2487.
- [43] R. Trotta, R. R. de Austri and C. P. d. Heros, *Prospects for dark matter detection with IceCube in the context of the CMSSM*, arXiv:0906.0366.
- [44] L. Roszkowski, R. R. de Austri and R. Trotta, *Efficient reconstruction of CMSSM parameters from LHC data - A case study*, arXiv:0907.0594.

- [45] P. Scott, J. Conrad, J. Edsjö, L. Bergström, C. Farnier and Y. Akrami, *Direct Constraints on Minimal Supersymmetry from Fermi-LAT Observations of the Dwarf Galaxy Segue 1*, arXiv:0909.3300.
- [46] P. Scott and S. Sivertsson, *Gamma-Rays from Ultracompact Primordial Dark Matter Minihalos*, arXiv:0908.4082.
- [47] D. E. Lopez-Fogliani, L. Roszkowski, R. R. de Austri and T. A. Varley, *A Bayesian Analysis of the Constrained NMSSM*, arXiv:0906.4911.
- [48] S. S. AbdusSalam, B. C. Allanach, F. Quevedo, F. Feroz and M. Hobson, *Fitting the Phenomenological MSSM*, arXiv:0904.2548.
- [49] B. C. Allanach, D. Grellscheid and F. Quevedo, *Genetic algorithms and experimental discrimination of SUSY models*, *JHEP* **07** (2004) 069 [arXiv:hep-ph/0406277].
- [50] K. H. Becks, S. Hahn and A. Hemker, *Genetic algorithms in elementary particle physics (In German)*, *Phys. Bl.* **50** (1994) 238; G. Organtini, *A genetic algorithm for optimization of selection algorithms in high energy physics*, Talk given at *Computing in High-energy Physics (CHEP 97)*, Berlin, Germany, 7-11 Apr 1997; S. Abdullin *et al.*, *GARCON: Genetic Algorithm for Rectangular Cuts Optimization. User's manual for version 2.0*, arXiv:hep-ph/0605143; S. Abdullin, *Genetic algorithm for SUSY trigger optimization in CMS detector at LHC*, *Nucl. Instrum. Methods* **A 502** (2003) 693; J. M. Link *et al.* [FOCUS Collaboration], *Application of Genetic Programming to High Energy Physics Event Selection*, *Nucl. Instrum. Methods* **A 551** (2005) 504 [arXiv:hep-ex/0503007]; J. M. Link *et al.* [FOCUS Collaboration], *Search for $\Lambda_c^+ \rightarrow pK^+\pi^-$ and $D_s^+ \rightarrow K^+K^+\pi^-$ Using Genetic Programming Event Selection*, *Phys. Lett.* **B 624** (2005) 166 [arXiv:hep-ex/0507103]; L. Teodorescu, *Gene expression programming approach to event selection in high energy physics*, *IEEE Trans. Nucl. Sci.* **53** (2006) 2221; M. Mjahed, *Search for the Higgs boson at LHC by using Genetic Algorithms*, *Nucl. Instrum. Methods* **A 559** (2006) 199; R. Berlich and M. Kunze, *Parametric optimization with evolutionary strategies in particle physics*, *Nucl. Instrum. Methods* **A 534** (2004) 147.
- [51] J. F. Markham and T. D. Kieu, *Evolutionary algorithms applied to Landau-gauge fixing*, *Nucl. Phys. Proc. Suppl.* **73** (1999) 868 [arXiv:hep-lat/9809143]; O. Oliveira and P. J. Silva, *Gribov copies and gauge fixing in lattice gauge theories*, *Nucl. Phys. Proc. Suppl.* **106** (2002) 1088 [arXiv:hep-lat/0110035]; O. Oliveira and P. J. Silva, *An algorithm for Landau gauge fixing in lattice QCD*, *Comput. Phys. Commun.* **C158** (2004) 73 [arXiv:hep-lat/0309184]; A. Yamaguchi and H. Nakajima, *Landau Gauge Fixing Supported by Genetic Algorithm*, *Nucl. Phys. Proc. Suppl.* **83** (2000) 840 [arXiv:hep-lat/9909064]; A. Yamaguchi and A. Sugamoto, *Genetic Algorithm for Lattice Gauge Theory: On SU(2) and U(1) on 4 dimensional lattice, how to hitchhike to thermal equilibrium state*, *Nucl. Phys. Proc. Suppl.* **83** (2000) 837 [arXiv:hep-lat/9909063]; A. Yamaguchi, *Genetic Algorithm for SU(2) Gauge Theory on a 2-dimensional Lattice*, *Nucl.*

- Phys. Proc. Suppl.* **73** (1999) 847 [arXiv:hep-lat/9809068]; A. Yamaguchi, *Genetic Algorithm for $SU(N)$ gauge theory on a lattice*, arXiv:hep-lat/9808001; G. M. von Hippel, R. Lewis and R. G. Petry, *Evolutionary Fitting Methods for the Extraction of Mass Spectra in Lattice Field Theory*, *Comput. Phys. Commun.* **C178** (2008) 713 [arXiv:0707.2788]; G. M. von Hippel, R. Lewis and R. G. Petry, *Using evolutionary algorithms to extract field theory mass spectra*, *PoS LAT2007* (2007) 043 [arXiv:0710.0014]; GAs have also been used to train neural networks, see e.g. J. Rojo and J. Rojo and J. I. Latorre, *Neural network parametrization of spectral functions from hadronic tau decays and determination of QCD vacuum condensates*, *JHEP* **01** (2004) 055 [arXiv:hep-ph/0401047]; A. Hoecker *et al.*, *TMVA - Toolkit for Multivariate Data Analysis*, arXiv:physics/0703039.
- [52] L. Teodorescu, *Evolutionary Computation in High Energy Physics*, arXiv:0804.0369.
- [53] C. Bogdanos and S. Nesseris, *Genetic Algorithms and Supernovae Type Ia Analysis*, *JCAP* **05** (2009) 006 [arXiv:0903.2805]; J. Liesenborgs, S. De Rijcke, H. Dejonghe and P. Bekaert, *Non-parametric inversion of gravitational lensing systems with few images using a multi-objective genetic algorithm*, arXiv:0707.2538; J. Liesenborgs, S. De Rijcke and H. Dejonghe, *A genetic algorithm for the non-parametric inversion of strong lensing systems*, *Mon. Not. Roy. Astron. Soc.* **367** (2006) 1209 [arXiv:astro-ph/0601124]; B. J. Brewer and G. F. Lewis, *When Darwin Met Einstein: Gravitational Lens Inversion with Genetic Algorithms*, arXiv:astro-ph/0501202; A. Petiteau, S. Yu and S. Babak, *The search for spinning black hole binaries using a genetic algorithm*, arXiv:0905.1785; J. Crowder, N. J. Cornish and L. Reddinger, *Darwin meets Einstein: LISA data analysis using genetic algorithms*, *Phys. Rev. D* **73** (2006) 063011 [arXiv:gr-qc/0601036]; D. J. Marshall, G. Joncas and A. P. Jones, *Distribution and characteristics of Infrared Dark Clouds using genetic forward modelling*, arXiv:0908.3851.
- [54] C. Fernandez-Ramirez, E. Moya de Guerra, A. Udias and J. M. Udias, *Properties of Nucleon Resonances by means of a Genetic Algorithm*, *Phys. Rev. C* **77** (2008) 065212 [arXiv:0805.4178]; C. Winkler and H. M. Hofmann, *Determination of bound state wave functions by a genetic algorithm*, *Phys. Rev. C* **55** (1997) 684 [arXiv:nucl-th/9412032]; D. G. Ireland, S. Janssen and J. Ryckebusch, *A genetic algorithm analysis of N^* resonances in $p(\gamma, K^+)\Lambda$ reactions*, *Nucl. Phys. A* **740** (2004) 147 [arXiv:nucl-th/0312103]; S. Janssen, D. G. Ireland and J. Ryckebusch, *Extraction of N^* information from the limited $p(\gamma, K^+)\Lambda$ data set*, *Phys. Lett. B* **562** (2003) 51 [arXiv:nucl-th/0302047]; C. Fernandez-Ramirez, E. Moya de Guerra and J. M. Udias, *Effective Lagrangian approach to pion photoproduction from the nucleon*, *Ann. Phys.* **321** (2006) 1408 [arXiv:nucl-th/0509020]; C. Fernandez-Ramirez, E. Moya de Guerra and J. M. Udias, *Eta Photoproduction as a Test of the Extended Chiral Symmetry*, *Phys. Lett. B* **651** (2007) 369 [arXiv:0706.0616].
- [55] By CDF Collaboration and D0 Collaboration, *A Combination of CDF and D0 Results on the Mass of the Top Quark*, arXiv:0803.1683.

- [56] W. M. Yao *et al.* [Particle Data Group], *Review of Particle Physics*, *J. Phys.* **G 33** (2006) 1 and 2007 partial update for the 2008 edition.
- [57] K. Hagiwara, A. D. Martin, D. Nomura and T. Teubner, *Improved predictions for $g-2$ of the muon and $\alpha_{\text{QED}}(M_Z^2)$* , *Phys. Lett.* **B 649** (2007) 173 [arXiv:hep-ph/0611102].
- [58] See <http://lepewwg.web.cern.ch/LEPEWWG>.
- [59] J. P. Miller, E. de Rafael and B. L. Roberts, *Muon $g-2$: Review of Theory and Experiment*, *Rept. Prog. Phys.* **70** (2007) 795 [arXiv:hep-ph/0703049].
- [60] E. Barberio *et al.* [Heavy Flavor Averaging Group (HFAG) Collaboration], *Averages of b -hadron properties at the end of 2006*, arXiv:0704.3575.
- [61] A. Abulencia *et al.* [CDF - Run II Collaboration], *Measurement of the $B_s - \bar{B}_s$ oscillation frequency*, *Phys. Rev. Lett.* **97** (2006) 062003 [arXiv:hep-ex/0606027]; A. Abulencia *et al.* [CDF Collaboration], *Observation of $B_s - \bar{B}_s$ oscillations*, *Phys. Rev. Lett.* **97** (2006) 242003 [arXiv:hep-ex/0609040].
- [62] J. Dunkley *et al.* [The WMAP Collaboration], *Five-year Wilkinson Microwave Anisotropy Probe (WMAP) Observations: Likelihoods and parameters from the WMAP data*, *Astrophys. J. Suppl.* **180** (2009) 306 [arXiv:0803.0586].
- [63] The CDF Collaboration, *Search for $B_s \rightarrow \mu^+ \mu^-$ and $B_d \rightarrow \mu^+ \mu^-$ decays in $p\bar{p}$ collisions with CDF-II*, CDF note 8956 (August 2007).
- [64] The LEP Higgs Working Group, <http://lephiggs.web.cern.ch/LEPHIGGS>; G. Abbiendi *et al.* [the ALEPH Collaboration, the DELPHI Collaboration, the L3 Collaboration and the OPAL Collaboration, The LEP Working Group for Higgs Boson Searches], *Search for the standard model Higgs boson at LEP*, *Phys. Lett.* **B 565** (2003) 61 [arXiv:hep-ex/0306033].
- [65] A. Heister *et al.* [ALEPH Collaboration], *Absolute mass lower limit for the lightest neutralino of the MSSM from $e^+ e^-$ data at $s^{1/2}$ up to 209 GeV*, *Phys. Lett.* **B 583** (2004) 247.
- [66] LEP SUSY Working Group for the ALEPH, DELPHI, L3 and OPAL collaborations, <http://lepsusy.web.cern.ch/lepsusy>.
- [67] A. Heister *et al.* [ALEPH Collaboration], *Search for scalar leptons $e^+ e^-$ collisions at center-of-mass energies up to 209 GeV*, *Phys. Lett.* **B 526** (2002) 206 [arXiv:hep-ex/0112011].
- [68] P. Achard *et al.* [L3 Collaboration], *Search for scalar leptons and scalar quarks at LEP*, *Phys. Lett.* **B 580** (2004) 37 [arXiv:hep-ex/0310007].
- [69] J. Abdallah *et al.* [DELPHI Collaboration], *Searches for supersymmetric particles in $e^+ e^-$ collisions up to 208 GeV and interpretation of the results within the MSSM*, *Euro. Phys. Journ.* **C31** (2004) 421 [arXiv:hep-ex/0311019].

- [70] Available from: <http://superbayes.org>.
- [71] B. C. Allanach, *SOFTSUSY: a program for calculating supersymmetric spectra*, *Comput. Phys. Commun.* **C143** (2002) 305 [arXiv:hep-ph/0104145]; Available from: <http://projects.hepforge.org/softsusy/>.
- [72] P. Gondolo, J. Edsjö, P. Ullio, L. Bergström, M. Schelke and E. A. Baltz, *DarkSUSY: Computing supersymmetric dark matter properties numerically*, *JCAP* **07** (2004) 008 [arXiv:astro-ph/0406204]; Available from: <http://www.physto.se/~edsjo/darksusy/>.
- [73] S. Heinemeyer, W. Hollik and G. Weiglein, *The Masses of the Neutral CP-even Higgs Bosons in the MSSM: Accurate Analysis at the Two-Loop Level*, *Euro. Phys. Journ.* **C9** (1999) 343 [arXiv:hep-ph/9812472]; S. Heinemeyer, W. Hollik and G. Weiglein, *FeynHiggs: a program for the calculation of the masses of the neutral CP-even Higgs bosons in the MSSM*, *Comput. Phys. Commun.* **C124** (2000) 76 [arXiv:hep-ph/9812320]; G. Degrandi, S. Heinemeyer, W. Hollik, P. Slavich and G. Weiglein, *Towards High-Precision Predictions for the MSSM Higgs Sector*, *Euro. Phys. Journ.* **C28** (2003) 133 [arXiv:hep-ph/0212020]; M. Frank, T. Hahn, S. Heinemeyer, W. Hollik, H. Rzehak and G. Weiglein, *The Higgs Boson Masses and Mixings of the Complex MSSM in the Feynman-Diagrammatic Approach*, *JHEP* **02** (2007) 047 [arXiv:hep-ph/0611326]; Available from: <http://www.feynhiggs.de/>.
- [74] Available from: <http://www.lapp.in2p3.fr/lapth/micromegas/>.
- [75] H. Flacher, M. Goebel, J. Haller, A. Hocker, K. Moenig and J. Stelzer, *Gfitter - Revisiting the Global Electroweak Fit of the Standard Model and Beyond*, *Euro. Phys. Journ.* **C60** (2009) 543 [arXiv:0811.0009].
- [76] For a classic introduction to GAs, see D. E. Goldberg, *Genetic Algorithms in Search, Optimization and Machine Learning*, Addison-Wesley (1989).
- [77] For recent introductions to GAs, see e.g. S. N. Sivanandam and S. N. Deepa, *Introduction to Genetic Algorithms*, Springer (2007); A. E. Eiben and J. E. Smith, *Introduction to Evolutionary Computing*, Springer (2008); M. Affenzeller, S. Winkler, S. Wagner and A. Beham, *Genetic Algorithms and Genetic Programming: Modern Concepts and Practical Applications*, Chapman & Hall/CRC (2009).
- [78] For a modern treatment of GAs, see D. E. Goldberg, *Genetic Algorithms: The Design of Innovation*, Springer (2010) to appear.
- [79] J. H. Holland, *Adaptation in Natural and Artificial Systems*, Ann Arbor: The University of Michigan Press (1975), Second Edition: Cambridge, MIT Press (1992).
- [80] P. Charbonneau, *Astrophys. J. Suppl.* **101** (1995) 309; P. Charbonneau and B. Knapp, 1996, A User's Guide to PIKAIA 1.0, NCAR Technical Note 418+IA (Boulder: National Center for Atmospheric Research); P. Charbonneau, 2002, Release Notes for

PIKAIA 1.2, NCAR Technical Note 451+STR (Boulder: National Center for Atmospheric Research).

- [81] PIKAIA can be downloaded from:
<http://www.hao.ucar.edu/modeling/pikaia/pikaia.php>.
- [82] S. N. Sivanandam and S. N. Deepa, *Genetic Algorithms Reference, Volume I: Crossover for single-objective numerical optimization problems*, Published by Tomasz Dominik Gwiazda (2006).
- [83] B. C. Allanach, G. Belanger, F. Boudjema and A. Pukhov, *Requirements on collider data to match the precision of WMAP on supersymmetric dark matter*, *JHEP* **12** (2004) 020 [arXiv:hep-ph/0410091].
- [84] K. Griest and D. Seckel, *Three exceptions in the calculation of relic abundances*, *Phys. Rev. D* **43** (1991) 3191.
- [85] K. L. Chan, U. Chattopadhyay and P. Nath, *Naturalness, weak scale supersymmetry and the prospect for the observation of supersymmetry at the Tevatron and at the LHC*, *Phys. Rev. D* **58** (1998) 096004 [arXiv:hep-ph/9710473]; J. L. Feng, K. T. Matchev and T. Moroi, *Multi-TeV scalars are natural in minimal supergravity*, *Phys. Rev. Lett.* **84** (2000) 2322 [arXiv:hep-ph/9908309]; J. L. Feng, K. T. Matchev and T. Moroi, *Focus points and naturalness in supersymmetry*, *Phys. Rev. D* **61** (2000) 075005 [arXiv:hep-ph/9909334]; J. L. Feng, K. T. Matchev and F. Wilczek, *Neutralino Dark Matter in Focus Point Supersymmetry*, *Phys. Lett. B* **482** (2000) 388 [arXiv:hep-ph/0004043].
- [86] A. Djouadi, M. Drees and J. L. Kneur, *Neutralino dark matter in mSUGRA: Reopening the light Higgs pole window*, *Phys. Lett. B* **624** (2005) 60 [arXiv:hep-ph/0504090].
- [87] C. Boehm, A. Djouadi and M. Drees, *Light scalar top quarks and supersymmetric dark matter*, *Phys. Rev. D* **62** (2000) 035012 [arXiv:hep-ph/9911496].
- [88] R. L. Arnowitt, B. Dutta and Y. Santoso, *Coannihilation effects in supergravity and D-brane models*, *Nucl. Phys. B* **606** (2001) 59 [arXiv:hep-ph/0102181].
- [89] J. R. Ellis, K. A. Olive and Y. Santoso, *Calculations of Neutralino-Stop Coannihilation in the CMSSM*, *Astropart. Phys.* **18** (2003) 395 [arXiv:hep-ph/0112113].
- [90] P. Bechtle, O. Brein, S. Heinemeyer, G. Weiglein and K. E. Williams, *HiggsBounds: Confronting Arbitrary Higgs Sectors with Exclusion Bounds from LEP and the Tevatron*, arXiv:0811.4169.
- [91] Z. Ahmed *et al.* [CDMS Collaboration], *Search for Weakly Interacting Massive Particles with the First Five-Tower Data from the Cryogenic Dark Matter Search at the Soudan Underground Laboratory*, *Phys. Rev. Lett.* **102** (2009) 011301 [arXiv:0802.3530].

- [92] J. Angle *et al.* [XENON Collaboration], *First Results from the XENON10 Dark Matter Experiment at the Gran Sasso National Laboratory*, *Phys. Rev. Lett.* **100** (2008) 021303 [arXiv:0706.0039].
- [93] W. B. Atwood *et al.* [LAT Collaboration], *The Large Area Telescope on the Fermi Gamma-ray Space Telescope Mission*, *Astrophys. J.* **697** (2009) 1071 [arXiv:0902.1089].
- [94] E. A. Baltz *et al.*, *Pre-launch estimates for GLAST sensitivity to Dark Matter annihilation signals*, *JCAP* **07** (2008) 013 [arXiv:0806.2911].

Paper VI

Erik Zackrisson, Pat Scott, Claes-Erik Rydberg, Fabio Iocco, Bengt Edvardsson, Göran Östlin, Sofia Sivertsson, Adi Zitrin, Tom Broadhurst & Paolo Gondolo

Finding high-redshift dark stars with the James Webb Space Telescope
Submitted to ApJ, arXiv:1002.3368 (2010).

FINDING HIGH-REDSHIFT DARK STARS WITH THE JAMES WEBB SPACE TELESCOPE

ERIK ZACKRISSON^{1,8*}, PAT SCOTT^{2,8}, CLAES-ERIK RYDBERG^{1,8}, FABIO IOCCO³, BENGT EDVARDSSON⁴, GÖRAN ÖSTLIN^{1,8},
 SOFIA SIVERTSSON^{5,8}, ADI ZITRIN⁶, TOM BROADHURST⁶ & PAOLO GONDOLO⁷

Submitted to ApJ on February 5, 2010

ABSTRACT

The first stars in the history of the Universe are likely to form in the dense central regions of $\sim 10^5$ – $10^6 M_\odot$ cold dark matter halos at $z \approx 10$ –50. The annihilation of dark matter particles in these environments may lead to the formation of so-called dark stars, which are predicted to be cooler, larger, more massive and potentially more long-lived than conventional population III stars. Here, we investigate the prospects of detecting high-redshift dark stars with the upcoming James Webb Space Telescope (JWST). We find that dark stars at $z > 6$ are intrinsically too faint to be detected by JWST. However, by exploiting foreground galaxy clusters as gravitational telescopes, certain varieties of cool ($T_{\text{eff}} \leq 30000$ K) dark stars should be within reach at redshifts up to $z \approx 10$. If the lifetimes of dark stars are sufficiently long, many such objects may also congregate inside the first galaxies. We demonstrate that this could give rise to peculiar features in the integrated spectra of galaxies at high redshifts, provided that dark stars make up at least $\sim 1\%$ of the total stellar mass in such objects.

Subject headings: Dark matter – Galaxies: high-redshift – stars: general – cosmology

1. INTRODUCTION

The first stars in the history of the Universe are predicted to form inside $\sim 10^5$ – $10^6 M_\odot$ minihalos at redshifts $z \approx 10$ –50 (e.g. Yoshida et al. 2003). Due to the lack of efficient coolants in the primordial gas at these early epochs, the resulting population III stars are believed to be very massive ($\gtrsim 100 M_\odot$; e.g. Abel et al. 2002; Bromm et al. 2002), hot (effective temperature $T_{\text{eff}} \sim 10^5$ K; e.g. Bromm et al. 2001) and short-lived (≈ 2 –3 Myr; Schaerer 2002). Non-rotating population III stars with masses of 50 – $140 M_\odot$ or $M > 260 M_\odot$ are expected to collapse directly to black holes, whereas stars with masses of 140 – $260 M_\odot$ may produce luminous pair-instability supernovae (e.g. Heger et al. 2002). The latter may enrich the ambient medium with heavy elements and initiate the transition to the normal mode of star formation (population I and II, with a characteristic stellar mass $< 1 M_\odot$) known from the low-redshift Universe. The highly energetic radiation emitted from population III stars during their lifetimes may also have played an important role in cosmic reionization at $z > 6$ (e.g. Sokasian et al. 2004; Trenti & Stiavelli 2009). An observational confirmation of very massive population III stars would be an important breakthrough in the study

of the star formation, chemical enrichment and reionization history of the Universe.

The James Webb Space Telescope¹⁰(JWST), scheduled for launch in 2014, has been designed to study the epoch of the first light, reionization and galaxy assembly, but is not expected to be able to directly detect individual population III stars at $z \gtrsim 10$. Searches for population III stars with the JWST would instead focus on the pair-instability supernovae produced at the end of their lifetimes (Weinmann & Lilly 2005), or on $\sim 10^5$ – $10^7 M_\odot$ clusters of population III stars (Bromm et al. 2001; Scannapieco et al. 2003; Trenti et al. 2009; Johnson et al. 2009; Johnson 2009). Other alternatives are to look for the spectral signatures of population III stars forming in pockets of unenriched gas within high-redshift galaxies (Tumlinson & Shull 2000; Schaerer 2002, 2003; Dijkstra & Wyithe 2007; Johnson et al. 2008), or their integrated contribution to the infrared extragalactic background light (Cooray et al. 2009).

It has recently been recognized that annihilation of dark matter in the form of Weakly Interacting Massive Particles (WIMPs; e.g. the lightest supersymmetric or Kaluza-Klein particles, or an extra inert Higgs boson) may have generated a first population of stars with properties very different from the canonical population III (Spolyar et al. 2008). Because the first stars are likely to form in the high-density central regions of minihalos, annihilation of dark matter into standard model particles could serve as an additional energy source alongside or instead of nuclear fusion. This leads to the formation of so-called dark stars, which are predicted to be cooler, larger, more massive and potentially longer-lived than conventional population III stars (Spolyar et al. 2008; Iocco 2008; Freese et al. 2008; Iocco et al. 2008; Yoon et al. 2008; Taoso et al. 2008; Natarajan et al. 2009; Freese et al. 2009; Spolyar et al. 2009; Umeda et al. 2009; Ripamonti et al. 2009). Sim-

* E-mail: ez@astro.su.se

¹ Department of Astronomy, Stockholm University, 10691 Stockholm, Sweden

² Department of Physics, Stockholm University, 10691 Stockholm, Sweden

³ Institut d'Astrophysique de Paris, UMR 7095-CNRS Paris, Université Pierre et Marie Curie, Boulevard Arago 98bis, 75014, Paris, France

⁴ Department of Physics and Astronomy, Uppsala Astronomical Observatory, Box 516, 751 20 Uppsala, Sweden

⁵ Department of Theoretical Physics, Royal Institute of Technology (KTH), 10691 Stockholm, Sweden

⁶ School of Physics and Astronomy, Tel Aviv University, Israel
⁷ Physics Department, University of Utah, Salt Lake City, UT84112, USA

⁸ Oskar Klein Centre for Cosmoparticle Physics, AlbaNova University Centre, 10691 Stockholm, Sweden

¹⁰ <http://www.jwst.nasa.gov>

ilar effects have been seen in studies of the impacts of dark matter upon population I and II stars (Salati & Silk 1989; Fairbairn et al. 2008; Scott et al. 2008, 2009a; Casanellas & Lopes 2009).

A significant population of high-redshift dark stars could have important consequences for the formation of intermediate and supermassive black holes (Spolyar et al. 2009), for the cosmic evolution of the pair-instability supernova rate (Iocco 2009), for the X-ray extragalactic background and for the reionization history of the Universe (Schleicher et al. 2009). Effects such as these can be used to indirectly constrain the properties of dark stars, but no compelling evidence for or against a dark star population at high redshifts has so far emerged. Here, we explore a more direct approach – the prospects for detection of population III dark stars using the JWST.

While the bolometric luminosities of high-mass dark stars are of the same order as those of more conventional population III stars (e.g. Yoon et al. 2008; Spolyar et al. 2009), their lower temperatures (Freese et al. 2008; Taoso et al. 2008; Yoon et al. 2008; Spolyar et al. 2009) act to shift the bulk of their energy output closer to the wavelength range of the JWST detectors ($0.6\text{--}29\ \mu\text{m}$). For the redshift range relevant for studies of first stars with the JWST ($z \lesssim 15$), this implies that dark stars may attain continuum fluxes in the observer’s frame that are higher than those of population III star powered entirely by fusion.

The expected lifespan of dark stars is a crucial aspect when attempting to assess the detectability of such objects at high redshifts. In principle, dark stars could live indefinitely, provided that there is ample dark matter available to fuel them. Dark stars are powered by gravitationally-contracted dark matter, pulled into their core as infalling gas steepens the gravitational potential during the formation phase. Because annihilation depletes the dark matter present within a star, ordinary fusion processes eventually take over as the dominant power source if the dark matter is not replenished. At this point, the dark star will essentially transform into a conventional population III star, albeit more massive because the increased duration of the formation phase has allowed it to accrete more gas. The dark matter present within the star during formation will last only for a few million years. These reserves may later be replenished by scattering of WIMPs on nucleons, causing them to lose energy and become captured in the stellar core. This could boost the longevity of dark stars substantially (Iocco et al. 2008; Freese et al. 2008; Yoon et al. 2008; Taoso et al. 2008; Spolyar et al. 2009; Iocco 2009). The ongoing replenishment of the dark matter through capture and the resultant increase in longevity rely upon a number of strong assumptions and approximations, and the feasibility of such a mechanism is still yet to be proven by detailed calculations (Sivertsson & Gondolo 2010).

Whether the capture process will be efficient depends on two factors: the scattering cross-sections of the dark matter particles with ordinary nucleons, and the amount and density of dark matter available for capture from the star’s surroundings. The WIMP-nucleon scattering cross-sections can be constrained by direct detection experiments (e.g. Savage et al. 2008; Ahmed et al. 2009)

and searches for neutrinos produced by annihilation in the Sun (e.g. Abbasi et al. 2009). The question of the amount of dark matter available for refueling is more complicated (Sivertsson & Gondolo 2010). In a pristine halo, WIMP annihilations and scatterings during the formation stage would eventually deplete orbits with low angular momenta and result in a cavity of reduced dark matter density in the vicinity of the dark star. Whether infalling WIMPs could restore the balance before the star evolves into a supernova or a black hole may depend on the overall structural evolution of the minihalo (e.g. contraction, mergers with other halos), on tidal interactions of the dark star with subhalos, gas clouds and possibly other population III stars within the minihalo itself. Should a violent event cause the dark star to venture far from the centre of the minihalo, the dark matter density would very quickly become too low to sustain further dark matter burning. At the current time, estimates of the dark star lifetime in the presence of capture range from a few times 10^5 to 10^{10} years (e.g. Yoon et al. 2008; Iocco 2009; Sivertsson & Gondolo 2010). Many of the mechanisms mentioned above for replenishing the dark matter in the centre of the dark star have moreover not yet been explored. In this paper, we will therefore treat the duration of the dark star phase as a free parameter.

Model atmospheres and evolutionary histories of dark stars are presented in Sect. 2. The detectability of isolated dark stars, with and without the effects of gravitational lensing by foreground galaxy clusters, is explored in Sect. 3. In Sect. 4, we explain how high-redshift dark stars can be distinguished from other objects based on their JWST colours, and discuss the possibility of detecting the spectral signatures of dark stars in the first generations of galaxies. Sect. 5 summarizes our findings. Throughout this paper, we will assume a Λ CDM cosmology with $\Omega_\Lambda = 0.73$, $\Omega_M = 0.27$ and $H_0 = 72\ \text{km s}^{-1}\text{Mpc}^{-1}$.

2. MODELS FOR DARK STARS

2.1. Stellar structure and evolution

As described in the previous section, two physical processes exist for bringing dark matter into a star: gravitational contraction, and capture by nuclear scattering. Studies of the structure, formation and evolution of dark stars have so far employed one of two simulation techniques: either a ‘formationary’ or a ‘hydrostatic’ approach. In general, either physical process (or both) can be included with either simulation technique. Most studies to date employing the formationary approach have only included gravitational contraction, whereas most studies following the hydrostatic approach have only included capture by nuclear scattering. There are however notable examples of both hydrostatic (Iocco et al. 2008) and formationary (Spolyar et al. 2009) studies which include both physical processes.

The formationary approach follows the initial collapse of the pre-stellar gas cloud, the resultant gravitational contraction of its dark matter halo, and the subsequent formation of the dark star (Spolyar et al. 2008; Freese et al. 2008; Natarajan et al. 2009; Ripamonti et al. 2009; Spolyar et al. 2009; Ripamonti et al. 2010). This approach captures the salient points of dark star formation and early evolu-

TABLE 1
DARK STAR MODELS

WIMP mass	$M (M_{\odot})^a$	$R (\text{cm})^a$	$\log_{10}(g)^b$	$T_{\text{eff}} (\text{K})^a$	$t_{\text{burn}} (\text{yr})$	$t_{\text{SA}} (\text{yr})$	$t_{\text{max}} (\text{yr})$	Atmosphere	$\max(z_{\text{obs}})^c$
1 GeV	106	2.4×10^{14}	-0.612	5.4×10^3	$> 10^{10}$	2.0×10^5	2.0×10^7	MARCS	10
	371	2.7×10^{14}	-0.170	5.9×10^3	$> 10^{10}$	1.2×10^6	1.2×10^8	MARCS	11
	690	1.1×10^{14}	0.879	7.5×10^3	$> 10^{10}$	2.4×10^7	5.0×10^8	MARCS	11
	756	3.7×10^{13}	1.865	1.0×10^4	$> 10^{10}$	2.3×10^8	5.0×10^8	TLUSTY	9
	793	5.7×10^{12}	3.511	3.0×10^4	$> 10^{10}$	8.7×10^8	5.0×10^8	TLUSTY	11
	824	5.8×10^{11}	5.512	1.1×10^5	6.2×10^6	4.9×10^9	6.2×10^6	TLUSTY	0.5
100 GeV	106	7.0×10^{13}	0.458	5.8×10^3	$> 10^{10}$	6.0×10^6	5.0×10^8	MARCS	6
	479	8.4×10^{13}	0.955	7.8×10^3	$> 10^{10}$	2.2×10^7	5.0×10^8	MARCS	11
	716	1.1×10^{13}	2.895	2.3×10^4	$> 10^{10}$	2.9×10^8	5.0×10^8	TLUSTY	15
	756	2.0×10^{12}	4.399	5.5×10^4	2.2×10^9	1.6×10^9	5.0×10^8	TLUSTY	3
	787	5.8×10^{11}	5.492	1.1×10^5	5.9×10^6	4.5×10^9	5.9×10^6	TLUSTY	0.5
	106	2.2×10^{13}	1.463	6.0×10^3	$> 10^{10}$	1.7×10^8	5.0×10^8	MARCS	2
10 TeV	256	2.2×10^{13}	1.846	8.0×10^3	$> 10^{10}$	3.1×10^8	5.0×10^8	MARCS	4
	327	2.0×10^{13}	2.036	1.0×10^4	$> 10^{10}$	2.8×10^8	5.0×10^8	TLUSTY	5
	399	6.6×10^{12}	3.085	2.5×10^4	$> 10^{10}$	2.9×10^8	5.0×10^8	TLUSTY	7
	479	2.9×10^{12}	3.879	3.2×10^4	$> 10^{10}$	1.9×10^9	5.0×10^8	TLUSTY	2
	550	6.0×10^{11}	5.307	9.5×10^4	1.3×10^7	3.6×10^9	1.3×10^7	TLUSTY	0.5
	553	4.8×10^{11}	5.503	1.1×10^5	5.1×10^6	3.9×10^9	5.1×10^6	TLUSTY	< 0.5

^a from Spolyar et al. (2009)^b in units of $\text{g cm}^{-1} \text{s}^{-2}$ ^c This observability limit is set by the requirement that a single dark star should be sufficiently bright in at least one JWST filter to give a 5σ detection after a 100 h exposure, if a gravitational magnification of $\mu = 160$ is assumed (see Sect. 3).

tion, which are primarily governed by the annihilation of the gravitationally-contracted dark matter. The strategy is not optimised for dealing with the stellar evolution after formation, because it relies on either full hydrodynamic simulations (Natarajan et al. 2009; Ripamonti et al. 2009, 2010) or analytical approximations to them (Spolyar et al. 2008, 2009), becoming either too numerically-demanding or reliant upon simple polytropes once the star has condensed.

The hydrostatic approach assumes some initial model for either a main-sequence (Scott et al. 2008; Yoon et al. 2008; Taoso et al. 2008; Scott et al. 2009a; Casanellas & Lopes 2009) or pre-main sequence star (Iocco et al. 2008; Umeda et al. 2009; Casanellas & Lopes 2009). This model is then run through a modified quasi-hydrostatic stellar evolution code (e.g. Scott et al. 2009b) and evolved with the inclusion of energy injection by WIMP annihilation. Late-stage evolution is typically dominated by the dark matter distribution outside the star and the resultant rate at which WIMPs are captured by the nuclear scattering process. Progress has been made in including some early-stage effects, like gravitationally-contracted dark matter (Iocco et al. 2008) and gas accretion (Umeda et al. 2009), but the realism of such simulations ultimately suffers from their inability to deal with times before hydrostatic equilibrium is reached. For our purposes, the most significant finding in hydrostatic studies was the possibility that the lifetimes of dark stars might be extended. In this situation, WIMP-dominated models ‘stall’ (either temporarily or permanently) when they reach an equilibrium configuration somewhere on the Hayashi track (Fairbairn et al. 2008; Scott et al. 2008; Iocco et al. 2008; Yoon et al. 2008; Taoso et al. 2008). For a given stellar mass, the position is essentially dependent only on the WIMP capture rate (Scott et al. 2009a), and does not depend strongly on whether simulations are started from the main or pre-main

sequence (Casanellas & Lopes 2009).

The formationary approach produces more realistic protostellar structures, whereas the hydrostatic one allows more accurate modelling of long-term evolution. It is likely that the results of more sophisticated simulations, where formation and later quasi-hydrostatic evolution are treated self-consistently and detailed capture calculations are also included, would resemble a superimposition of the hydrostatic results upon the formationary ones. Depending upon the time required for dark matter captured by nuclear scattering to become a significant contributor to a star’s energy budget, three outcomes are possible:

1. The star may stall directly on the evolutionary paths described by Spolyar et al. (2009) during its march towards the main sequence.
2. The star may contract onto the ZAMS as per the Spolyar et al. (2009) paths, and then re-inflate as annihilation of captured dark matter pushes it back up the Hayashi track.
3. The star might travel only some of the way to the ZAMS, but then be turned around and partially re-inflate as the captured dark matter asserts itself.

Scenario 1 would typically be associated with a very quick onset of annihilation from dark matter captured by nuclear scattering, 2 would result if capture takes a very long time to assert itself, and 3 is an intermediate scenario. The amount of time the captured population takes to become significant is most sensitive to the total capture rate, but also to the time required for equilibrium to be achieved between capture and annihilation, and the time required for WIMPs to thermalise inside the star. These quantities in turn depend very strongly on the adopted models for the WIMP particle (mass, annihilation cross-section and scattering cross-section) and

the dark matter halo (density and velocity structure). In particular, these dependencies are rather degenerate; the impact of a short equilibrium timescale can for example be mimicked by a denser dark matter halo. This picture is further complicated by the fact that accretion may also continue to some degree in scenarios 1 and 3, because it may not have been halted by radiative feedback when the star draws close to the main sequence. The more massive a star becomes, the more dark matter is needed to keep it from contracting onto the main sequence.

Where in the HR diagram a stalled configuration occurs depends upon the total capture rate of dark matter; different annihilation rates are required to support an equilibrium structure at different locations on the Hayashi track. For a fixed stellar mass, greater rates of capture are required to support a star further from the ZAMS, i.e. at earlier stages in its contraction. However, larger stellar masses require substantially higher capture rates, so in realistic formation scenarios this effect will be countered to some degree by accretion. Which effect dominates depends upon the actual accretion rate during the formation phase.

How long the stalling phase persists is determined by the timescale over which the star's hydrogen remains undepleted at a given position on the Hayashi track, and how long capture can be realistically maintained at the given rate. The hydrogen burning timescale is a function of the central temperature and density of the star (i.e. the position on the Hayashi track), so is therefore also a function of the capture rate. At low capture rates, nuclear burning takes over relatively quickly regardless of how long capture continues, whereas at high capture rates it can in principle remain suppressed (or even entirely absent) for an indefinite period, unless capture drops because the WIMP halo has been depleted.

For very low capture rates – where stars stall only very briefly near the main sequence (e.g. very late on the Spolyar et al. tracks) – the longest possible lifetime of a dark star is set by the hydrogen-burning lifetime. This is the approximate maximum time t_{burn} that it would take for all the core hydrogen to be converted to helium, if the star were not to contract any further. In the case of the first stars, this is given by the rate-limiting step of the pp-chain ($p + p \rightarrow d + e^+ + \nu_e$), such that

$$t_{\text{burn}} = \frac{1}{2m_p r_{pp}(T_c, \rho_c)}. \quad (1)$$

Here m_p is the proton mass, T_c and ρ_c are the central temperature and density of the star, and r_{pp} is the nuclear reaction rate, given in Cox (2000).

For very high capture rates, the longest plausible lifetime of a dark star is instead set by the time required for the surrounding dark matter density to drop below that required to sustain the star, due to self-annihilation in the halo. Once the density of the halo is lowered, capture is reduced and the star contracts and gradually moves onto the main sequence. The halo density required to power a dark star of a given mass and luminosity can be estimated using Eq. (14) in Iocco et al. (2008). The self-annihilation time t_{SA} for a halo with a given dark matter density can then be obtained by e.g. inverting Eq. (6) in Scott & Sivertsson (2009). The self-annihilation times obtained in this manner are rather

approximate, relying on a number of assumptions we already know to be violated in the first stars (a constant halo self-annihilation rate and the constant infall of WIMPs from a uniform, unbound dark matter halo with an assumed velocity structure). A more conservative approach, which is thus also much less dependent on the adopted halo model, is to take the corresponding upper limit on stellar lifetimes to be $\sim 100 t_{\text{SA}}$, which is the strategy adopted in this paper.

The capture and evolutionary histories of the first stars are clearly very dependent upon the adopted dark matter particle and halo models. To parameterise these uncertainties, as a simple approximation we consider models stalling at various positions on the evolutionary tracks of Spolyar et al. (2009). These models occupy similar positions in the HR diagram to those computed from ZAMS starting models (e.g. Iocco et al. 2008), despite the rather different physical interpretation of the two scenarios. We allow stars to stall at various positions on these tracks for times of up to $t_{\text{stall}} = 5 \times 10^8$ yr. This upper limit roughly corresponds to the highest lifetimes considered realistic by Iocco (2009). To also take into account the effects of nuclear burning and halo self-annihilation, we limit the plausible lifetimes for any given model to values below

$$t_{\text{max}} = \min(t_{\text{stall}}, t_{\text{burn}}, 100 t_{\text{SA}}). \quad (2)$$

The parameters for these models are listed in Table 1¹¹. This age span allows dark stars forming as early as $z = 30$ to survive until $z \approx 10$, and those forming as late as $z = 10$ to survive until the end of reionization ($z \approx 6$). We consider models computed with three different WIMP masses (1 GeV, 100 GeV and 10 TeV) in the ‘minimal capture’ approximation of Spolyar et al. (2009) in which WIMP annihilation and nuclear fusion contribute equally to the total stellar luminosity; further details can be found in that paper.

2.2. Model atmosphere spectra

To compute the expected spectral energy distributions (SEDs) of dark stars, we have used the MARCS stellar atmosphere code (Gustafsson et al. 2008) for $T_{\text{eff}} \leq 8000$ K objects and the TLUSTY code (Hubeny & Lanz 1995) for $T_{\text{eff}} \geq 10000$ K. Since neither code is able to handle objects in the $T_{\text{eff}} \approx 8000$ – 10000 K range, we have interpolated the evolutionary tracks to produce replacement points just outside this temperature region whenever possible. In a few cases, it turned out to be necessary to adopt surface gravities $\log(g)$ slightly different from those given by the Spolyar et al. (2009) track to get convergence from MARCS. Neither the omission of the $T_{\text{eff}} \approx 8000$ – 10000 K data points, nor the $\log(g)$ deviations have any significant impact on the results of this paper.

Provided that the properties of dark matter allow the formation of dark stars, objects of this type are ex-

¹¹ Due to convergence problems with the stellar atmosphere models for certain combinations of parameter values, the 100 GeV WIMP track in Table 1 has one data point less than the track in Spolyar et al. (2009). This does not have any impact on the results from the present paper, since the parameter space sampling of the converged models is more than sufficient to reveal the overall trends in magnitude and colour evolution. The 10 TeV WIMP track also contains one data point more than the Spolyar et al. track to better bracket the 8000–10000 K divide.

pected to be among the first stars forming in the history of the Universe, and therefore to have extremely low metallicities Z , possibly at the level given by Big Bang nucleosynthesis (this implies $Z \sim 10^{-9}$, mainly due to Li; e.g. Iocco et al. 2007). All models therefore assume primordial abundances of H and He. For computational reasons, the MARCS atmospheres assume an overall metallicity of $Z = 2.5 \times 10^{-7}$ (corresponding to $[\text{Fe}/\text{H}] = -5$ with the α -enhanced abundance ratios discussed in Gustafsson et al. 2008), whereas the TLUSTY have been computed at $Z = 0$. Tests indicate that this minor inconsistency amounts to an uncertainty in the final JWST magnitudes of ~ 0.01 mag, which is irrelevant for the present study.

The TLUSTY models cover the restframe wavelength range 0.015–300 μm , whereas the MARCS model cover 0.13–20 μm . While parts of the spectra at wavelengths shortward of 0.13 μm may be redshifted into the range of the JWST detectors (0.6–29 μm) at $z > 4$, the fluxes in this part of the spectra are too small for detection. The wavelength coverage of our models is therefore more than adequate for our needs. To obtain JWST magnitudes, the model spectra have been convolved with the filter profiles for all the broadband filters available for the NIRCam (0.6–5 μm) and MIRI (5–29 μm) instruments, and calibrated using the AB system. This calibration, which will be used throughout this paper, is based on physical fluxes and defined so that an object with a constant flux per unit frequency interval of 3631 Jy has zero AB-magnitudes m_{AB} in all filters. The rest-frame stellar atmosphere spectra as well as the AB magnitudes (as a function of redshift from $z = 0$ to $z = 20$ in steps of $\Delta z = 0.5$) for the dark star models of Table 1 are available in electronic format from: <http://www.astro.su.se/~ez>

3. THE DETECTABILITY OF HIGH-REDSHIFT DARK STARS

3.1. Dark stars in random fields

In Fig. 1, we present the AB magnitudes of all dark star models from Table 1 as a function of redshift ($z = 1$ –20) in the NIRCam F444W filter. Also included are two estimated JWST detection thresholds for point sources, indicated by dashed horizontal lines. The first one is based on 10σ detections for 10^4 s exposures (thick dashed) and the second on 5σ detections after 100 h (3.6×10^5 s) exposures (thin dashed). The former represent the fiducial JWST detection limits listed on the JWST homepage¹², whereas the latter roughly correspond to the magnitude limits expected for ‘ultra deep field’ type observations.

It is immediately clear that all dark star models lie significantly below both these detection thresholds at high redshifts. At $z = 10$ –20, the intrinsic luminosities of the dark stars convert into apparent magnitudes that are 4–14 magnitudes too faint. Hence, without the magnification boost of a foreground galaxy cluster, JWST will not be able to detect individual population III dark stars at the redshifts where they formed. Long-lived dark stars surviving until the end of reionization ($z \approx 6$) appear somewhat brighter, but are still at least 2.5 magnitudes below the detection limit.

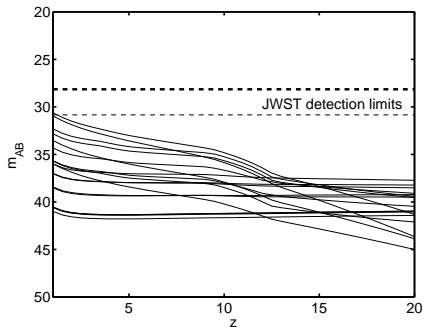


FIG. 1.— The predicted apparent AB magnitudes of dark stars at $z = 1$ –20 in the NIRCam/F444W filter. Each solid line corresponds to a separate dark star model from Table 1. The dashed horizontal lines correspond to the JWST detection limits for a 10σ detection of a point source after 10^4 s of exposure (thick dashed) and for a 5σ detection of a point source after 3.6×10^5 s (100 h) of exposure (thin dashed). At $z = 10$ –20, the dark stars are 4–14 magnitudes too faint for detection. Hence, without the magnification boost of a foreground galaxy cluster, JWST will not be able to detect individual population III dark stars at the redshifts where they formed. Long-lived dark stars surviving until the end of reionization ($z \approx 6$) appear somewhat brighter, but are still at least 2 magnitudes below the detection limit.

Some of the dark star models in Fig. 1 exhibit F444W magnitudes which change very little as a function of redshifts. This is due to the steep spectra of the $T_{\text{eff}} > 20000$ K dark stars, which attain their peak fluxes at rest wavelengths $< 0.2 \mu\text{m}$ (i.e. on the short-wavelength side of the F444W filter for all redshifts in the plotted range). As the redshift is increased, intrinsically brighter parts of their spectra are redshifted into the F444W filter, and this almost exactly compensated for the increased luminosity distance.

In Fig. 2, we display AB magnitudes for all dark stars from Table 1 at $z = 6$ and $z = 10$ as a function of the central wavelengths of all broad JWST filters. The JWST detection limits, defined as in Fig. 1, are also included. All dark star models from Table 1 lie significantly faintward of these thresholds, regardless of which filter is used. However, a magnification of $\mu = 160$ due to gravitational lensing by a foreground galaxy cluster (see Sect. 3.2) would shift all models upward by ≈ 5.5 magnitudes (as indicated by the vertical arrow) and shift certain varieties of dark stars into the brightness regime detectable by the NIRCam instrument (but not by MIRI). This is the case for several of the $T_{\text{eff}} \leq 8000$ K dark stars (red lines) and a couple of the $8000 < T_{\text{eff}} \leq 30000$ K dark stars (green lines) at both $z = 6$ and $z = 10$.

In Fig. 3 we demonstrate the need for using synthetic stellar atmosphere spectra (as compared to pure black body spectra) for predictions of this type. In Fig. 3a, the MARCS spectra for the $106 M_{\odot}$ ($T_{\text{eff}} = 5400$ K) dark star and the TLUSTY spectra for the $756 M_{\odot}$ ($T_{\text{eff}} = 10000$ K) dark star from the 1 GeV WIMP track in Table 1 are compared to black body spectra based on identical temperatures and bolometric luminosities. At rest frame wavelengths of $\lambda > 0.4 \mu\text{m}$, the shape of the continua are very similar for the stellar atmosphere and black body SEDs, but the presence of breaks in the stellar atmosphere spectra (most notably the Balmer break at

¹² <http://www.jwst.nasa.gov/>

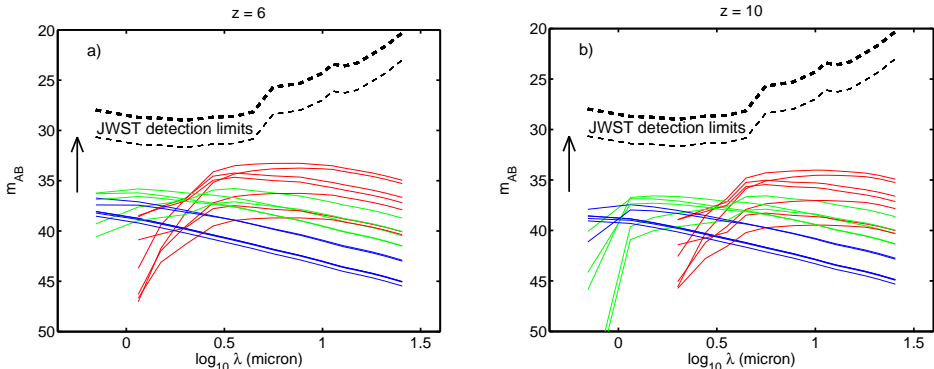


FIG. 2.— The predicted apparent AB magnitudes of dark stars at $z = 6$ (a) and $z = 10$ (b), as a function of central wavelength of the JWST broadband filters. Each solid line corresponds to a separate dark star model from Table 1. These lines have been colour-coded according to the effective temperatures of the dark stars: $T_{\text{eff}} \leq 8000$ K (red), $8000 \text{ K} < T_{\text{eff}} \leq 30000$ K (green) and $T_{\text{eff}} > 30000$ K (blue). The dashed horizontal lines correspond to the JWST detection limits for a 10σ detection of a point source after 10^4 s of exposure (thick dashed) and for a 5σ detection of a point source after 3.6×10^5 s (100 h) of exposure (thin dashed). The progressively brighter detection thresholds at central wavelengths higher than 4.4μ ($\log_{10} \lambda > 0.65$) compared to NIRCам (central filter wavelengths $\log_{10} \lambda \leq 0.65$). In both panels, all dark star models lie significantly faintward of the detection thresholds in all filters, implying that their intrinsic brightnesses are too low to be detected by JWST. However, a magnification of $\mu = 160$ due to gravitational lensing by a foreground galaxy cluster (see Sect. 3.2) would shift all models upward by 5.5 magnitudes (as indicated by the vertical arrow) and allow certain varieties of dark stars into the brightness regime detectable by the NIRCам instrument. This is the case for some of the $T_{\text{eff}} \leq 30000$ K dark stars (green and red lines) at both $z = 6$ and $z = 10$. The reason why the red lines end abruptly at $1.15 \mu\text{m}$ ($\log_{10} \lambda = 0.06$) for $z = 6$ and at $2.0 \mu\text{m}$ ($\log_{10} \lambda = 0.3$) for $z = 10$ is that the short-wavelength limit ($0.13 \mu\text{m}$) of the MARCS model spectra have entered the bluer filters at these redshifts. Since this happens at $m_{\text{AB}} > 38$, which is a brightness regime inaccessible to the JWST, this has no impact on the present study.

$\lambda \approx 0.36\mu\text{m}$) will introduce substantial differences once these are redshifted into the JWST filters. The stellar atmosphere SEDs also contain a large number of absorption lines, but these will have far smaller effect of the broadband fluxes discussed here. In Fig. 3b, we show the difference between the magnitudes derived from black body and the synthetic stellar atmosphere spectra in the NIRCам F444W filter. The different lines represent the six dark star models from Table 1 for a WIMP mass of 1 GeV. The solid lines correspond to the MARCS (thick lines) and TLUSTY (thin lines) dark star SEDs plotted in Fig. 3a. As seen, there are substantial differences for the cooler ($\lesssim 10000$ K) dark stars, whereas the differences for hotter dark stars are below 0.5 mag. This is primarily because the hotter stars become progressively more black body-like at the relevant wavelengths. For instance, the $0.36\mu\text{m}$ break (which makes the black body spectra overpredict the F444W fluxes at $z \gtrsim 9$) is far less prominent in the hotter dark stars. We conclude, that while black body spectra may be useful for deriving order-of-magnitude estimates of JWST fluxes for the hotter dark stars, detailed stellar atmosphere models are required to accurately predict the fluxes for cool dark stars at high redshifts.

3.2. Dark stars magnified by gravitational lensing

Fig. 1 and 2 demonstrate that all dark stars in Table 1 are *intrinsically* too faint at $z \geq 6$ to be detected by JWST, even if extremely long exposure times ($t_{\text{exp}} = 3.6 \times 10^5$ s, i.e. 100 h) are considered. The only hope of detecting isolated dark stars with JWST at these redshifts would then be to exploit the gravitational lensing provided by a foreground galaxy cluster. Galaxy clusters at $z \approx 0.1$ – 0.6 can in principle boost

the fluxes of high-redshift objects by up to factors ~ 100 (e.g. Bradač et al. 2009; Maizy et al. 2009). As shown in Fig. 2, this would be sufficient to lift some of the cooler ($T_{\text{eff}} < 30000$ K) dark star models above the JWST detection threshold. For each separate dark star model, the entries in the $\text{max}(z_{\text{obs}})$ column in Table 1 indicate the maximum redshifts at which 5σ detections are possible in at least one JWST filter after 3.6×10^5 s (100 h) exposures, assuming a magnification of $\mu = 160$ (see below). No dark stars are detectable at $z > 15$, even when this boost due to lensing is taken into account.

How many dark stars at $z \approx 10$ would one then expect to detect in a survey of a single lensing cluster? This depends on the magnification properties of the cluster, on the cosmic star formation history of dark stars and on their typical lifetimes τ . While gravitational lensing boosts the fluxes of background objects, their surface number densities are at the same time diluted by a factor equal to the magnification μ . In a region with angular area θ^2 and magnification μ , one can show that the expected number of dark stars N_{DS} in the redshift interval $[z_{\text{min}}, z_{\text{max}}]$ is given by:

$$N_{\text{DS}} = c\theta^2 \int_{z_{\text{min}}}^{z_{\text{max}}} \int_{t(z)}^{t(z)-\tau} \frac{\text{SFR}(t)d_{\text{os}}(z)^2(1+z)^3}{\mu(z)M_{\text{DS}}} dt dz \quad (3)$$

where $\text{SFR}(t)$ is the star formation rate (in units of $M_{\odot} \text{ Mpc}^{-3} \text{ yr}^{-1}$) of dark stars at cosmic epoch $t(z)$, M_{DS} is the dark star mass (assumed to be the same for all such objects) and $d_{\text{os}}(z)$ is the angular size distance between the observer and source at redshift z . In the case of flat ΛCDM cosmologies, the derivative $\frac{d}{dz}$ in eq.(3) is given by:

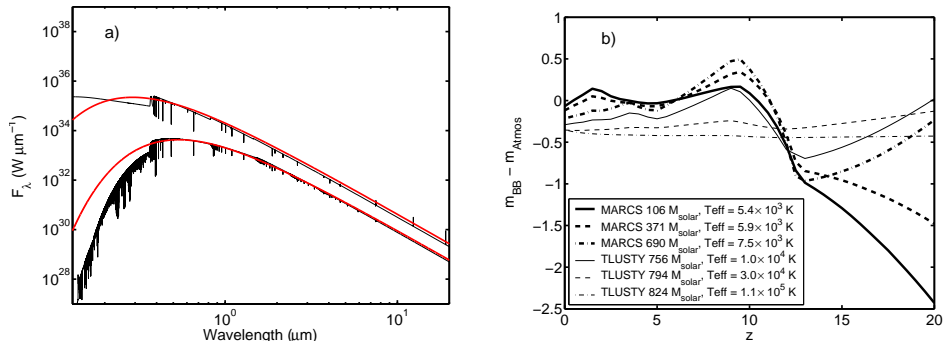


FIG. 3.— Synthetic stellar atmosphere spectra compared to black body spectra for dark stars. **a)** The SEDs of the $106 M_{\odot}$, $T_{\text{eff}} = 5400$ K (lower SEDs) and the $756 M_{\odot}$, $T_{\text{eff}} = 10000$ K (upper SEDs, multiplied by 100 to avoid cluttering) dark stars predicted for a 1 GeV WIMP. The black lines correspond to the synthetic stellar atmosphere SEDs generated by MARCS (for the lower, $T_{\text{eff}} = 5400$ K spectra) and TLUSTY (for the upper $T_{\text{eff}} = 10000$ K spectra), whereas the red lines correspond to black body spectra generated for identical temperatures and bolometric luminosities. The obvious differences are the lack of breaks (most notable at $\approx 0.36 \mu\text{m}$) and absorption lines in the black body spectra. **b)** The difference between the black body AB magnitudes m_{BB} and the synthetic stellar atmosphere AB magnitudes m_{Atmos} in the NIRCам F444W filter. The different lines represent the six dark star models from Table 1 for a 1 GeV WIMP. The solid lines correspond to the MARCS (thick line) and TLUSTY (thin lines) dark star SEDs plotted in **a)**. There are substantial differences between m_{BB} and m_{Atmos} for the cooler ($\lesssim 10000$ K) dark stars, whereas the differences for hotter dark stars are below 0.5 mag. This is primarily because the hotter stars become progressively more black body-like at the relevant wavelengths. For instance, the $0.36 \mu\text{m}$ break (which gives rise to the negative $m_{\text{BB}} - m_{\text{Atmos}}$ at $z \gtrsim 9$) is far less prominent for hotter objects.

$$\frac{dt}{dz} = \frac{1}{H_0(1+z)[\Omega_M(1+z)^3 + \Omega_\Lambda]^{1/2}} \quad (4)$$

When exploring the prospects of detecting isolated dark stars in the high-magnification regions of a foreground galaxy cluster, we have adopted MACS J0717.5+3745 at $z = 0.546$ as our lensing cluster. This object has the largest angular Einstein radius detected so far, with a relatively shallow surface mass-density profile which boosts the projected area corresponding to high magnifications (Zitrin et al. 2009). Both of these properties combine to make this the best lens currently known for the study of faint objects at very high redshifts. For this cluster, the angular area over which the magnification is in the range $\mu = 100\text{--}300$ (with an average magnification $\bar{\mu} \approx 160$) for sources at $z_s = 6\text{--}20$ is $\approx 0.3 \text{ arcmin}^2$.

For the cosmic star formation history $\text{SFR}(t)$ of dark stars, we have explored three different scenarios from Trenti & Stiavelli (2009) for single population III stars forming through H_2 cooling in minihalos. These three scenarios differ in their assumptions concerning the amount of Lyman-Werner (hereafter LW) feedback expected during the relevant epochs. LW radiation is emitted by hot, high-mass stars, destroys H_2 and inhibits further population III star formation along this cooling channel. The very massive, fusion-driven population III stars that Spolyar et al. (2009) envision as the descendants of dark stars will emit copious amounts of LW radiation. However, if many of the population III stars that form through H_2 cooling (population III.1 stars in the notation suggested by Greif & Bromm 2006) go through a long-lived dark star phase (during which LW fluxes are insignificant due to the very low effective temperatures of these objects), this could substantially delay the onset of the LW feedback compared to scenarios with no dark stars. Hence, the amount of LW feedback at a given

epoch is expected to depend both on the fraction f_{DS} of population III.1 stars that at some point become dark stars, and the typical duration τ of this phase. The three scenarios from Trenti & Stiavelli (2009) that we consider are hereafter referred to as *standard LW*, *reduced LW* and *no LW*, and correspond to the cosmic star formation histories of population III stars formed through H_2 in minihalos depicted in their Figs. 1, 2 and 3, respectively. The standard LW scenario, which we consider suitable for very small f_{DS} and short τ , pushes the bulk of population III star formation to higher redshifts than the other two (possibly more suitable for large f_{DS} and τ). Whereas all population III star formation has effectively ceased by $z \approx 10$ in the standard LW model, significant formation of such stars continues to lower redshifts in the other two scenarios.

In Fig. 4, we plot the apparent AB magnitudes of selected dark star models versus the number of dark stars expected within the high-magnification regions ($\mu = 100\text{--}300$; $\bar{\mu} \approx 160$) of MACS J0717.5+3745 per unit redshift interval. These plots are based on the assumption of $f_{\text{DS}} = 1$, i.e. that *all* population III stars formed through H_2 cooling in minihalos become dark stars, and that all such dark stars display similar properties (in terms of mass, temperature, radius and lifetime). In reality, this may not be very realistic. The individual merger history of each minihalo is likely to give rise to some variation in the central CDM density. Some minihalos may also host multiple stars (Turk et al. 2009; Stacy et al. 2009), which could cause some or all of the population III stars forming in such systems to wander out of the minihalo centre where dark matter annihilation is the most efficient. The predictions in Fig. 4 can, however, easily be rescaled to other dark star fractions by shifting the curves downward by a factor f_{DS} .

The left column of Fig. 4 displays the results for the $690 M_{\odot}$, $T_{\text{eff}} = 7500$ K dark star from the 1 GeV WIMP track and the right column the corresponding results for

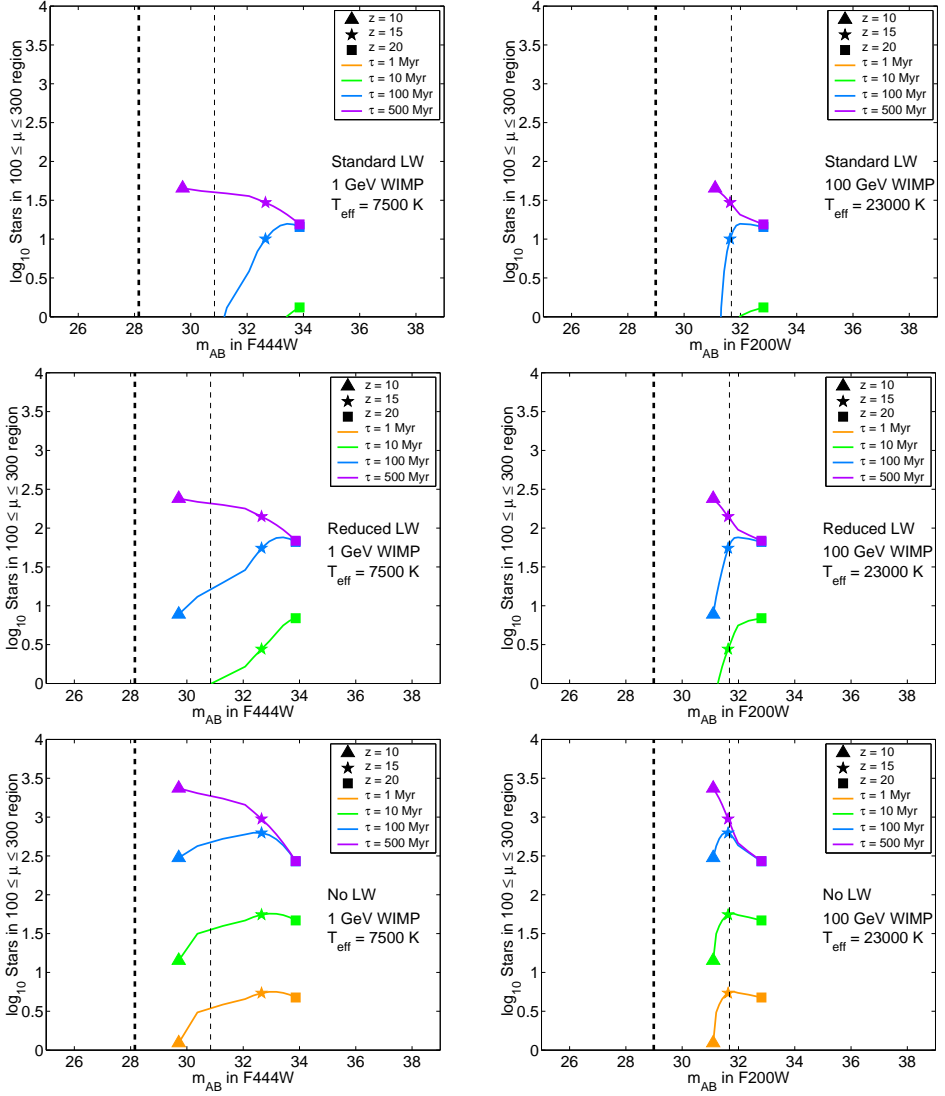


FIG. 4.— The number of dark stars per unit redshift interval predicted within the high-magnification regions ($\mu = 100\text{--}300$) of the galaxy cluster MACS J0717.5+3745, as a function of their apparent AB magnitudes in the JWST/NIRCam F444W (left column) and F200W (right column) filters. In the left column, the $690 M_{\odot}$ dark star model with $T_{\text{eff}} = 7500$ K from the 1 GeV WIMP track has been used, and in the right column the $716 M_{\odot}$ dark star with $T_{\text{eff}} = 23000$ K from the 100 GeV WIMP track. Within each panel, the differently coloured lines correspond to dark star life times of $\tau = 1$ Myr (orange), 10 Myr (green), 100 Myr (blue) and 500 Myr (purple). Symbols along these lines indicate dark star redshifts of $z = 10$ (triangle), $z = 15$ (star) and $z = 20$ (square). The different rows correspond to the standard LW (top row), reduced LW (middle row) and no LW (bottom row) star formation histories for population III stars in minihalos (Trenti & Stiavelli 2009). The vertical lines within each panel represent the JWST detection thresholds for 10σ detections after 10^4 s exposures (thick dashed) and 5σ detections after 3×10^5 s (100 h) exposures (thin dashed). All population III stars forming through H_2 cooling in minihalos are here assumed to go through a dark star phase with identical properties, but the results can easily be generalized by scaling the curves downward by the dark star fraction f_{DS} .

the $716 M_{\odot}$, $T_{\text{eff}} = 23000$ K dark star from the 100 GeV WIMP track. Due to the different temperatures of these dark stars, the AB-magnitudes in the NIRCcam F444W filter are used in the left column and the NIRCcam F200W filter in the right column. For each dark star model, we consider lifetimes of $\tau = 10^6$ (orange lines), 10^7 (green lines), 10^8 (blue lines) and $\tau = 5 \times 10^8$ yr (purple lines). The three rows of panels in Fig. 4 correspond to the cosmic population III star formation histories with standard LW (top row), reduced LW (middle row) and no LW feedback (bottom row). The different markers within each panel indicate the AB-magnitudes and numbers of dark stars at redshifts $z = 10$ (triangle), $z = 15$ (star) and $z = 20$ (square).

In general, long dark star lifetimes τ imply larger numbers of dark stars at detectable brightnesses. In the case of the $690 M_{\odot}$, $T_{\text{eff}} = 7500$ K dark star (right column), considerable numbers (≥ 10) of dark stars are expected to be sufficiently bright for detection (at 5σ after 3.6×10^5 s) in the high-magnification regions of MACS J0717.5+3745 at $z \approx 10$ –11, provided that their lifetimes are $\approx 5 \times 10^8$ yrs. This holds regardless of which of the three feedback scenarios is adopted. For the reduced LW and no LW feedback models, significant dark stars are expected even if the lifetime is closer to $\tau = 10^7$ yrs. In the no LW scenario, even $\tau = 10^6$ yrs dark stars can be detected behind MACS J0717.5+3745, but only in modest numbers (< 10). The situation for the $716 M_{\odot}$, $T_{\text{eff}} = 23000$ K dark star (right column) is similar, except that this model remains detectable up to a redshift of $z \approx 15$.

Dark stars with $\tau = 5 \times 10^8$ yr do not show the same decline in their expected numbers when going from $z = 15$ to $z = 10$ as dark stars with shorter lifespan do. This happens because $\tau = 5 \times 10^8$ yr dark stars have lifetimes that exceed the cosmic age intervals between adjacent redshift bins, allowing such objects to accumulate at lower redshifts, even though the cosmic star formation rate of population III stars is declining at these epochs for all three feedback scenarios. The Trenti & Stiavelli (2009) models do not allow us to trace the star formation history to epochs at $z < 10$, even though the star formation rate clearly remains non-zero at $z = 10$ in both the reduced LW and no LW feedback scenarios. In fact, $\tau = 5 \times 10^8$ yrs dark stars forming at $z \geq 10$ in these feedback scenarios will survive in detectable numbers to even lower redshifts ($z \approx 6$), even if one artificially sets their formation rates to zero at $z < 10$.

In summary, cool ($T_{\text{eff}} \leq 30000$ K) and long-lived ($\tau \gtrsim 10^7$ yr) dark stars may well be detected at $z \approx 10$ in sizeable numbers within a single, ultra deep JWST field if one takes advantage of the magnifying power of a foreground galaxy cluster. In the case of high τ ($\gtrsim 10^8$ yr) and cosmic star formation scenarios which imply significant dark star formation at $z < 15$, several dark stars may be even seen even if only a minor fraction ($f_{\text{DS}} \sim 0.01$ – 0.1) of all population III stars forming in minihalos become dark stars with temperatures in the detectable range.

4. DISCUSSION

4.1. How to distinguish isolated dark stars from other objects

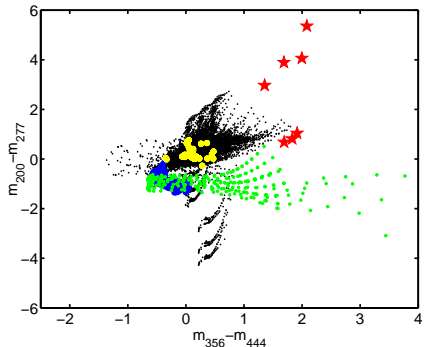


FIG. 5.— The JWST/NIRCcam $m_{356} - m_{444}$ vs. $m_{200} - m_{277}$ colours of $T_{\text{eff}} < 10000$ K dark stars at $z = 10$ (red star symbols) compared to a number of potential interlopers in multiband surveys: star clusters or galaxies at $z = 0$ –15 (black dots), AGN template spectra at $z = 0$ –20 (yellow dots), Milky Way stars with $T_{\text{eff}} = 2000$ – 50000 K and $Z = 0.001$ – 0.020 (blue dots) and Milky Way brown dwarfs with $T_{\text{eff}} = 130$ – 2200 K (green dots). Since the dark stars reside a region of this colour-colour diagram that is disconnected from those occupied by these other objects, it should be possible to identify possible dark star candidates in deep multiband JWST/NIRCcam surveys of the high-magnification regions of lensing clusters.

As demonstrated in Sect. 3.2, certain varieties of $z \approx 10$ dark stars may be sufficiently bright and numerous to be detected by JWST/NIRCcam survey of the high-magnification regions of a foreground galaxy cluster. But how does one identify such objects among the overwhelming number of mundane interlopers located in front of, inside or beyond the lensing cluster?

Given the many degeneracies involved in the interpretation of broadband photometry, there may well be unresolvable ambiguities in some cases. However, many of the cooler high-redshift dark stars should stand out in multiband survey data because of their unusual colours. This is demonstrated in Fig. 5, where we plot the colour indices $m_{356} - m_{444}$ vs. $m_{200} - m_{277}$ (based on AB-magnitudes in the JWST/NIRCcam F200W, F277W, F356W and F444W filters) at $z = 10$ for all dark stars from Table 1 with $T_{\text{eff}} < 10000$ K. The colours of these models (red star symbols) are compared to the colours predicted for a wide range of galaxies, star clusters, active galactic nuclei (AGN) and Milky Way stars. The cloud of black dots in Fig. 5 indicate the colours of integrated stellar populations (star clusters and galaxies) generated with the Zackrisson et al. (2001) spectral synthesis model. These predictions are based on instantaneous-burst¹³, Salpeter-IMF stellar populations at redshifts $z = 0$ –15 with metallicities in the range $Z = 0.001$ – 0.020 , ages ranging from 10^6 yr up to the age of the Universe at each redshift and a rest-frame stellar dust reddening of $E(B - V) = 0$ – 0.5 mag assuming the Calzetti et al. (2000) extinction law. Also included in Fig. 5 are the expected colours of foreground stars with $T_{\text{eff}} = 2000$ – 50000 K and $Z = 0.001$ – 0.020 in the Milky Way (i.e. at $z = 0$), based on the Lejeune et al. (1998) compila-

¹³ This is a conservative choice, since allowing for more extended star formation histories would only result in a more restricted colour coverage for these objects

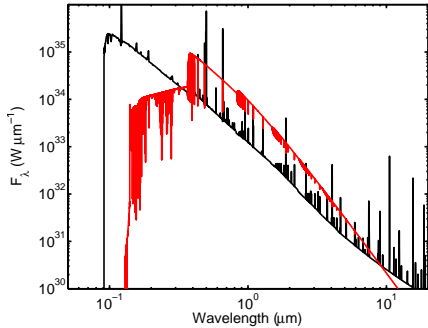


FIG. 6.— The rest-frame spectrum of a $10^6 M_{\odot}$, $Z = 0.001$, Salpeter-IMF stellar population (stellar mass range $0.08\text{--}120 M_{\odot}$) which has formed stars at a constant rate for 10^8 yrs (black line) with a superimposed contribution (red line) from ten $T_{\text{eff}} = 7500$ K, $690 M_{\odot}$ dark stars (from the 1 GeV WIMP track). Despite making up only 0.7% of the stellar mass in this galaxy, these dark stars give rise to an upturn in the spectrum at rest-frame wavelengths longward of $0.4 \mu\text{m}$. In a $z = 10$ object, this spectral feature should appear longward of $4.4 \mu\text{m}$ and could serve as a tell-tale signature of cool dark stars within the first galaxies.

tion of synthetic stellar atmosphere spectra (blue dots), and the colours of Milky Way brown dwarfs in the $130\text{--}2200$ K range based on the Burrows et al. (2003, 2006) models (green dots). The yellow dots represent the template AGN spectra of Hopkins et al. (2007) for bolometric luminosities $\log_{10} L_{\text{bol}}/L_{\odot} = 8.5\text{--}14.0$, at redshifts $z = 0\text{--}20$. Since none of these potential interlopers have $m_{356} - m_{444}$ and $m_{200} - m_{277}$ colours that overlap with those of cool $z \approx 10$ dark stars, a diagnostic diagram of this type can be used to cull objects that are clearly *not* dark stars from multiband survey data. However, given that $T_{\text{eff}} < 10000$ K dark stars are unlikely to attain apparent magnitudes brighter than $m_{AB} \approx 30$ at their peak wavelengths (even when boosted by gravitational lensing; see Fig. 2b), and can realistically only be detected in one or two NIRCam filters, follow-up spectroscopy of the remaining dark star candidates will be required to establish their exact nature. This will admittedly be very challenging, but a very coarse spectrum can possibly be obtained for $m_{AB} \approx 30$ objects with JWST/NIRSpec (assuming a 3.6×10^5 s exposure). Objects of this type may also be suitable targets for the 42 m European Extremely Large Telescope¹⁴ (E-ELT).

4.2. The spectral signature of dark stars in high-redshift galaxies

The first galaxies are expected to form at $z \approx 10\text{--}13$ in CDM halos with total masses around $10^8 M_{\odot}$ (e.g. Johnson et al. 2008, 2009; Greif et al. 2008; Ricotti 2009). At the time of assembly, each such object is likely to contain a number of minihalos in which population III stars have already formed (Greif et al. 2008). If some of these population III stars go through a long-lived ($\tau \gtrsim 10^8$ yr) dark star phase, several dark stars may in principle congregate inside the first generation of galaxies and give rise to tell-tale signatures in their integrated spectra. In Fig. 6, we display the rest-frame spectrum

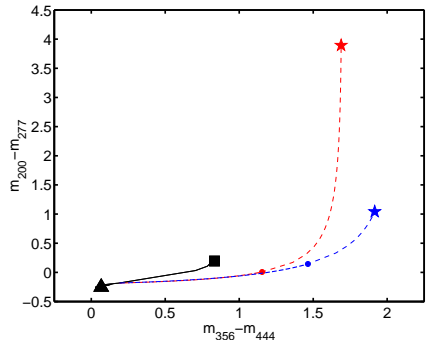


FIG. 7.— The JWST/NIRCam $m_{356} - m_{444}$ vs. $m_{200} - m_{277}$ colour evolution as a function of age for a $z = 10$, low-metallicity ($Z = 0.001$), Salpeter-IMF galaxy experiencing a short burst of star formation (10^8 yrs) and passive evolution thereafter (black line). The black triangle indicates an age of 10^6 yr and the black square 5×10^8 yr (roughly the age of the Universe at this redshift). The star symbols indicate the colours of two cool, $z = 10$ dark stars from Table 1: the 7500 K, $690 M_{\odot}$ model from the 1 GeV WIMP track (blue star) and the 5800 K, $106 M_{\odot}$ model from the 100 GeV WIMP track (red star). Both of these (as is the case for all $T_{\text{eff}} < 10000$ K dark stars observed in these filters; see Fig. 5) are considerably redder than the colours expected for galaxies, regardless of their age. Dashed lines indicate how the colours of the model galaxy (at an assumed age of 10^8 yrs) would shift if it were to contain dark stars of either of the two types. The filled circles along the dashed tracks indicate mixtures at which these dark stars make up 1% of the stellar mass in the model galaxy. These points are also significantly redder than the reddest point along the galaxy track, indicating that a $\sim 1\%$ stellar mass fraction in dark stars within $z \approx 10$ galaxies would be detectable through multiband photometry.

predicted by the Zackrisson et al. (2001) population synthesis model for a 10^8 yr old, low-metallicity ($Z = 0.001$, i.e. population II), Salpeter-IMF (mass range $0.08\text{--}120 M_{\odot}$) stellar population which has formed stars at a constant rate. This population has been assigned a stellar mass of $10^6 M_{\odot}$, which – for a $10^8 M_{\odot}$ halo with baryon fraction $f_{\text{bar}} \approx 0.7$ – corresponds to $\sim 10\%$ of the baryonic mass in stars, in rough agreement with the models of Ricotti (2009) for a $z \approx 10$ galaxy. The predicted NIRCam magnitudes of this object lie around $m_{AB} \approx 33\text{--}34$ which would make it sufficiently bright for detection if seen through a gravitational lens with magnification $\mu \gtrsim 10$. Superposed on the spectrum of this high-redshift galaxy is the integrated contribution from ten $T_{\text{eff}} = 7500$ K (the $690 M_{\odot}$ models from the 1 GeV WIMP track) dark stars (red line). These dark stars, which contribute only 0.7% of the stellar mass in this galaxy, give rise to a conspicuous red bump in the spectrum at rest-frame wavelengths longward of $0.36 \mu\text{m}$ (this corresponds to wavelengths longer than $3.96 \mu\text{m}$ at $z = 10$). Because of this, galaxies that contain many cool dark stars are expected to display anomalously red colours.

In Fig. 7, we display the $m_{356} - m_{444}$ vs. $m_{200} - m_{277}$ colour evolution (black solid line) as a function of age for the synthetic galaxy from Fig. 6 at $z = 10$. Here, the age runs from 10^6 yr (black triangle) up to the age of the Universe at this redshift ($\approx 5 \times 10^8$ yr). Also indicated are the colours of two cool dark stars: the 7500 K model from the 1 GeV WIMP track (blue star) and

¹⁴ <http://www.eso.org/sci/facilities/eelt/>

the 5800 K model from the 100 GeV WIMP track (red star). Due to their low temperatures, these two dark stars are far redder than the model galaxy in both colours plotted. As shown in Fig. 5, this is generally the case for $T_{\text{eff}} < 10000$ K dark stars observed in these filters. The galaxy is here assumed to go through a short burst of star formation (forming stars at a constant rate for 10^8 yrs), after which it evolves passively. This gives a conservative estimate of the colour difference between galaxies and dark stars. Allowing a more extended star formation episode or a star formation rate that increases over time would only increase the discrepancy between the colours of dark stars and the model galaxy. The dashed lines indicate how the colours of a 10^8 yr galaxy would shift in this diagram, if it were to harbour dark stars of the type considered. The filled circles along each such mixing track indicate the position at which the dark stars make up 1% of the total stellar mass. Since these points are significantly redder in the $m_{356} - m_{444}$ colour than the reddest point along the standard galaxy track, a $\sim 1\%$ stellar mass fraction in dark stars would result in very peculiar colours for $z = 10$ galaxies and should allow such objects to be identified as candidate ‘dark star galaxies’ in JWST multiband survey data.

5. SUMMARY

In this paper, we have investigated the prospects of detecting very massive, high-redshift dark stars using the JWST. While individual dark stars at $z > 6$ will be intrinsically too faint for detection, we demonstrate that the magnification provided by a foreground galaxy cluster will make certain varieties of long-lived ($\tau \geq 10^7$ yrs) and cool ($T_{\text{eff}} \leq 30000$ K) detectable at redshifts up to $z \approx 10$. We argue that it should be possible to identify at least some of these dark stars in photometric NIRCам

surveys due to their peculiar colours. If the lifetimes of dark stars are sufficiently long, they may also congregate during the hierarchical assembly of the first galaxies. We find that this could give rise to distinct signatures in the integrated NIRCам colours of high-redshift galaxies, provided that dark stars make up at least $\sim 1\%$ of the overall stellar mass in these objects.

After this paper was submitted to ApJ, another paper dealing with the prospects of detecting high-redshift dark stars with the JWST was posted on the arXiv (Freese et al. 2010). The two studies differ in their assumptions concerning the masses of dark stars. Whereas we have considered objects up to $\approx 800 M_{\odot}$, Freese et al. present models for ‘supermassive dark stars’ (with masses up to $10^7 M_{\odot}$) and argue that such objects may be sufficiently bright for detection by JWST even without gravitational lensing.

EZ, CER and GÖ acknowledge grants from the Swedish National Space Board. EZ, PS, CER, BE, GÖ and SS acknowledge funding support from the Swedish Research Council. FT acknowledges support from the 7th European Community research program FP7/2007/2013 within the framework of convention #235878. GÖ is a Royal Swedish Academy of Sciences Research Fellow, supported by a grant from the Knut and Alice Wallenberg foundation. PG acknowledges partial support by NSF Award PHY-0456825. The authors are indebted to Marcia J. Rieke and Kay Justtanont for giving us access to the NIRCам and MIRI broadband filter profiles prior to public release.

REFERENCES

- Abbasi, R., et al. 2009, Phys. Rev. Lett., 102, 201302
 Abel, T., Bryan, G. L., Norman, M. L. 2002, Science, 295, 93
 Ahmed, Z., et al. 2009, Phys. Rev. Lett., 102, 011301
 Bradač, M., et al., ApJ, in press (arXiv0910.2708)
 Bromm, V., Kudritzki, R. P., Loeb, A. 2001, ApJ, 552, 464
 Bromm, V., Coppi, P. S., Larson, R. B. 2002, ApJ, 564, 23
 Burrows, A., Sudarsky, D., Lunine, J. I. 2003, ApJ., 596, 587
 Burrows, A., Sudarsky, D., Hubeny, I., 2006, ApJ 640, 1063
 Calzetti, D., Armus, L., Bohlin, R. C., Kinney, A. L., Koornneef, J., & Storchi-Bergmann, T. 2000, ApJ, 533, 682
 Casanellas, J., & Lopes, I. 2009, arXiv:0909.1971
 Cooray, A., et al. 2009, Science White Paper for the US Astro 2010-2020 Decadal Survey (arXiv0902.2372)
 Cox, A. N., ed. 2000, Allen’s astrophysical quantities (Springer-Verlag, New York)
 Dijkstra, M., & Wyithe, J. S. B. 2007, MNRAS, 379, 1589
 Fairbairn, M., Scott, P., & Edsjö, J. 2008, Phys. Rev. D, 77, 047301
 Freese, K., Spolyar, D., & Aguirre, A. 2008, JCAP, 11, 14
 Freese, K., Bodenheimer, P., Spolyar, D., Gondolo, P. 2008, ApJ, 685, L101
 Freese, K., Gondolo, P., Sellwood, J. A., & Spolyar, D. 2009, ApJ, 693, 1563
 Freese, K., Ilie, C., Spolyar, D., Valluri, M., Bodenheimer, P. 2010, arXiv1002.2233
 Greif, T. H., & Bromm, V. 2006, MNRAS, 373, 128
 Greif, T. H., Johnson, J. L., Klessen, R. S., & Bromm, V. 2008, MNRAS, 387, 1021
 Gustafsson, B., Edvardsson, B., Eriksson, K., Jørgensen, U. G., Nordlund, Å., & Plez, B. 2008, A&A 486, 951
 Heger, A., Woosley, S., Baraffe, I. & Abel, T. 2002, in Lighthouses of the Universe: The Most Luminous Celestial Objects and Their Use for Cosmology, eds. M. Gilfanov, R. Sunyaev, and E. Churazov, ESO Astrophysics symposia, Springer-Verlag, p. 369 (astro-ph/0112059)
 Hopkins, P. F., Richards, G. T., Hernquist, L. 2007, ApJ, 654, 731
 Hubeny, I., & Lanz, T. 1995, ApJ, 439, 875
 Iocco, F., Mangano, G., Miele, G., Pisanti, O., & Serpico, P. D. 2007, Phys. Rev. D 75, 087304
 Iocco, F. 2008, ApJ, 677, L1
 Iocco, F., Bressan, A., Ripamonti, E., Schneider, R., Ferrara, A., & Marigo, P. 2008, MNRAS, 390, 1655
 Iocco, F. 2009, Nucl. Phys. Proc. Suppl. 194, 82
 Johnson, J. L., Greif, T. H., & Bromm, V. 2008, MNRAS, 388, 26
 Johnson, J. L., Greif, T. H., Bromm, V., Klessen, R. S., & Ippolito, J. 2009, MNRAS, 399, 37
 Johnson, J. L. 2009, arXiv0911.1294
 Lejeune, T., Cuisinier, F., & Buser, R. 1998, A&AS 130, 65
 Maizy, A., Richard, J., De Leo, M. A., Pelló, R., Kneib, J. P. 2009, A&A, in press (arXiv0910.4910)
 Natarajan, A., Tan, J. C., & O’Shea, B. W. 2009, ApJ, 692, 574
 Ricotti, M., 2009, arXiv0911.2793
 Ripamonti, E., Iocco, F., Bressan, A., Schneider, R., Ferrara, A., & Marigo, P. 2009, in Identification of dark matter 2008, PoS, p.75
 Ripamonti, E., Iocco, F., Bressan, A., Schneider, R., Ferrara, A., & Marigo, P. 2010, in preparation
 Salati, P., & Silk, J. 1989, ApJ, 338, 24
 Savage, C., Gelmini, G., Gondolo, P., & Freese, K. 2008, JCAP, 4, 10
 Scannapieco, E., Schneider, R., & Ferrara, A. 2003, ApJ, 589, 35

- Schaefer, D. 2002, *A&A*, 382, 28
- Schaefer, D. 2003, *A&A*, 397, 527
- Schleicher, D. R. G., Banerjee, R., & Klessen, R. S. 2009, *PhRvD*, 79, 3510
- Scott, P., Edsjö, J., & Fairbairn, M. 2008, in *Dark Matter in Astroparticle and Particle Physics: Dark 2007.*, ed. H. K. Klapdor-Kleingrothaus & G. F. Lewis (World Scientific, Singapore), 387–392 (arXiv:0711.0991)
- Scott, P., Fairbairn, M., & Edsjö, J. 2009a, *MNRAS*, 394, 82
- Scott, P., Edsjö, J., & Fairbairn, M. 2009b, arXiv:0904.2395
- Scott, P., Sivertsson, S. 2009, *Phys. Rev. Lett.*, 103, 211301
- Sivertsson, S., Gondolo, P. 2010, in preparation
- Sokasian, A., Yoshida, N., Abel, T., Hernquist, L., & Springel, V. 2004, *MNRAS*, 350, 47
- Spolyar, D., Freese, K., & Gondolo, P. 2008, *Phys. Rev. Lett.*, 100, 051101
- Spolyar, D., Bodenheimer, P., Freese, K., Gondolo, P. 2009, *ApJ*, submitted (arXiv0903.3070)
- Stacy, A., Greif, T. H., & Bromm, V. 2009, *MNRAS*, in press (arXiv0908.0712)
- Taoso, M., Bertone, G., Meynet, G., & Ekström, S. 2008, *Phys. Rev. D*, 78, 13510
- Trenti, M., & Stiavelli, M. 2009, *ApJ*, 694, 879
- Trenti, M., Stiavelli, M., & Shull, M. 2009, *ApJ*, 694, 879
- Tumlinson, J., & Shull, J. M. 2000, *ApJ*, 528, L65
- Turk, M. J., Abel, T., & O'Shea, B. 2009, *Science*, 325, 601T
- Umeda, H., Yoshida, N., Nomoto, K., Tsuruta, S., Sasaki, M., & Ohkubo, T. 2009, arXiv:0908.0573
- Weinmann, S. M., & Lilly, S. J. 2005, *ApJ*, 624, 526
- Yoon, S.-C., Iocco, F., Akiyama, S. 2008, *ApJ*, 688, L1
- Yoshida, N., Abel, T., Hernquist, L., & Sugiyama, N. 2003, *ApJ*, 592, 645
- Zackrisson, E., Bergvall, N., Olofsson, K., & Siebert, A. 2001, *A&A*, 375, 814
- Zitrin, A., Broadhurst, T., Rephaeli, Y., Sadeh, S. 2009, *ApJ* 707, L102